Experimental and Theoretical Studies of TAML® Activators :

Pharmaceuticals Degradation, Nuclear Tunneling and Electronic Structure Analysis

A dissertation submitted in partial fulfillment of

the requirements for the degree of

Doctor of Philosophy

Longzhu Q. Shen

Department of Chemistry

Carnegie Mellon University

Pittsburgh, PA 15213

May 6, 2013

Dedicated   to

my   Father

my   Sister

and   my   Beloved   Yanhong

羁 鸟 恋 旧 林，池 鱼 思 故 渊。

久 在 樊 笼 里，何 时 返 自 然？

天 地 有 正 气，杂 然 赋 流 形。

下 则 为 河 岳，上 则 为 日 星。

于 人 曰 浩 然，沛 乎 塞 苍 冥。

See   the   invisible,   Do   the   impossible.

Learn   to   be   flexible,   and   you'll   be   Invincible.

The   greatest   pleasure   in   the   world

is   to   do   what   people   say   you   cannot.

If you have not achieved it after the nth attempt,

it is simply because you have not yet tried the n+1th.

𝔚𝔦𝔰𝔰𝔢𝔫   𝔪𝔞𝔠𝔥𝔱   𝔣𝔯𝔢𝔦.

Contents

4   Nulear Tunneling in $[\text{Fe}^{\text{V}}(\text{O})(\text{B}^*)]^{-1}$ Mediated Intermolecular C$-$H Bond Activation   109

List of Tables

List of Figures

List of Schemes

Preface

Green chemistry is interdisciplinary by nature. This motivated me to pursue on this course since the beginning of my Ph.D. The reason that I like to stand in the interdisciplinary arena is because interfaces, to my believe, are the places where innovation burgeons and discovery thrives. What's more, green chemistry orients all these multiple disciplines toward the sustainability direction. To vault cross fields, in my opinion, requires two fundamental conditions. One is an open-minded leadership and the other one is a multidimensional research subject. Dr. Collin's research group and his research object TAML activators present such an opportunity. To study the electronic structure, reactivity and mechanistics of TAML activators requires an integration of knowledge from physical, theoretical, analytical, computational and many other fields in chemistry. It embodies my vision of the anchor points for green chemistry described in chapter 1.

Projecting green chemistry on to the combined basis based on its principles, challenges and technical domain maps out my Ph.D. training plan. Each chapter of this thesis can reflect the connection between technical knowledge and green chemistry focal points.

Chapter 1 — overview of green chemistry as an interdisciplinary arena

Chapter 2 — research at United Nations on the issues of persistent organic pollutants and toxic elements

Chapter 3 — theoretical study the electronic configuration of Co complexes and analysis on the influence on electronic state by the ligand effects with the vision for water splitting

Chapter 4 — theoretical study on nuclear tunneling effects in Fe(V) mediated intermolecular C-H bond activation to shed light on the reaction mechanisms that can be potentially helpful to decontaminate hydrocarbons

Chapter 5 — application of TAML activators in degrading recalcitrant active pharmaceutical ingredient sertraline which shows TAML mirroring cytochrome P450 metabolism

Chapter 6 — application of TAML activators in degrading persistent and disruptive active pharmaceutical ingredient prozac which inspires green pharmaceutical design

Looking back the distance I have covered during my Ph.D., every step I made was under the strong encouragement and constant support from my advisors, friends and family. I would like to take advantage of this opportunity to acknowledge the care and help from you all.

Terrence Collins : Terry, it goes beyond my language capability to find the exact right word to carry the precise meaning that I would like to present to you. I think "open-minded leadership" is the closest I can think of for at the moment. In my view, leadership and management are two different things. One is about "doing the right thing" while the other one is about "doing things right". There are many managers in the world but hardly a good leader. Your vision into the future goes beyond my imagination and your scope of knowledge is always of my admiration. Without your leadership, no way the depth and the breath of my exposure during my Ph.D. training could even be imaginable. Through working you, I learnt that freedom is the summit of the mountain of humanity; however, the path to it is full of thorns and thistles. Only the brave souls fueled with unshakable self-confidence and dauntless

determination can sustain to their dream destination. I truly appreciate for all the wisdom you have shared with me in the past years. They enlightened me both not only how to do world-class science but also on how to be a man. Among all, what has benefited me most is the inequivalent opportunities that have been fostered by your leadership, with which I could attempt and achieve a multidimensional development of myself.

Mark Bier : Mark, I still remembered the first time I sat in your class. Your highly organized presentation really captured me. An idol of clearness has appeared. I was immediately attracted to mass spectrometry. Under your directions, I have accumulated a lot of knowledge of the field and it has benefited more than I can measure. You're a person who is ready to lend your hand when need is around. Such a quality makes me always look up to you and crave for opportunities to work with you. One thing you told me that I still remember today is that "one of the responsibilities of a professor is to help young people grow." You said so and you did so. You have created numerous opportunities for me to raise my horizon and expand my connections in the field of mass spectrometry and the analytical society on a broader scale. I always look forward a pleasant and rewarding experience when I have a chance to work with you. I remembered the my first conference experience in US was attending the ASMS conference with you in Philadelphia in 2009. I remembered the pleasant conversations we had together while walking to the conference center for the ASMS conference in Denver in 2011. I will never forget the most innovative CO_2 artwork project under your supervision in 2012. I can not say thank you enough for the countless help on mass spectrometry and many opportunities for career development. In one word, working with you always makes me feel fulfilled.

Emile Bominaar : Emile, you are probably the deepest person I have seen so far in my life. I feel like I am a person who always attempts to go a bit deeper whenever

possible. This kind of mentality makes it not easy for me to reach satisfaction while seeking solutions to a problem or an explanation for an interesting observation. Sometimes, I even feel it is hard to share my feelings with someone even. But things have changed since I started working with you. You seem to know all the fundamentals and based on that your analysis always comes out convincing. I really feel lucky to have the chance to work on the Co electronic structure and the nuclear tunneling project. Through those projects and many personal conversations, I feel my horizon on quantum mechanics has been upgraded significantly. In addition to the deepness of your scientific knowledge, I am really amazed by your way of presenting the answers to the questions in perceptible ways. Sometime I am sloppy at math derivations. After working with you, I gradually become clearer and better organized. That is a tremendous improvement for me. Apart from your superior intelligence, I also admire that you're a caring person. You create a lot of opportunities for your students to learn better and achieve more. I really cherish the opportunity of working with you and truly appreciate the generous help from you. You have built a great professor imagine that I always look up to.

Catalina Achim : Catalina, you are the person who updated my view of chemistry. You class of transition metals was the start point for me to implement the molecular orbital theory in practicing chemistry. I can not tell how much it meant to me in revolutionizing my stance in chemistry. The ethics and communication issues in scientific research class coinstructed by you and Rongchao was extremely valuable to students who feel like taking academics as their career path. Apart from scientific advice, I also had a lot communications with you regarding to my career development. Your advice and suggestions helped me reorient myself multiple times in the directionless sea between now and future. I would like to thank you for all scientific knowledge and career advice from you. I believe they will guide me further on my professional

path.

Colin Horwitz : Colin, I want to take this opportunity to thank you for the all the help from you. I consulted your advice multiple times on the sertraline and fluoxetine degradation projects. Your scientific insight was indeed very helpful for me to conceive strategies to tackle those challenging problems. You're a very open-minded person. A lot of kind advice from you on my career development was enlightening and your constant encouragement was extremely important to me. Many thanks.

Alexander Ryabov : Sasha, you opened the door of chemical kinetics to me. It was a pleasant acquaintance. You also offered a lot of constructive suggestions on the revision of my sertraline manuscript. I also want to appreciate that. In addition, you also have organized many social occasions in the past years. I also enjoyed all those events.

Dwight Tshudy : Dwight, we had a great collaboration on the sertraline and fluoxetine projects. You knowledge on chromatography injected howling momentum to the progress of these two projects. I have learned tremendously on chromatography through working with you. I really appreciate your help.

Michael Hendrich : Mike , I want to thank you for introducing the fundamentals of EPR and Mössbauer spectroscopy to me. My exposure to these two fields dramatically elevated my scientific stance. Up to day, I still enjoy digesting the knowledge whenever I can. I asked a lot of questions when I was in your class. Some of them were quite naïve when I look at them today. Regardless, you were always patient with me and found time to help me. That really touched me as a student. I want to say "thank you" for all the time from you to help me gain deeper understanding on paramagnetism of transition metals. Their values are beyond measure to me for now and future.

Tomasz Kowalewski : Tomek, it was unforgettable time to work with you and Rongchao in Lab IV in 2009. My knowledge and skills on mathematica was tremendously en-

hanced through this experience. The unmatchable analytical and graphing capability of this wonderful software really empowered me incalculably on my research. All the figures of chromatograms, mass spectra, UV-Vis spectra, kinetic data analysis, and all the mathematical derivations were produced using mathematica. I really appreciate that I got access to this omnipotent skill through working with you.

Miguel Llinás : Miguel, I'm so glad that I have attended the advanced NMR under your instruction in 2010. It have not only boosted my vision on NMR, but also enhanced my understanding of quantum mechanics. In addition, your affirmation on the merit of my use of LaTeX was real encouragement to me. I would like to thank you as a great professor as well as a great guider.

Roberto Gil : Roberto , I'd like to thank you for all the help on the NMR spectroscopy. It has become one key analytical techniques in my graduate research. The causal NMR class in the Summer 2010 opened the door of NMR to me. Built on top of that, I went further into the delicate and powerful technique. It was a fun as well as rewarding experience.

David Yaron : David, I had discussions with you on the thermodynamic calculations using gaussian. I have enhanced several fundamental concepts from talking with you . Other than that, I also consulted you multiple times in regard to the future opportunities in the theoretical trajectory. Your suggestions were always encouraging and inspiring. I want to thank you for your help from multiple aspects.

Rongchao Jin : Rongchao, I felt very lucky to know you and work with you. I have sought advice from you several times, either in your office or on the air plane back to Pittsburgh, on the career development. Your analysis and suggestions were very instructive to me. I truly appreciate that.

Gayathri Withers : Gayathri , you gave me a lot of help the NMR facility. It happened that my research often times requires non-routine techniques on the NMR operations.

For my customized-request, you always tried to cover the extra miles to help me meet my analytical needs. Because of the help from you, I was able to collect high quality data for my research . I thank you for all the help from you in the past years.

Rea Freeland : Rea, my completion of my Ph.D. program is indispensable of all the kind advice from you. I have consulted your advice at various stages of my Ph.D., sometimes at very short notice. Every time, you could find time to address my concerns and suggest strategical plans for betterment. I really truly appreciate your kind help.

Soumen Kundu : Soumen, we entered the program in the same year and have spent a lot of wonderful times together. Your breath of knowledge and width of mind is of my admiration. You're a countable colleague and a great friend. You have helped me countlessly on organic chemistry. I enjoyed our wonderful and fruitful collaboration on the Fe(V) C-H bond activation work. I also enjoyed the great runs and laughs we had together. It was my great pleasure to have friend like you. I truly hope you can enjoy your new research in Canada and hope to have chance to work with your again in the future.

Evan Beach : Evan, I started my program by working with you. You set up a great example for me in performing analytical chemistry in an organized and detailed manner. In addition, your synthesis of sertraline ketone was an inestimable to the project of sertraline. You also provided a lot of wise advice on my personal advancement. I really appreciate all that I have learnt from you.

William Chadwick Ellis : Chad, it was really great to know you and have the opportunities to work with during my Ph.D. In my opinion, you are a good leader, not only for your vision in science, but also from the care for the people behind you. I had an unforgettable experience working with you the Co project. I had learned a lot more than I can imagine through it. You also kindly offered a lot of advice on the career

development. I can not tell how much gratitude I owe to you.

Natalya Khanina : Natalya, it was my great pleasure to work with you on the sertraline project. Your work on the quantitative analysis of sertraline degradation products was fabulous and it resulted in a key figure in the publication. I very much appreciate your work.

Matt DeNardo : Matt, we have spent a lot of times together to attend conferences or other social events. You're such a knowledgeable and helpful person. I turned to your help on organic chemistry and computer related issues for unnumbered times. You helped me out munificently all the times. I don't know how to say thank you enough to you. I believe your intelligence and creativity will pave your way for a great future.

Karla Arias : Karla, you're one of the most friendly and helpful person I have ever seen. We had a lot of great times together in multiple occasions. The trip to Europe in the summer 2012 was most unforgettable. I also enjoyed working with on the environmental group sustainability projects. Steve helped us with a magnificent photograph of the CO_2 artwork. I really enjoyed the great times I had with you and Steve, and thank you both for all the help.

Iulia Sacui : Iulia, we hung out often since the beginning of our Ph.D. program. You're such a great friend who always thinks for and cares about her friends. We spent a lot of times together in many social occasions. I have learned a lot about American culture from you. I hope you have been enjoying your postdoc experience and start your new career.

Halimatu Mohammed : Hali, it is great to know you and become your friend along the Ph.D. program. We had a lot of good times together. You taught me spiritual power such as optimism and determination. I thank you very much for that. Also, bring my thanks to Mohammed for the driving lessons.

Bethany Drake : Beth, it was a great experience to work with you in the lab. You're

a very helpful, friendly and highly organized person. Through working with you, I have learned a lot about planning and organization. You and Derek offered a lot of help to me in terms of American culture and need for early settlement. We also have attended many scientific meetings and social gathering together. It was an unforgettable memory. I hope you enjoy your work at EPA.

Jesse Miller : Jesse, hacky sack buddy. I do miss those wonderful hacky sack times. What I miss more is your character — ready to help and willing to offer. This virtue is always worth my learning. I hope you enjoy your current work at EPA.

Ronald Ripper : Ron, I am very to get to know you and learn to operate Ion Chromatography (IC) under your instruction. Your knowledge on the instrumentation and generous help under short notice was extremely important to my research. Many thanks.

Valerie Bridge : Valerie, I can not even recall how many times I stopped by your office to ask questions or help, and how many times you responded my quest amazingly soon. You know all the details about the department and the university. When my request is beyond your scope, you also helped to point me to the right directions. I really appreciate all that help from you.

Sara Wainer : Sara, I received a lot of help from you on the matters such as classroom reservations, supporting letters, and many others. Most of times, I needed quickest answer that can be given to my questions. You provided the immediate help almost every time. Thank you much for all you have done that have made all the processes I need to go through smooth and straightforward.

Brenda Chambers : Brenda, you gave a lot of help to me during my Ph.D. period. The one I remembered most clearly is the cater menu in 2011. It was my first time to try to organize a seminar event. Lack of experience, I was desperate for advice on best meal choice for the event with the limited budget. Your kind offer no difference

from water to the thirst. Please accept my thanks for this and many other occasions you have helped me generously.

Patsey Hadlock : Patsey, you helped most with my reimbursement request. Somehow I usually missed something on the forms I submitted in. You were always patient and helpful in getting them through after back and forth communication with me. I want to thank you for all the extra time and effort you have spent to help me.

Heather Juzwa : Heather, it is a great pleasure to know you and work with in the ACS local society. Your level of leadership is beyond measure. The working experience with you indeed helped escalate my position on how to work with professionals. Please accept my best thankfulness to you.

Eric Lanni : Eric, you're such a helpful and resourceful person on mass spectrometry instrumentation. I'll never forget the great experience I had together with you on building the APPI (atmospheric photo ionization) source. At that time, I was just beginner to mass spectrometry. You offered a lot of your time to help me. I'm ever thankful to you for all your help.

Penlin Ye : Penglin, we knew each other for a long time. You helped me in multiple aspects, ranging from driving to career advice. You're a super helpful person and a great friend. I truly appreciate all the help I have obtained from you.

Zheng Cui : Zheng, you're a caring person and a great friend. You offered a lot of kind advice to me and Yanhong. Your wisdom and foresight were priceless to us. I'm super grateful for knowing you and being your friend.

Lirong Wang : Lirong, it is great to know you in the late stage of my Ph.D. You offered a lot of suggestions to in my career development suggestions. I really want to express my sincere thanks to you for all that help.

Matthew Stadler : Matt, you kindly offered a lot of kitchen goods when I just arrived in Pittsburgh. Many thanks for that and a lot of help on other matters.

In the end, I also would like to thank my family for their constant encouragement. Without it, I could not imagine of going through the Ph.D. program.

Father, you have taught me so well on the mental fortitude by setting yourself as a perfect example. The strong will power of recovery from the attack of a stroke has spurred my momentum to charge toward my goal of life with full strength. Even though there are meant to be hurdles and barriers on the way to my destiny, I am hopeful and affirmative because of the dauntless virtue I have inherited from you. It is the greatest fortune I can have and be proud of. I'm determined to keep the spirit on and always pursue better and higher throughout my entire life. Thanks so much father for that gift from you.

Jingjing, my lovely sister. Although you're younger than me, you have endured a lot more than I have by entering the real world much earlier. You're very successful as a pharmaceutical professional. But the way to it is far way from easy. Your determination and courage to chase after your dream is of my great admiration and has inspired me in multiple ways. I wish all the best to you. I sincerely hope you can attend my graduation ceremony in May.

Yanhong, my beloved. Your love and support to me deify all my words. I just feel so lucky to be your husband that I could share with you all those laughs and tears. I can not tell how much I admire your entrepreneurship and how much it has encouraged me to be forward looking. I believe our dream will eventually come under our collaborative effort. I love you.

Abstract

Green chemistry concerns the scientific disciplines that support sustainability as their zenith. Sustainability has both temporal and spacial dimensions. The addition of the spacial dimension to it has significantly enhanced its visibility and horizon. Green chemistry, as an important subset of sustainability, radiates broadly and this entails a pursuer to choose their spectrum of interest. Therefore, I defined the technical domain of green chemistry from my perspective. Through projecting green chemistry onto the primary basis composed by the principle domain defined by Prof. Anastas and challenges domain interpreted by Prof. Collins and the technical domain by my definition, I mapped out my green chemistry trajectory. In a word, my Ph.D. training can be summarized as a research journey of combating persistent organic pollutants, characterizing the electronic signature of catalysts for renewable energy generation and catalytically oxidizing active pharmaceutical ingredients and hydrocarbons via a combinatorial avenues of computation, analysis and scientific inference. In view of the problem space of green chemistry, seeking renewable energies and eliminating persistent, disrupting or toxic compounds appear on the higher levels according to Prof. Collins. I attempted to tackle all the four problems to certain degrees during my Ph.D.

Energy has propelled the engine of human civilization for hundreds of years. Today, the fossil fuels, the natural reserves we rely upon in the past, have approached their

limit. More significantly, their continuing use shadows the sustainable future of human beings as well as the lives of all forms on this planet. An urgent need horizons for better ways to capture and convert solar energy to carbon neutral forms of chemical energy. The lesson from photosynthesis provides a promising answer — water splitting. To mimic this process, developing catalysts for water cleavage becomes the central theme. Among all the earth abundant and inexpensive elements, Co stands out for its high efficiency and dual capability of water reduction and oxidation. Between the two, water oxidation presents the major challenge. Co(IV) was shown to be the active intermediate in this chemical conversion. This highlights the importance of precise characterization of the electronic structure Co containing catalysts. To this end, I combined the spectroscopic information and DFT calculation to clarify the literature ambiguity in the diagnosis of Co containing complexes, and theoretically projects the avenue to acquire a Co(IV) electronic state in coordination complexes.

The study of eliminating persistent organic pollutants was performed in the United Nations in the summer 2011. Apart from a technical summary of my research, I also identified two important causes that impasse on many environmental issues between nations. This signifies a global leadership that can unify and usher the international strength toward the sustainable summit.

The research experience in the United Nations showed hydrocarbons and their halogenated derivatives are very resistant to natural attenuation. Then I started my fervent pursuit of hydrocarbon hydroxylation study via theoretical modeling. Comparing theoretical with experimental studies, the reaction rates of $[\text{Fe}^{\text{V}}(\text{O})(\text{B}^*)]^{-1}$ with ethylbenzene (EtBZ) and its isotope labeled species EtBZ-d10 differ in three respects: (i) the initial $[\text{Fe}^{\text{V}}(\text{O})(\text{B}^*)]^{-1}$ decay rate for the substrate EtBZ-d10 is slower than that for EtBZ, (ii) the slope of the $\ln(k/T)$ vs. $1/T$ plot of EtBZ-d10 is smaller than that for EtBZ over the experimental temperature range, and (iii) the extrapolated tan-

gents of the kinetic curves give a large, negative intercept difference, Int(EtBZ) - Int(EtBZ-d10) < 0 at the limit $1/T \to 0$. Theoretical analysis, based on density functional theory calculations of thermodynamic parameters of the reaction species and Bell's model for tunneling through quadratic barriers, shows that (i) and (ii) result from isotope-induced changes in both the zero-point energies and nuclear tunneling, whereas (iii) is exclusively an isotope mass effect on tunneling. The research result points out nuclear tunneling has a significant contribution to the hydrocarbon hydroxylation process. A theoretical model was proposed that can be used to predict absolute rate constants outside the experimental fathomable range.

In addition to persistent molecules, endocrine disrupting chemicals also deserve special attention. Active Pharmaceutical Ingredients (APIs) have been recognized as a hot-spot environmental pollutants largely due to their high disrupting potency. These anthropocentric synthetics compounds are mostly designed to aim at evolutionarily conserved targets to trigger biological responses at minute levels and optimized for extra degradation resistance for stable shelf lives. All these therapeutic benefits translate into ecotoxicity concerns when the parent compounds or their metabolites are released to the environment. A large body of literature has linked the exposure to APIs to Biological disasters. Under such a context, I applied TAML activators to treat to highly prescribed antidepressant drugs, Zoloft and Prozaic. The API for each is sertraline and fluoxetine.

In the sertraline degradation study, I demonstrated that TAML activators at nanomolar concentrations in water activate hydrogen peroxide to rapidly degrade this persistent API. While all the API is readily consumed, degradation slows significantly at one intermediate, sertraline ketone. The process occurs from neutral to basic pH. The pathway has been characterized through four early intermediates which reflect the metabolism of sertraline, providing further evidence that TAML activator/perox-

ide reactive intermediates mimic those of cytochrome P450 enzymes. TAML catalysts have been designed to exhibit considerable variability in reactivity and this provides an excellent tool for observing degradation intermediates of widely differing stabilities. Two elusive, hydrolytically sensitive intermediates and likely human metabolites, sertraline imine and N-desmethylsertraline imine, could be identified only by using a fast-acting catalyst. The more stable intermediates and known human metabolites, desmethylsertraline and sertraline ketone, were most easily detected and studied using a slow-acting catalyst. The resistance of sertraline ketone to aggressive TAML activator/peroxide treatment marks it as likely to be environmentally persistent and signals that its environmental effects are important components of the full implications of sertraline use.

Fluoxetine, represents the first member of the serotonin receptor reuptake inhibitors (SSRIs) family and is one of the most successful among all members. Its top prescription record among SSRIs and extra stability leads to prevalent occurrence in the environment. Environmental studies showed that FLX can be toxic to aquatic species at trace level of exposure and disruptive to their neurosystems. Therefore, it is urgent to seek an environmentally friendly solution to diminish the harm FLX can potentially bring to the environment. Treatment with TAML activators and hydrogen peroxide, fluoxetine was shown to be rapidly degraded to harmless endpoints. An elusive intermediate along the degradation pathway was proposed and its fleet fate was studied using DFT calculations. The cascade breakdown feature of FLX under TAML$^{®}$/H$_2$O$_2$ treatment inspires green pharmaceutical design.

Chapter 1

Green Chemistry toward Sustainability — Challenges and Opportunities

> "I wish it need not have happened in my time," said Frodo.
>
> "So do I," said Gandalf, "and so do all who live to see such times. But that is not for them to decide. All we have to decide is what to do with the time that is given to us."
>
> — J.R.R.Tolkien

1.1   Green Chemistry — an Interdisciplinary Arena

According to the definition by US Environmental Protection Agency (EPA), green chemistry is the design of chemical products and processes that reduce or eliminate the use or generation of hazardous substances. Green chemistry applies across the life cycle of a chemical product, including its design, manufacture, and use.[1] Twelve principles were formulated by Dr. Anastas and Dr. Warner as the framework of the field.[2]

1. Prevention

2. Atom Economy

3. Less Hazardous Chemical Synthesis

4. Designing Safer Chemicals

5. Safer Solvents and Auxiliaries

6. Design for Energy Efficiency

7. Use of Renewable Feedstocks

8. Reduce Derivatives

9. Catalysis

10. Design for Degradation

11. Real-time Analysis for Pollution Prevention

12. Inherently Safer Chemistry for Accident Prevention

Another interpretation of the focal points of green chemistry is provided by Dr. Collins in his class at Carnegie Mellon University.[3] As seen in Figure 1.1, Dr. Collins predicts six grant challenges in the green chemistry field — developing green synthesis methodologies, developing chemistry processes to utilize renewable feedstocks, developing safe energy strategies, design against the use toxic element in chemical

processes, eliminating persistent molecular compounds, design against endocrine disruptors. The relative challenging levels among these six important questions in green chemistry are ranked in an increasing order from bottom to top as indicated by the upward arrow on the very right of Figure 1.1.

Figure 1.1: Paramount questions and great challenges in Green Chemistry presented by Dr. Collins. Top four levels with fonts highlighted in pink denotes my devotion during my Ph.D. research. Adapted from Prof. T. J. Collin's lecture notes (Introduction to Green Chemistry (09510), 2012 Spring, Carnegie Mellon University) with permission.

The interpretation of green chemistry by Dr. Collins and Dr. Anastas defines two domains for the field, i.e. the principle domain and the challenge domain. What bridges these two domains is the interdisciplinary pathway. Green chemistry covers a ever imaginable broadness in the scope of chemistry and interfaces with numerous disciplines outside chemistry. With no attempt to be complete, here a few examples

are listed below. The fields have interfaced with green chemistry include but not limited to organic chemistry,[4–6] analytical chemistry,[7,8] catalysis,[9] nano chemistry,[10] pharmaceutical chemistry,[11] industrial processes,[12] photophysical chemistry,[13] computational chemistry,[14] toxicology,[15,16] environmental policy[17] and etc.

Given the broadness of green chemistry as an interdisciplinary arena mentioned above, it necessitates an unconventional cross-boundary approach for study. It appeals to be an ideal situation if one can be versatile and in-depth in each subjects in green chemistry. However, for the given limited time for each man and unremitting progress of science, it is probably unrealistic to master all the knowledge in such a broad front as defined by green chemistry. Thus, a more rational and important approach for a scholar in this field to define their own focus and range of technical interests. With such a spirit, I defined my technical framework for green chemistry (Figure 1.2) and presented it to my Ph.D. program graduate committee.

Figure 1.2 outlines a few scientific corner stones that I would like to anchor on and in my vision that support the spin of the green planet on top. I'd like to call this framework as the technical domain of green chemistry to my definition. Together with the principle and challenges domains, I view three domains for green chemistry and green chemistry can be interconverted between each other according to certain rules. It is conceivable to project green chemistry onto the primary basis of the three domains and one can chart the course of voyage in the green Pacific.

To pursue this ambitious and highly integrated green blueprint, an encouraging academic medium and a diversified research subject form the foundation. The open-minded leadership of Prof. Collins and the TAML® activators developed under his leadership provide such an opportunity. TAML® activators are a group of synthetic efficient enzyme mimickers.[18] Its invention opens the interests on theoretical study of its electronic structure,[19,20] characterization of active reaction intermediate,,[21–23]
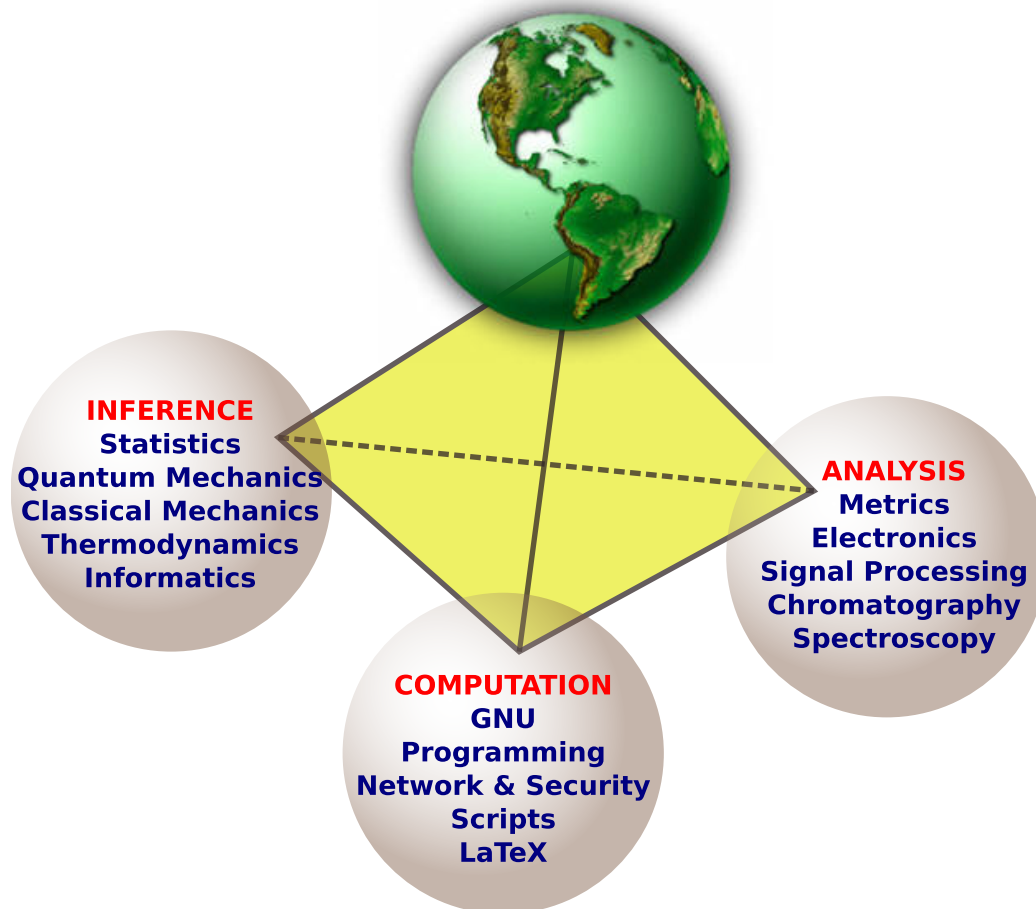
Figure 1.2: Technical framework in support of the green summit

its reaction stability and reactivity,[24–29] its application in renewable energy genera-tion[30] and its application in water purification.[29,31–36] Clearly, research on TAML® activators spans a wide spectrum of scientific disciplines. Many of the publications listed above are actually the fruitful outcome of collaborations among researchers with diverse expertise. Needless to say, the central aim of TAML® activators at deliver-ing environmental benefits and its physical nature as an interesting subject among multiple discipline create a good topic for my Ph.D. study.

Up to this point, this ship to discover is almost ready to set for sail. But before entering the endless ocean, a compass is a must-to-have instrument for directions

when no landmark can be consulted. That compass is the sustainable ethics.

1.2 Green Chemistry and Sustainable Ethics

According to the Brundtland Commission of the United Nations on March 20, 1987, sustainable development is "development that meets the needs of the present without compromising the ability of future generations to meet their own needs."[37] In this definition, the emphasis is placed on the strategical management of existing resources with the mind for future needs. Undeniably, it constructed the ultimate destiny for green chemistry as well as many other social and scientific sectors progressing toward the future, although the long-run foresight might not be accessible by the immediate vicinity philosophy. A more generalized definition of sustainability, given by International Union for Conservation of Nature (IUCN), is the capacity to maintain a certain process or state, as "improving the quality of human life while living within the carrying capacity of supporting ecosystems".[38,39] This definition covers the spacial character of sustainability and stresses the conservation of the serving capacity of the ecological system from now and on.

The capacity of ecosystems to be self-renewing, dynamically adaptive, and supportive of humanity depends on interaction of networks and biogeochemical pathways.[40,41] However, this interwoven ecological system and its service function is being severely damaged by imprudent human activities. Many chemicals and their products, despite their intention for benefits, are detrimental to biodiversity, human health, and the service functions of the entire ecosystem. It poses an alarming threat. If no counteracting measures are taken to curb the trend in time and at the right scale, the continuity of human civilization is endangered. The accumulative harmful effect can certainly be foreseen to lead catastrophic effects for the future generations. But

the damage indeed has already started and progresses with faster paces. So, in my opinion, it is crucially important to position the concept of sustainability in the immediate temporal and spacial perspectives to make aware the urgency of the issue and desperate need for green innovations.

Sustainability, in my view, is the overarching guidance for green chemistry but not limited to green chemistry. The walks of all lives and science of all disciplines need to appreciate the significance of sustainable practice from all perspectives. With the ultimate aim of sustainability in watch, green chemistry can be pursued.

1.3 Advanced Analytical Techniques in Environmental Monitoring

To eliminate the treat, we should first identify and quantify the treat. Advancement of analytical technologies provide an indispensable scope through which the environmental contaminants can be exposed. Speaking of trace level detection, mass spectrometry has to be mentioned for its known quality of searching a needle in a haystack.

The foundation of mass spectrometry probably started with J. J. Thomson's discovery of electrons and determination of its mass-to-charge ratio in 1886. Later, he constructed the first mass spectrometer in 1913 and observed isotopes for neon.[42] In 1923, F. W. Aston measured mass defect using mass spectrometry.[43] This sensational discovery together with Albert Einstein's deduction and later developed quantum mechanics laid the foundation of nuclear fusion theory,[44] which can be the shortcut toward to energy sustainable path if can be realized. This is another instance that convergence of multiple disciplinary endeavors can pave the way for sustainability.

The most significant contribution to mass spectrometry or even the entire analytical

society for the 20 century can probably be ascribed to the development of electron spray ionization (ESI) on mass spectrometry by J. Fenn.[45,46] The ionization mechanism of ESI will be discussed below.

The overall ion formation process in ESI includes three major stages: production of charged droplets from the electrospray capillary tip, repetitive shrinkage of the charged droplets and the ultimate gas-phase ions formation, as schematized in Figure 1.3
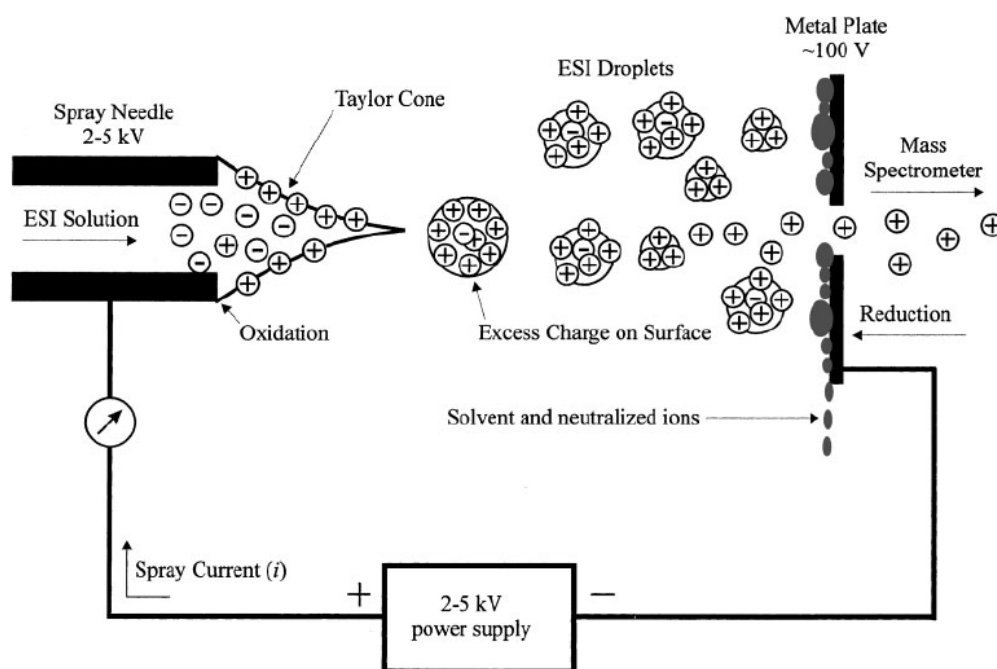
Figure 1.3: Schematic drawing to illustrate the ionization mechanism in ESI. Reprinted from N.B.Cech and C.G.Enke, Mass. Spectrom. Rev. 2002, 20, 364 with permission. ©2002 Wiley Periodicals, Inc.

• Charged Droplets Production

A voltage of 2 - 5 kV is applied between the metal capillary (ESI needle) and the counter electrode. This potential can be positive or negative, depending on the analytical purpose. For simplification, only the positive mode will be discussed here. The metal capillary typically has the dimension of 0.2 mm O.D. and 0.1 mm I.D.,

located 1 - 3 cm away from the counter electrode. The high electric potential and the narrow capillary leads to a strong electric field ($E_c \approx 10^6$ V/m), which can be evaluated by eqn (1.1).[47]

$$E_c = \frac{2\,V_c}{r_c \, \ln\left(\dfrac{4\,d}{r_c}\right)} \tag{1.1}$$

where V_c is the applied potential, r_c is the capillary O.D. and d is the distance between the capillary tip and the counter electrode. The imposed strong electric field pulls the cations moving downfield toward the capillary tip and drives the anions drifting away from the surface, known as electrophoretic movement.[48] As the electrostatic force counterbalances the surface tension, a "Taylor" cone[49] takes shape at the tip. If the applied field is sufficiently high, the "Taylor" cone is destabilized and a fine jet will emerge from the cone tip which degrades into charged droplets. The onset potential for the electrospray to occur is given by Taylor.[49]

$$V_{on} = 2 \times 10^5 \sqrt{\gamma\, r_c} \, \ln\left(\frac{4\,d}{r_c}\right) \tag{1.2}$$

where γ is the surface tension of the spray solvent and r_c is the ESI needle O.D.

It can be seen from the equation that there exits an inverse relationship between the surface tension and the onset voltage. For instance, the onset voltage for methanol is 2.2 kV, whose surface tension is 0.023 Nm^{-2} and that for water is 4.0 kV, whose surface tension is 0.073 Nm^{-2}.

• Charged Droplets Evaporation and Fission

The charged droplets shrink their volumes as a result of solvent evaporation. The charge on the droplets is expected to be maintained during the evaporation process because ion transfer from liquid to gas phase is highly endoergic.[47] The net result of

droplet surfaces diminish with charge conservation leads to accumulation of electrostatic repulsion on the surface. When a droplet's diameter D and charge q satisfy the Rayleigh equation,[50] uneven coulombic fission occurs to produce offspring droplets.

$$q^2 = 8\,\pi^2\,\epsilon_0\,\gamma\,D^3 \qquad (1.3)$$

where ϵ_0 is the permittivity of vacuum.

The offspring droplets usually carry off 2% of the parent mass but 15% of the parent charge.[50] The diameter of the offspring droplets can be approximated by eqn (1.3).[51]

$$d \approx \left[\frac{\gamma}{\rho} \left(\frac{\epsilon}{K} \right)^2 \right]^{1/3} \qquad (1.4)$$

where d is the diameter of the offspring droplet, γ, ρ, ϵ and K are the surface tension, density, permittivity and conductivity of the solvent. It is shown in the equation that size of the offspring is approximately independent of the parents. Relieving from the coulombic stress, the offspring droplets continue to evaporate until approaching the Rayleigh limit again and another fission will occur. This process repeats itself to produce smaller and smaller droplets, as shown in figure 2. The time scale for evaporation is usually on the order of hundreds of milliseconds. Also, as the droplet sizes become smaller, the time span for the next generation droplets production is shortened.

• Gas-phase Ion Formation

The offspring droplets undergo a series of successive fission steps and eventually lead to gaseous ions. The final creation of gas-phase ions have been addressed by two theoretical models, the charge residue model (CRM), proposed by Dole and coworker,[52,53] and the ion evaporation model (IEM), proposed by Iribarne and Thomson.[54,55] CRM states that the successive fission process is continuously shedding offing offspring
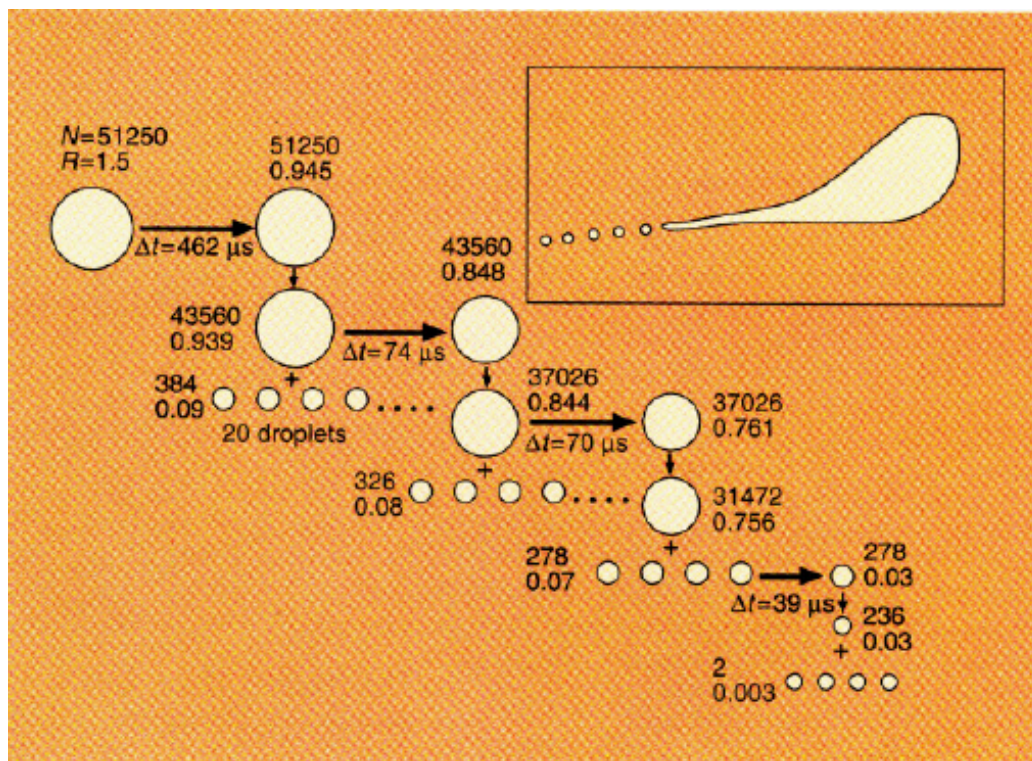
Figure 1.4: Scheme of droplets fission process in ESI. Reprint of P. Kebarle and L. Tang. Anal. Chem. 1993, 65, 977A with permission. ©1993 American Chemical Society.

droplets until only a signal ion is left. IEM maintains that solvated ions are possibly emitted from droplets directly when the electric field is strong enough and their radii become small enough. Both models have found experimental support. The IEM is usually involved in the production of small ions such as the conventional inorganic and organic ions, while CRM is involved in the production of macroions such as the globular proteins.[56,57]

The electrophoretic process makes ESI a special continuous electric current device. The electric circuit starts from the positive terminal of the power supply, enters the solution via a metallic contact, follows the charged droplets arriving at the counter electric plate and goes back into the negative end of the power supply, as depicted in figure 1. In order to maintain the flow of current and keep the charge balanced in the

solution, electrochemical oxidation reactions must occur at the liquid-metal interface of the capillary. Thus, ESI can be viewed as a special electrolytic cell.[58,59]

$$M(s) \longrightarrow M^{2+}(aq) + 2\,e^-$$
$$4\,OH^-(aq) \longrightarrow O_2(g) + 2\,H_2O + 4\,e^-$$
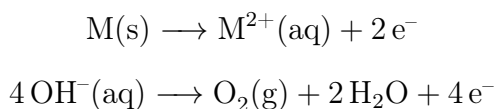
The amount of the electrons produced during the electrochemical reactions equal the amount of the charge separated at the tip of the electrospray capillary. It is expected that the oxidation reaction will happen predominantly on the the substance with the lowest reduction potential, which can be the metallic electrode, the ions present in the solution or the spray solvent itself.

When interfacing with chromatography, the hyphened technology demonstrated exceedingly power in scrutinizing the environmental media for chemical information.[60,61] In my research, mass spectrometry and coupled chromatography-mass spectrometry were heavily employed in molecular structure elucidation and quantitation (chapter 5 and 6).

1.4   Active Pharmaceutical Ingredients (API) and their Concerns in the Environment

Pharmaceuticals made of synthetic chemicals are designed to alleviate human pathological syndromes or protect people from potential health threat. After completing their clinical mission, pharmaceuticals or their active metabolites enter the second phase of their life cycle after released into the environment. As result of advancement of modern analytical techniques, active pharmaceutical ingredients (APIs) are detected in trace amount level the environment,[62–64] especially in water bodies, such as waste water,[65,66] surface water[67] and even drinking water.[68,69] They soon were

recognized as a hot-spot environmental pollutants.[70] Although the current environmental concentrations of APIs are unlikely to pose acute toxicity to human being,[71,72] the limited knowledge about chronic exposure and synergic effects places a question mark in long-term risk assessment of APIs. Considering that these anthropocentric synthetic compounds are mostly designed to aim at evolutionarily conserved targets to trigger biological responses at minute levels and optimized for extra degradation resistance for stable shelf lives,[73,74] their potential link to ecotoxicity is worth special attention.[75] A large body of report that link the exposure to APIs to Biological disasters can found in literature. For example, a seven years of study shows that estrogenic ingredients in birth control pills induced the feminization of fish in an experimental lake in Canada and collapsed the whole fish population.[76] Also, diclofenac an anti-inflammatory drug has been found to cause 95% decline of Oriental white-backed vulture population in a national park in Pakistan.[77] Therefore, precautionary principles should be born in mind toward APIs risk evaluation and management.

Currently, water treatment methods are inadequate to remove pharmaceuticals from sewage treatment plants (STP).[78–82] Although, advanced sewage treatment methods (e.g. ozonation,[83] osmosis[84] etc) exist, their utilization is limited owing to the economic and sustainable consideration.[85] Therefore, there is a great impetus to seek for environmentally friendly and economically viable technologies to treat the current pressing issue of pharmaceuticals in the environment.

1.5 Mimicking Enzymes in Decontaminating Environmental Pollutants

Chemically speaking, there are two major ways to destroy a molecule, one is oxidation and the other is hydrolysis. Oxidation is well availed by nature as a mechanism for

living beings to fight against invasion of foreign substance, including pharmaceuticals. Oxidation reactions is mainly catalyzed enzymes of the cytochrome P450 (CYP) superfamily.[86,87] This process is termed as phase I metabolism in pharmacokinetics.[88] The reaction mechanisms by P450 have been extensively reviewed.[89–91] To give a brief overview, it can be categorized into hydroxylation, dehydorgenation and epoxidation etc. The analysis and argument for the P450 reaction mechanism is primarily based on the reactive species compound I (Cpd I).[91] Spectroscopic characterization pointed Cpd I is best described as a Fe(IV) unit exchange coupled to a ligand-based radical.[92] To mimic superior effectiveness and efficiency of CYP450 for the purpose of environmental decontamination, it is natural to build a catalytic unit with the similar electronic identity as Cpd I.

TAML® activators are provide a ligand framework to host many metals. Fe has been so far shown the outstanding performance in catalytic reactions. Spectroscopic evidence plus theoretical analysis has established the identity of Fe^V as the product of exposure to peroxide.[23] This reactive species is equivalent to Cpd I in CYP 450. Kinetic mechanistic studies supported that TAML® activators are good peroxidase mimickers. Given the fact that Fe TAML® activators functionally simulate CYP450 in theory and have an environmentally compatible elemental composition, it is expected this family of catalysts can find good use in sustainable water purification, especially answering the challenging issues with pharmaceuticals in the environment. This part of research is detailed in chapter 5 and 6.

1.6   Dissertation Roadmap

These three representations can be viewed as three domains for green chemistry, viz principles domain (list 1.1), problems domain (Figure 1.1) and technical domain

(Figure 1.2). Green chemistry can be transformed among these domains and was made integrable by choosing TAML activators as the integrand. Motivated by this scientific and logical rationale, I set out my Ph.D. safari and built this album along the way. To provide a roadmap for my trip, Table 1.1 is prepared. It illustrates the connection among the three green chemistry domains for each chapter of this thesis .

Table 1.1: Green chemistry projection and mapping in three domains. Numbers correspond to the items for the problems or principles domain. "C" represents "computation", "A" represents "analysis" and "I" represents "inference" as given in figure Figure 1.2

chapter	problems domain	principles domain	technical domain
2	2 , 3	1	A
3	4	6	C, I, A
4	2	9, 10	C, I, A
5	1, 2	9, 11	C, A
6	1, 2	4, 9, 10, 11	C, A

1.7 References

[1] *Green Chemistry definition by US EPA.* http://www.epa.gov/greenchemistry/.

[2] P. T. Anastas, J. C. Warner, *Green Chemistry: Theory and Practice*, Oxford University Press, USA, **2000**.

[3] T. J. Collins, *Introduction to Green Chemistry*, **2012**.

[4] V. Polshettiwar, R. S. Varma. Aqueous microwave chemistry: a clean and green synthetic tool for rapid drug discovery. *Chem. Soc. Rev.* **2008**, *37*, 1546–57.

[5] R. a. Sheldon. Fundamentals of green chemistry: efficiency in reaction design. *Chem. Soc. Rev.* **2012**, *41*, 1437–51.

[6] M.-O. Simon, C.-J. Li. Green chemistry oriented organic synthesis in water. *Chem. Soc. Rev.* **2012**, *41*, 1415–27.

[7] C. Bendicho, I. Lavilla, F. Pena-Pereira, V. Romero. Green chemistry in analytical atomic spectrometry: a review. *J. Anal. At. Spectrom.* **2012**, *27*, 1831.

[8] M. Tobiszewski, A. Mechlińska, J. Namieśnik. Green analytical chemistry–theory and practice. *Chem. Soc. Rev.* **2010**, *39*, 2869–78.

[9] G. Centi, S. Perathoner. Catalysis and sustainable (green) chemistry. *Catal. Today* **2003**, *77*, 287–297.

[10] V. Polshettiwar, R. S. Varma. Green chemistry by nano-catalysis. *Green Chem.* **2010**, *12*, 743.

[11] J. L. Tucker. Green Chemistry, a Pharmaceutical Perspective. *Org. Process Res. Dev.* **2006**, *10*, 315–319.

[12] P. J. Dunn. The importance of green chemistry in process research and development. *Chem. Soc. Rev.* **2012**, *41*, 1452–61.

[13] J. M. Herrmann, M. Lacroix. Environmental photocatalysis in action for green chemistry. *Kinet. Catal.* **2010**, *51*, 793–800.

[14] R. R. Wagner, D. W. Ball. Towards new green high energy materials. Computational chemistry on nitro-substituted urea. *J. Mol. Model.* **2011**, *17*, 2965–71.

[15] A. M. Voutchkova, T. G. Osimitz, P. T. Anastas. Toward a comprehensive molecular design framework for reduced hazard. *Chem. Rev.* **2010**, *110*, 5845–82.

[16] Y.-M. Tan, R. Conolly, D. T. Chang, R. Tornero-Velez, M. R. Goldsmith, S. D. Peterson, C. C. Dary. Computational toxicology: application in environmental chemicals. *Methods Mol. Biol.* **2012**, *929*, 9–19.

[17] J. Thornton. Implementing green chemistry. An environmental policy for sustainability. *Pure Appl. Chem.* **2001**, *73*, 1231–1236.

[18] A. Ghosh, D. a. Mitchell, A. Chanda, A. D. Ryabov, D. L. Popescu, E. C. Upham, G. J. Collins, T. J. Collins. Catalase-peroxidase activity of iron(III)-TAML activators of hydrogen peroxide. *J. Am. Chem. Soc.* **2008**, *130*, 15116–26.

[19] M. M. Conradie, J. Conradie, A. Ghosh. A DFT overview of high-valent iron, cobalt and nickel tetraamidomacrocyclic ligand (TAML) complexes: the end of innocence? *J. Inorg. Biochem.* **2006**, *100*, 620–6.

[20] A. Chanda, F. T. de Oliveira, T. J. Collins, E. Münck, E. L. Bominaar. Density functional theory study of the structural, electronic, and magnetic properties of a mu-oxo bridged dinuclear Fe(IV) complex based on a tetra-amido macrocyclic ligand. *Inorg. Chem.* **2008**, *47*, 9372–9.

[21] A. Ghosh, F. Tiago de Oliveira, T. Yano, T. Nishioka, E. S. Beach, I. Kinoshita, E. Münck, A. D. Ryabov, C. P. Horwitz, T. J. Collins. Catalytically active mu-Oxodiiron(IV) oxidants from Iron(III) and dioxygen. *J. Am. Chem. Soc.* **2005**, *127*, 2505–13.

[22] A. Chanda, D.-L. Popescu, F. Tiago de Oliveira, E. L. Bominaar, A. D. Ryabov, E. Münck, T. J. Collins. High-valent iron complexes with tetraamido macrocyclic ligands: structures, Mössbauer spectroscopy, and DFT calculations. *J. Inorg. Biochem.* **2006**, *100*, 606–19.

[23] F. Tiago de Oliveira, A. Chanda, D. Banerjee, X. Shan, S. Mondal, L. Que, E. L. Bominaar, E. Münck, T. J. Collins. Chemical and spectroscopic evidence for an FeV-oxo complex. *Science* **2007**, *315*, 835–8.

[24] M. J. Bartos, S. W. Gordon-Wylie, B. G. Fox, L. James Wright, S. T. Weintraub, K. E. Kauffmann, E. Münck, K. L. Kostka, E. S. Uffelman, C. E. Rickard, K. R. Noon, T. J. Collins. Designing ligands to achieve robust oxidation catalysts. Iron based systems. *Coord. Chem. Rev.* **1998**, *174*, 361–390.

[25] A. Ghosh, A. D. Ryabov, S. M. Mayer, D. C. Horner, D. E. Prasuhn, S. Sen Gupta, L. Vuocolo, C. Culver, M. P. Hendrich, C. E. F. Rickard, R. E. Norman, C. P. Horwitz, T. J. Collins. Understanding the mechanism of H(+)-induced demetalation as a design strategy for robust iron(III) peroxide-activating catalysts. *J. Am. Chem. Soc.* **2003**, *125*, 12378–9.

[26] A. Chanda, A. D. Ryabov, S. Mondal, L. Alexandrova, A. Ghosh, Y. Hangun-Balkir, C. P. Horwitz, T. J. Collins. Activity-stability parameterization of homogeneous green oxidation catalysts. *Chem. Eur. J.* **2006**, *12*, 9336–45.

[27] D.-L. Popescu, A. Chanda, M. J. Stadler, S. Mondal, J. Tehranchi, A. D. Ryabov, T. J. Collins. Mechanistically inspired design of Fe(III)-TAML peroxide-activating catalysts. *J. Am. Chem. Soc.* **2008**, *130*, 12260–1.

[28] S. Z. Sullivan, A. Ghosh, A. S. Biris, S. Pulla, A. M. Brezden, S. L. Collom, R. M. Woods, P. Munshi, L. Schnackenberg, B. S. Pierce, G. K. Kannarpady. Fe-complex of a tetraamido macrocyclic ligand: Spectroscopic characterization and catalytic oxidation studies. *Chem. Phys. Lett.* **2010**, *498*, 359–365.

[29] S. Kundu, A. Chanda, L. Espinosa-Marvan, S. K. Khetan, T. J. Collins. Facile destruction of formulated chlorpyrifos through green oxidation catalysis. *Catal. Sci. Technol.* **2012**, *2*, 1165.

[30] W. C. Ellis, N. D. McDaniel, S. Bernhard, T. J. Collins. Fast water oxidation using iron. *J. Am. Chem. Soc.* **2010**, *132*, 10990–1.

[31] S. S. Gupta, M. Stadler, C. a. Noser, A. Ghosh, B. Steinhoff, D. Lenoir, C. P. Horwitz, K.-W. Schramm, T. J. Collins. Rapid total destruction of chlorophenols by activated hydrogen peroxide. *Science* **2002**, *296*, 326–8.

[32] D. Banerjee, A. L. Markley, T. Yano, A. Ghosh, P. B. Berget, E. G. Minkley, S. K. Khetan, T. J. Collins. Green Oxidation Catalysis for Rapid Deactivation of Bacterial Spores. *Angew. Chem.* **2006**, *118*, 4078–4081.

[33] A. Chanda, S. K. Khetan, D. Banerjee, A. Ghosh, T. J. Collins. Total degradation of fenitrothion and other organophosphorus pesticides by catalytic oxidation employing Fe-TAML peroxide activators. *J. Am. Chem. Soc.* **2006**, *128*, 12058–9.

[34] N. Chahbane, D. Lenoir, S. Souabi, T. J. Collins, K.-W. Schramm. FeIII-TAML-Catalyzed Green Oxidative Decolorization of Textile Dyes in Wastewater. *CLEAN-Soil, Air, Water* **2007**, *35*, 459–464.

[35] N. W. Shappell, M. a. Vrabel, P. J. Madsen, G. Harrington, L. O. Billey, H. Hakk, G. L. Larsen, E. S. Beach, C. P. Horwitz, K. Ro, P. G. Hunt, T. J. Collins. Destruction of estrogens using Fe-TAML/peroxide catalysis. *Environ. Sci. Technol.* **2008**, *42*, 1296–300.

[36] L. Q. Shen, E. S. Beach, Y. Xiang, D. J. Tshudy, N. Khanina, C. P. Horwitz, M. E. Bier, T. J. Collins. Rapid, biomimetic degradation in water of the persistent drug sertraline by TAML catalysts and hydrogen peroxide. *Environ. Sci. Technol.* **2011**, *45*, 7882–7.

[37] *Our common future: Chapter 2, towards sustainable development. Report of the world commission on environment and development. A/42/427*, Tech. Rep., United nations, **1987**.

[38] *Caring for the Earth: A Strategy for Sustainable Living*, Tech. Rep., IUC-N/UNEP/WWF, **1991**.

[39] R. K. Buter, a. F. J. Raan. Identification and analysis of the highly cited knowledge base of sustainability science. *Sustainability Science* **2012**, 253–267.

[40] F. S. Chapin, E. S. Zavaleta, V. T. Eviner, R. L. Naylor, P. M. Vitousek, H. L. Reynolds, D. U. Hooper, S. Lavorel, O. E. Sala, S. E. Hobbie, M. C. Mack, S. Díaz. Consequences of changing biodiversity. *Nature* **2000**, *405*, 234–42.

[41] B. J. Cardinale, J. E. Duffy, A. Gonzalez, D. U. Hooper, C. Perrings, P. Venail, A. Narwani, G. M. Mace, D. Tilman, D. a. Wardle, A. P. Kinzig, G. C. Daily, M. Loreau, J. B. Grace, A. Larigauderie, D. S. Srivastava, S. Naeem. Biodiversity loss and its impact on humanity. *Nature* **2012**, *486*, 59–67.

[42] J. J. Thomosn, *Rays of Positive Electricity and Their Application to Chemical Analysis*, Longmans Green, London, **1913**.

[43] F. W. Aston, *Mass Spectra and Isotopes 2nd ed.*, Edward Arnold, London, **1942**.

[44] G. McCraken, P. Stott, *Fusion the energy of the universe 2nd ed.*, Elsevier, Amsterdam, **2013**.

[45] J. Fenn, M. Mann, C. Meng, S. Wong, C. Whitehouse. Electrospray ionization for mass spectrometry of large biomolecules. *Science* **1989**, *246*, 64–71.

[46] J. B. Fenn. Electrospray wings for molecular elephants (Nobel lecture). *Angew. Chem., Int. Ed. Engl.* **2003**, *42*, 3871–94.

[47] P. Kebarle, L. Tang. From ions in solution to ions in the gas phase - the mechanism of electrospray mass spectrometry. *Anal. Chem.* **1993**, *65*, 972A–986A.

[48] R. B. Cole. Some tenets pertaining to electrospray ionization mass spectrometry. *J. Mass Spectrom.* **2000**, *35*, 763–72.

[49] G. Taylor. Disintegration of Water Drops in an Electric Field. *Proc. R. Soc. A* **1964**, *280*, 383–397.

[50] A. Gomez, K. Tang. Charge and fission of droplets in electrostatic sprays. *Phys. Fluids* **1994**, *6*, 404.

[51] J. Fernández de la Mora. On the Outcome of the Coulombic Fission of a Charged Isolated Drop. *J. Colloid Interface Sci.* **1996**, *178*, 209–218.

[52] M. Dole. Molecular Beams of Macroions. *J. Chem. Phys.* **1968**, *49*, 2240.

[53] L. L. Mack. Molecular Beams of Macroions. II. *J. Chem. Phys.* **1970**, *52*, 4977.

[54] J. V. Iribarne. On the evaporation of small ions from charged droplets. *J. Chem. Phys.* **1976**, *64*, 2287.

[55] B. a. Thomson, J. V. Iribarne. Field induced ion evaporation from liquid surfaces at atmospheric pressure. *J. Chem. Phys.* **1979**, *71*, 4451.

[56] P. Kebarle. A brief overview of the present status of the mechanisms involved in electrospray mass spectrometry. *J. Mass Spectrom.* **2000**, *35*, 804–17.

[57] N. Felitsyn, M. Peschke, P. Kebarle. Origin and number of charges observed on multiply-protonated native proteins produced by ESI. *Int. J. Mass Spectrom.* **2002**, *219*, 39–62.

[58] G. J. Van Berkel, F. Zhou. Characterization of an Electrospray Ion Source as a Controlled-Current Electrolytic Cell. *Anal. Chem.* **1995**, *67*, 2916–2923.

[59] N. B. Cech, C. G. Enke. Practical implications of some recent studies in electrospray ionization fundamentals. *Mass Spectrom. Rev.* **2002**, *20*, 362–87.

[60] K. B. Tomer. Separations Combined with Mass Spectrometry. *Chem. Rev.* **2001**, *101*, 297–328.

[61] M. Gros, M. Petrović, D. Barceló. Multi-residue analytical methods using LC-tandem MS for the determination of pharmaceuticals in environmental and wastewater samples: a review. *Anal. Bioanal. Chem.* **2006**, *386*, 941–52.
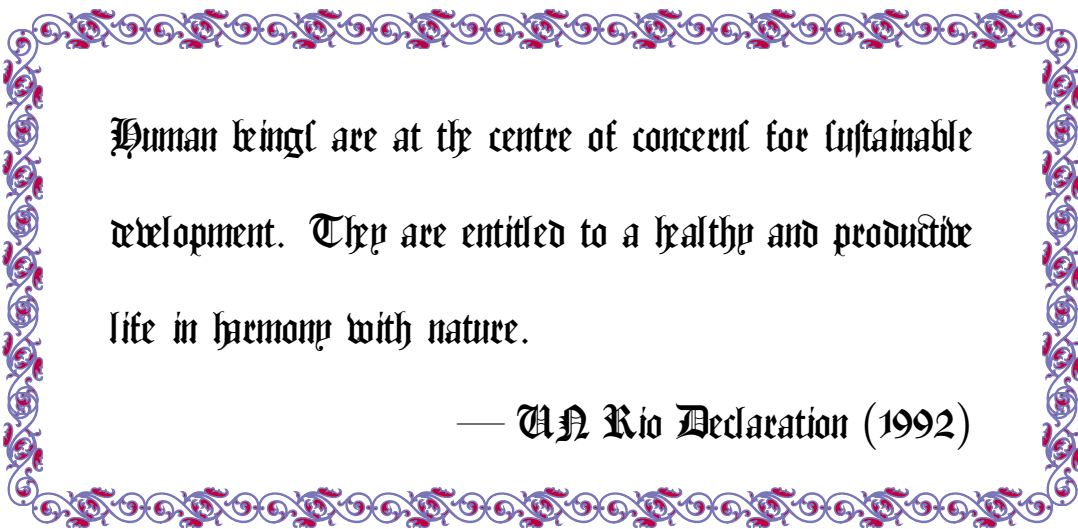
[62] I. S. Ruhoy, C. G. Daughton. Types and quantities of leftover drugs entering the environment via disposal to sewage–revealed by coroner records. *Sci. Total Environ.* **2007**, *388*, 137–48.

[63] S. C. Monteiro, A. B. A. Boxall. Occurrence and fate of human pharmaceuticals in the environment. *Rev. Environ. Contam. Toxicol.* **2010**, *202*, 53–154.

[64] K. Kümmerer. Pharmaceuticals in the Environment. *Annu. Rev. Environ. Resour.* **2010**, *35*, 57–75.

[65] A. Nikolaou, S. Meric, D. Fatta. Occurrence patterns of pharmaceuticals in water and wastewater environments. *Anal. Bioanal. Chem.* **2007**, *387*, 1225–34.

[66] G. Pojana, A. Fantinati, A. Marcomini. Occurrence of environmentally relevant pharmaceuticals in Italian drinking water treatment plants. *Int. J. Environ. Anal. Chem.* **2011**, *91*, 537–552.

[67] Y. Valcárcel, S. González Alonso, J. L. Rodríguez-Gil, a. Gil, M. Catalá. Detection of pharmaceutically active compounds in the rivers and tap water of the Madrid Region (Spain) and potential ecotoxicological risk. *Chemosphere* **2011**, *84*, 1336–48.

[68] S. Webb, T. Ternes, M. Gibert, K. Olejniczak. Indirect human exposure to pharmaceuticals via drinking water. *Toxicol. Lett.* **2003**, *142*, 157–167.

[69] E. Vulliet, C. Cren-Olivé, M.-F. Grenier-Loustalot. Occurrence of pharmaceuticals and hormones in drinking water treated from surface waters. *Environ. Chem. Lett.* **2009**, *9*, 103–114.

[70] D. R. Dietrich, S. F. Webb, T. Petry. Hot spot pollutants: pharmaceuticals in the environment. *Toxicol. Lett.* **2002**, *131*, 1–3.

[71] M. Crane, C. Watts, T. Boucard. Chronic aquatic environmental risks from exposure to human pharmaceuticals. *Sci. Total Environ.* **2006**, *367*, 23–41.

[72] V. L. Cunningham, S. P. Binks, M. J. Olson. Human health risk assessment from the presence of human pharmaceuticals in the aquatic environment. *Regul. Toxicol. Pharm.* **2009**, *53*, 39–45.

[73] B. Halling-Sørensen, S. Nors Nielsen, P. Lanzky, F. Ingerslev, H. Holten Lützhøft, S. Jørgensen. Occurrence, fate and effects of pharmaceutical substances in the environment- A review. *Chemosphere* **1998**, *36*, 357–393.

[74] C. G. Daughton, T. a. Ternes. Pharmaceuticals and personal care products in the environment: agents of subtle change? *Environ. Health Perspect.* **1999**, *107 Suppl 6*, 907–38.

[75] J. P. Seiler. Pharmacodynamic activity of drugs and ecotoxicology - can the two be connected? *Toxicol. Lett.* **2002**, *131*, 105–115.

[76] K. a. Kidd, P. J. Blanchfield, K. H. Mills, V. P. Palace, R. E. Evans, J. M. Lazorchak, R. W. Flick. Collapse of a fish population after exposure to a synthetic estrogen. *PNAS* **2007**, *104*, 8897–901.

[77] J. L. Oaks, M. Gilbert, M. Z. Virani, R. T. Watson, C. U. Meteyer, B. a. Rideout, H. L. Shivaprasad, S. Ahmed, M. J. I. Chaudhry, M. Arshad, S. Mahmood, A. Ali, A. A. Khan. Diclofenac residues as the cause of vulture population decline in Pakistan. *Nature* **2004**, *427*, 630–3.

[78] T. A. Ternes. Occurrence of drugs in German sewage treatment plants and rivers. *Water Res.* **1998**, *32*, 3245–3260.

[79] a. Tauxe-Wuersch, L. F. De Alencastro, D. Grandjean, J. Tarradellas. Occurrence of several acidic drugs in sewage treatment plants in Switzerland and risk assessment. *Water Res.* **2005**, *39*, 1761–72.

[80] N. Lindqvist, T. Tuhkanen, L. Kronberg. Occurrence of acidic pharmaceuticals in raw and treated sewages and in receiving waters. *Water Res.* **2005**, *39*, 2219–28.

[81] R. H. Lindberg, K. Björklund, P. Rendahl, M. I. Johansson, M. Tysklind, B. a. V. Andersson. Environmental risk assessment of antibiotics in the Swedish environment with emphasis on sewage treatment plants. *Water Res.* **2007**, *41*, 613–9.

[82] N. Nakada, K. Kiri, H. Shinohara, A. Harada, K. Kuroda, S. Takizawa, H. Takada. Evaluation of pharmaceuticals and personal care products as water-soluble molecular markers of sewage. *Environ. Sci. Technol.* **2008**, *42*, 6347–53.

[83] R. Rosal, a. Rodríguez, J. a. Perdigón-Melón, M. Mezcua, M. D. Hernando, P. Letón, E. García-Calvo, a. Agüera, a. R. Fernández-Alba. Removal of pharmaceuticals and kinetics of mineralization by O(3)/H(2)O(2) in a biotreated municipal wastewater. *Water Res.* **2008**, *42*, 3719–28.

[84] J. Radjenović, M. Petrović, F. Ventura, D. Barceló. Rejection of pharmaceuticals in nanofiltration and reverse osmosis membrane drinking water treatment. *Water Res.* **2008**, *42*, 3601–10.

[85] O. a. H. Jones, P. G. Green, N. Voulvoulis, J. N. Lester. Questioning the excessive use of advanced treatment to remove organic micropollutants from wastewater. *Environ. Sci. Technol.* **2007**, *41*, 5085–9.

[86] F. P. Guengerich, D. C. Liebler. Enzymatic activation of chemicals to toxic metabolites. *Crit. Rev. Toxicol.* **1985**, *14*, 259–307.

[87] F. Guengerich. Enzymatic oxidation of xenobiotic chemicals. *Crit. Rev. Biochem. Mol. Biol.* **1990**, *25*, 97–153.

[88] W. Lohmann, U. Karst. Biomimetic modeling of oxidative drug metabolism : Strategies, advantages and limitations. *Anal. Bioanal. Chem.* **2008**, *391*, 79–96.

[89] M. Sono, M. Roach, E. Coulter, J. Dawson. Heme-Containing Oxygenases. *Chem. Rev.* **1996**, *96*, 2841–2887.

[90] I. Denisov, T. Makris, S. Sligar, I. Schlichting. Structure and chemistry of cytochrome P450. *Chem. Rev.* **2005**, *105*, 2253–2277.

[91] F. P. Guengerich. Common and Uncommon Cytochrome P450 Reactions Related to Metabolism and Chemical Toxicity. *Chem. Res. Toxicol.* **2001**, *14*, 611–650.

[92] J. Rittle, M. T. Green. Cytochrome P450 compound I: capture, characterization, and C-H bond activation kinetics. *Science* **2010**, *330*, 933–7.

Chapter 2

Research on the Elimination of Persistent Organic Pollutants at the United Nations— Defining the Horizon

> Human beings are at the centre of concerns for sustainable development. They are entitled to a healthy and productive life in harmony with nature.
>
> — UN Rio Declaration (1992)

2.1   Introductory Remark

As stated in the chapter 1, the ultimate goal of green chemistry is to enable sustainable development. To reach this defining goal, the development of environmentally benign technologies upon which to base a sustainable civilization will be essential. But it will not be enough. In my opinion, strong intellectual ties between green chemistry and sustainability ethics will be required. Developing a global technical leadership that is competent in managing resources for the welfare of the near and distant future will also be a key element of success. To practice at integrating sustainability ethics and green chemistry on a meaningful stage, I was fortunate in the summer of 2011 to be able to join the United Nations to conduct research on how the world should embark on the next phase of eliminating persistent organic pollutants (POPs).

2.2   Sustainable Development and Sound Chemical Management

The unconstrained activities of man in transforming his surroundings has gradually reached the scale that incalculable harm to health and the environment had already been inflicted via the chemical contamination of water, air, soil, and living things. The issues has become so conspicuous and pressing that the UN General Assembly decided to convene the Stockholm Conference in 1972 with the focus on human interactions with the environment. The meeting agreed upon a Declaration composed of 26 principles concerning the environment and development:[1]

1. Human rights must be asserted, apartheid and colonialism condemned.

2. Natural resources must be safeguarded.

3. The Earth's capacity to produce renewable resources must be maintained.

4. Wildlife must be safeguarded.

5. Non-renewable resources must be shared and not exhausted.

6. Pollution must not exceed the environment's capacity to clean itself.

7. Damaging oceanic pollution must be prevented.

8. Development is needed to improve the environment.

9. Developing countries therefore need assistance.

10. Developing countries need reasonable prices for exports to carry out environmental management.

11. Environment policy must not hamper development.

12. Developing countries need money to develop environmental safeguards.

13. Integrated development planning is needed.

14. Rational planning should resolve conflicts between environment and development.

15. Human settlements must be planned to eliminate environmental problems.

16. Governments should plan their own appropriate population policies.

17. National institutions must plan development of states' natural resources.

18. Science and technology must be used to improve the environment.

19. Environmental education is essential.

20. Environmental research must be promoted, particularly in developing countries.

21. States may exploit their resources as they wish but must not endanger others.

22. Compensation is due to states thus endangered.

23. Each nation must establish its own standards.

24. There must be cooperation on international issues.

25. International organizations should help to improve the environment.

26. Weapons of mass destruction must be eliminated.

In 1987 in the World Commission on the Environment and Development, the UN

defined sustainable development as development that meets the needs of the present

without compromising the ability of future generations to meet their own needs.[2] In 1992, the United Nations Conference on Environment and Development (UNCED) was held in Rio and reached a framework convention on climate.[3] In 2000 the UN listed environmental sustainability as one of the Millennium Development Goals.[4] Judging from this historical record and from on-going efforts that I observed at the UN, it is reasonable to assert that sustainability has reached the top of the UN's development agenda. However, numerous practices are blocking effective sustainable development, among which the release of hazardous chemicals is the most formidable. Chemical pollution continues to devastate biodiversity, harden soils and degrade the land. Some chemicals are known to disrupt the hormonal control of cellular development and signaling at environmentally relevant concentrations. The collective phenomena, called endocrine disruption, are tectonic of significance to sustainability as some everyday chemicals are clearly able to produce impaired organisms at tiny concentrations. Moreover, evidence continues to mount that the adverse effects are multi-generational. Numerous chemicals damage immune and reproductive systems and cause cancer, often via endocrine disruption mechanisms Thus, the complexity of the effects of chemicals on living organisms and the often attendant irreversibility and trans-generational effects of the resulting damage represent massive challenges to sustainability. To address the health and environmental challenges of chemicals, the Stockholm Convention on Persistent Organic Pollutants (POPs)[5] was adopted in May 2001 and entered into force in May 2004. Initially, twelve chemicals were listed for restriction and elimination under three separate categories; 1. pesticides, 2. industrial chemicals and, 3. unintentional by-products. Later at the fourth and fifth Conference of the Parties (COP) in May 2009 and April 2011, another ten chemicals were added, giving the present POPs list of twenty-two chemicals.

Examples of POPs are; organochlorine pesticides such as DDT, chlordane, and lin-

dane, industrial chemicals such as polychlorinated biphenyl(PCBs), perfluorooctane sulfonic acid (PFOS) and its salts and perfluorooctane sulfonyl fluoride (POSF), and unintentional byproducts such as polychlorinated dibenzo-p-dioxins and dibenzofurans (PDCD/Fs).

2.3   PCBs Elimination

Given the broad range, it is not feasible to cover every designated POP in the following discussion. I have chosen PCBs as a representative set and I will discuss the current state of technological approaches for eliminating PCBs.

PCBs are a set of 209 molecules comprising every possible case of chlorine for hydrogen substitution on biphenyl. The physico-chemical properties of PCBs vary depending on the chlorine content and substitution pattern. As the chlorine content increases, PCBs range from light mobile colorless oils through thick syrups to light yellow resinous solids . Other properties such as viscosity, melting point, boiling point, and density etc. also vary according to the chlorine content. PCBs may have distinct odors but many are odorless. They are highly soluble in non-polar organic solvents such as mineral oils. They are chemically inert, thermally stable, flame-proofing, and electrically insulating. When treated at extreme high temperature (1000°C) in the presence of oxygen, PCBs decompose predominantly into carbon dioxide, water and hydrochloric acid, and significantly also produce small quantities of polychlorinated-p-dioxins/furans (FCDD/Fs).

The broadly useful technical properties of PCBs have inspired a wide range of applications. Large scale industrial production started in 1929 and was concentrated in a relatively small number of countries : Austria, China, Czechoslovakia, France, Germany, Italy, Japan, Russia, Spain, the United Kingdom and the United States.

PCBs were marketed under a multitude of trade names. The primary manufacturer in North America, Monsanto Chemical Company, marketed PCBs primarily under the trade name, Aroclor. Aroclor refers to a mixture of phenyl compounds with different degree of chlorination, indicated by a four digit number system. For example, Aroclor 1242 represents chlorinated biphenyl that is 42% chlorine by weight. The primary uses of PCBs included dielectric fluids in transformers and capacitors, hydraulic fluids, plasticizers, flame-retardants, and adhesives etc., with dielectric fluids accounting for 60% of the total use. According to Basel Convention,[6] any substance or material with a PCB concentration greater than 50 ppm are considered as PCBs.

Once they have entered the environment, PCBs can easily cycle between air, water and soil and exhibit extreme resistance to degradation. They are picked up into the bodies of small organisms and fish in water, and efficiently migrate and magnify up the food web.[7] Fat loving PCBs preferentially deposit in adipose tissues and the liver.[8] Evidence has shown that PCBs have hepatotoxic potential, can disrupt thyroid hormones, may alter immune status and neurological behavior, and cause menstrual disturbance and sperm morphology.[7,9–13] Some PCBs have dioxin-like properties and are carcinogenic. To facilitate the risk assessment and regulatory control of PCB mixtures, PCDD and PCDF, the concept of toxic equivalent factors (TEFs) were initially developed in 1998[14] and reevaluated in 2005.[15] Please see 2.6.1 for the TEF values. By summing up contributions of individual TEF, one can calculate the toxic equivalent (TEQ).

$$\text{TEQ} = \sum_i \text{PCDD}_i \times \text{TEF}_i + \sum_i \text{PCDF}_i \times \text{TEF}_i + \sum_i \text{PCB}_i \times \text{TEF}_i \qquad (2.1)$$

The primary international efforts on PCBs elimination are described in Annex A, Part II of the Stockholm Convention.[5] Parties to the Convention are obliged to elim-

inate equipment and oils containing PCBs from use by 2025 and bring these under environmentally sound waste management by 2028. The Annex A-C of Stockholm Convention 2009 and an amendment to Annex A in 2011 were attached in the section 2.6.2. At the fourth conference of parties, the PCBs Elimination Network (PEN) was formed with the aim of improving coordination and cooperation among stakeholders from different sectors with the goal of achieving the environmentally sound management of PCBs.

In terms of technologies, there are several effective options for PCBs destruction.[16] High temperature incineration is the most widely used. When performed properly, this technology can destroy PCBs up to 99.9999%. However, when inadequately executed, the risks of emissions of harmful substances are high. Another high temperature method is called "plasma arc". The plasma is created by arcing high current density. Inert gas under pressure is passed through the arc into a sealed container of waste material, reaching temperatures up 15,000 °C. At these temperatures, most types of waste are broken into atomic components in a gaseous form. A separate technology is to abstract halogens from hydrocarbons using hydrogen atoms. One approach focuses on reacting hydrogens with PCBs at high temperature (850°C) and low pressure, yielding primarily methane and hydrogen chloride and "minor" amounts of other low molecular weight hydrocarbons, including benzene. The destruction efficiencies are 99.9999% for PCBs. A separate approach relies on generating hydrogen atoms via a patented technology that is based on catalytic decomposition in a basic environment. It involves treatment of liquid and solid wastes in the presence of a reagent mixture consisting of a high boiling point hydrocarbon, sodium hydroxide and a proprietary catalyst. When heated to about 300°C, the system produces highly reactive hydrogen atoms that proceed to cleave carbon and chlorine bonds. Metallic sodium can be used to destroy PCBs in mineral oil. The approach has been used

widely for in-situ removal of PCBs from active transformers. Another approach utilizes super-critical water oxidation. At temperatures and pressures above the critical point of water (374°C and 22.1 MPa), organic materials become highly soluble in water and react rapidly with oxygen or hydrogen peroxide to produce carbon dioxide, water and inorganic acids or salts.

Based on my studies, it is clear that significant progress has been made in combating POPs. However, the journey has been long and hard, and PCBs are only one set among the 22 POP challenges. Today, the extremely toxic pesticide aldicarb, a single drop of which is capable of killing an adult human, is still being used extensively in the US and 25 additional countries.[17] Annually, between 1% and 3% of farm workers worldwide suffer from pesticides poisoning and 1 million require hospitalization.[17] A combination of coal burning and the use of illegal pesticides is being blamed for causing abnormally high rate of birth defects in countries such as China.[18] Countless tragic stories caused by poor management of chemicals reoccur year after year. Why has it been so difficult to end this chemical mayhem?

2.4 Outlook

After much back and forth pondering, I have identified in my own mind two dominant causes for the current stalemate. The first cause is the divergence of value systems. What might mean a great deal to some might mean little to others. For example, what is the value of nature? To the American Indian, it provides the life-dependent sustenance and should be lived in complete harmony with. On the other hand, to the western explorers of America, the unspoiled wilderness was a huge blank canvas, which had long been waiting for the human touch to paint a picture. The value of nature was its potential for exploitation, an exploitation that is not bounded by nature's

resilience. Over time, many people in America gradually developed an increasing appreciation of the beauty and value of nature of its own sake, and started realizing its vulnerability and determined to preserve the vestige of the once abundant and self-sustaining ecological system. Two groups of opinions on the value of nature, entrepreneurial utilitarianism vs. environmental conservationism, formed and the chasm between them kept widening. As industrialization further expanded and nature was ever more forcefully adapted to suit the near term human needs, the tension between environmental conservation and exploitation deepened and became seemingly irreconcilable. Today, the current dominating anthropocentric and monopolar value systems still ascribe little value to protecting nature out into the distant future, which is the very essence of sustainability. The second cause will go by a term that I will now coin and define. The term is "first-personism", which means the concerns of one person do not necessarily go beyond their first-hand personal experience. Now let me elaborate it by a conversation between a business professional and myself in New York in the summer of 2011. It began with my worrisome description of the current global climate change scenario and the urgency for curbing its encroaching sustainability. Somehow this appearingly self-evident issue did not resonant with Lily. She told me that she could not sense the urgency of the climate change simply because she has not been affected personally. Even although she had learned from the news that communities in south Asia were more frequently flooded nowadays, she claimed it was very hard for her to imagine the impact of such disasters due to the lack of personal experience in America. Apparently, even the impact of Katrina on New Orleans was not close enough. Apparently, only a first-hand experience would suffice to deliver the appropriate understanding. What's more, she assured that she was representing the average American with this point of view. Accepting this face value, it would be no wonder about the resistence to the Kyoto protocol.

Obviously, the difference in opinions exists. Obviously, the task is huge to get people to think broadly. But one should not forget that status quo is nothing unbreakable. The foundational ideas of human civilization have been immensely varied historically and are constantly evolving. The seven continents were once thought never to have been one. Electrons were thought not to spin. Enzymes were thought to be nothing more than proteins. But all these ideas have been proved wrong with the progress of science. It is science that redirected our thinking and expanded our vision. What has fueled the flame of science is the desire of human beings to understand reality and use that understanding to improve the human condition. Looking back into history, from the clean air act to the clean water act, from snowmobiles in Yellowstone to oil pipelines in Alaska, many environmental struggles have ended up as arguments over whether or not science and technology could provide solutions to the attendant technology-induced pollution problems. The question is often whether or not technology can dig us out technology-derived problems. As the body of environmentally compatible technologies and polices has grown, we have achieved cleaner air and water and improved health. Many environmental problems have been solved at local levels employing both technological and policy tools where the people who have forced and/or enacted the solutions are the same people who were experiencing the adverse effects of pollution. Because of the way the cause-and-effect dynamic is experienced, local problems are far easier to solve than global problems. At the global level, numerous technologies are slowly wearing down the ecosphere in ways that are not immediate apparent to the polluters. Industrial chemicals and pharmaceuticals are good examples. This set of human-made products were created with the intention of bettering the human condition or improving human health. But often, the near-term advantages are gained at the expense of long-term sustainability and this dynamic is extremely difficult to counteract given the way our civilization has evolved.

Ultimately, sustainability demands that all technologies are essential to the function of civilization are compatible with the long-term common good. This means there is a great need for promoting green science and technologies and for developing a global leadership that can competently align civilization building and sustainability. Such a leadership would care about all nations. It would not allow less advantaged jurisdictions to become the repositories of hazardous waste or other forms of wealthier countries exploiting poorer countries. Solutions to environmental problems would be framed on the global scale whenever appropriate. A competent global sustainability leadership would belong not to individual nations but would instead unite all nations in pursuing sustainability.

2.5 References

[1] *Report from the United Nations Conference on the Human Environment held in Stockholm,* **1972**. http://www.unep.org/Documents.Multilingual/Default.asp?DocumentID=97.

[2] *Our common future: Chapter 2, towards sustainable development. Report of the world commission on environment and development. A/42/427*, Tech. Rep., United nations, **1987**.

[3] *The United Nations Framework Convention on Climate Change*, **1992**. http://www.un.org/millenniumgoals/poverty.shtml.

[4] *United Nations Millennium Development Goals*, **2000**. http://www.un.org/millenniumgoals/poverty.shtml.

[5] *Stockholm Convention.* http://chm.pops.int/Convention/tabid/54/Default.aspx.

[6] *Basel Convention.* http://www.basel.int/TheConvention/Overview/TextoftheConvention/tabid/1275/Default.aspx.

[7] *Toxicological Profile for Polychlorinated Biphenyls (PCBs)*, Tech. Rep., U.S. Department of Health and Human Services, **2000**.

[8] *Preparation of a National Environmentally Sound Management Plan for PCBs and PCB-Contaminated Equipment*, Tech. Rep., Secretariat of the Basel Convention, **2003**.

[9] *Polychlorinated biphenyl hazards to fish, wildlife, and inverteberates : a synoptic view*, Tech. Rep., U.S. Fish and Wildlife Service, **1986**.

[10] *Opinion of the SCF on the Risk Assessment of Dioxins and Dioxin-like PCBs in Food*, Tech. Rep., European Commission, Scientific Committee on Food, **2000**.

[11] E. E. McConnell. Comparative toxicity of PCBs and related compounds in various species of animals. *Environ. Health Perspect.* **1985**, *60*, 29–33.

[12] J. C. Larsen. Risk assessments of polychlorinated dibenzo- p-dioxins, polychlorinated dibenzofurans, and dioxin-like polychlorinated biphenyls in food. *Mol. Nutr. Food Res.* **2006**, *50*, 885–96.

[13] A. Gies, G. Neumeier, M. Rappolder, R. Konietzka. Risk assessment of dioxins and dioxin-like PCBs in food–comments by the German Federal Environmental Agency. *Chemosphere* **2007**, *67*, S344–9.

[14] M. Van den Berg, L. Birnbaum, a. T. Bosveld, B. Brunström, P. Cook, M. Feeley, J. P. Giesy, a. Hanberg, R. Hasegawa, S. W. Kennedy, T. Kubiak, J. C. Larsen, F. X. van Leeuwen, a. K. Liem, C. Nolt, R. E. Peterson, L. Poellinger, S. Safe, D. Schrenk, D. Tillitt, M. Tysklind, M. Younes, F. Waern, T. Zacharewski. Toxic equivalency factors (TEFs) for PCBs, PCDDs, PCDFs for humans and wildlife. *Environ. Health Perspect.* **1998**, *106*, 775–92.

[15] M. Van den Berg, L. S. Birnbaum, M. Denison, M. De Vito, W. Farland, M. Feeley, H. Fiedler, H. Hakansson, A. Hanberg, L. Haws, M. Rose, S. Safe, D. Schrenk, C. Tohyama, A. Tritscher, J. Tuomisto, M. Tysklind, N. Walker, R. E. Peterson. The 2005 World Health Organization reevaluation of human and Mammalian toxic equivalency factors for dioxins and dioxin-like compounds. *Toxicol. Sci.* **2006**, *93*, 223–41.

[16] *Inventory of World-wide PCB Destruction Capacity*, **2004**.

[17] *The Deadly Chemicals in Cotton*, Tech. Rep., Environmental Justice Foundation in collaboration with Pesticide Action Network UK, **2007**.

[18] a. Ren, X. Qiu, L. Jin, J. Ma, Z. Li, L. Zhang, H. Zhu, R. H. Finnell, T. Zhu. Association of selected persistent organic pollutants in the placenta with the risk of neural tube defects. *PNAS* **2011**, *108*, 12770–12775.

2.6 Appendices

2.6.1 TEF Values

Table 2.1: TEF values by WHO

Compound	WHO 1998 TEF	WHO 2005 TEF
chlorinated dibenzo-p-dioxins		
2,3,7,8-TCDD	1	1
1,2,3,7,8-PeCDD	1	1
1,2,3,4,7,8-HxCDD	0.1	0.1
1,2,3,6,7,8-HxCDD	0.1	0.1
1,2,3,7,8,9-HxCDD	0.1	0.1
1,2,3,4,6,7,8-HpCDD	0.01	0.01
OCDD	0.0001	0.0003
chlorinated dibenzofurans		
2,3,7,8-TCDF	0.1	0.1
1,2,3,7,8-PeCDF	0.05	0.03
2,3,4,7,8-PeCDF	0.5	0.3
1,2,3,4,7,8-HxCDF	0.1	0.1
1,2,3,6,7,8-HxCDF	0.1	0.1
1,2,3,7,8,9-HxCDF	0.1	0.1
2,3,4,6,7,8-HxCDF	0.1	0.1
1,2,3,4,6,7,8-HpCDF	0.01	0.01
1,2,3,4,7,8,9-HpCDF	0.01	0.01
OCDF	0.0001	0.0003

non-ortho substituted PCBs

PCB 77	0.0001	0.0001
PCB 81	0.0001	0.0003
PCB 126	0.1	0.1
PCB 169	0.01	0.03

mono-ortho substituted PCBs

105	0.0001	0.00003
114	0.0005	0.00003
118	0.0001	0.00003
123	0.0001	0.00003
156	0.0005	0.00003
157	0.0005	0.00003
167	0.00001	0.00003
189	0.0001	0.00003

References[14,15]

2.6.2 Stockholm Convention Annex A-C 2009 and Amendment 2011

Annex A   ELIMINATION

Part I

Chemical	Activity	Specific exemption[1]
Aldrin* CAS No: 309-00-2	Production	None
	Use	Local ectoparasiticide Insecticide
Alpha hexachlorocyclohexane* CAS No: 319-84-6	Production	None
	Use	None
Beta hexachlorocyclohexane* CAS No: 319-85-7	Production	None
	Use	None
Chlordane* CAS No: 57-74-9	Production	As allowed for the Parties listed in the Register
	Use	Local ectoparasiticide Insecticide Termiticide Termiticide in buildings and dams Termiticide in roads Additive in plywood adhesives
Chlordecone* CAS No: 143-50-0	Production	None
	Use	None
Dieldrin* CAS No: 60-57-1	Production	None
	Use	In agricultural operations
Endrin* CAS No: 72-20-8	Production	None
	Use	None
Heptachlor* CAS No: 76-44-8	Production	None
	Use	Termiticide Termiticide in structures of houses Termiticide (subterranean) Wood treatment In use in underground cable boxes
Hexabromobiphenyl* CAS No: 36355-01-8	Production	None
	Use	None
Hexabromodiphenyl ether* and heptabromodiphenyl ether*	Production	None
	Use	Articles in accordance with the provisions of Part IV of this Annex

Chemical	Activity	Specific exemption[1]
Hexachlorobenzene CAS No: 118-74-1	Production	As allowed for the Parties listed in the Register
	Use	Intermediate Solvent in pesticide Closed system site limited intermediate[2]
Lindane* CAS No: 58-89-9	Production	None
	Use	Human health pharmaceutical for control of head lice and scabies as second line treatment
Mirex* CAS No: 2385-85-5	Production	As allowed for the Parties listed in the Register
	Use	Termiticide
Pentachlorobenzene* CAS No: 608-93-5	Production	None
	Use	None
Polychlorinated biphenyls (PCB)*	Production	None
	Use	Articles in use in accordance with the provisions of Part II of this Annex
Tetrabromodiphenyl ether* and pentabromodiphenyl ether*	Production	None
	Use	Articles in accordance with the provisions of Part V of this Annex
Toxaphene* CAS No: 8001-35-2	Production	None
	Use	None

Notes:

(i) Except as otherwise specified in this Convention, quantities of a chemical occurring as unintentional trace contaminants in products and articles shall not be considered to be listed in this Annex;

---

[1] Please note that, as at 17 May 2009, there were no Parties registered for the specific exemptions listed in Annex A pertaining to aldrin, chlordane, dieldrin, heptachlor, hexachlorobenzene, and mirex. Therefore, in accordance with paragraph 9 of Article 4 of the Convention, no new registrations may be made with respect to such exemptions, which appear in grey text in the table.

[2] Please note that, although the specific exemption for the use of hexachlorobenzene as closed-system site-limited intermediate is no longer available, this use is still possible in accordance with note (iii) of Part I of this Annex.

(ii) This note shall not be considered as a production and use specific exemption for purposes of paragraph 2 of Article 3. Quantities of a chemical occurring as constituents of articles manufactured or already in use before or on the date of entry into force of the relevant obligation with respect to that chemical, shall not be considered as listed in this Annex, provided that a Party has notified the Secretariat that a particular type of article remains in use within that Party. The Secretariat shall make such notifications publicly available;

(iii) This note, which does not apply to a chemical that has an asterisk following its name in the Chemical column in Part I of this Annex, shall not be considered as a production and use specific exemption for purposes of paragraph 2 of Article 3. Given that no significant quantities of the chemical are expected to reach humans and the environment during the production and use of a closed-system site-limited intermediate, a Party, upon notification to the Secretariat, may allow the production and use of quantities of a chemical listed in this Annex as a closed-system site-limited intermediate that is chemically transformed in the manufacture of other chemicals that, taking into consideration the criteria in paragraph 1 of Annex D, do not exhibit the characteristics of persistent organic pollutants. This notification shall include information on total production and use of such chemical or a reasonable estimate of such information and information regarding the nature of the closed-system site-limited process including the amount of any non-transformed and unintentional trace contamination of the persistent organic pollutant-starting material in the final product. This procedure applies except as otherwise specified in this Annex. The Secretariat shall make such notifications available to the Conference of the Parties and to the public. Such production or use shall not be considered a production or use specific exemption. Such production and use shall cease after a ten-year period, unless the Party concerned submits a new notification to the Secretariat, in which case the period will be extended for an additional ten years unless the Conference of the Parties, after a review of the production and use decides otherwise. The notification procedure can be repeated;

(iv) All the specific exemptions in this Annex may be exercised by Parties that have registered exemptions in respect of them in accordance with Article 4 with the exception of the use of polychlorinated biphenyls in articles in use in accordance with the provisions of Part II, which may

be exercised by all Parties, the use of hexabromodiphenyl ether and heptabromodiphenyl ether in accordance with the provisions of Part IV, and the use of tetrabromodiphenyl ether and pentabromodiphenyl ether in accordance with the provisions of Part V of this Annex.

Part II   Polychlorinated biphenyls

Each Party shall:

(a) With regard to the elimination of the use of polychlorinated biphenyls in equipment (e.g. transformers, capacitors or other receptacles containing liquid stocks) by 2025, subject to review by the Conference of the Parties, take action in accordance with the following priorities:

(i)   Make determined efforts to identify, label and remove from use equipment containing greater than 10 per cent polychlorinated biphenyls and volumes greater than 5 litres;

(ii)   Make determined efforts to identify, label and remove from use equipment containing greater than 0.05 per cent polychlorinated biphenyls and volumes greater than 5 litres;

(iii) Endeavour to identify and remove from use equipment containing greater than 0.005 percent polychlorinated biphenyls and volumes greater than 0.05 litres;

(b) Consistent with the priorities in subparagraph (a), promote the following measures to reduce exposures and risk to control the use of polychlorinated biphenyls:

(i)   Use only in intact and non-leaking equipment and only in areas where the risk from environmental release can be minimised and quickly remedied;

(ii)   Not use in equipment in areas associated with the production or processing of food or feed;

(iii) When used in populated areas, including schools and hospitals, all reasonable measures to protect from electrical failure which could result in a fire, and regular inspection of equipment for leaks;

(c) Notwithstanding paragraph 2 of Article 3, ensure that equipment containing polychlorinated biphenyls, as described in subparagraph (a), shall not be exported or imported except for the purpose of environmentally sound waste management;

(d) Except for maintenance and servicing operations, not allow recovery for the purpose of reuse in other equipment of liquids with polychlorinated biphenyls content above 0.005 per cent;

(e) Make determined efforts designed to lead to environmentally sound waste management of liquids containing polychlorinated biphenyls and equipment contaminated with polychlorinated biphenyls having a polychlorinated biphenyls content above 0.005 per cent, in accordance with paragraph 1 of Article 6, as soon as possible but no later than 2028, subject to review by the Conference of the Parties;

(f) In lieu of note (ii) in Part I of this Annex, endeavour to identify other articles containing more than 0.005 per cent polychlorinated biphenyls (e.g. cable-sheaths, cured caulk and painted objects) and manage them in accordance with paragraph 1 of Article 6;

(g) Provide a report every five years on progress in eliminating polychlorinated biphenyls and submit it to the Conference of the Parties pursuant to Article 15;

(h) The reports described in subparagraph (g) shall, as appropriate, be considered by the Conference of the Parties in its reviews relating to polychlorinated biphenyls. The Conference of the Parties shall review progress towards elimination of polychlorinated biphenyls at five year intervals or other period, as appropriate, taking into account such reports.

Part III   Definitions

For the purpose of this Annex:

(a) "Hexabromodiphenyl ether and heptabromodiphenyl ether" means 2,2',4,4',5,5'-hexabromodiphenyl ether (BDE-153, CAS No: 68631-49-2), 2,2',4,4',5,6'-hexabromodiphenyl ether (BDE-154, CAS No: 207122-15-4), 2,2',3,3',4,5',6-heptabromodiphenyl ether (BDE-175, CAS No: 446255-22-7), 2,2',3,4,4',5',6-heptabromodiphenyl ether (BDE-183, CAS No: 207122-16-5) and other hexa- and heptabromodiphenyl ethers present in commercial octabromodiphenyl ether.

(b) "Tetrabromodiphenyl ether and pentabromodiphenyl ether" means 2,2',4,4'-tetrabromodiphenyl ether (BDE-47, CAS No: 5436-43-1) and 2,2',4,4',5-pentabromodiphenyl ether (BDE-99, CAS No: 60348-60-9) and other tetra- and pentabromodiphenyl ethers present in commercial pentabromodiphenyl ether.

STOCKHOLM CONVENTION ON PERSISTENT ORGANIC POLLUTANTS

37

Part IV   Hexabromodiphenyl ether and heptabromodiphenyl ether

1. A Party may allow recycling of articles that contain or may contain hexabromodiphenyl ether and heptabromodiphenyl ether, and the use and final disposal of articles manufactured from recycled materials that contain or may contain hexabromodiphenyl ether and heptabromodiphenyl ether, provided that:

    (a) The recycling and final disposal is carried out in an environmentally sound manner and does not lead to recovery of hexabromodiphenyl ether and heptabromodiphenyl ether for the purpose of their reuse;

    (b) The Party takes steps to prevent exports of such articles that contain levels/concentrations of hexabromodiphenyl ether and heptabromodiphenyl ether exceeding those permitted for the sale, use, import or manufacture of those articles within the territory of the Party; and

    (c) The Party has notified the Secretariat of its intention to make use of this exemption.

2. At its sixth ordinary meeting and at every second ordinary meeting thereafter the Conference of the Parties shall evaluate the progress that Parties have made towards achieving their ultimate objective of elimination of hexabromodiphenyl ether and heptabromodiphenyl ether contained in articles and review the continued need for this specific exemption. This specific exemption shall in any case expire at the latest in 2030.

Part V   Tetrabromodiphenyl ether and pentabromodiphenyl ether

1. A Party may allow recycling of articles that contain or may contain tetrabromodiphenyl ether and pentabromodiphenyl ether, and the use and final disposal of articles manufactured from recycled materials that contain or may contain tetrabromodiphenyl ether and pentabromodiphenyl ether, provided that:

    (a) The recycling and final disposal is carried out in an environmentally sound manner and does not lead to recovery of tetrabromodiphenyl ether and pentabromodiphenyl ether for the purpose of their reuse;

    (b) The Party does not allow this exemption to lead to the export of articles containing levels/concentrations of tetrabromodiphenyl ether and pentabromodiphenyl ether that exceed those permitted to be sold within the territory of the Party; and

(c) The Party has notified the Secretariat of its intention to make use of this exemption.

2. At its sixth ordinary meeting and at every second ordinary meeting thereafter the Conference of the Parties shall evaluate the progress that Parties have made towards achieving their ultimate objective of elimination of tetrabromodiphenyl ether and pentabromodiphenyl ether contained in articles and review the continued need for this specific exemption. This specific exemption shall in any case expire at the latest in 2030.

STOCKHOLM CONVENTION ON PERSISTENT ORGANIC POLLUTANTS

39

Annex B   RESTRICTION

Part I

Chemical	Activity	Acceptable purpose or specific exemption[3]
DDT (1,1,1-trichloro-2,2-bis (4-chlorophenyl)ethane) CAS No: 50-29-3	Production	Acceptable purpose: Disease vector control use in accordance with Part II of this Annex Specific exemption: Intermediate in production of dicofol Intermediate
	Use	Acceptable purpose: Disease vector control in accordance with Part II of this Annex Specific exemption: Production of dicofol Intermediate
Perfluorooctane sulfonic acid (CAS No: 1763-23-1), its salts[a] and perfluorooctane sulfonyl fluoride (CAS No: 307-35-7) [a] For example: potassium perfluorooctane sulfonate (CAS No: 2795-39-3); lithium perfluorooctane sulfonate (CAS No: 29457- 72-5); ammonium perfluorooctane sulfonate (CAS No: 29081-56-9); diethanolammonium perfluorooctane sulfonate (CAS No: 70225-14-8); tetraethylammonium perfluorooctane sulfonate (CAS No: 56773-42-3); didecyldimethylammonium perfluorooctane sulfonate (CAS No: 251099-16-8)	Production	Acceptable purpose: In accordance with Part III of this Annex, production of other chemicals to be used solely for the uses below. Production for uses listed below. Specific exemption: As allowed for Parties listed in the Register.
	Use	Acceptable purpose: In accordance with Part III of this Annex for the following acceptable purposes, or as an intermediate in the production of chemicals with the following acceptable purposes: • Photo-imaging • Photo-resist and anti-reflective coatings for semi-conductors • Etching agent for compound semi-conductors and ceramic filters • Aviation hydraulic fluids • Metal plating (hard metal plating) only in closed-loop systems • Certain medical devices (such as ethylene tetrafluoroethylene copolymer (ETFE) layers and radio-opaque ETFE production, in-vitro diagnostic medical devices, and CCD colour filters)

Chemical	Activity	Acceptable purpose or specific exemption[3]
		• Fire-fighting foam • Insect baits for control of leaf-cutting ants from *Atta spp.* and *Acromyrmex spp.* Specific exemption: For the following specific uses, or as an intermediate in the production of chemicals with the following specific uses: • Photo masks in the semiconductor and liquid crystal display (LCD) industries • Metal plating (hard metal plating) • Metal plating (decorative plating) • Electric and electronic parts for some colour printers and colour copy machines • Insecticides for control of red imported fire ants and termites • Chemically driven oil production • Carpets • Leather and apparel • Textiles and upholstery • Paper and packaging • Coatings and coating additives • Rubber and plastics

Notes:

(i) Except as otherwise specified in this Convention, quantities of a chemical occurring as unintentional trace contaminants in products and articles shall not be considered to be listed in this Annex;

---

[3] Please note that, as at 17 May 2009, there were no Parties registered for the specific exemptions listed in Annex B pertaining to DDT. Therefore, in accordance with paragraph 9 of Article 4 of the Convention, no new registrations may be made with respect to such exemptions, which appear in grey text in the table.

(ii)   This note shall not be considered as a production and use acceptable purpose or specific exemption for purposes of paragraph 2 of Article 3. Quantities of a chemical occurring as constituents of articles manufactured or already in use before or on the date of entry into force of the relevant obligation with respect to that chemical, shall not be considered as listed in this Annex, provided that a Party has notified the Secretariat that a particular type of article remains in use within that Party. The Secretariat shall make such notifications publicly available;

(iii) This note shall not be considered as a production and use specific exemption for purposes of paragraph 2 of Article 3. Given that no significant quantities of the chemical are expected to reach humans and the environment during the production and use of a closed-system site-limited intermediate, a Party, upon notification to the Secretariat, may allow the production and use of quantities of a chemical listed in this Annex as a closed-system site-limited intermediate that is chemically transformed in the manufacture of other chemicals that, taking into consideration the criteria in paragraph 1 of Annex D, do not exhibit the characteristics of persistent organic pollutants. This notification shall include information on total production and use of such chemical or a reasonable estimate of such information and information regarding the nature of the closed-system site-limited process including the amount of any non-transformed and unintentional trace contamination of the persistent organic pollutant-starting material in the final product. This procedure applies except as otherwise specified in this Annex. The Secretariat shall make such notifications available to the Conference of the Parties and to the public. Such production or use shall not be considered a production or use specific exemption. Such production and use shall cease after a ten-year period, unless the Party concerned submits a new notification to the Secretariat, in which case the period will be extended for an additional ten years unless the Conference of the Parties, after a review of the production and use decides otherwise. The notification procedure can be repeated;

(iv)   All the specific exemptions in this Annex may be exercised by Parties that have registered in respect of them in accordance with Article 4.

Part II   DDT (1,1,1-trichloro-2,2-bis(4-chlorophenyl)ethane)

1. The production and use of DDT shall be eliminated except for Parties that have notified the Secretariat of their intention to produce and/or use it. A DDT Register is hereby established and shall be available to the public. The Secretariat shall maintain the DDT Register.

2. Each Party that produces and/or uses DDT shall restrict such production and/or use for disease vector control in accordance with the World Health Organization recommendations and guidelines on the use of DDT and when locally safe, effective and affordable alternatives are not available to the Party in question.

3. In the event that a Party not listed in the DDT Register determines that it requires DDT for disease vector control, it shall notify the Secretariat as soon as possible in order to have its name added forthwith to the DDT Register. It shall at the same time notify the World Health Organization.

4. Every three years, each Party that uses DDT shall provide to the Secretariat and the World Health Organization information on the amount used, the conditions of such use and its relevance to that Party's disease management strategy, in a format to be decided by the Conference of the Parties in consultation with the World Health Organization.

5. With the goal of reducing and ultimately eliminating the use of DDT, the Conference of the Parties shall encourage:

    (a) Each Party using DDT to develop and implement an action plan as part of the implementation plan specified in Article 7. That action plan shall include:

        (i)   Development of regulatory and other mechanisms to ensure that DDT use is restricted to disease vector control;

        (ii)   Implementation of suitable alternative products, methods and strategies, including resistance management strategies to ensure the continuing effectiveness of these alternatives;

        (iii) Measures to strengthen health care and to reduce the incidence of the disease.

    (b) The Parties, within their capabilities, to promote research and development of safe alternative chemical and non-chemical products, methods and strategies for Parties using DDT, relevant to the conditions of those countries and with the goal of decreasing the human and economic burden of disease. Factors to be promoted when considering alternatives or combinations of alternatives shall include the human health risks and

environmental implications of such alternatives. Viable alternatives to DDT shall pose less risk to human health and the environment, be suitable for disease control based on conditions in the Parties in question and be supported with monitoring data.

6. Commencing at its first meeting, and at least every three years thereafter, the Conference of the Parties shall, in consultation with the World Health Organization, evaluate the continued need for DDT for disease vector control on the basis of available scientific, technical, environmental and economic information, including:

(a) The production and use of DDT and the conditions set out in paragraph 2;

(b) The availability, suitability and implementation of the alternatives to DDT; and

(c) Progress in strengthening the capacity of countries to transfer safely to reliance on such alternatives.

7. A Party may, at any time, withdraw its name from the DDT Registry upon written notification to the Secretariat. The withdrawal shall take effect on the date specified in the notification.

Part III   Perfluorooctane sulfonic acid, its salts, and perfluorooctane sulfonyl fluoride

1. The production and use of perfluorooctane sulfonic acid (PFOS), its salts and perfluorooctane sulfonyl fluoride (PFOSF) shall be eliminated by all Parties except as provided in Part I of this Annex for Parties that have notified the Secretariat of their intention to produce and/or use them for acceptable purposes. A Register of Acceptable Purposes is hereby established and shall be available to the public. The Secretariat shall maintain the Register of Acceptable Purposes. In the event that a Party not listed in the Register determines that it requires the use of PFOS, its salts or PFOSF for the acceptable purposes listed in Part I of this Annex it shall notify the Secretariat as soon as possible in order to have its name added forthwith to the Register.

2. Parties that produce and/or use these chemicals shall take into account, as appropriate, guidance such as that given in the relevant parts of the general guidance on best available techniques and best environmental practices given in Part V of Annex C of the Convention.

3. Every four years, each Party that uses and/or produces these chemicals shall report on progress made to eliminate PFOS, its salts and PFOSF and submit information on such progress to the Conference of the Parties pursuant to and in the process of reporting under Article 15 of the Convention.

4. With the goal of reducing and ultimately eliminating the production and/or use of these chemicals, the Conference of the Parties shall encourage:

   (a) Each Party using these chemicals to take action to phase out uses when suitable alternatives substances or methods are available;

   (b) Each Party using and/or producing these chemicals to develop and implement an action plan as part of the implementation plan specified in Article 7 of the Convention;

   (c) The Parties, within their capabilities, to promote research on and development of safe alternative chemical and non-chemical products and processes, methods and strategies for Parties using these chemicals, relevant to the conditions of those Parties. Factors to be promoted when considering alternatives or combinations of alternatives shall include the human health risks and environmental implications of such alternatives.

5. The Conference of the Parties shall evaluate the continued need for these chemicals for the various acceptable purposes and specific exemptions on the basis of available scientific, technical, environmental and economic information, including:

   (a) Information provided in the reports described in paragraph 3;

   (b) Information on the production and use of these chemicals;

   (c) Information on the availability, suitability and implementation of alternatives to these chemicals;

   (d) Information on progress in building the capacity of countries to transfer safely to reliance on such alternatives.

6. The evaluation referred to in the preceding paragraph shall take place no later than in 2015 and every four years thereafter, in conjunction with a regular meeting of the Conference of the Parties.

7. Due to the complexity of the use and the many sectors of society involved in the use of these chemicals, there might be other uses of these chemicals of which countries are not presently aware. Parties which become aware of other uses are encouraged to inform the Secretariat as soon as possible.

8. A Party may, at any time, withdraw its name from the Register of acceptable purposes upon written notification to the Secretariat. The withdrawal shall take effect on the date specified in the notification.

9. The provisions of note (iii) of Part I of Annex B shall not apply to these chemicals.

Annex C   UNINTENTIONAL PRODUCTION

Part I   Persistent organic pollutants subject to the requirements of Article 5

This Annex applies to the following persistent organic pollutants when formed and released unintentionally from anthropogenic sources:

Chemical
Hexachlorobenzene (HCB) (CAS No: 118-74-1) Pentachlorobenzene (PeCB) (CAS No: 608-93-5) Polychlorinated biphenyls (PCB) Polychlorinated dibenzo-p-dioxins and dibenzofurans (PCDD/PCDF)

Part II   Source categories

Hexachlorobenzene, pentachlorobenzene, polychlorinated biphenyls, and polychlorinated dibenzo-p-dioxins and dibenzofurans are unintentionally formed and released from thermal processes involving organic matter and chlorine as a result of incomplete combustion or chemical reactions. The following industrial source categories have the potential for comparatively high formation and release of these chemicals to the environment:

(a) Waste incinerators, including co-incinerators of municipal, hazardous or medical waste or of sewage sludge;

(b) Cement kilns firing hazardous waste;

(c) Production of pulp using elemental chlorine or chemicals generating elemental chlorine for bleaching;

(d) The following thermal processes in the metallurgical industry:

(i)   Secondary copper production;

(ii)   Sinter plants in the iron and steel industry;

(iii) Secondary aluminium production;

(iv)   Secondary zinc production.

Part III   Source categories

Hexachlorobenzene, pentachlorobenzene, polychlorinated biphenyls, and polychlorinated dibenzo-*p*-dioxins and dibenzofurans may also be unintentionally formed and released from the following source categories, including:

(a) Open burning of waste, including burning of landfill sites;

(b) Thermal processes in the metallurgical industry not mentioned in Part II;

(c) Residential combustion sources;

(d) Fossil fuel-fired utility and industrial boilers;

(e) Firing installations for wood and other biomass fuels;

(f) Specific chemical production processes releasing unintentionally formed persistent organic pollutants, especially production of chlorophenols and chloranil;

(g) Crematoria;

(h) Motor vehicles, particularly those burning leaded gasoline;

(i) Destruction of animal carcasses;

(j) Textile and leather dyeing (with chloranil) and finishing (with alkaline extraction);

(k) Shredder plants for the treatment of end of life vehicles;

(l) Smouldering of copper cables;

(m) Waste oil refineries.

Part IV   Definitions

1. For the purposes of this Annex:

(a) "Polychlorinated biphenyls" means aromatic compounds formed in such a manner that the hydrogen atoms on the biphenyl molecule (two benzene rings bonded together by a single carbon-carbon bond) may be replaced by up to ten chlorine atoms; and

(b) "Polychlorinated dibenzo-*p*-dioxins" and "polychlorinated dibenzofurans" are tricyclic, aromatic compounds formed by two benzene rings connected by two oxygen atoms in polychlorinated dibenzo-*p*-dioxins and by one oxygen atom and one carbon-carbon bond in polychlorinated

dibenzofurans and the hydrogen atoms of which may be replaced by up to eight chlorine atoms.

2. In this Annex, the toxicity of polychlorinated dibenzo-*p*-dioxins and dibenzofurans is expressed using the concept of toxic equivalency which measures the relative dioxin-like toxic activity of different congeners of polychlorinated dibenzo-*p*-dioxins and dibenzofurans and coplanar polychlorinated biphenyls in comparison to 2,3,7,8-tetrachlorodibenzo-*p*-dioxin. The toxic equivalent factor values to be used for the purposes of this Convention shall be consistent with accepted international standards, commencing with the World Health Organization 1998 mammalian toxic equivalent factor values for polychlorinated dibenzo-*p*-dioxins and dibenzofurans and coplanar polychlorinated biphenyls. Concentrations are expressed in toxic equivalents.

Part V   General guidance on best available techniques and best environmental practices

This Part provides general guidance to Parties on preventing or reducing releases of the chemicals listed in Part I.

A. General prevention measures relating to both best available techniques and best environmental practices

Priority should be given to the consideration of approaches to prevent the formation and release of the chemicals listed in Part I. Useful measures could include:

(a) The use of low-waste technology;

(b) The use of less hazardous substances;

(c) The promotion of the recovery and recycling of waste and of substances generated and used in a process;

(d) Replacement of feed materials which are persistent organic pollutants or where there is a direct link between the materials and releases of persistent organic pollutants from the source;

(e) Good housekeeping and preventive maintenance programmes;

(f) Improvements in waste management with the aim of the cessation of open and other uncontrolled burning of wastes, including the burning of landfill sites. When considering proposals to construct new waste disposal facilities, consideration should be given to alternatives such as activities

to minimize the generation of municipal and medical waste, including resource recovery, reuse, recycling, waste separation and promoting products that generate less waste. Under this approach, public health concerns should be carefully considered;

(g) Minimization of these chemicals as contaminants in products;

(h) Avoiding elemental chlorine or chemicals generating elemental chlorine for bleaching.

B. Best available techniques

The concept of best available techniques is not aimed at the prescription of any specific technique or technology, but at taking into account the technical characteristics of the installation concerned, its geographical location and the local environmental conditions. Appropriate control techniques to reduce releases of the chemicals listed in Part I are in general the same. In determining best available techniques, special consideration should be given, generally or in specific cases, to the following factors, bearing in mind the likely costs and benefits of a measure and consideration of precaution and prevention:

(a) General considerations:

(i)   The nature, effects and mass of the releases concerned: techniques may vary depending on source size;

(ii)   The commissioning dates for new or existing installations;

(iii) The time needed to introduce the best available technique;

(iv)   The consumption and nature of raw materials used in the process and its energy efficiency;

(v)   The need to prevent or reduce to a minimum the overall impact of the releases to the environment and the risks to it;

(vi)   The need to prevent accidents and to minimize their consequences for the environment;

(vii) The need to ensure occupational health and safety at workplaces;

(viii) Comparable processes, facilities or methods of operation which have been tried with success on an industrial scale;

(ix)   Technological advances and changes in scientific knowledge and understanding.

(b) General release reduction measures: When considering proposals to construct new facilities or significantly modify existing facilities using processes that release chemicals listed in this Annex, priority consideration

should be given to alternative processes, techniques or practices that have similar usefulness but which avoid the formation and release of such chemicals. In cases where such facilities will be constructed or significantly modified, in addition to the prevention measures outlined in section A of Part V the following reduction measures could also be considered in determining best available techniques:

(i)   Use of improved methods for flue-gas cleaning such as thermal or catalytic oxidation, dust precipitation, or adsorption;

(ii)   Treatment of residuals, wastewater, wastes and sewage sludge by, for example, thermal treatment or rendering them inert or chemical processes that detoxify them;

(iii)   Process changes that lead to the reduction or elimination of releases, such as moving to closed systems;

(iv)   Modification of process designs to improve combustion and prevent formation of the chemicals listed in this Annex, through the control of parameters such as incineration temperature or residence time.

C. Best environmental practices

The Conference of the Parties may develop guidance with regard to best environmental practices.

An amendment to Annex A adopted by the Conference of the Parties to the Stockholm Convention on Persistent Organic Pollutants at its fifth meeting (Decision SC-5/3)

The Conference of the Parties,

1. Decides to amend part I of Annex A to the Stockholm Convention on Persistent Organic Pollutants to list therein technical endosulfan and its related isomers, with specific exemptions for production as allowed for the parties listed in the Register of Specific Exemptions and/or for use on crop-pest complexes as listed in accordance with the provisions of a new part VI of the annex by inserting the following row:

Chemical	Activity	Specific exemption
Technical endosulfan* (CAS No: 115-29-7) and its related isomers* (CAS No: 959-98-8 and CAS No: 33213-65-9)	Production	As allowed for the parties listed in the Register
	Use	Crop-pest complexes as listed in accordance with the provisions of part VI of this Annex

2. Decides to insert a new note (v) in part I of Annex A as follows:

Technical endosulfan (CAS No: 115-29-7), its related isomers (CAS No: 959-98-8 and CAS No: 33213-65-9) and endosulfan sulfate (CAS No: 1031-07-8) were assessed and identified as persistent organic pollutants.

3. Decides to insert a new Part VI in Annex A as follows:

Part VI

Technical endosulfan and its related isomers (endosulfan)
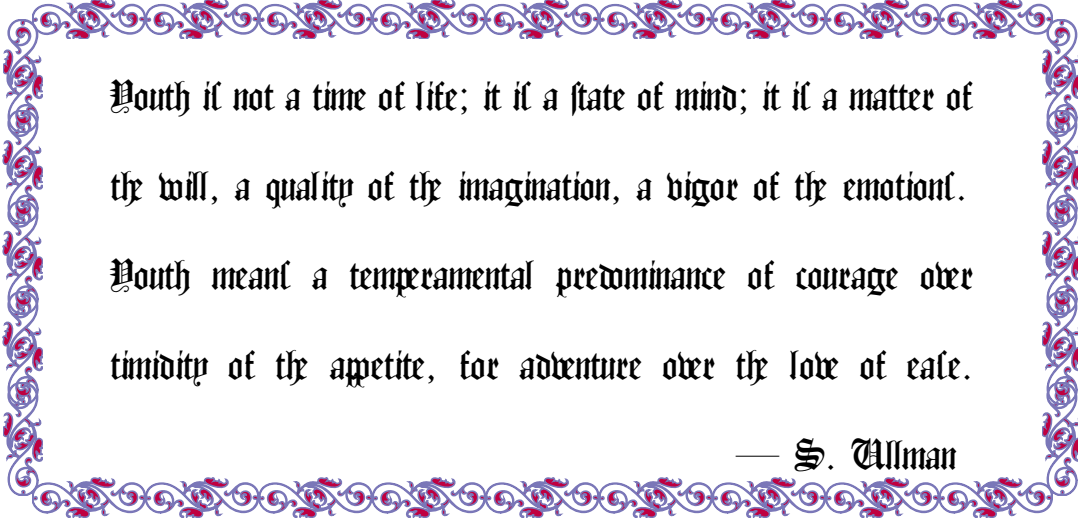
The production and use of endosulfan shall be eliminated except for parties that have notified the Secretariat of their intention to produce and/or use it in accordance with Article 4 of the Convention. Specific exemptions may be available for the use of endosulfan for the following crop-pest complexes:

Crop	Pest
Apple	Aphids
Arhar, gram	Aphids, caterpillars, pea semilooper, pod borer
Bean, cowpea	Aphids, leaf miner, whiteflies
Chilli, onion, potato	Aphids, jassids
Coffee	Berry borer, stem borers
Cotton	Aphids, cotton bollworm, jassids, leaf rollers, pink bollworm, thrips, whiteflies
Eggplant, okra	Aphids, diamondback moth, jassids, shoot and fruit borer
Groundnut	Aphids
Jute	Bihar hairy caterpillar, yellow mite
Maize	Aphids, pink borer, stem borers
Mango	Fruit flies, hoppers
Mustard	Aphids, gall midges
Rice	Gall midges, rice hispa, stem borers, white jassid
Tea	Aphids, caterpillars, flushworm, mealybugs, scale insects, smaller green leafhopper, tea geometrid, tea mosquito bug, thrips
Tobacco	Aphids, oriental tobacco budworm
Tomato	Aphids, diamondback moth, jassids, leaf miner, shoot and fruit borer, whiteflies
Wheat	Aphids, pink borer, termites

Reference: C.N.703.2011.TREATIES-8 (Depositary Notification)

Chapter 3

Theoretical Investigation of the Electronic Configuration of Co in its Coordination Environment

Youth is not a time of life; it is a state of mind; it is a matter of the will, a quality of the imagination, a vigor of the emotions. Youth means a temperamental predominance of courage over timidity of the appetite, for adventure over the love of ease.

— S. Ullman

3.1 Abstract

Fossils fuels, the ancient deposit of solar energy, have propelled the engine of human civilization since her birth till today. After hundreds of years of excavation and combustion, not only this reserve approaches its exhaustion, but also its use shadows the sustainable future of human beings as well as the lives of all forms on this planet. An urgent need emerges for environmentally benign ways of utilizing solar energy. Photosynthesis provides a promising answer — water splitting. To mimic this process, developing catalysts for water cleavage is the central theme. Among all the earth abundant and inexpensive elements, Co stands out for its high efficiency and dual capability of water reduction and oxidation. Between the two, water oxidation presents the major challenge. Co(IV) was shown to be the active intermediate in this chemical conversion. This highlights the importance of unambiguous characterization of the electronic structure for Co containing catalysts. To this end, the research of this chapter combines the spectroscopic information and DFT calculations to clarify the literature ambiguity in the diagnosis of Co containing complexes, and theoretically projects the ligand environment in favor of hosting a Co(IV) electronic state in an octahedral-like coordination complex.

3.2 Introduction

Energy has fueled human cultural development since its beginning.[1,2] From taming of fire to riding on steam, from electricity to nuclear power, every celebrating step of human civilization in history also witnessed a revolution in use of energy. Given the significance of energy to our existence and advancement, it is natural to quest the source of energies. The majority of the energies used in industry and our lives is probably can be traced back to be solar radiations.[3] Solar energy utilization can be

done via two general means, conversion for immediate use and storage for future use. Photovoltaics represent the former case. Despite of their deployment, the intermittent and diffuse nature of solar energy put a question mark on the efficiency and economical viability on this use for electricity generation.[4] On the other hand, solar energy storage in the form of chemical energy is the way nature has chosen to power our planet for billions of years.[5] Fossil fuels are a long-term accumulative result of such an effort and have been generously passed down to us by nature. After hundreds of years of industrious exploitation, we are reaching the point of depleting this luxury reserve.[6,7] Moreover, the adverse environmental consequences of burning fossil fuels has become more and more conspicuous with the continuing expansion on its scale to meet the need of the growing human population.

Earth ground temperature increase was first noticed in 1896.[8] Afterward, many studies were devoted to tracing the possible causes for this change. The result pointed that the green house effect is likely to be responsible for the global temperature increase and modern climate change is anthropogenic.[9–11] As seen in Figure 3.1, atmospheric CO_2 concentration entered an unprecedented level during human history and it continues climbing up to today. This undoubtedly emphasizes the inherent connection between the anthropogenic climate change and CO_2 emission from fossil fuel consumption.[12]

To answer the global energy crisis and pave the way for sustainable development, alternative use of solar energy with the aim of decarbonization, high efficiency and cost-effectiveness is under ardent pursuit.[13] Hydrogen as the product[14,15] of water splitting in photosynthesis holds a great promise. Hydrogen as a energy resource bears the merits of high energy density,[16] great transferability, storability, ecological acceptability and renewability.[17] Therefore, simulating photosynthesis to produce solar fuels would represent the most important breakthrough of modern science.[18]

Figure 3.1: Artwork — "What's CO_2 Got to Do with It?". It was on exhibition in the Carnegie Mellon University Artpark Lab from April 1st, 2012 to May 31st, 2012. The blue curve on the graph depicts the atmospheric carbon dioxide (CO_2) concentration variation over the past 800,000 years. To construct the curve, CO_2 concentration data from ice coring studies in Antarctica[19–22] were consulted and mathematically scaled to fit the dimension of the displaying fence (51 ft x 4 ft). Based on the calculation, six 39 ft long LED ropes were connected and curved accordingly to render the CO_2 concentration profile. The ropes were attached to the fence by more than 500 tie wraps. The LED lights are charged by solar panels during day times and give off distinctive blue light at night. CO_2 forms an indispensable link in the global carbon cycle. It oscillates with ice ages for the major portion of the entire portrayed time period in the artwork and is largely bounded between 272 and 299 ppm. However, over the last two millennia, an unprecedented growth in the atmospheric CO_2 concentration has been occurring with expanded human activities as highlighted by the upward spiraling rope. The project was sponsored by the ACS local section sustainability programming grant. The photo was taken by Steve Ellington.

Water splitting is a thermodynamic uphill process.[23] Diret photodissociation of water is not feasible due to the lack of overlap between the solar spectrum and the electronic absorption range of water.[24] Nature accomplishes this task by designing two separate catalytic centers[25–28] — water oxidation and hydrogen production. To design an artificial synthesis system, a set of principles have been proposed.[29] From the economic perspective, earth abundant and inexpensive metal elements are the appealing for making catalysts. Co, Fe, and Ni fall in this category and their development for catalytic water splitting have been reviewed recently.[30] Co catalyzed water reduction and oxidation can be dated back to 1970's.[31,32] Further studies by Nocera and Frei revealed the outstanding performance of Co-Pi[33–36] and Co_3O_4[37] in water splitting. Co was the first made to show visible light-driven H_2 production without the aid of noble metals.[38] Reports of using Co-Pi in conjunction with silicon semiconductors to simulate artificial leaf has appeared in recent literature.[39,40] Among the three elements, Co is only one that has demonstrated the dual ability for water reduction and oxidation, and it has displayed the inequivalently high turn-over frequency (TOF).[30] A review on Co containing catalysts in water lysis was published lately.[41]

Water oxidation is recognized as the bottleneck for developing a solar fuel cell.[42] To attain this goal, chemical, electrochemical and photochemical schemes were outlined and the last means was rationalized with the potential to achieve water splitting under the right conditions.[43] Tremendous efforts have been devoted to molecular catalysts design for the purpose of water oxidation. The oxidation catalyst in photosynthesis system II (PSII) is a $CaMn_4$ core cluster with a cubane structural motif.[44–47] Analysis across a broad range of biological species discloses extremely low structural diversity for the cubane motif. This fact implies the importance of cubane geometry in its role of water oxidation from the evolutionary perspective.[48] Superimposition of Co-Pi and Co_3O_4 with the catalytical core of PSII demonstrate high similarity.[48–50] Co(IV)

was proposed to play a key catalytic role in water oxidation.[51,52] Therefore, precise characterization of the electronic structure and state of Co is crucial to understanding the chemistry of Co mediated water oxidation.

To probe the electronic structure of Co containing molecules, electron paramagnetic resonance spectroscopy (EPR) presents a powerful tool. Co salt or organometallic complexes have been characterized by EPR are very few[53–60] and their EPR patterns show little consistency. This sheds doubts on the accuracy in description of the electronic structures of the Co complexes. Paradoxical phenomenon was encountered in our effort of characterizing Co−D* complexes. A Co nuclear originated hyperfine splitting pattern and the overall isotropic EPR spectrum blurs the dividing line between Co^{IV} and $[Co^{III}-Ligand•]$. To decipher the puzzle, DFT calculation on Co−D* and several Co containing complexes were performed. As a result, the real electronic character of Co−D* was unveiled. In addition, a theoretical projection on the structural foundation to achieve the Co(IV) electronic state was also provided.

3.3 Paradoxical Spectroscopic Observation of Co-D* Complexes and Electronic Structure Elucidation by DFT Calculations

Several Co complexes,[57,61] namely $[Co(D^*)(tBuPy)_2]$, $[Co(D^*)(tBuCN)_2]$ and $[Co(PAC)(tBuPy)_2]$ (see 3.7.1 for the nomenclature definition) were synthesized in Collins' group and characterized by EPR. The EPR spectra of these three compounds share two common features : isotropic g values and a 8-line hyperfine pattern indicative of interaction between the paramagnetic electron with the nuclear ^{57}Co (I=$7/2$), as shown in Figure 3.2 and Figure 3.3.
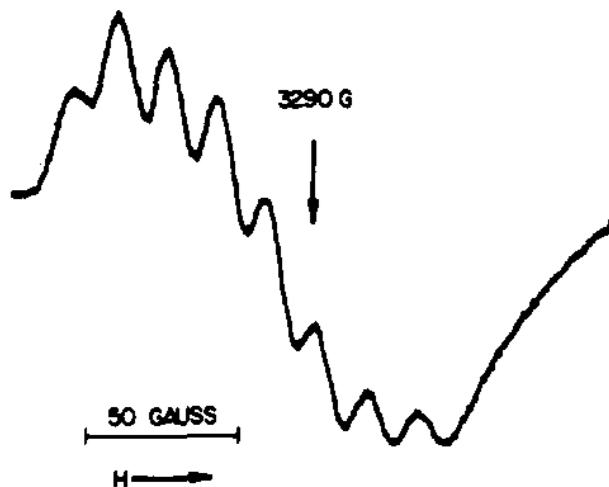
Figure 3.2: EPR spectrum for $[Co(PAC)(tBuPy)_2]$. Reprint with permission from F.C.Anson, T.J.Collins and R. J. Coots et al. J. Am. Chem. Soc. 1984, 106, 5037. ©1984 American Chemical Society Chemical Society.

The remarkable resemblance of the EPR properties of the three complexes suggests that they have similar electronic states. To address the question of whether the radical in these cobalt complexes is metal- or ligand-based, we have performed density functional theory (DFT) calculations.

As expected, DFT gives similar solutions for all the complexes. The spin density plots and d orbital splitting diagram are shown in Figure 3.4. It is clear from the spin density plots that the paramagnetic electron is highly delocalized with only marginal fraction of residence on the metal. The electronic structures of all three complexes, as obtained by DFT, are thus best described as low-spin Co(III) ligand-radical states, like the one depicted by the qualitative orbital level scheme in Figure 3.4 (a). The orbital scheme reflects the distorted octahedral crystal field in $[Co(D^*)(tBuPy)_2]$, with the lower t2 set accommodating the six d-electron of the diamagnetic Co(III). It is important for the understanding of the EPR data to realize that the radical-electron-containing orbital, ϕ, has a small but non-negligible component at the metal, $\phi \sim \phi_R + \epsilon\, d_{yz}$, where ϕ_R is confined to the ligand and ϵ is a coefficient $\ll 1$.
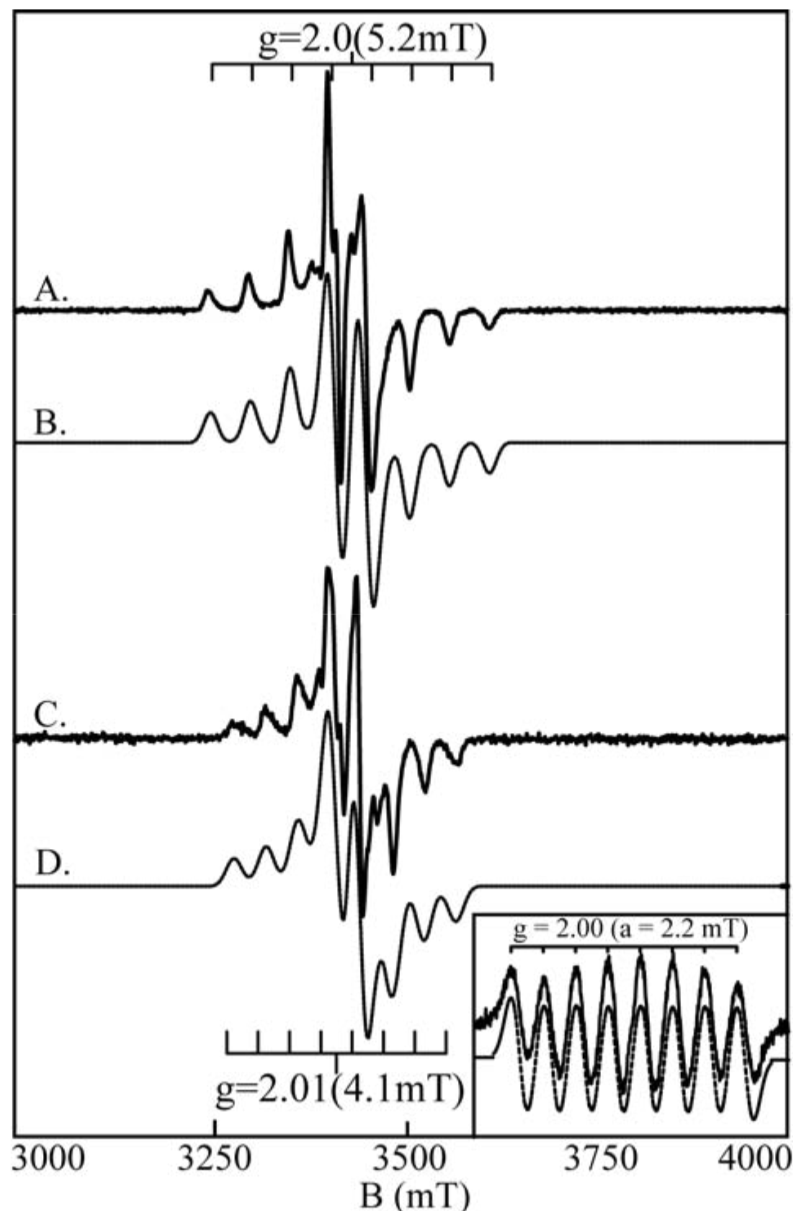
Figure 3.3: EPR spectra for $[Co(D^*)(tBuPy)_2]$ (A) and $[Co(D^*)(tBuCN)_2]$(C). Simulation of the EPR data (B and D) are shown underneath their their respective spectra. For $[Co(D^*)(tBuPy)_2]$, $g_x = g_y = 2.000$, $g_z = 2.003$ and $A_x = A_y$=16 MHz, A_z=143 MHz. For $[Co(D^*)(tBuCN)_2]$, $g_x = g_y = 2.000$, $g_z = 2.005$ and $A_x = A_y$=16 MHz, A_z=115 MHz. Instrument conditions: (A-D) microwaves, 9.65 GHz, 0.002mW; modulation, 0.5 mT; temperature 8.2K. Inset: microwave, 9.78 GHz, 20 mW; modulation, 1.0 mT; temperature 298K. Reprint with permission from W. C. Ellis, "Green design, synthesis, characterization and application of a novel family of Fe(III)-TAML peroxide activating homogeneous catalysts", Ph.D. thesis, Carnegie Mellon University, 2010
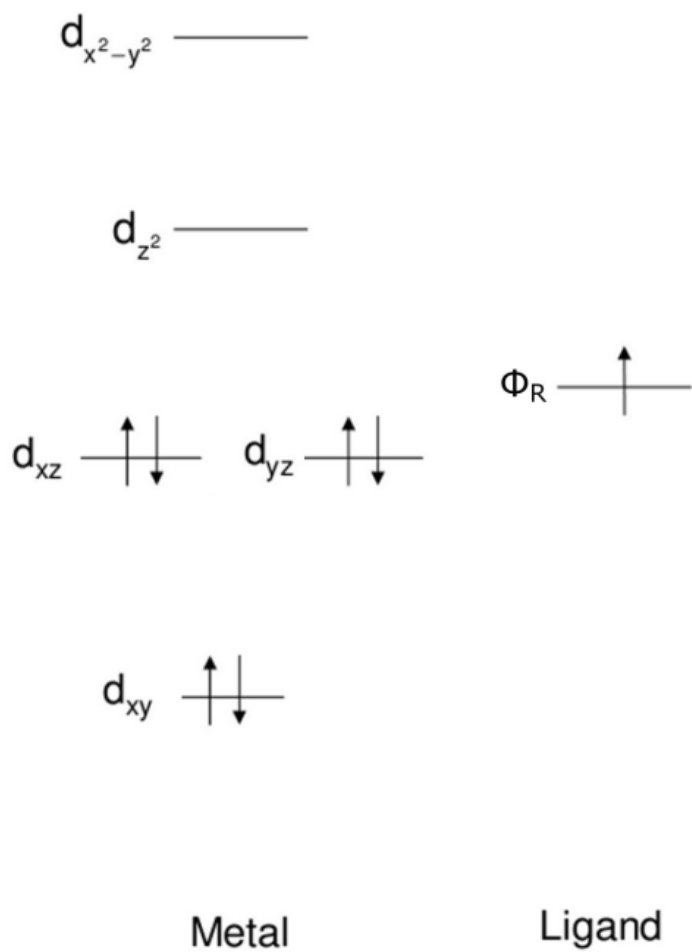
(a) d-orbitals splitting diagram for $[\text{Co(D}^*)(\text{tBuPy})_2]$
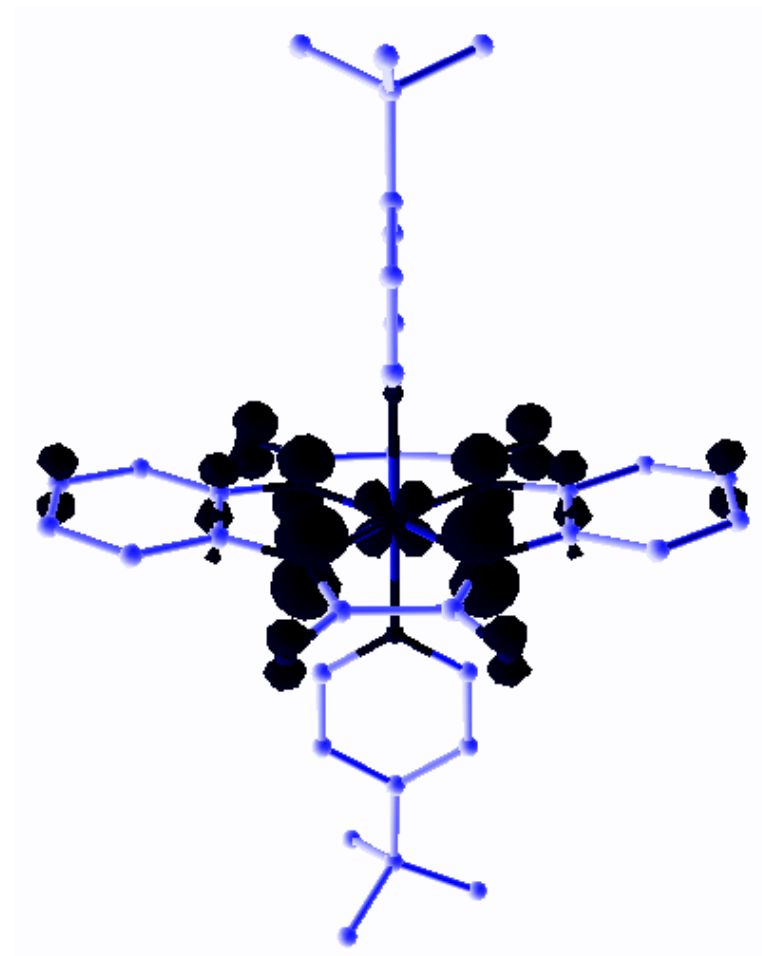
(b) spin density plot for $[\text{Co(D}^*)(\text{tBuPy})_2]$

Figure 3.4: Spin density plots and d-orbitals splitting diagram
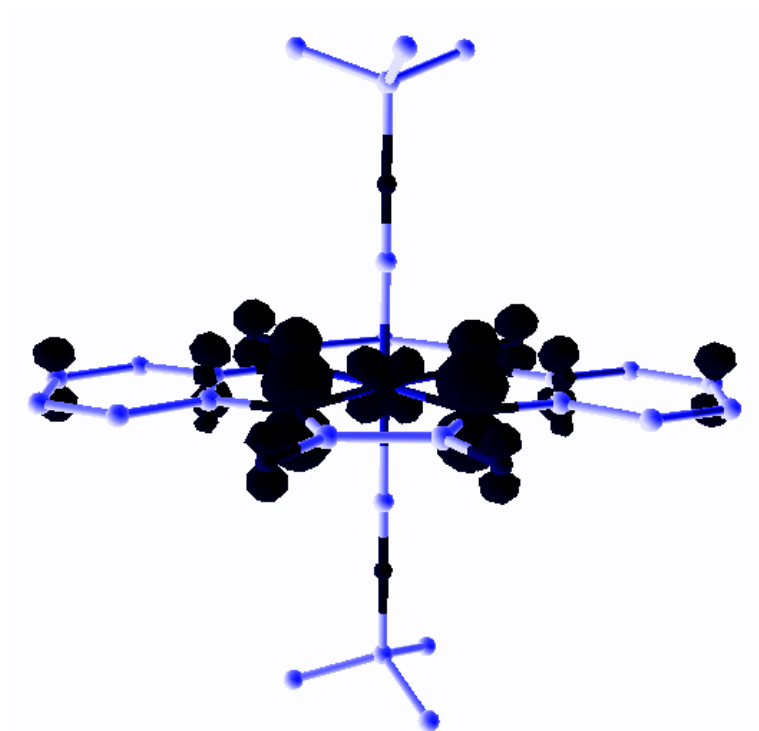
(a) spin density plot for $[Co(D^*)(tBuCN)_2]$
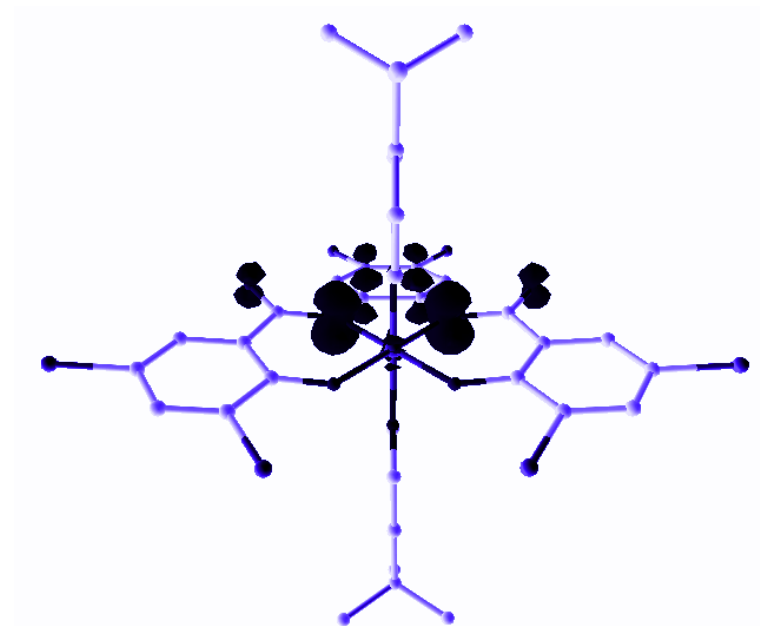
(b) spin density plot for $[Co(PAC)(tBuPy)_2]$

Figure 3.4 continued

The resulting spin populations, P, of the cobalt ions in the three complexes are listed in Table 3.1 and show values P < 0.1, which are compared to P = 1 for the free S = ½ Co(IV) ion, and unambiguously qualify the DFT solutions of the three complexes as ligand-based radical states. The table lists also the values calculated for the Fermi contact coupling constant (A^{FC}) and the largest component of the spin-dipolar coupling (A^{SD}) as well as the ratios (A^{FC}/A_0^{FC}) and (A^{SD}/A_0^{SD}).

Table 3.1: DFT results for Fermi contact couplings, spin-dipolar couplings, their relative values, and spin populations

Complex	A^{FC} (MHz) [a]	A^{SD} (MHz) [b]	(A^{FC}/A_0^{FC}) [c]	(A^{SD}/A_0^{SD}) [d]	P [e]
Co^{IV} ion	-241.0	-510.8	1.00	1.00	1.00
$[Co(D^*)(tBuPy)_2]$	-35.1	-43.8	0.15	0.09	0.09
$[Co(D^*)(tBuCN)_2]$	-32.2	-32.2	0.14	0.09	0.09
$[Co(PAC)(tBuPy)_2]$	-27.0	-14.6	0.11	0.03	0.01

[a] : Fermi contact coupling in $\hat{\boldsymbol{I}}_{Co}\,\tilde{\boldsymbol{A}}^{FC}\,\hat{\boldsymbol{S}}_{Co}$ with $S_{Co} = 1/2$

[b] : Component with largest magnitude of spin-dipolar coupling tensor in $\hat{\boldsymbol{I}}_{Co}\,\tilde{\boldsymbol{A}}^{SD}\,\hat{\boldsymbol{S}}_{Co}$ with $S_{Co} = 1/2$

[c] : A_0^{FC} is Fermi contact coupling of free ion.

[d] : A_0^{SD} is component with largest magnitude of spin-dipolar contact coupling of free low-spin Co^{IV} ion with unpaired electron in d_{yz}

[e] : P is the Mulliken spin population of Co

The last three columns of Table 3.1 reveal that the A-ratios and the spin populations for the coordinated cobalt ions show a similar reduction compared to the values for the free Co(IV) ion. Since the Co(IV) ion has strong hyperfine interactions, even a small admixture of Co(IV) character into the wavefunction already gives rise to sizable hyperfine coupling constants. This result proves the inadequacy of the naïve criterion that the observation of ^{59}Co hyperfine splitting is the signature of a metal-based radical.

The correlation between A values and spin populations indicates that the former quantities provide a reliable measure for classifying the nature of the radical states. The A values calculated for the complexes in Table 3.1 are in excellent agreement with the hyperfine couplings deduced from EPR. The agreement validates the quality of the DFT solutions and classifies the four cobalt complexes as radical species with a preponderant ligand character. This conclusion is supported by the nearly isotropic $\tilde{\boldsymbol{g}}$ values, $g_i \approx 2$ (i = x, y, z) observed for these species, pointing toward a lack of orbital angular momentum, which is typical for radicals and untypical for transition metal ions, and by the observation of an EPR spectrum at ambient temperatures.

The present analysis reopens the quest for a genuine Co(IV) complex.

3.4   Theoretical Analysis of Co Electronic Structure under the Ligand Field Influence

The square bipyramidal complexes discussed in 3.4 demonstrate properties with preponderant ligand character of the orbital carrying the unpaired electrons in these systems. $[Co(Et)(Salen)]^{+1}$ distinguishes itself from the above-mentioned series of structurally related square-pyramidal complexes by anisotropic $\tilde{g}$ values ($g_1 = 2.213$, $g_2 = 2.090$, $g_3 = 1.993$) and hyperfine coupling $\tilde{A}$ tensors ($|A_1| = 72\,\text{MHz}$, $|A_2| = 40\,\text{MHz}$, $|A_3| = 27\,\text{MHz}$).[56] These two properties indicate that the radical in the ethyl-cobalt complexes is largely centered at the metal. This conclusion is further supported by the absence of EPR spectra in liquid solution.[56] To investigate the nature of the ethyl-cobalt species we have performed DFT calculations. In particular, two questions are to be addressed : (1) if the Co in these complexes can be described as a Co(IV) ion and (2) why the radical is, respectively, centered at the metal in the ethyl-cobalt species and at the ligand in the complexes of Table 3.1.

3.4.1   EPR Parameters Analysis for $[Co(Et)(Salen)]^{+1}$

The salient features of the electronic structure of $[Co(Et)(Salen)]^{+1}$ as obtained by DFT are shown in Figure 3.5. These include the presence of a strong, organometallic σ bond between the ethyl and the cobalt and an unpaired electron in the d_{yz} orbital (like the case of D^*, the x-axis is chosen along the C_2 axis of the Salen ligand and z is perpendicular to the ligand plane).

Figure 3.5 (a) reveals two low-lying d-d transitions, indicated by dashed arrows.

Spin orbit coupling of the ground state with the excitations $d^{\beta}_{x^2-y^2} \longrightarrow d^{\beta}_{yz}$ and $d^{\beta}_{xz} \longrightarrow d^{\beta}_{yz}$ yield orbital angular momentum along x and z, resulting in increments in the g-values, $\Delta g_x = g_x - 2 > 0$ and $\Delta g_z = g_z - 2 > 0$, respectively. Thus, the calculated orbital scheme correctly predicts that two of the g-values (g_1 and g_2) are larger than 2 while the third one ($g_3 = 1.998$) is essentially 2. The optimized geometry of $[Co(Et)(Salen)]^{+1}$ is shown in Figure 3.5(b).

(a) Orbital diagram
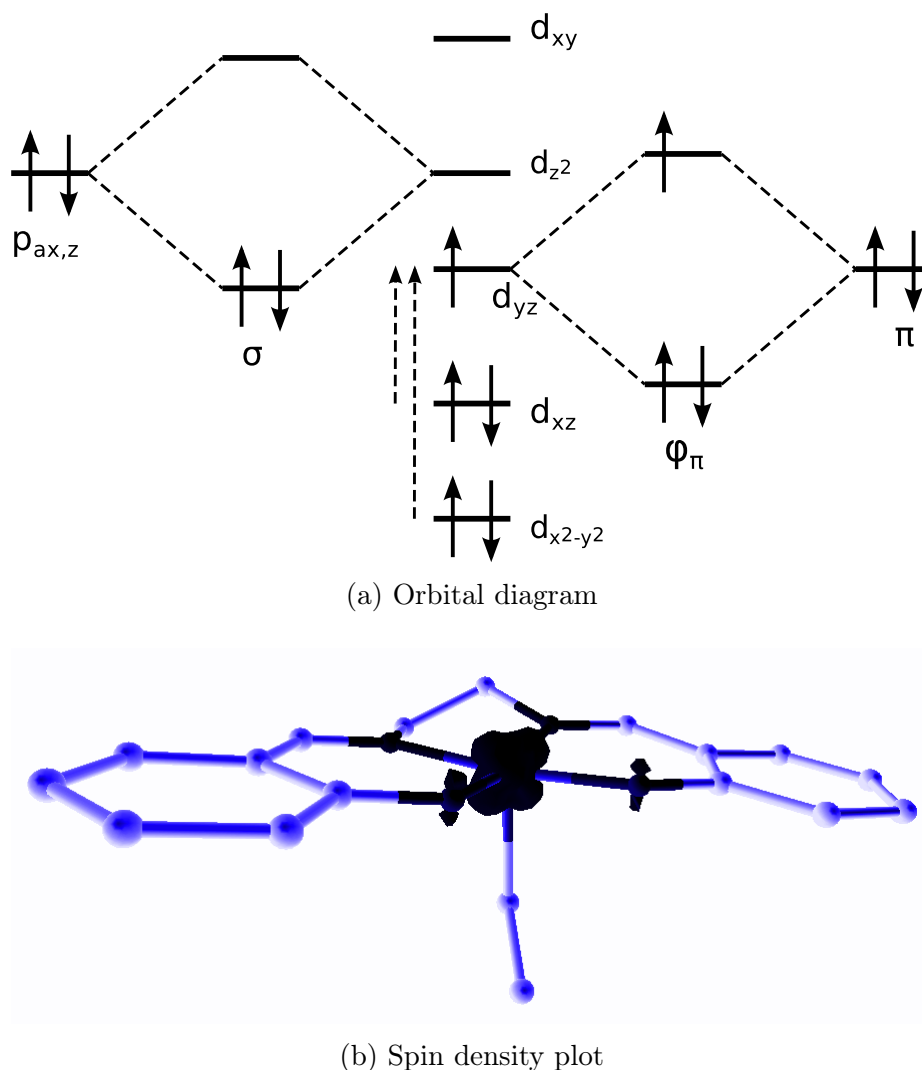
(b) Spin density plot

Figure 3.5: Schematic orbital diagram and spin density plot of $[Co(Et)(Salen)]^{+1}$. Dashed arrows indicate d-d transition excitations.

As an additional test of the DFT solutions for $[Co(Et)(Salen)]^{+1}$, the magnetic hy-

perfine coupling constants of Co (A-values) were analyzed. These values depend on three contributions, an isotropic Fermi contact term (FC), a spin-dipolar term (SD) and an orbital term (L) : $A = A^{\text{FC}} + A^{\text{SD}} + A^{\text{L}}$. Including all three terms and ignoring the small crossing terms resulting from the second order perturbation, the following expressions[62] are used for the three principal values of the A tensor for the scheme in Figure 3.5(a).

$$
\begin{aligned}
A_x &= \left(-\kappa - \frac{4}{7} + \Delta\, g_x \right) P \\
A_y &= \left(-\kappa + \frac{2}{7} \right) P \\
A_z &= \left(-\kappa - \frac{2}{7} + \Delta\, g_z \right) P
\end{aligned}
\tag{3.1}
$$

where $P = g_e\, g_n\, \mu_e\, \mu_n\, \langle r^{-3} \rangle_{\text{3d}}$. To obtain estimates of P, DFT values (see 3.7.3.1) for the free low-spin Co^{4+} ion with the unpaired electron in the d_{yz} orbital were used ($A^{SD}_{0,y} = {}^2/{}_7\, P_0$ cf. eqn 3.1, subscript 0 for Co^{IV} free ion) and solved $P_0 = 870$ MHz. Comparing the DFT predicted FC term A^{SD} between Co^{IV} free ion and $[\text{Co}(\text{Et})(\text{Salen})]^{+1}$ yields $A^{SD}/A^{SD}_0 = 0.46$ (subscript 0 for Co^{IV} free ion). So it is plausible to adopt $P \approx {}^1/{}_2\, P_0$. The orbital terms A^{L} are not provided by the DFT solution. Experimental values are used as surrogates. $\Delta\, g_x = g_1 - 2 = 0.218$ and $\Delta\, g_z = g_2 - 2 = 0.095$. Then $A^{\text{L}}_{x,y,z} = (\Delta\, g_x\, P, \sim 0, \Delta\, g_z\, P) = (95, 0, 41)$ MHz. Adding these values with the DFT estimates (see 3.7.3.1) of A^{FC} and A^{SD} for $[\text{Co}(\text{Et})(\text{Salen})]^{+1}$, the diagonal elements for the total hyperfine coupling tensor $\tilde{\boldsymbol{A}}$ is obtained as $A_{x,y,z} = (-274, -40, 114)$ MHz. With the mapping of $g_1 \longrightarrow g_x$, $g_2 \longrightarrow g_z$, $g_3 \longrightarrow g_y$, the predicted values must be compared with the experimental values $|A^{\text{expr}}_{1,3,2}| = (224, 76, 117)$ MHz. The comparison shows a satisfactory agreement between experiment and theory. [1] The analysis presented here identifies the principal

---

[1]The alternative mapping $g_1 \longrightarrow g_z$, $g_2 \longrightarrow g_x$, $g_3 \longrightarrow g_y$ yields a less satisfactory agreement.

axes of the g- and A-tensors with the Cartesian axes of the molecular frame. For example, the principal axis with the largest g- and A- values is directed along the C_2 axis of the Salen ligand. Furthermore, the analysis provides the signs of the $A_{1,2,3}$ values

3.4.2 Electronic Configuration Manifold

The electronic configuration shown in Figure 3.5 (a) can only be considered an idealization of the DFT state. Due to covalency, the unoccupied d orbitals in Figure 3.5 (a) are partially populated. Obviously, these populations affect the properties, such as the A values.

Table 3.2: Mulliken spin populations for $[Co(Et)(Salen)]^{+1}$

Orbital	Total Electron Population	Spin Population
d_{xy}	0.73	0.05
d_{z^2}	1.25	0.16
d_{yz}	1.40	0.58
d_{xz}	1.90	0.02
$d_{x^2-y^2}$	1.94	0.02
d orbitals sum	7.22	0.84
$p_{ax,z}$	0.89	-0.07

$p_{ax,z}$: axial ligand p orbital. see 3.7.3.2 for data sources.

Table 3.2 lists the DFT Mulliken total populations and the spin populations of 3d orbitals of Co and of p orbital of the ethyl axial ligand in $[Co(Et)(Salen)]^{+1}$. The d_{yz} population, which is 1 in the idealized configuration of Figure 3.5 (a), has actually a value of about 1.4 due to the donation of electron density with β spin from the Salen ligand. Consequently, the spin population of the d_{yz} orbital is lowered by about 0.4 to yield 0.6. This reduction lowers the values of the magnetic hyperfine parameters. The lowering was introduced in the analysis of the A values with eqn 3.1 by adopting

P about half of its value for the Co^{IV} free ion. The d_{xy} orbital (unoccupied in Figure 3.5 (a)) receives a population of about 0.7 electrons by σ donation from the Salen ligand that is made up of nearly equal amount of α and β spin density. The spin population of the Co can be decomposed into three contributions: 1.00 (the electron in d_{yz}^α), 0.34 (net donation of β spin density by Salen ligand, see 3.7.3.2), and 0.18 (net donation of α spin density by ethyl), which add up to the total of 0.84, the spin population listed for Co in Table 3.2. The latter ethyl-to-cobalt spin transfer is due to the spin polarization of the ethyl-cobalt bond by the unpaired electron in d_{yz}^α.

Restricting the set of orbitals shown, the DFT solution for $[Co(Et)(Salen)]^{+1}$ can be expressed by the configuration

$$\left| \sigma^\alpha \, \sigma'^\beta \, (d_{x^2-y^2})^2 \, (d_{xz})^2 \, d_{yz}^\alpha \, \pi_z^\alpha \, \phi_\pi^\beta \right| \qquad (3.2)$$

The orbitals $\sigma \approx \sigma' \approx 2^{-1/2}(p_{ax,z} + d_{z^2})$. represent the ethyl-cobalt bond, orbital π is located at the Salen ligand, and $\phi_\pi \approx cos(\theta)\,\pi_z + sin(\theta)\,d_{yz}$ in $[Co(Et)(Salen)]^{+1}$ mainly, but not entirely, located at the Salen ligand (the admixture with π causes the population of d_{yz} to rise above 1, Table 3.2). σ' expresses that the orbitals for the α and β electrons in the σ bond are not identical. The σ orbital for the α electron is slightly more polarized toward the cobalt than the σ' orbital for the β electron the exchange interaction with the unpaired α electron in d_{yz}. As a result the spin populations of the d_{z^2} and $p_{ax,z}$ are positive and negative, respectively (Table 3.2).

To address the electronic configuration of Co in $[Co(Et)(Salen)]^{+1}$, multiple scenarios need to be taken under consideration. Table 3.3 lists a number of potential formulations of the oxidation state by making different choices for the orbitals σ, σ' and ϕ_π. The oxidation states for Co listed range from IV to I and include axial and equatorial ligand based radicals. Co^{IV} is found when the σ electrons belong to ethyl,

Table 3.3: Formulation of $[Co(Et)(Salen)]^{+1}$ available within single determinant

σ	σ'	ϕ_π	Formulation
$p_{ax,z}$	$p_{ax,z}$	π	$Co^{IV}(m_s=1/2)$
d_{z^2}	$p_{ax,z}$	π	$Co^{III}(m_s=1)\; Et\bullet(m_s=-1/2)^a$
$p_{ax,z}$	$p_{ax,z}$	d_{yz}	$Co^{III}(m_s=0)\; Salen\bullet(m_s=1/2)$
d_{z^2}	d_{z^2}	π	$Co^{II}(m_s=1/2)$
d_{z^2}	$p_{ax,z}$	d_{yz}	$Co^{II}(m_s=1/2)\; Et\bullet(m_s=-1/2)\; Salen\bullet(m_s=1/2)$
d_{z^2}	d_{z^2}	d_{yz}	$Co^{I}(m_s=0)\; Salen\bullet(m_s=1/2)\;^a$

[a]Broken symmetry configurations representing antiferromagnetic bi- and tri-radical states.

$\sigma \approx \sigma' \approx p_{ax,z}$ (1st row of Table 3.3) while Co^{II} when σ electrons belong to Co, $\sigma \approx \sigma' \approx d_{z^2}$ (4th row of Table 3.3). Obviously, neither formulation describes the state of cobalt in $[Co(Et)(Salen)]^{+1}$. Although the Mulliken populations, 1.3 for d_{z^2} and 0.9 for $p_{ax,z}$ (Table 3.2), suggest that the state of cobalt is biased toward Co^{II}, it seems more meaningful to consider complex $[Co(Et)(Salen)]^{+1}$ and generally any complex in which (one of) the d orbitals participate in strong organometallic bonding, as members of a distinct class of oxidation states.

3.4.3 Ligand Field Influence on the Electronic Configuration of Co

The previous section (3.4.2) demonstrates the multiple possibilities in assigning the electronic configuration of $[Co(Et)(Salen)]^{+1}$. It is obvious from the discussion that ligands have a great influence on the metal electronic configuration. This section focuses on a quantitative analysis on the ligand effects on the metal electronic state. Table 3.4 lists Mulliken spin populations obtained from DFT calculations for series Salen and D^* complexes with different axial ligands, including the ethyl and tBuPy ligands in $[Co(Et)(Salen)]^{+1}$ and $[Co(tBuPy)_2(D^*)]$. The axial ligands have been arranged from left to right in the order of decreasing σ donor strength. In crossing

the table from left to right one observes a decrease in spin population of cobalt and a complementary increase in the spin population of the equatorial ligand. Thus, there is a shift of the radical from the cobalt to the equatorial ligand upon weakening the axial donor strength.

Table 3.4: Mulliken spin populations of $[Co(L_{ax})(L_{eq})]^n$

		L_{ax}		
		Et	Me	$(tBuPy)_2$
$L_{eq}=D^*$	$P(Co)$	0.74	0.63	0.09^b
	$P(L_{ax})$	0.37	0.46	0.92
	$P(L_{eq})$	-0.13	-0.09	-0.01
$L_{eq}=Salen$	$P(Co)$	0.84^a	0.63	0.06
	$P(L_{ax})$	0.34^a	0.48	0.95
	$P(L_{eq})$	-0.18^a	-0.11	0.01

[a]$[Co(Et)(Salen)]^{+1}$. [b]$[Co(tBuPy)_2(D^*)]$

The mechanism responsible for this behavior is illustrated in Figure 3.6. Strong axial electron donation inhibits transfer from the equatorial ligand to the cobalt and, thus, of the formation of an equatorial ligand radical. This situation is found in $[Co(Et)(Salen)]^{+1}$. Alternately, weak axial electron donation allows transfer from the equatorial ligand to the cobalt, resulting in the formation of an equatorial ligand radical. An essential condition for the formation of the ligand radical is the presence of the α spin electron in the receptor d_{yz} orbital, allowing only the transfer of β spin density (Figure 3.6, bottom). This situation is found in $[Co(tBuPy)_2(D^*)]$. In contrast, the acceptor orbital d_{z^2} of the axial donation is formally empty, enabling the transfer of both α and β electron density and precluding the formation of an axial radical (Figure 3.6, bottom). [2]

To quantify the impact of the axial ligand on the electronic state of Co, Table 3.5 list

---

[2]Table 3.4 reveals some negative spin density at the density which is due to the spin polarization mechanism described above.

the total spin populations in the d_{z^2} orbital of $[Co(Et)(Salen)]^{+1}$ and $[Co(tBuPy)_2(D^*)]$. It is noticed from the table that the variation of the total spin population on the d_{z^2} orbital as a function of axial ligand strength is astonishingly similar between two Co complexes. As the electron donating capacity of the axial ligand gradually weakens, the d_{z^2} orbital electron population decreases correspondingly. Along the same trend, the electronic character of Co complexes migrate from Co^{IV} to Co^{III}−Ligand•(Figure 3.6) due to diminishing power of the axial ligand in competition with the equatorial ligand. The quantitative information in Table 3.5 fortifies the qualitative illustration (Figure 3.6) on the mechanism on ligand effects on the electronic structure of the Co complexes.

(a) $[Co(Et)(Salen)]^{+1}$ (b) $[Co(tBuPy)_2(D^*)]$
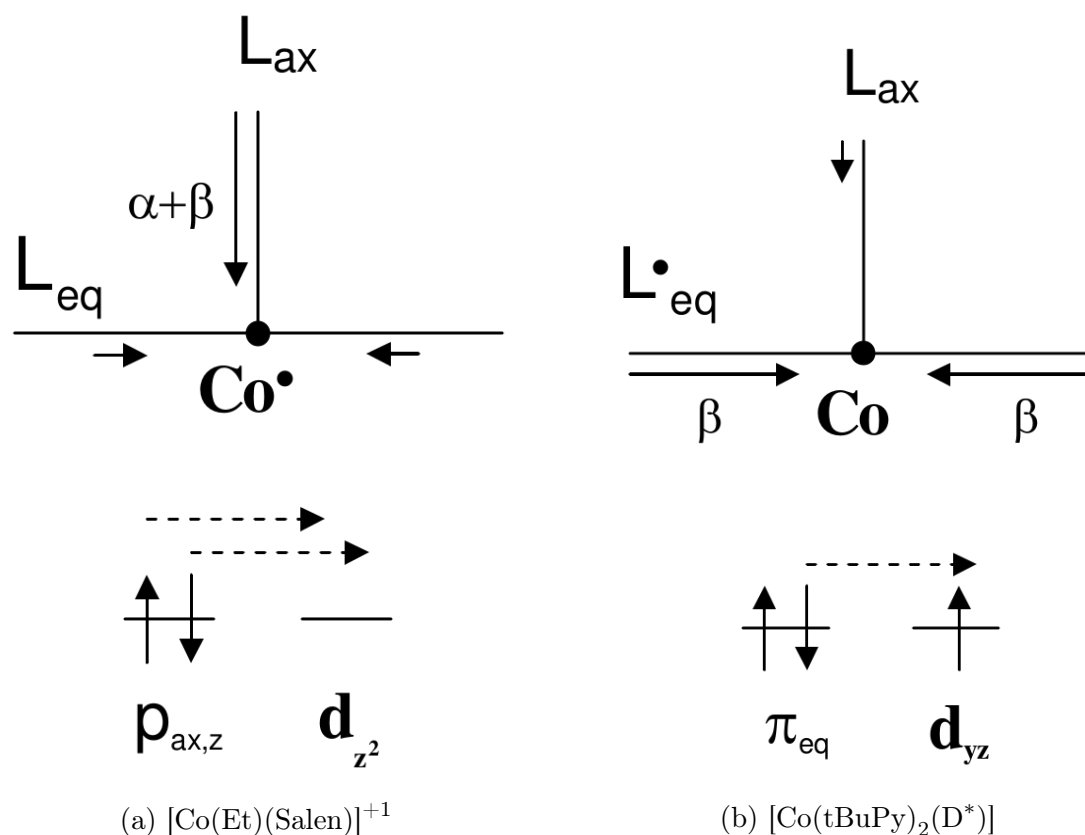
Figure 3.6: Relative importance and spin polarization of complementary ligand-to-metal electron donation pathways (top) and orbitals involved in the electron density transfer (bottom) in complex $[Co(Et)(Salen)]^{+1}$ (a) and $[Co(tBuPy)_2(D^*)]$(b)

Table 3.5: Total spin population in d_{z^2} for $[\text{Co(Et)(Salen)}]^{+1}$ and $[\text{Co(tBuPy)}_2(\text{D}^*)]$

Complex	Et	Me	$(\text{tBuPy})_2$
D^*	1.14	1.10	0.65
Salen	1.25	1.18	0.69

3.5 Conclusions

This chapter visited the topic of Co as a key element in designing water splitting catalysts. To appreciate the mechanism of Co oxidizing water, precise characterization of the reactive intermediate Co^{IV} becomes overridingly important. However, due to the lack of good knowledge about the bona fide Co^{IV} complexes, EPR spectroscopic diagnosis can lead to ambiguous assignment. In this study, DFT computation of the electronic structures for several Co complexes synthesized in Collins' group pointed out that the hyperfine feature is a naïve or even misleading signal in judging the electronic structure for Co complexes because of the unusual large coupling constants between the electrons and nucleus for this particular element. Under such circumstances, the combination between DFT calculation and spectroscopic evidence presents a significant advancement in electronic structure determination. As a result of this study, literature precedence on the electronic configuration of Co complexes deserve reexamination.

In addition, this research also investigated the ligand effects on the electronic state of Co in its coordination environment. An important conclusion drawn from the study is that the essential condition to formation of the ligand radical is the presence α spin electron in the receptor metal d orbital. To counteract this effect, strong electron donating axial ligands should be used in designing Co complexes to achieve the Co^{IV} state.

3.6 References

[1] L. A. White. Energy and the Evolution of Culture. *American Anthropologist* **1943**, *45*, 335–356.

[2] C. Mattick, E. Williams, B. Allenby. Historical Trends in Global Energy Consumption. *IEEE Technol. Soc. Mag.* **2010**, *29*, 22–30.

[3] D. Gust, T. a. Moore, A. L. Moore. Solar Fuels via Artificial Photosynthesis. *Acc. Chem. Res.* **2009**, *42*, 1890–1898.

[4] N. S. Lewis. Toward cost-effective solar energy use. *Science* **2007**, *315*, 798–801.

[5] L. P. VERNON, M. AVRON. PHOTOSYNTHESIS. *Annu. Rev. Biochem.* **1965**, *34*, 269–96.

[6] J. Chow, R. J. Kopp, P. R. Portney. Energy resources and global development. *Science* **2003**, *302*, 1528–31.

[7] R. F. Aguilera, R. G. Eggert, G. Lagos C.C., J. E. Tilton. Depletion and the Future Availability of Petroleum Resources. *The Energy Journal* **2009**, *30*.

[8] S. Arrhenius. On the influence of carbonic acid in the air upon the temperature of the ground. *Philosophical Magazine and Journal of Science Series 5* **1896**, *41*, 237–276.

[9] T. R. Karl, K. E. Trenberth. Modern global climate change. *Science* **2003**, *302*, 1719–23.

[10] J. E. Kutzbach, W. F. Ruddiman, S. J. Vavrus, G. Philippon. Climate model simulation of anthropogenic influence on greenhouse-induced climate change (early agriculture to modern): the role of ocean feedbacks. *Clim. Chang.* **2009**, *99*, 351–381.

[11] P. K. Jana, I. Saha. Correlation of green house molecules with global and surface temperature and its effect on environment. *Indian J. Phys.* **2011**, *85*, 667–682.

[12] M. Höök, X. Tang. Depletion of fossil fuels and anthropogenic climate change - A review. *Energy Policy* **2013**, *52*, 797–809.

[13] N. Lewis, D. Nocera. Powering the planet: Chemical challenges in solar energy utilization. *PNAS* **2006**, *103*, 15729–35.

[14] A. J. Esswein, D. G. Nocera. Hydrogen production by molecular photocatalysis. *Chem. Rev.* **2007**, *107*, 4022–47.

[15] T. Kodama, N. Gokon. Thermochemical cycles for high-temperature solar hydrogen production. *Chem. Rev.* **2007**, *107*, 4048–77.

[16] M. W. Kanan, Y. Surendranath, D. G. Nocera. Cobalt-phosphate oxygen-evolving compound. *Chem. Soc. Rev.* **2009**, *38*, 109–14.

[17] R. M. Navarro, M. C. Alvarez-Galván, J. a. Villoria de la Mano, S. M. Al-Zahrani, J. L. G. Fierro. A framework for visible-light water splitting. *Energy & Environmental Science* **2010**, *3*, 1865.

[18] N. Armaroli, V. Balzani. The future of energy supply: Challenges and opportunities. *Angew. Chem., Int. Ed. Engl.* **2007**, *46*, 52–66.

[19] J. Petit, J. Jouzel, D. Raynaud, N. Barkov. Climate and atmospheric history of the past 420,000 years from the Vostok ice core, Antarctica. *Nature* **1999**, *399*, 429–436.

[20] U. Siegenthaler, T. F. Stocker, E. Monnin, D. Lüthi, J. Schwander, B. Stauffer, D. Raynaud, J.-M. Barnola, H. Fischer, V. Masson-Delmotte, J. Jouzel. Stable carbon cycle-climate relationship during the Late Pleistocene. *Science* **2005**, *310*, 1313–7.

[21] J. Jouzel, V. Masson-Delmotte, O. Cattani, G. Dreyfus, S. Falourd, G. Hoffmann, B. Minster, J. Nouet, J. M. Barnola, J. Chappellaz, H. Fischer, J. C. Gallet, S. Johnsen, M. Leuenberger, L. Loulergue, D. Luethi, H. Oerter, F. Parrenin, G. Raisbeck, D. Raynaud, A. Schilt, J. Schwander, E. Selmo, R. Souchez, R. Spahni, B. Stauffer, J. P. Steffensen, B. Stenni, T. F. Stocker, J. L. Tison, M. Werner, E. W. Wolff. Orbital and millennial Antarctic climate variability over the past 800,000 years. *Science* **2007**, *317*, 793–6.

[22] D. Lüthi, M. Le Floch, B. Bereiter, T. Blunier, J.-M. Barnola, U. Siegenthaler, D. Raynaud, J. Jouzel, H. Fischer, K. Kawamura, T. F. Stocker. High-resolution

carbon dioxide concentration record 650,000-800,000 years before present. *Nature* **2008**, *453*, 379–82.

[23] A. J. Bard, M. A. Fox. Artificial Photosynthesis: Solar Splitting of Water to Hydrogen and Oxygen. *Acc. Chem. Res.* **1995**, *28*, 141–145.

[24] V. Balzani, L. Moggi, M. F. Manfrin, F. Bolletta, M. Gleria. Solar Energy Conversion by Water Photodissociation: Transition metal complexes can provide low-energy cyclic systems for catalytic photodissociation of water. *Science* **1975**, *189*, 852–6.

[25] J. P. McEvoy, G. W. Brudvig. Water-splitting chemistry of photosystem II. *Chem. Rev.* **2006**, *106*, 4455–83.

[26] G. Renger, T. Renger. Photosystem II: The machinery of photosynthetic water splitting. *Photosynth. Res.* **2008**, *98*, 53–80.

[27] J. C. Fontecilla-Camps, A. Volbeda, C. Cavazza, Y. Nicolet. Structure/function relationships of [NiFe]- and [FeFe]-hydrogenases. *Chem. Rev.* **2007**, *107*, 4273–303.

[28] C. Tard, C. J. Pickett. Structural and functional analogues of the active sites of the [Fe]-, [NiFe]-, and [FeFe]-hydrogenases. *Chem. Rev.* **2009**, *109*, 2245–74.

[29] W. Lubitz, E. J. Reijerse, J. Messinger. Solar water-splitting into H2 and O2: design principles of photosystem II and hydrogenases. *Energy & Environmental Science* **2008**, *1*, 15.

[30] P. Du, R. Eisenberg. Catalysts made of earth-abundant elements (Co, Ni, Fe) for water splitting: Recent progress and future challenges. *Energy & Environmental Science* **2012**, *5*, 6012.

[31] G. N. Schrauzer, R. J. Holland. Hydridocobaloximes. *J. Am. Chem. Soc.* **1971**, *93*, 1505–1506.

[32] G. L. Elizarova, L. G. Matvienko, N. V. Lozhkina, V. N. Parmon, K. I. Zamaraev. Homogeneous catalysts for dioxygen evolution from water. Water oxidation by trisbipyridylruthenium(III) in the presence of cobalt, iron and copper complexes. *React. Kinet. Catal. Lett.* **1981**, *16*, 191–194.

[33] M. W. Kanan, D. G. Nocera. In situ formation of an oxygen-evolving catalyst in neutral water containing phosphate and Co2+. *Science* **2008**, *321*, 1072–5.

[34] D. a. Lutterman, Y. Surendranath, D. G. Nocera. A self-healing oxygen-evolving catalyst. *J. Am. Chem. Soc.* **2009**, *131*, 3838–9.

[35] Y. Surendranath, M. Dinca, D. G. Nocera. Electrolyte-dependent electrosynthesis and activity of cobalt-based water oxidation catalysts. *J. Am. Chem. Soc.* **2009**, *131*, 2615–20.

[36] Y. Surendranath, M. W. Kanan, D. G. Nocera. Mechanistic studies of the oxygen evolution reaction by a cobalt-phosphate catalyst at neutral pH. *J. Am. Chem. Soc.* **2010**, *132*, 16501–9.

[37] F. Jiao, H. Frei. Nanostructured cobalt oxide clusters in mesoporous silica as efficient oxygen-evolving catalysts. *Angew. Chem., Int. Ed. Engl.* **2009**, *48*, 1841–4.

[38] T. Lazarides, T. McCormick, P. Du, G. Luo, B. Lindley, R. Eisenberg. Making hydrogen from water using a homogeneous system without noble metals. *J. Am. Chem. Soc.* **2009**, *131*, 9192–4.

[39] J. J. H. Pijpers, M. T. Winkler, Y. Surendranath, T. Buonassisi, D. G. Nocera. Light-induced water oxidation at silicon electrodes functionalized with a cobalt oxygen-evolving catalyst. *PNAS* **2011**, *108*, 10056–61.

[40] S. Y. Reece, J. a. Hamel, K. Sung, T. D. Jarvi, A. J. Esswein, J. J. H. Pijpers, D. G. Nocera. Wireless solar water splitting using silicon-based semiconductors and earth-abundant catalysts. *Science* **2011**, *334*, 645–8.

[41] V. Artero, M. Chavarot-Kerlidou, M. Fontecave. Splitting water with cobalt. *Angew. Chem., Int. Ed. Engl.* **2011**, *50*, 7238–66.

[42] X. Sala, I. Romero, M. Rodríguez, L. Escriche, A. Llobet. Molecular catalysts that oxidize water to dioxygen. *Angew. Chem., Int. Ed. Engl.* **2009**, *48*, 2842–52.

[43] M. Yagi, M. Kaneko. Molecular catalysts for water oxidation. *Chem. Rev.* **2001**, *101*, 21–35.

[44] K. N. Ferreira, T. M. Iverson, K. Maghlaoui, J. Barber, S. Iwata. Architecture of the photosynthetic oxygen-evolving center. *Science* **2004**, *303*, 1831–8.

[45] K. Sauer, J. Yano, V. K. Yachandra. X-ray spectroscopy of the Mn4Ca cluster in the water-oxidation complex of Photosystem II. *Photosynth. Res.* **2005**, *85*, 73–86.

[46] J. Barber. Crystal structure of the oxygen-evolving complex of photosystem II. *Inorg. Chem.* **2008**, *47*, 1700–10.

[47] Y. Umena, K. Kawakami, J.-R. Shen, N. Kamiya. Crystal structure of oxygen-evolving photosystem II at a resolution of 1.9 Å. *Nature* **2011**, *473*, 55–60.

[48] G. F. Swiegers, J. K. Clegg, R. Stranger. Structural similarities in enzymatic, homogeneous and heterogeneous catalysts of water oxidation. *Chemical Science* **2011**, *2*, 2254.

[49] M. Risch, V. Khare, I. Zaharieva, L. Gerencser, P. Chernev, H. Dau. Cobalt-oxo core of a water-oxidizing catalyst film. *J. Am. Chem. Soc.* **2009**, *131*, 6936–7.

[50] M. W. Kanan, J. Yano, Y. Surendranath, M. Dincă, V. K. Yachandra, D. G. Nocera. Structure and valency of a cobalt-phosphate water oxidation catalyst determined by in situ X-ray spectroscopy. *J. Am. Chem. Soc.* **2010**, *132*, 13692–701.

[51] B. S. Brunschwig, M. H. Chou, C. Creutz, P. Ghosh, N. Sutin. Mechanisms of water oxidation to oxygen: cobalt(IV) as an intermediate in the aquocobalt(II)-catalyzed reaction. *J. Am. Chem. Soc.* **1983**, *105*, 4832–4833.

[52] J. G. McAlpin, Y. Surendranath, M. Dinca, T. a. Stich, S. a. Stoian, W. H. Casey, D. G. Nocera, R. D. Britt. EPR evidence for Co(IV) species produced during water oxidation at neutral pH. *J. Am. Chem. Soc.* **2010**, *132*, 6882–3.

[53] J. Topich, J. Halpern. Organobis(dioximato)cobalt(IV) complexes: electron paramagnetic resonance spectra and electronic structures. *Inorg. Chem.* **1979**, *18*, 1339–1343.

[54] F. F. Pfaff, S. Kundu, M. Risch, S. Pandian, F. Heims, I. Pryjomska-Ray, P. Haack, R. Metzinger, E. Bill, H. Dau, P. Comba, K. Ray. An oxocobalt(IV) complex stabilized by Lewis acid interactions with scandium(III) ions. *Angew. Chem., Int. Ed. Engl.* **2011**, *50*, 1711–5.

[55] J. Harmer, S. Van Doorslaer, I. Gromov, M. Bröring, G. Jeschke, A. Schweiger. A Pulse EPR and ENDOR Investigation of the Electronic Structure of a σ-Carbon-Bonded Cobalt(IV) Corrole. *J. Phys. Chem. B* **2002**, *106*, 2801–2811.

[56] G. A. Nikitaeva, A. T. Nikitaev, K. I. Zamaraev, A. L. Sigan, I. Y. Levitin, M. E. Vol'pin. ESR spectra and electronic structure of the oxidized forms of alkyl-bis (salicylidenato) ethylenediaminecobalt. *J. Struct. Chem.* **1978**, *19*, 243–247.

[57] F. C. Anson, T. J. Collins, R. J. Coots, S. L. Gipson, T. G. Richmond. Synthesis and characterization of stable cobalt(IV) coordination complexes: molecular structure of trans-[.eta.4-1,2-bis(3,5-dichloro-2-hydroxybenzamido)-4,5-dichlorobenzene]bis(4-tert-butylpyridine)cobalt(IV). *J. Am. Chem. Soc.* **1984**, *106*, 5037–5038.

[58] T. J. Collins, R. D. Powell, C. Slebodnick, E. S. Uffelman. Stable highly oxidizing cobalt complexes of macrocyclic ligands. *J. Am. Chem. Soc.* **1991**, *113*, 8419–8425.

[59] B. K. Bower, M. Findlay, J. C. W. Chien. Electron paramagnetic resonance of tetrakis(1-norbonyl) vanadium and cobalt. *Inorg. Chem.* **1974**, *13*, 759–760.

[60] M. Koikawa, M. Gotoh, H. Kawa, S. Kida, T. Kohzuma. Synthesis and characterization of cobalt(III) and cobalt(IV) complexes of N-(2-hydroxyphenyl)salicylamide and homologues. *J. Chem. Soc., Dalton Trans.* **1989**, 1613.

[61] W. C. Ellis, *Green design, synthesis, characterization and application of a novel family of Fe(III)-TAML peroxide activating homogeneous catalysts*, Ph.D. thesis, Carnegie Mellon University, **2010**.

[62] E. I. Solomon, A. B. P. Lever (Eds.), *Inorganic Electronic Structure and Spectroscopy*, John Wiely & Sons, Inc., **2006**.

[63] W. Feng, K. Yamato, L. Yang, J. S. Ferguson, L. Zhong, S. Zou, L. Yuan, X. C. Zeng, B. Gong. Efficient kinetic macrocyclization. *J. Am. Chem. Soc.* **2009**, *131*, 2629–37.

[64] A. D. Becke. Density-functional thermochemistry. III. The role of exact exchange. *J. Chem. Phys.* **1993**, *98*, 3–7.

[65] A. D. Becke. Density-functional exchange-energy approximation with correct asymptotic behavior. *Phys. Rev. A* **1988**, *38*, 3098–3100.

[66] C. Lee, W. Yang, R. G. Parr. Development of the Colle-Salvetti correlation-energy formula into a functional of the electron density. *Phys. Rev. B* **1988**, *37*, 785–789.

[67] M. J. Frisch, G. W. Trucks, H. B. Schlegel, G. E. Scuseria, M. A. Robb, J. R. Cheeseman, J. A. Montgomery, T. Vreven, K. N. Kudin, J. C. Burant, J. M. Millam, S. S. Iyengar, J. Tomasi, V. Barone, B. Mennucci, M. Cossi, G. Scalmani, N. Rega, G. A. Petersson, H. Nakatsuji, M. Hada, M. Ehara, K. Toyota, R. Fukuda, J. Hasegawa, M. Ishida, T. Nakajima, Y. Honda, O. Kitao, H. Nakai, M. Klene, X. Li, J. E. Knox, H. P. Hratchian, J. B. Cross, V. Bakken, C. Adamo, J. Jaramillo, R. Gomperts, R. E. Stratmann, O. Yazyev, A. J. Austin, R. Cammi, C. Pomelli, J. W. Ochterski, P. Y. Ayala, K. Morokuma, G. A. Voth, P. Salvador, J. J. Dannenberg, V. G. Zakrzewski, S. Dapprich, A. D. Daniels, M. C. Strain, O. Farkas, D. K. Malick, A. D. Rabuck, K. Raghavachari, J. B. Foresman, J. V. Ortiz, Q. Cui, A. G. Baboul, S. Clifford, J. Cioslowski, B. B. Stefanov, G. Liu, A. Liashenko, P. Piskorz, I. Komaromi, R. L. Martin, D. J. Fox, T. Keith, A. M. A. Laham, C. Y. Peng, A. Nanayakkara, M. Challacombe, P. M. W. Gill, B. Johnson, W. Chen, M. W. Wong, C. Gonzalez, J. A. Pople, *Gaussian 03, Revision B.05*, **2003**.

3.7   Appendices

3.7.1   2D Molecular Drawings for the Ligands in Study

This chapter follows the convention below to name a Co-containing complex.

$$[M(L_{eq})(L_{ax})_n]^m$$
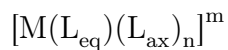
where M refers to the metal, L_{eq} — equatorial ligand, L_{ax} — axial ligand, n — number of the ligands, m — charge state.

The ligands nomenclature are shown in Figure 3.7.
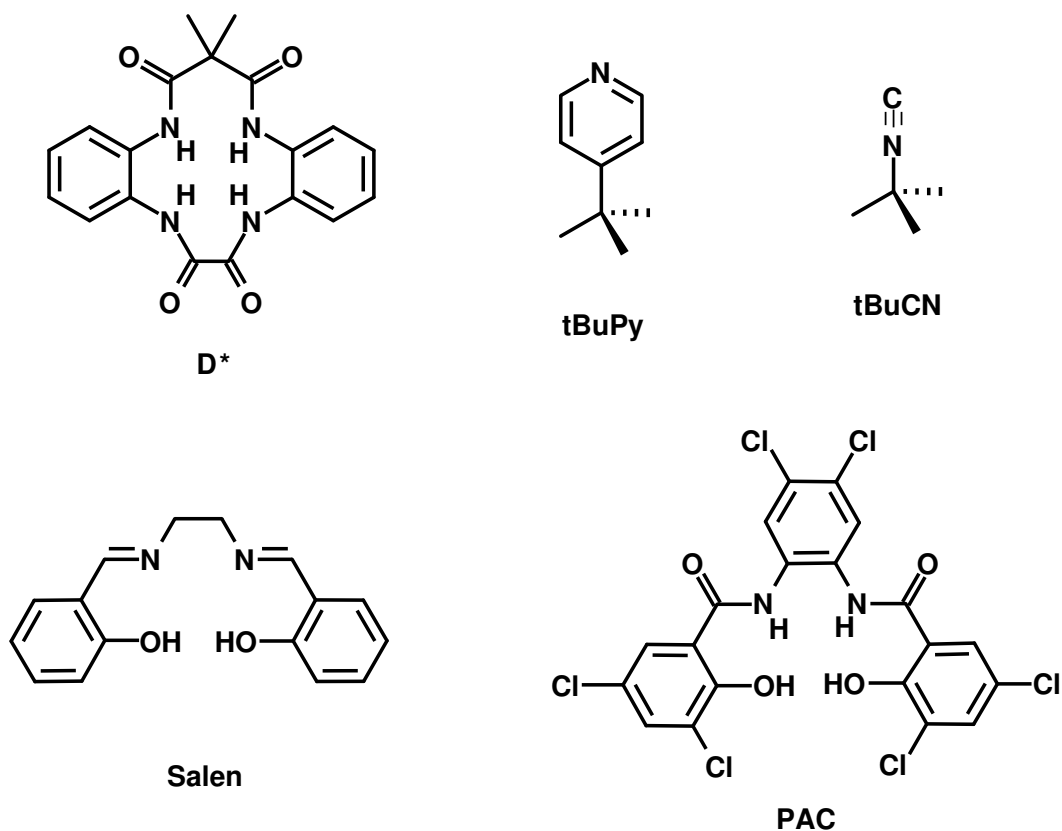
Figure 3.7: Ligands nomenclature

3.7.2 Conformational Analysis to Demystify the Synthetic Yield Puzzle

3.7.2.1 Introduction
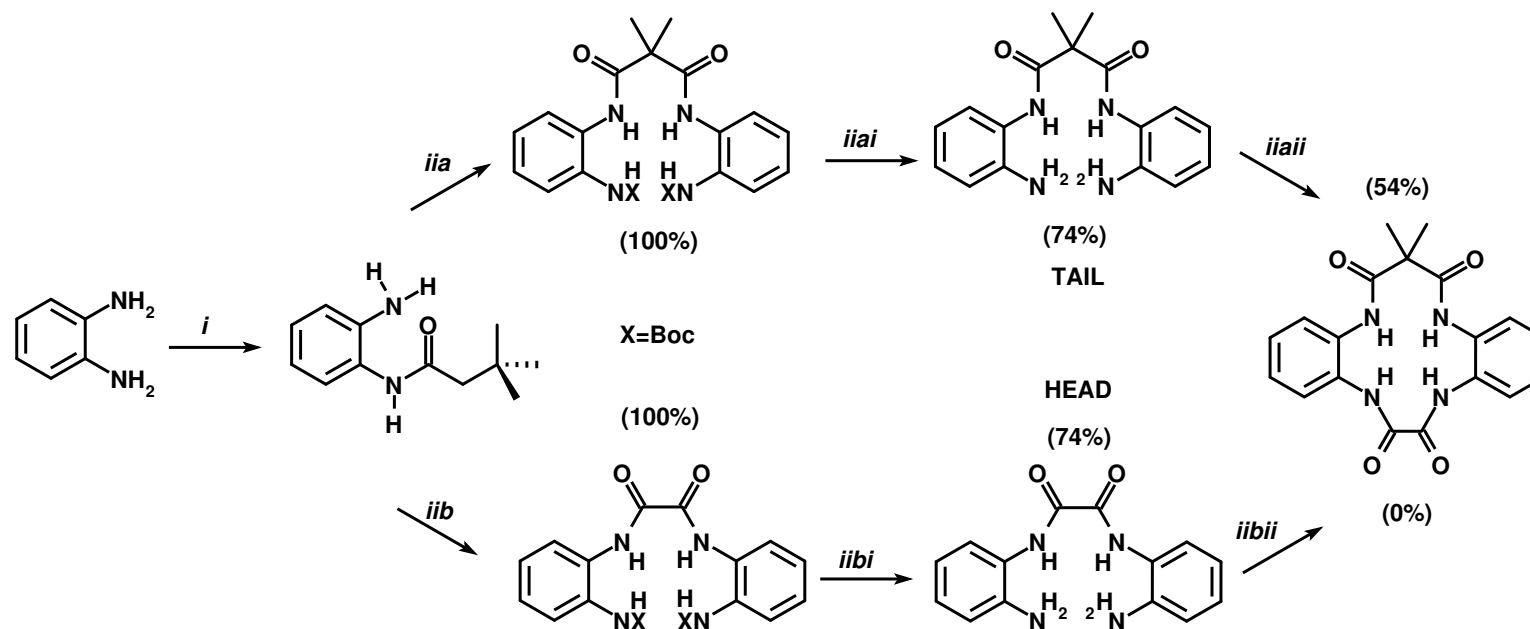
Figure 3.8: D* ligand synthetic routes adapted from Dr. Ellis' Ph.D. thesis[61]

In designing the synthetic routes for D* ligand, two strategies were conceived as depicted in Figure 3.8. What appears puzzling is the drastic difference in the yield between route *iia* (54%) and *iib* (0%). This section is about investigating the possible causes for this mysterious synthetic yield discrepancy.

Steric effect is known to be influential on macrocyclization.[63] To close the ring to form D* in our case, the distance between the open-ended nitrogens in the "HEAD" and "TAIL" moiety (Figure 3.8) is critical. The ideal condition can be foreseen as the energetic advantageous conformers overlaps with the geometrical favorable conformation for the ring closure. In investigation of conformational variability entails sampling in the conformational space. This task seems to enormous with the molecular structures of the "HEAD" and "TAIL" moieties (Figure 3.8).

(a) "HEAD" moiety
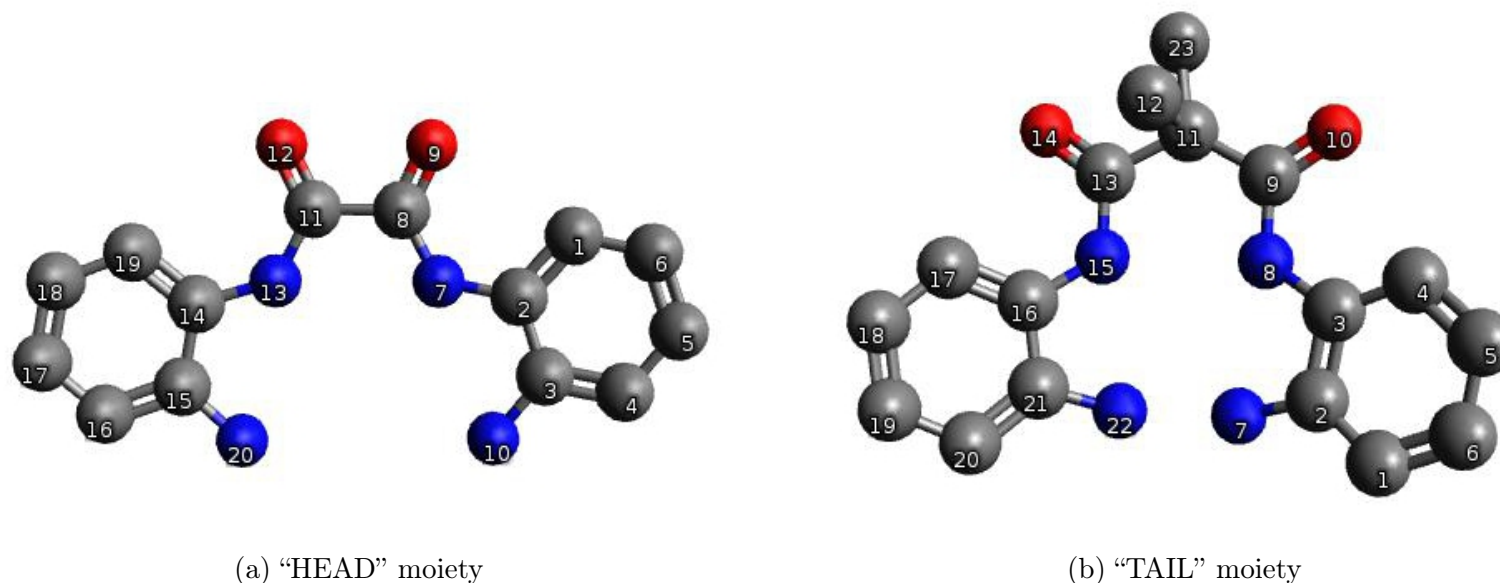
(b) "TAIL" moiety

Figure 3.9: Snap shots of the molecular structure for the "HEAD" and the "TAIL" moieties. Color coding: red – oxygen, blue – nitrogen, grey – carbon. Hydrogen atoms are omitted for clarity.

A closer inspection tells that both the "HEAD" and the "TAIL" moieties have relatively rigid frameworks. The major structural difference between them lie in the hydrocarbon linker between the two bezenediamine rings, i.e. the dihedral angles, 13-11-8-7 for the "HEAD", and 15-13-11-9 and 13-11-9-8 for the "TAIL" (Figure 3.9). Numerical variation from two to three carbons in the linker has direct impact on the distance between primary amines (N-N distance) in stereochemically preferred conformations. Sampling the dihedral angle space provides an economic strategy to explore the conformational space.

3.7.2.2 Simplified Model

As discussed in the previous section, sampling the total freedoms of the two molecules can now be simplified by sampling the dihedral angle space. To illustrate this concept, I built a simplified model and show that the N-N distance can have a simple mathematical relationship with respect to the dihedral angle for the "HEAD" moiety.
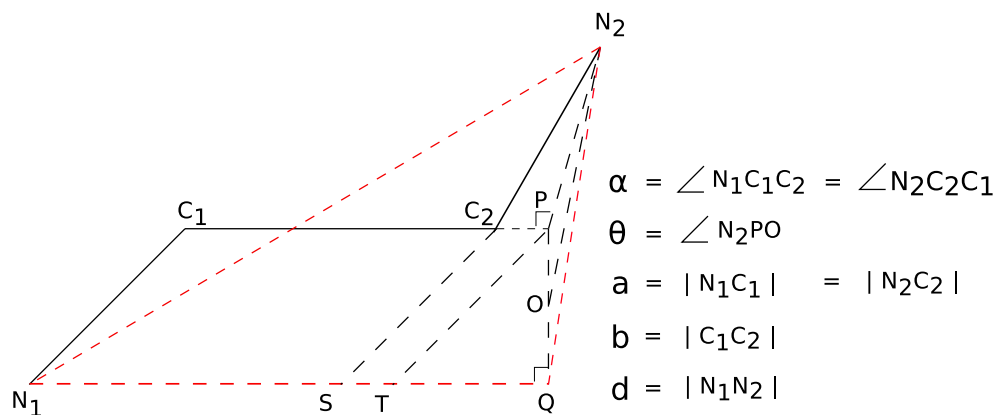
Figure 3.10: Simplified "HEAD" rotation model. N_1 in the model is equal to N_{20} in the "HEAD" moiety in Fig. 1 (a), C_1 equal to C_{11}, C_2 equal to C_8 and N_2 equal to N_{10}. Black solid lines represent the molecular frame work. Black and red dashed lines are auxiliary lines. They are created using the following procedure. Draw N_1S ∥ C_1C_2 and C_2S ∥ C_1N_1. Draw N_2P ⊥ C_1C_2 and meet C_1C_2 in the extended line at P. Draw N_2O ⊥ plane $N_1C_1C_2$ and meet the plane at O. Connect PO and extend PO to meet extended N_1S at Q. Draw PT ∥ C_2S and meet N_1Q at T. Connect N_2Q and N_1N_2

Proof of some geometrical relations.

Proof.

$$\left. \begin{array}{l} N_2P \;\perp\; C_1P \\[2mm] N_2O \;\perp\; \text{plane } N_1C_1P \end{array} \right\} \Rightarrow \left. \begin{array}{l} PO \;\perp\; C_1P \\[2mm] N_2P \;\perp\; C_1P \end{array} \right\} \Rightarrow \left. \begin{array}{l} C_1P \;\perp\; \text{plane } N_2PQ \\[2mm] N_1Q \;\parallel\; C_1P \end{array} \right\} \Rightarrow N_1Q \perp N_2Q$$

$\square$

Derivation of $|N_1N_2|$ in terms of dihedral angle θ

$$d^2 = |N_1N_2|^2 = |N_1O|^2 + |N_2Q|^2$$

$$
\begin{aligned}
|N_2Q|^2 &= |N_2P|^2 + |PQ|^2 - 2|N_2P||PQ|cos\theta \\[2mm]
&= a^2 \, sin^2(\pi - \alpha) + a^2 \, sin^2(\pi - \alpha) - 2a^2 \, sin(\pi - \alpha) \, sin(\pi - \alpha) \, cos\theta \\[2mm]
&= 2 \, a^2 \, sin^2\alpha \, (1 - cos\theta)
\end{aligned}
$$

$$
\begin{aligned}
|N_1Q| &= |N_1S| + |ST| + |TQ| \\[2mm]
&= b + a \, cos(\pi - \alpha) + a \, cos(\pi - \alpha) \\[2mm]
&= b - 2 \, a \, cos\alpha \\[2mm]
|N_1Q|^2 &= (b - 2 \, a \, cos\alpha)^2
\end{aligned}
$$

Therefore

$$d = \sqrt{2 \, a^2 \, sin^2\alpha \, (1 - cos\theta) + (b - 2 \, a \, cos\alpha)^2} \tag{3.3}$$

As seen in eqn 3.3, the free N distance can be represented by a function of the dihedral angel ($N_1{-}C_1{-}C_2{-}N_2$).

3.7.2.3   Dihedral Angle Space Sampling

To sample the dihedral angle space of the "HEAD" and "TAIL" moieties, relaxed potential surface scan strategy was employed. Theoretical level was chosen to be B3lyp density functional[64–66] and 6-31G(d) was set as the basis set. Gaussian 03[67] computation suite was employed for the study. Dihedral angle rotation step is set to be 15°. The dihedral angle ranges were set within $[0°, 180°]$ for 13-11-8-7 and 13-11-9-8, and $[0°, 345°]$ for 15-13-11-9 (Figure 3.9). The computational results are analyzed below.

Boltzmann Distribution of Conformers
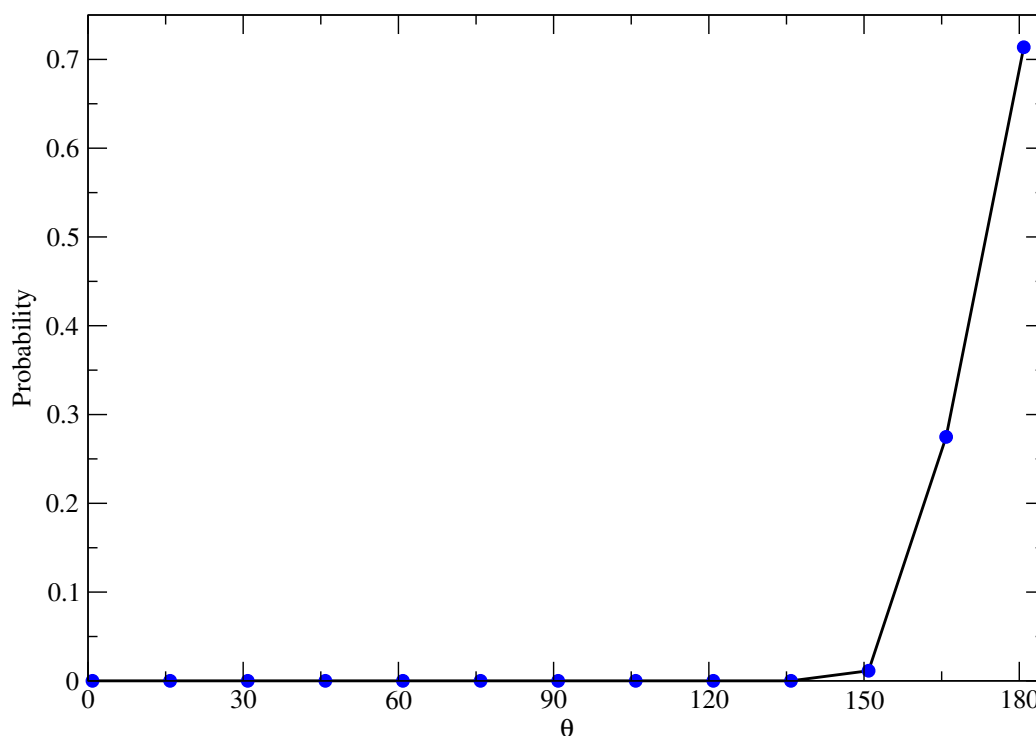
Figure 3.11: Probability distribution of "HEAD" moiety conformers

For the "HEAD" moiety, Figure 3.12 (a) displays the positive correlation between N-N distance and dihedral angle θ. The great resemblance between Figure 3.12 (a) and (b) shows the good approximation by the simple mathematical model (eqn 3.3).

Dihedral Angle vs N-N Distance
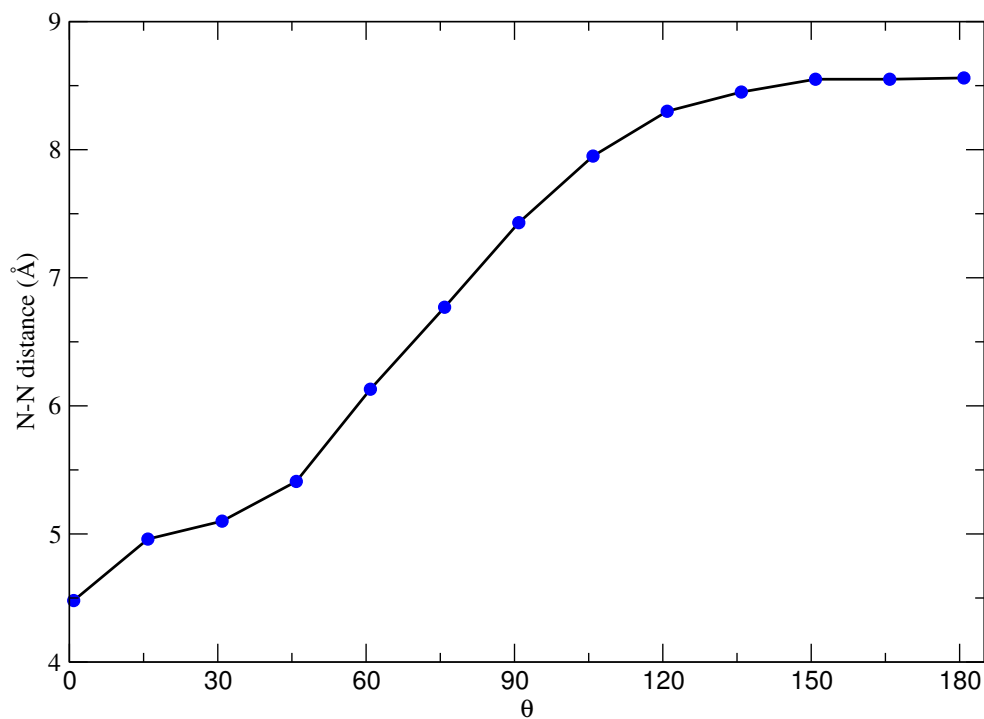
(a) DFT sampling result
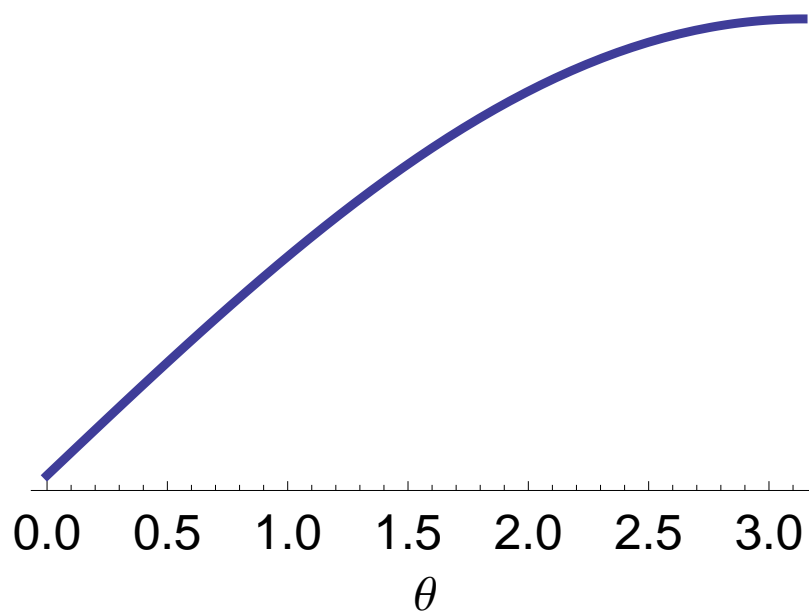
(b) theoretical prediction (eqn 3.3)

Figure 3.12: Dihedral angle vs. N-N distance plot

Conversion of energy profile into probability distribution using Boltzmann relation at room temperature results Figure 3.11. The conformers with the dihedral angle zero degree correspond to the most favorable geometries for macrocyclization. However, their population is approximately zero at room temperature.

(a) Probability

(b) N-N distance vs. dihedral angle
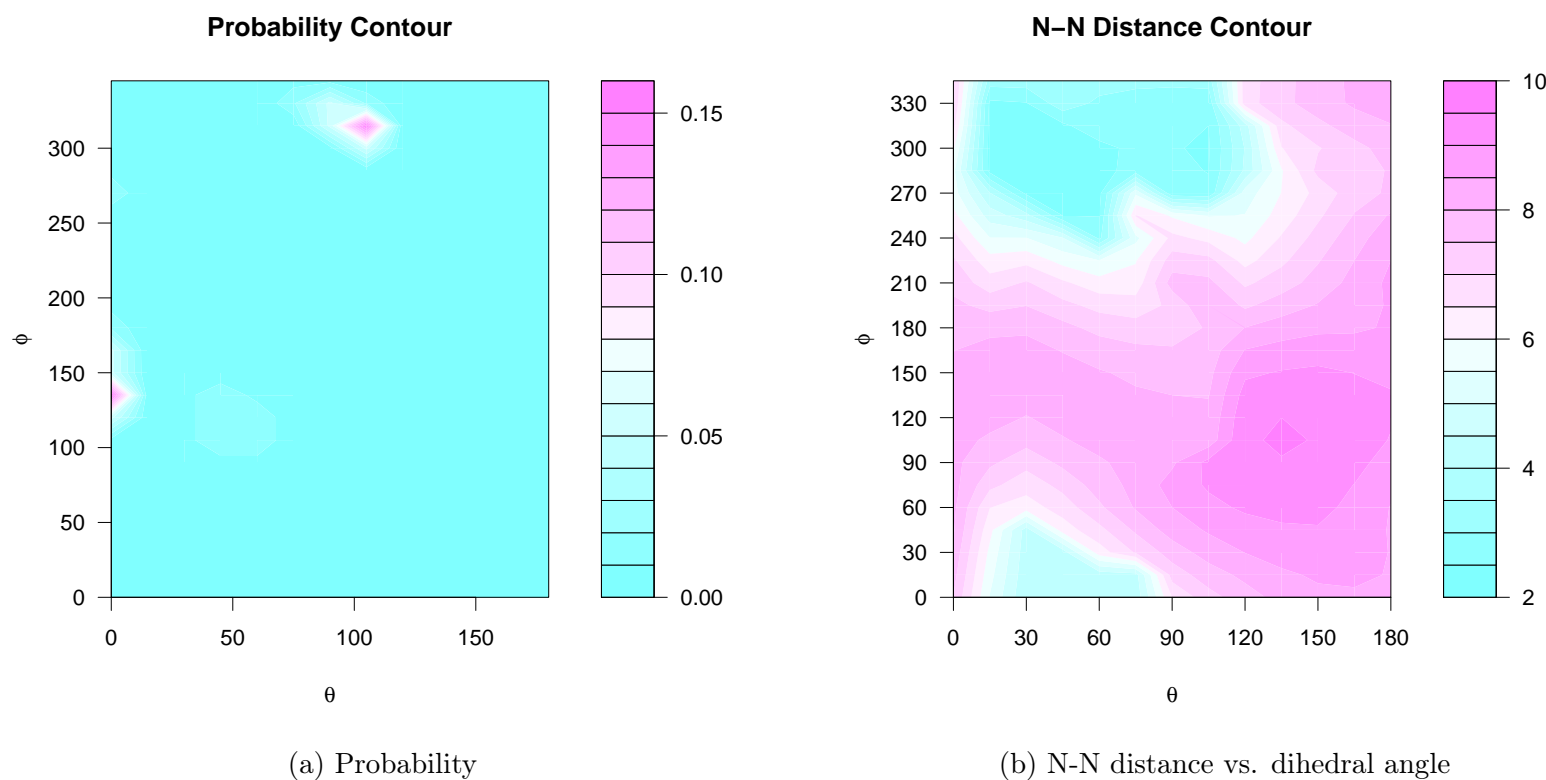
Figure 3.13: Probability and N-N distance contour plot for the "TAIL" moiety.

For the "TAIL" moiety, the energy contour plot was converted to probability distribution plot also, as in Figure 3.13 (a). Clearly, two clusters of conformers have predominant probabilities over all the rest. The cluster in the vicinity of the $(\theta\,\phi)$ coordinate (100,320) corresponds to the cyclolization favorable conformations. Please refer Figure 3.13 (b) for the N-N distance for this cluster of conformers.

If the energy barrier 15 kJ/mol with respect to the lowest conformer and N-N distance 5 are used as the cyclolization criteria, the cyclolization possible conformers account for 37.88% for the "TAIL" and 0.00% for the "HEAD". This result successfully explained the yield difference for the two reaction routes.

3.7.3 Parameters Extracted from DFT Calculations for the Electronic Structure Analysis

3.7.3.1 DFT Predicted EPR Parameters

CoIV$-$Dstar$-$(tBuCN)2

	Atom	Isotropic Fermi Contact Couplings			
		a.u.	MegaHertz	Gauss	10($-$4) cm$-$1
7	N(14)	0.00873	2.81949	1.00606	0.94048
11	N(14)	0.01776	5.73851	2.04764	1.91416
15	Co(59)	$-$0.03046	$-$32.22909	$-$11.50014	$-$10.75047
16	N(14)	0.00880	2.84453	1.01500	0.94883
19	N(14)	0.01784	5.76401	2.05674	1.92267
45	N(14)	$-$0.00045	$-$0.14652	$-$0.05228	$-$0.04887
59	N(14)	$-$0.00045	$-$0.14641	$-$0.05224	$-$0.04884

Atom		Anisotropic Spin Dipole Couplings in Principal Axis System						
		a.u.	MegaHertz	Gauss	10($-$4) cm$-$1		Axes	
	Baa	$-$0.1146	$-$4.421	$-$1.577	$-$1.475	0.5206	0.8537	$-$0.0140
7 N(14)	Bbb	$-$0.1107	$-$4.271	$-$1.524	$-$1.425	0.8538	$-$0.5205	0.0072
	Bcc	0.2254	8.692	3.101	2.899	0.0011	0.0157	0.9999
	Baa	$-$0.1837	$-$7.083	$-$2.527	$-$2.363	0.7561	$-$0.6543	0.0123
11 N(14)	Bbb	$-$0.1752	$-$6.757	$-$2.411	$-$2.254	0.6545	0.7560	$-$0.0089
	Bcc	0.3589	13.841	4.939	4.617	$-$0.0035	0.0148	0.9999
	Baa	$-$0.3704	$-$46.768	$-$16.688	$-$15.600	1.0000	0.0006	0.0033
15 Co(59)	Bbb	0.1556	19.654	7.013	6.556	$-$0.0005	0.9997	$-$0.0260
	Bcc	0.2147	27.115	9.675	9.044	$-$0.0033	0.0260	0.9997
	Baa	$-$0.1154	$-$4.452	$-$1.589	$-$1.485	$-$0.5204	0.8538	$-$0.0144
16 N(14)	Bbb	$-$0.1115	$-$4.301	$-$1.535	$-$1.435	0.8539	0.5204	$-$0.0017
	Bcc	0.2270	8.753	3.123	2.920	$-$0.0061	0.0132	0.9999
	Baa	$-$0.1846	$-$7.118	$-$2.540	$-$2.374	0.7535	0.6574	$-$0.0064
19 N(14)	Bbb	$-$0.1761	$-$6.791	$-$2.423	$-$2.265	$-$0.6574	0.7534	$-$0.0132
	Bcc	0.3606	13.909	4.963	4.639	$-$0.0039	0.0142	0.9999

		a.u.			$10(-4)$ cm-1	Axes		
	Baa	−0.0048	−0.183	−0.065	−0.061	0.0112	0.9998	−0.0153
45 N(14)	Bbb	−0.0019	−0.072	−0.026	−0.024	0.9996	−0.0108	0.0266
	Bcc	0.0066	0.256	0.091	0.085	−0.0264	0.0156	0.9995
	Baa	−0.0048	−0.184	−0.066	−0.061	−0.0124	0.9999	−0.0119
59 N(14)	Bbb	−0.0019	−0.072	−0.026	−0.024	0.9997	0.0121	−0.0233
	Bcc	0.0066	0.256	0.091	0.085	0.0231	0.0122	0.9997

#

EPR A Values Prediction

#	Atom	a.u.	MegaHertz	Gauss	$10(-4)$ cm-1	Axes		
#	15 Co(59)	−0.4009	−78.9971	−28.1881	−26.3505	1.0000	0.0006	0.0033
#	15 Co(59)	0.1251	−12.5751	−4.4871	−4.1945	−0.0005	0.9997	−0.0260
#	15 Co(59)	0.1842	−5.1141	−1.8251	−1.7065	−0.0033	0.0260	0.9997
#	7 N(14)	−0.1059	−1.6015	−0.5709	−0.5345	0.5206	0.8537	−0.0140
#	7 N(14)	−0.1020	−1.4515	−0.5179	−0.4845	0.8538	−0.5205	0.0072
#	7 N(14)	0.2341	11.5115	4.1071	3.8395	0.0011	0.0157	0.9999
#	11 N(14)	−0.1659	−1.3445	−0.4794	−0.4488	0.7561	−0.6543	0.0123
#	11 N(14)	−0.1574	−1.0185	−0.3634	−0.3398	0.6545	0.7560	−0.0089
#	11 N(14)	0.3767	19.5795	6.9866	6.5312	−0.0035	0.0148	0.9999
#	16 N(14)	−0.1066	−1.6075	−0.5740	−0.5362	−0.5204	0.8538	−0.0144
#	16 N(14)	−0.1027	−1.4565	−0.5200	−0.4862	0.8539	0.5204	−0.0017
#	16 N(14)	0.2358	11.5975	4.1380	3.8688	−0.0061	0.0132	0.9999
#	19 N(14)	−0.1668	−1.3540	−0.4833	−0.4513	0.7535	0.6574	−0.0064
#	19 N(14)	−0.1583	−1.0270	−0.3663	−0.3423	−0.6574	0.7534	−0.0132
#	19 N(14)	0.3784	19.6730	7.0197	6.5617	−0.0039	0.0142	0.9999

#

CoIV−Dstar−(tBuPy)2

Isotropic Fermi Contact Couplings

Atom	a.u.	MegaHertz	Gauss	$10(-4)$ cm-1
7 N(14)	0.00941	3.03882	1.08433	1.01364
11 N(14)	0.01762	5.69305	2.03142	1.89900
15 Co(59)	−0.03314	−35.05952	−12.51011	−11.69460
16 N(14)	0.00934	3.01823	1.07698	1.00677
19 N(14)	0.01757	5.67839	2.02619	1.89411
43 N(14)	−0.00188	−0.60669	−0.21648	−0.20237
44 N(14)	−0.00105	−0.33844	−0.12076	−0.11289

Anisotropic Spin Dipole Couplings in Principal Axis System

Atom		a.u.	MegaHertz	Gauss	$10(-4)$ cm-1	Axes		
	Baa	−0.1196	−4.612	−1.646	−1.538	0.4508	0.8768	0.1673
7 N(14)	Bbb	−0.1158	−4.465	−1.593	−1.489	0.8921	−0.4487	−0.0529
	Bcc	0.2353	9.077	3.239	3.028	−0.0287	−0.1731	0.9845
	Baa	−0.1847	−7.124	−2.542	−2.376	0.7425	−0.6614	−0.1062
11 N(14)	Bbb	−0.1767	−6.815	−2.432	−2.273	0.6698	0.7351	0.1045
	Bcc	0.3614	13.939	4.974	4.650	0.0089	−0.1487	0.9888
	Baa	−0.3466	−43.764	−15.616	−14.598	0.9999	0.0022	0.0152
15 Co(59)	Bbb	0.1349	17.034	6.078	5.682	−0.0020	0.9999	−0.0155
	Bcc	0.2117	26.730	9.538	8.916	−0.0153	0.0154	0.9998
	Baa	−0.1179	−4.547	−1.623	−1.517	−0.4405	0.8811	−0.1720
16 N(14)	Bbb	−0.1141	−4.402	−1.571	−1.468	0.8969	0.4401	−0.0425
	Bcc	0.2320	8.949	3.193	2.985	−0.0382	0.1730	0.9842
	Baa	−0.1847	−7.122	−2.541	−2.376	0.7440	0.6599	−0.1048
19 N(14)	Bbb	−0.1766	−6.813	−2.431	−2.272	−0.6681	0.7360	−0.1093
	Bcc	0.3613	13.934	4.972	4.648	0.0050	0.1513	0.9885
	Baa	−0.0033	−0.129	−0.046	−0.043	0.9508	0.0189	−0.3093
43 N(14)	Bbb	0.0008	0.032	0.011	0.011	−0.0183	0.9998	0.0048
	Bcc	0.0025	0.097	0.034	0.032	0.3094	0.0011	0.9509
	Baa	−0.0060	−0.230	−0.082	−0.077	0.9813	0.0241	0.1911
44 N(14)	Bbb	−0.0003	−0.013	−0.005	−0.004	−0.1913	0.0082	0.9815
	Bcc	0.0063	0.244	0.087	0.081	−0.0221	0.9997	−0.0127

#

```
#                               EPR  A  Values  Prediction
#         Atom            a.u.    MegaHertz   Gauss    10(−4) cm−1           Axes
#    15   Co(59)        −0.3797   −78.8235  −28.1261  −26.2926    0.9999    0.0022    0.0152
#    15   Co(59)         0.1018   −18.0255   −6.4321   −6.0126   −0.0020    0.9999   −0.0155
#    15   Co(59)         0.1786    −8.3295   −2.9721   −2.7786   −0.0153    0.0154    0.9998
#     7   N(14)         −0.1102    −1.5732   −0.5617   −0.5244    0.4508    0.8768    0.1673
#     7   N(14)         −0.1064    −1.4262   −0.5087   −0.4754    0.8921   −0.4487   −0.0529
#     7   N(14)          0.2447    12.1158    4.3233    4.0416   −0.0287   −0.1731    0.9845
#    11   N(14)         −0.1671    −1.4309   −0.5106   −0.4770    0.7425   −0.6614   −0.1062
#    11   N(14)         −0.1591    −1.1220   −0.4006   −0.3740    0.6698    0.7351    0.1045
#    11   N(14)          0.3790    19.6320    7.0054    6.5490    0.0089   −0.1487    0.9888
#    16   N(14)         −0.1086    −1.5288   −0.5460   −0.5102   −0.4405    0.8811   −0.1720
#    16   N(14)         −0.1048    −1.3838   −0.4940   −0.4612    0.8969    0.4401   −0.0425
#    16   N(14)          0.2413    11.9672    4.2700    3.9918   −0.0382    0.1730    0.9842
#    19   N(14)         −0.1671    −1.4436   −0.5148   −0.4819    0.7440    0.6599   −0.1048
#    19   N(14)         −0.1590    −1.1346   −0.4048   −0.3779   −0.6681    0.7360   −0.1093
#    19   N(14)          0.3789    19.6124    6.9982    6.5421    0.0050    0.1513    0.9885
#========================================================================================
```

CoIV–PAC–(tBuPy)2

```
========================================================================================
                  Isotropic  Fermi  Contact  Couplings
         Atom                a.u.        MegaHertz        Gauss       10(−4) cm−1
     1   Co(59)           −0.02551      −26.99157       −9.63126       −9.00342
    12   N(14)             0.02769        8.94620        3.19223        2.98413
    13   N(14)             0.02813        9.08796        3.24281        3.03142
    14   N(14)             0.02918        9.42879        3.36443        3.14511
    15   N(14)             0.02686        8.67856        3.09672        2.89485
========================================================================================
           Anisotropic  Spin  Dipole  Couplings  in  Principal  Axis  System
         Atom            a.u.    MegaHertz   Gauss    10(−4) cm−1           Axes
                Baa    −0.1153    −14.566    −5.197    −4.859    1.0000    0.0047   −0.0024
     1 Co(59)   Bbb     0.0435      5.499     1.962     1.834    0.0038   −0.3208    0.9471
                Bcc     0.0718      9.066     3.235     3.024   −0.0037    0.9471    0.3208
                Baa    −0.2767    −10.671    −3.808    −3.559   −0.5907    0.7805   −0.2048
    12 N(14)    Bbb    −0.2648    −10.214    −3.645    −3.407    0.8004    0.5988   −0.0266
                Bcc     0.5415     20.884     7.452     6.966   −0.1019    0.1797    0.9784
                Baa    −0.2793    −10.773    −3.844    −3.593    0.5937    0.7771   −0.2090
    13 N(14)    Bbb    −0.2673    −10.311    −3.679    −3.439    0.7974   −0.6030    0.0230
                Bcc     0.5467     21.084     7.523     7.033    0.1082    0.1803    0.9776
                Baa    −0.0193     −0.745    −0.266    −0.248    0.0070    0.9722    0.2342
    14 N(14)    Bbb    −0.0138     −0.533    −0.190    −0.178    1.0000   −0.0072    0.0003
                Bcc     0.0331      1.278     0.456     0.426   −0.0020   −0.2342    0.9722
                Baa    −0.0182     −0.702    −0.251    −0.234    0.0059    0.9200   −0.3919
    15 N(14)    Bbb    −0.0134     −0.516    −0.184    −0.172    1.0000   −0.0043    0.0050
                Bcc     0.0316      1.219     0.435     0.407   −0.0029    0.3919    0.9200
#========================================================================================
```

```
#                               EPR  A  Values  Prediction
#         Atom            a.u.    MegaHertz   Gauss    10(−4) cm−1           Axes
#     1   Co(59)        −0.1408   −41.5576  −14.8283  −13.8624    1.0000    0.0047   −0.0024
#     1   Co(59)         0.0180   −21.4926   −7.6693   −7.1694    0.0038   −0.3208    0.9471
#     1   Co(59)         0.0463   −17.9256   −6.3963   −5.9794   −0.0037    0.9471    0.3208
#    12   N(14)         −0.2490    −1.7248   −0.6158   −0.5749   −0.5907    0.7805   −0.2048
#    12   N(14)         −0.2371    −1.2678   −0.4528   −0.4229    0.8004    0.5988   −0.0266
#    12   N(14)          0.5692    29.8302   10.6442    9.9501   −0.1019    0.1797    0.9784
#    13   N(14)         −0.2512    −1.6850   −0.6012   −0.5616    0.5937    0.7771   −0.2090
#    13   N(14)         −0.2392    −1.2230   −0.4362   −0.4076    0.7974   −0.6030    0.0230
#    13   N(14)          0.5748    30.1720   10.7658   10.0644    0.1082    0.1803    0.9776
#    14   N(14)          0.0099     8.6838    3.0984    2.8971    0.0070    0.9722    0.2342
#    14   N(14)          0.0154     8.8958    3.1744    2.9671    1.0000   −0.0072    0.0003
#    14   N(14)          0.0623    10.7068    3.8204    3.5711   −0.0020   −0.2342    0.9722
#    15   N(14)          0.0087     7.9766    2.8457    2.6608    0.0059    0.9200   −0.3919
```

```
#   15   N(14)       0.0135   8.1626   2.9127   2.7228   1.0000  −0.0043   0.0050
#   15   N(14)       0.0585   9.8976   3.5317   3.3018  −0.0029   0.3919   0.9200
#
```

CoIV−Et−Salen

Isotropic Fermi Contact Couplings

Atom	a.u.	MegaHertz	Gauss	10(−4) cm−1
8 Co(59)	−0.10631	−112.47021	−40.13217	−37.51603
11 N(14)	−0.00858	−2.77202	−0.98912	−0.92465
14 N(14)	−0.00754	−2.43481	−0.86880	−0.81217

Anisotropic Spin Dipole Couplings in Principal Axis System

Atom		a.u.	MegaHertz	Gauss	10(−4) cm−1	Axes		
	Baa	−2.0360	−257.102	−91.741	−85.760	0.0451	0.9971	−0.0618
8 Co(59)	Bbb	0.5670	71.597	25.548	23.882	0.9211	−0.0654	−0.3838
	Bcc	1.4690	185.505	66.193	61.878	0.3867	0.0396	0.9214
	Baa	−0.0571	−2.202	−0.786	−0.735	0.1980	0.9745	−0.1056
11 N(14)	Bbb	−0.0488	−1.881	−0.671	−0.627	0.9477	−0.2178	−0.2332
	Bcc	0.1059	4.083	1.457	1.362	0.2502	0.0539	0.9667
	Baa	−0.0605	−2.332	−0.832	−0.778	−0.1789	0.9192	−0.3507
14 N(14)	Bbb	−0.0510	−1.968	−0.702	−0.656	0.9830	0.1819	−0.0246
	Bcc	0.1115	4.300	1.534	1.434	−0.0411	0.3492	0.9362

```
#                                EPR A Values Prediction
#    Atom            a.u.    MegaHertz    Gauss    10(−4) cm−1         Axes
#    8   Co(59)    −2.1423  −369.5722  −131.8732  −123.2760   0.0451   0.9971  −0.0618
#    8   Co(59)     0.4607   −40.8732   −14.5842   −13.6340   0.9211  −0.0654  −0.3838
#    8   Co(59)     1.3627    73.0348    26.0608    24.3620   0.3867   0.0396   0.9214
#   11   N(14)     −0.0657    −4.9740    −1.7751    −1.6597   0.1980   0.9745  −0.1056
#   11   N(14)     −0.0574    −4.6530    −1.6601    −1.5516   0.9477  −0.2178  −0.2332
#   11   N(14)      0.0973     1.3110     0.4679     0.4374   0.2502   0.0539   0.9667
#   14   N(14)     −0.0680    −4.7668    −1.7008    −1.5902  −0.1789   0.9192  −0.3507
#   14   N(14)     −0.0585    −4.4028    −1.5708    −1.4682   0.9830   0.1819  −0.0246
#   14   N(14)      0.1040     1.8652     0.6652     0.6218  −0.0411   0.3492   0.9362
#
```

CoIV ion

Isotropic Fermi Contact Couplings

Atom	a.u.	MegaHertz	Gauss	10(−4) cm−1
1 Co(59)	−0.22781	−241.00088	−85.99510	−80.38924

Anisotropic Spin Dipole Couplings in Principal Axis System

Atom		a.u.	MegaHertz	Gauss	10(−4) cm−1	Axes		
	Baa	−4.0449	−510.782	−182.260	−170.378	0.0000	1.0000	0.0000
1 Co(59)	Bbb	2.0224	255.391	91.130	85.189	0.0000	0.0000	1.0000
	Bcc	2.0224	255.391	91.130	85.189	1.0000	0.0000	0.0000

```
#                                EPR A Values Prediction
#    Atom            a.u.    MegaHertz    Gauss    10(−4) cm−1         Axes
#    1   Co(59)    −4.2727  −751.7829  −268.2551  −250.7672   0.0000   1.0000   0.0000
#    1   Co(59)     1.7946    14.3901     5.1349     4.7998   0.0000   0.0000   1.0000
#    1   Co(59)     1.7946    14.3901     5.1349     4.7998   1.0000   0.0000   0.0000
#
```

FeIII ion

```
===============================================================================
                    Isotropic  Fermi  Contact  Couplings
         Atom                a.u.          MegaHertz        Gauss        10(−4) cm−1
    1   Fe(57)            −0.21838        −31.67315      −11.30177      −10.56502
===============================================================================
            Anisotropic  Spin  Dipole  Couplings  in  Principal  Axis  System
         Atom                a.u.     MegaHertz    Gauss    10(−4) cm−1        Axes
                    Baa   −1.2682    −21.957     −7.835     −7.324    0.0000   0.0000   1.0000
    1  Fe(57)  Bbb   −1.0138    −17.552     −6.263     −5.855    1.0000   0.0000   0.0000
                    Bcc    2.2820     39.508     14.098     13.179    0.0000   1.0000   0.0000
#===============================================================================
#
#                         EPR A Values Prediction
#       Atom            a.u.    MegaHertz    Gauss    10(−4) cm−1        Axes
#    1   Fe(57)      −1.4866   −53.6302   −19.1368   −17.8890    0.0000   0.0000   1.0000
#    1   Fe(57)      −1.2322   −49.2251   −17.5648   −16.4200    1.0000   0.0000   0.0000
#    1   Fe(57)       2.0636     7.8349     2.7962     2.6140    0.0000   1.0000   0.0000
#===============================================================================
```

3.7.3.2   Spin Populations of Co Complexes

```
#################################################################################
CoIV−Ethyl−Dstar
===============================================================================
    Gross  orbital  populations:
                        TOTAL      ALPHA       BETA        SPIN
             D 0      1.14277    0.63774    0.50503    0.13273
             D+1      1.94653    0.97558    0.97094    0.00465
             D−1      1.42151    0.98108    0.44044    0.54065
             D+2      1.91782    0.96463    0.95318    0.01146
             D−2      0.78239    0.41155    0.37085    0.04071

===============================================================================
 Mulliken  atomic  spin  densities:
                1
     1   C       0.020125
     2   C      −0.006929
     3   C       0.015717
     4   C      −0.004160
     5   C       0.023782
     6   C      −0.001597
     7   N       0.064331
     8   Co      0.740211
     9   C      −0.140114
    10   N       0.035629
    11   C       0.000179
    12   O       0.044408
    13   N       0.035439
    14   C       0.000680
    15   O       0.043094
    16   C       0.013065
    17   C      −0.003040
    18   C       0.021104
    19   C      −0.001042
    20   C       0.018238
    21   C      −0.007327
    22   N       0.061494
    23   C      −0.005140
    24   O       0.017164
    25   C      −0.001380
    26   C      −0.000500
    27   C      −0.000939
    28   C      −0.005547
```

```
29   O      0.020104
30   H     −0.000193
31   H     −0.001055
32   H     −0.000178
33   H     −0.001288
34   H     −0.001156
35   H     −0.000939
36   H     −0.000292
37   H     −0.000066
38   H     −0.000248
39   H     −0.000201
40   H     −0.000187
41   H     −0.000198
42   H     −0.000259
43   H     −0.000061
44   H      0.002833
45   H      0.005307
46   C      0.011146
47   H     −0.008167
48   H     −0.000779
49   H     −0.001068
Sum of Mulliken spin densities=    1.00000
```

===
###

###
CoIV−Methyl−Dstar

===
```
   Gross orbital populations:
                        TOTAL    ALPHA    BETA     SPIN
            D 0        1.10005   0.59530  0.50476  0.09052
            D+1        1.95268   0.97807  0.97460  0.00347
            D−1        1.47353   0.98445  0.48906  0.49540
            D+2        1.92072   0.96358  0.95715  0.00643
            D−2        0.77239   0.40205  0.37034  0.03171
```

===
```
 Mulliken atomic spin densities:
                1
     1   C      0.021583
     2   C     −0.006611
     3   C      0.019426
     4   C     −0.005533
     5   C      0.027275
     6   C     −0.001103
     7   N      0.075327
     8   Co     0.632858
     9   C     −0.100491
    10   N      0.040844
    11   C     −0.000206
    12   O      0.046987
    13   N      0.041603
    14   C     −0.000239
    15   O      0.047022
    16   C      0.020511
    17   C     −0.005830
    18   C      0.028315
    19   C     −0.001062
    20   C      0.022309
    21   C     −0.006725
    22   N      0.077700
    23   C     −0.007456
    24   O      0.020819
    25   C     −0.001516
    26   C     −0.000474
```

```
27   C    −0.000931
28   C    −0.007151
29   O     0.020037
30   H    −0.000181
31   H    −0.001121
32   H    −0.000212
33   H    −0.001470
34   H    −0.001527
35   H    −0.001161
36   H    −0.000308
37   H    −0.000051
38   H    −0.000304
39   H    −0.000179
40   H    −0.000223
41   H    −0.000221
42   H    −0.000210
43   H    −0.000074
44   H     0.004367
45   H     0.004194
46   H     0.001394
Sum of Mulliken spin densities=    1.00000
```

###

###
CoIV−Dstar−(tBuPy)2

```
    Gross orbital populations:
                        TOTAL      ALPHA      BETA       SPIN
            D 0        0.65199    0.32683    0.32516    0.00168
            D+1        1.90476    0.97336    0.93140    0.04197
            D−1        1.89807    0.97382    0.92424    0.04958
            D+2        0.78505    0.39087    0.39418   −0.00331
            D−2        1.91995    0.96027    0.95968    0.00059
```

```
 Mulliken atomic spin densities:
                  1
     1   C     0.015666
     2   C     0.073835
     3   C    −0.030765
     4   C     0.068895
     5   C     0.029015
     6   C     0.019967
     7   N     0.089864
     8   C    −0.015141
     9   C     0.000257
    10   C    −0.001259
    11   N     0.143301
    12   C    −0.022543
    13   C    −0.022672
    14   O     0.032012
    15   Co    0.086405
    16   N     0.088477
    17   C    −0.014963
    18   O     0.065548
    19   N     0.143291
    20   C     0.028465
    21   C     0.068687
    22   C    −0.031098
    23   C     0.074406
    24   C     0.014922
    25   C     0.020664
    26   O     0.031897
    27   O     0.066014
```

```
  28   C    −0.000881
  29   H     0.000459
  30   H    −0.001422
  31   H    −0.001186
  32   H    −0.003790
  33   H    −0.003765
  34   H    −0.001396
  35   H    −0.000312
  36   H    −0.000082
  37   H    −0.000323
  38   H     0.000437
  39   H    −0.001218
  40   H    −0.000278
  41   H    −0.000272
  42   H    −0.000018
  43   N    −0.002872
  44   N     0.001432
  45   C    −0.000310
  46   C    −0.000604
  47   C    −0.000056
  48   C    −0.000579
  49   C    −0.000340
  50   H    −0.000245
  51   H     0.000042
  52   C    −0.000001
  53   H     0.000041
  54   H    −0.000230
  55   C    −0.001876
  56   C     0.000691
  57   C    −0.001718
  58   C     0.000804
  59   C    −0.003484
  60   H    −0.000250
  61   H    −0.000041
  62   C     0.000109
  63   H    −0.000063
  64   H     0.000586
  65   C    −0.000008
  66   C    −0.000043
  67   C    −0.000042
  68   H    −0.000016
  69   H     0.000000
  70   H     0.000002
  71   H    −0.000015
  72   H     0.000002
  73   H     0.000000
  74   H    −0.000001
  75   H    −0.000001
  76   H     0.000000
  77   C     0.000004
  78   C    −0.000004
  79   C    −0.000006
  80   H    −0.000002
  81   H     0.000001
  82   H     0.000000
  83   H    −0.000002
  84   H    −0.000001
  85   H     0.000000
  86   H     0.000000
  87   H     0.000000
  88   H     0.000000
Sum of Mulliken spin densities=   1.00000
```

##
CoIV−ethyl−salen

==

Gross orbital populations:

	TOTAL	ALPHA	BETA	SPIN
D 0	1.24985	0.70720	0.54265	0.16454
D+1	1.39750	0.98828	0.40922	0.57906
D−1	1.90438	0.96130	0.94308	0.01824
D+2	1.93556	0.97776	0.95780	0.01996
D−2	0.72948	0.38901	0.34047	0.04856

==

Mulliken atomic spin densities:

		1
1	C	0.074522
2	C	−0.031346
3	C	0.049936
4	C	−0.037711
5	C	0.070358
6	C	−0.046356
7	O	0.109218
8	Co	0.836917
9	C	−0.186120
10	C	−0.042617
11	N	0.023303
12	C	−0.004172
13	C	−0.004213
14	N	0.025073
15	C	−0.044144
16	C	0.079076
17	C	−0.027709
18	C	0.048663
19	C	−0.036625
20	C	0.072634
21	C	−0.049339
22	O	0.107129
23	H	−0.002434
24	H	0.001250
25	H	−0.003294
26	H	0.001768
27	H	0.001047
28	H	−0.002486
29	H	0.001286
30	H	−0.003189
31	H	0.001637
32	H	0.000589
33	H	0.005108
34	H	−0.000031
35	H	0.005380
36	H	−0.000471
37	H	0.007370
38	C	0.011592
39	H	0.005335
40	H	−0.013568
41	H	−0.002750
42	H	−0.000616

Sum of Mulliken spin densities=   1.00000

==

##

##
CoIV−methyl−salen

==

Gross orbital populations:

	TOTAL	ALPHA	BETA	SPIN

	TOTAL	ALPHA	BETA	SPIN
D 0	1.18219	0.63733	0.54485	0.09249
D+1	1.91296	0.96310	0.94986	0.01324
D−1	1.47564	0.98632	0.48932	0.49700
D+2	1.94447	0.97701	0.96746	0.00955
D−2	0.71674	0.37543	0.34132	0.03412

Mulliken atomic spin densities:

		1
1	C	−0.059182
2	C	0.095833
3	C	−0.032309
4	C	0.064093
5	C	−0.047254
6	C	0.093989
7	C	−0.052664
8	N	0.038261
9	C	−0.004831
10	C	−0.004580
11	N	0.036075
12	C	−0.050409
13	C	0.091261
14	C	−0.032619
15	C	0.062863
16	C	−0.046568
17	C	0.091147
18	C	−0.056249
19	O	0.131922
20	Co	0.646735
21	O	0.136988
22	C	−0.119787
23	H	0.002252
24	H	−0.003210
25	H	0.001638
26	H	−0.004265
27	H	0.002113
28	H	0.001658
29	H	−0.003136
30	H	0.001593
31	H	−0.004132
32	H	0.001973
33	H	0.001236
34	H	0.006172
35	H	0.000052
36	H	0.006291
37	H	−0.000155
38	H	0.003520
39	H	0.003687

Sum of Mulliken spin densities=   1.00000

###

###
CoIV−Salen−(tBuPy)2

Gross orbital populations:

	TOTAL	ALPHA	BETA	SPIN
D 0	0.68800	0.34471	0.34328	0.00143
D+1	1.91175	0.95748	0.95427	0.00322
D−1	1.89268	0.97572	0.91695	0.05877
D+2	1.95024	0.97564	0.97459	0.00104
D−2	0.70481	0.35118	0.35362	−0.00243

Mulliken atomic spin densities:
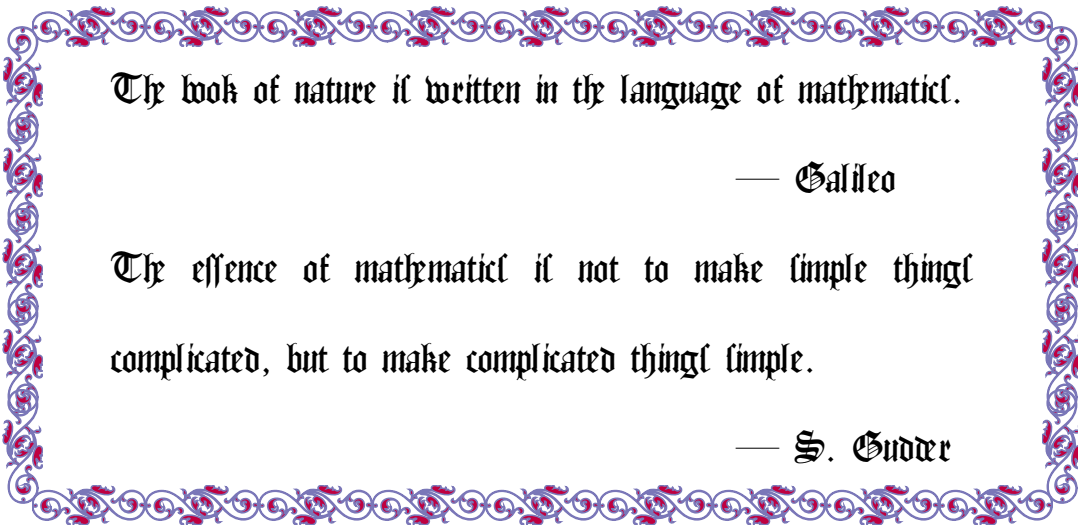
```
                 1
    1   C     −0.047232
    2   C      0.098438
    3   C     −0.004270
    4   C      0.124004
    5   C     −0.082534
    6   C      0.180807
    7   C     −0.041634
    8   N      0.046281
    9   C     −0.003845
   10   C     −0.003542
   11   N      0.055339
   12   C     −0.047507
   13   C      0.110245
   14   C     −0.006709
   15   C      0.137629
   16   C     −0.091643
   17   C      0.199777
   18   C     −0.053673
   19   O      0.200795
   20   Co     0.056239
   21   O      0.185232
   22   N      0.000288
   23   H     −0.006193
   24   H      0.002655
   25   H     −0.008172
   26   H      0.001395
   27   H      0.001505
   28   H     −0.006829
   29   H      0.002953
   30   H     −0.009022
   31   H      0.001580
   32   H      0.001758
   33   H      0.005224
   34   H      0.000127
   35   H      0.004898
   36   H      0.001694
   37   C     −0.001408
   38   C      0.001297
   39   C     −0.001122
   40   C      0.001158
   41   C     −0.001702
   42   H      0.000062
   43   H     −0.000069
   44   H      0.000026
   45   H     −0.000049
   46   H     −0.001221
   47   N     −0.002494
   48   C     −0.000681
   49   C      0.000843
   50   C     −0.000358
   51   C      0.000451
   52   C     −0.000326
   53   H     −0.000200
   54   H     −0.000039
   55   H      0.000008
   56   H     −0.000046
   57   H     −0.000190
 Sum  of  Mulliken  spin  densities=     1.00000
```

Chapter 4

Nulear Tunneling in $[\text{Fe}^{\text{V}}(\text{O})(\text{B}^*)]^{-1}$ Mediated Intermolecular C−H Bond Activation

The book of nature is written in the language of mathematics.

— Galileo

The essence of mathematics is not to make simple things complicated, but to make complicated things simple.

— S. Gudder

4.1 Abbreviations

KIE : kinetic isotope effect

ZPE : zero point energy

imν : imaginary frequency

EtBZ : ethylbenzene

EtBZ-d10 : fully deuterated ethylbenzene

H or ^{1}H : hydrogen atom

D or ^{2}H : deuterium

int : intercept

eqn : equation

$[\text{Fe}^{\text{V}}(\text{O})(\text{B}^*)]^{-1}$: $[\text{Fe}^{\text{V}}(\text{O})(\text{B}^*)]^{-1}$ refers to a member in the TAML catalysts family. Please refer Figure 4.6 for the structure view.

kinetic curve : $\ln(k/T)$ vs. $1/T$ plot

4.2 Abstract

Nuclear tunneling in a phenomenon rooted in quantum mechanics. It plays a significant and sometimes predominant role in many chemical and biochemical processes. The detection of nuclear tunneling phenomenon of $[\text{Fe}^{\text{V}}(\text{O})(\text{B}^*)]^{-1}$ mediated hydrogen atom extraction from EtBZ was based on three discrepancies between the reaction rates of $[\text{Fe}^{\text{V}}(\text{O})(\text{B}^*)]^{-1}$ with EtBZ and its isotope labeled species EtBZ-d10: (i) the initial $[\text{Fe}^{\text{V}}(\text{O})(\text{B}^*)]^{-1}$ decay rate for the substrate EtBZ-d10 is slower than that for EtBZ, (ii) the slope of the $\ln(k/T)$ vs. $1/T$ plot of EtBZ-d10 is smaller than that for EtBZ over the experimental temperature range, and (iii) the extrapolated tangents of the kinetic curves give a large, negative intercept difference, Int(EtBZ) - Int(EtBZ-d10) < 0 at the limit $1/T \to 0$. Theoretical analysis, based on density

functional theory calculations of thermodynamic parameters of the reaction species and Bell's model for tunneling through quadratic barriers, shows that (i) and (ii) result from isotope-induced changes in both the zero-point energies and nuclear tunneling, whereas (iii) is exclusively an isotope mass effect on tunneling. Based on a thermodynamic analysis, a temperature independent indicator to signal nuclear tunneling was proposed. A semiclassical theoretical model was constructed with the capability of predicting absolute rate constants outside the scope of experimentally fathomable range.

4.3 Nuclear Tunneling its Significance in Chemistry

Quantum mechanics gives rise to three important consequences related to chemical reactions, reaction barrier, zero point energy and tunneling effect.[1] Among all, tunneling is particularly fascinating for its exemplification of the wave aspect of matter. Electron tunneling pioneered the tunneling studies,[2,3] and soon their importance in chemical and biochemical processed were realized. It was proposed that the efficiency of electron transfer chain in biology can be an outcome of tunneling engineering.[4,5] Certainly, electrons tunneling is only one snap shot of the entire tunneling panorama. Nuclear tunneling also appear extremely intriguing. Transferring proton,[6,7] hydrogen atom,[8,9] hydride,[10,11] and carbon[12,13] have been explored in a broad range of chemical systems. The role of nuclear tunneling in the chemical reactions remains an energetic topic in literature.[14,15] For instance, nuclear tunneling was invoked in the explanation of proton mobility in hydrogen-bonded systems.[16–18] Hydrogen and hydride transfer are known to be important to many enzyme catalytic reactions and the tunneling effect is often found in company. It has been reported that 60%[10] and 85%[19] of the

reactive flux went through tunneling in two hydride transfer reactions. Although the relative importance of tunneling is expected to diminish when the temperature is raised, significant hydrogen tunneling effects persist at room temperature[20] and even up to 65°C in alcohol dehydrogenases.[21] It was even argued that protein motions may facilitate the tunneling process,[22–26] although this view remains contentious.[14] Given the mounting evidence of the quantum effects on chemical reactions, it is of great interest to measure the deviation of a chemical system from its classical expectation of the transition state theory.[27,28]

Kinetic isotope effect (KIE) is a phenomenon rooted in quantum mechanics. It is manifested by the fact that the rate constant ratio between the lighter isotopic species and heavier counterpart is greater than one. Other than that, parameters from empirical relation Arrhenius' equation(eqn 4.1) are also often used to indicate KIE.

$$k = A \exp\left(\frac{-E_a}{RT}\right) \tag{4.1}$$

Based on derivation and modeling, the isotopic preexponential factor ratio ($A_Q = \frac{A_H}{A_D}$) has a theoretical range of $(0.5, \sqrt{2})$[29] and the activation energy E_a difference $(E_a^H - E_a^D)$ is less than 1.2 kcalmol.[30] In essence, KIEs exceeding certain nucleus and temperature dependent thresholds[31,32] are the hallmark of tunneling. Also, the extremely appealing as well as puzzling observation of the high efficiency in enzymatic catalysis was shown out of the realm of ZPE argument.[33] It should be realized that atoms can not be treated as particle model alone. Tunneling is not whether it has occurred but whether it has been detected.[6] Therefore, quantum correction needs to be introduced into the classical transition state theory to better describe the kinetics of chemical reactions.[34] A number of studies have amended classical transition state theory with quantum corrections. Variational transition state theory[35–37]

variationally optimized the dividing surface between reactants and products. By combining the variational optimization of the dynamical bottleneck and multidimensional quantum mechanical tunneling dynamics, the ensemble-averaged variational transition state theory with multidimensional tunneling was developed to predict the rate constants for enzyme-catalyzed reactions.[38,39] Another approach to include nuclear quantum effects is the Feynman path integral.[40,41] The path integral quantum transition state theory formulation allows for computing the quantum rate constants. Centroid molecular dynamic simulations[42,43] can be applied to aquire quantum activation free energies. Based on the Feynman path integral formulation, a quantized classical path[44,45] approach was proposed to gain higher computational efficiency. It is essentially a quantum path integral correction applied to the classical trajectories. Alternate hybrid quantum/classical approaches have also been proposed.[46,47]

Most theoretical methodologies that include tunneling effects in the kinetic models were designed for enzymatic reactions, where the geometry and motion of proteins have great influence on chemistry. Therefore, sophisticated sampling schemes were developed and improved to attain better depiction of the physical picture of the reaction dynamics and higher accuracy in calculation output. For synthetic organometallic chemical reactions, the situation can be much simplified due to the lack of protein pockets. In this research, we employed a semiclassical approach to incorporate quantum tunneling factor from Bell's model[48] as a pre-exponential factor in the classical rate equation to study the kinetics of H atom abstraction from EtBZ and EtBZ-10 by $[Fe^{V}(O)(B^{*})]^{-1}$. Based on this model, we found that more than 90% of the reaction flux undergoes tunneling in the abstraction reaction. We were also able to distinguish ZPE and nuclear tunneling contributions to the KIE effect and make projection for the rate constants outside the scope of experimental fathom. In addition, we propose a temperature-independent criterion to test the appreciableness of nuclear tunneling.

4.4 Activation Entropy or Nuclear Tunneling

According to the classical transition state theory,[27,28] the rate constant is related to the activation free energy by eqn 4.2.

$$k = \kappa \, \frac{k_B \, T}{h} \exp\left(\frac{-\Delta \, G^{\ddagger}}{R \, T} \right) \tag{4.2}$$

where k is rate constant, κ is a transmission factor, k_B is Boltzmann constant, T is absolute temperature, R is gas constant, h is Planck constant and $\Delta \, G^{\ddagger}$ is activation free energy.
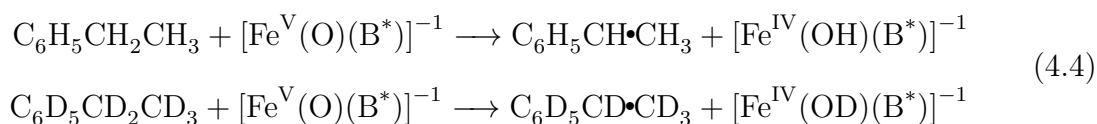
Free energy is expressed in terms of entropy(S) and enthalpy(H) in eqn 4.2, and κ is treated as unity and linearized to yield eqn 4.3.

$$\ln\left(\frac{k}{T} \right) = -\frac{\Delta \, H^{\ddagger}}{R \, T} + \ln\left(\frac{k_B}{h} \right) + \frac{\Delta \, S^{\ddagger}}{R} \tag{4.3}$$

Eqn 4.3 provides a convenient way to acquire important thermodynamic parameters $\Delta \, H^{\ddagger}$ and $\Delta \, S^{\ddagger}$ by sampling multiple kinetic data within a narrow temperature window. What needs to be kept in mind is that eqn 4.3 is an approximation rather than an exact relation. To use it, one has to ensure that κ can be approximated as unity and the sampled data points are within a temperature range that is narrow enough to hold the linearity of kinetic curve. However, in the presence of quantum effect, such as nuclear tunneling, the condition of unity transmission can not be justified. Therefore, the thermodynamic quantity activation entropy obtained via the classical method is actually the quantum nuclear tunneling effect. This is the central topic of this section.

4.4.1 Discrepancy between DFT Predication and Experimental Analysis

The rate-determining, hydrogen atom abstraction step eqn 4.4 in the $[\text{Fe}^{\text{V}}(\text{O})(\text{B}^*)]^{-1}$-mediated hydroxylation of ethylbenzene (EtBZ) and its isotopologue EtBZ-d10 has been analyzed with density function theory calculations.

$$\text{C}_6\text{H}_5\text{CH}_2\text{CH}_3 + [\text{Fe}^{\text{V}}(\text{O})(\text{B}^*)]^{-1} \longrightarrow \text{C}_6\text{H}_5\text{CH}\bullet\text{CH}_3 + [\text{Fe}^{\text{IV}}(\text{OH})(\text{B}^*)]^{-1}$$
$$\text{C}_6\text{D}_5\text{CD}_2\text{CD}_3 + [\text{Fe}^{\text{V}}(\text{O})(\text{B}^*)]^{-1} \longrightarrow \text{C}_6\text{D}_5\text{CD}\bullet\text{CD}_3 + [\text{Fe}^{\text{IV}}(\text{OD})(\text{B}^*)]^{-1}$$

$$(4.4)$$

The calculations were performed for the substrate, the Fe^{V} intermediate, the reaction complex, the transition state, and the product state in which the nucleus and electron of the hydrogen atom are transferred from EtBZ to $\text{Fe}^{\text{V}}(\text{O})$, resulting in hydroxylation of the terminal oxo and one-electron reduction of iron. The Gibbs free energy of activation, including electronic, vibrational, rotational, and translational contributions, was evaluated using the thermodynamic properties facility of the Gaussian 09[49] software package and compared with the value deduced from the slopes of the Eyring $(\ln(k/T)$ vs. $T^{-1})$ plots (referred as kinetic curves hereafter) for the two isotopologues. The comparison reveals two major differences. First, the calculated KIE effect, which has a value that is consistent with the difference between the zero point energies (ZPEs) for EtBZ and EtBZ-d10, is about three times smaller than observed (Table 4.1). Second, linear extrapolation of the kinetic curves calculated in the experimental temperature range to $T^{-1} \to 0$ yields only a small positive difference between the intercepts for the two isotopologues, denoted as Int(EtBZ) - Int(EtBZ-d10), which is at odds with the conventionally treated experimental kinetic data (eqn 4.3) that imply a large negative value for this difference (Table 4.2). This interesting observation triggered further theoretical investigation.

Table 4.1: ZPE contribution to experimentally determined KIE

Measure	KIE	T/K	Source
rate constant ratio	25.6	233.16	Experimental
ZPE difference	9.4	233.16	DFT Computation

Table 4.2: Activation entropy difference between EtBZ and EtBZ-d10

T/K	$\dfrac{\Delta S_{\text{H}}^{\ddagger} - \Delta S_{\text{D}}^{\ddagger}}{\text{J mol}^{-1}\text{K}^{-1}}$	$\left\lvert\dfrac{\Delta S_{\text{H}}^{\ddagger} - \Delta S_{\text{D}}^{\ddagger}}{\Delta S_{\text{H}}^{\ddagger}}\right\rvert$	Source
/	-35	0.200	Experimental
233.16	+0.9	0.006	DFT Calculation

4.4.2 Phenomenological Activation Entropy Difference as a Temperature Independent Testimony for Nuclear Tunneling

Activation entropy isotope effect is defined as the activation entropy difference between the substrate with the composition of naturally most abundantly occurring elements and its monodeuterated isotopolouge in which the atomic bonding connectivity is transformed at the transition state. The phenomenological activation entropy isotope effect refers to the cases that the active entropy is obtained by implementing eqn 4.3 after linearizing the kinetic curves. In this section, a proof will be given to show that the sign of the phenomenological activation entropy isotope effect is an indicator for nuclear tunneling.

Define $\theta \equiv T^{-1}$, eqn 4.2 becomes eqn 4.5.

$$k = \frac{k_B}{h\,\theta}\exp\left(\frac{-\theta\,\Delta G^{\ddagger}}{R}\right) \tag{4.5}$$

Rearrange eqn 4.5, take the logarithm and derivative with respective to θ, and substitute the outcome expression with free energy relationship, one arrives at eqn 4.6

$$\left.\begin{aligned}\ln(k\,\theta) = \ln\left(\frac{k_B}{h}\right) - \frac{\theta\,\Delta G^{\ddagger}}{R} &\implies \frac{\mathrm{d}\,\ln(k\,\theta)}{\mathrm{d}\,\theta} = -\frac{1}{R}\left(\Delta G^{\ddagger} + \theta\frac{\mathrm{d}\,\Delta G^{\ddagger}}{\mathrm{d}\,\theta}\right)\\[2mm] \Delta G^{\ddagger} = \Delta H^{\ddagger} - \theta^{-1}\Delta S^{\ddagger} &\implies \theta\frac{\mathrm{d}\,\Delta G^{\ddagger}}{\mathrm{d}\,\theta} = \frac{\mathrm{d}\,\Delta H^{\ddagger}}{\mathrm{d}\,\theta}\theta + \frac{\Delta S^{\ddagger}}{\theta} - \frac{\mathrm{d}\,\Delta S^{\ddagger}}{\mathrm{d}\,\theta}\end{aligned}\right\}$$

$$\implies \frac{\mathrm{d}\,\ln(k\,\theta)}{\mathrm{d}\,\theta} = -\frac{1}{R}\left(\Delta H^{\ddagger} + \frac{\mathrm{d}\,\Delta H^{\ddagger}}{\mathrm{d}\,\theta}\theta - \frac{\mathrm{d}\,\Delta S^{\ddagger}}{\mathrm{d}\,\theta}\right) \tag{4.6}$$

Notice that eqn 4.6 is commonly used to approximate $\Delta H^{\ddagger}$. This introduces an error $\left(\theta\dfrac{\mathrm{d}\,\Delta H^{\ddagger}}{\mathrm{d}\,\theta} - \dfrac{\mathrm{d}\,\Delta S^{\ddagger}}{\mathrm{d}\,\theta}\right)$ in the numerical result. It necessitates a proof that the above quantity is negligible to one's interest before such a maneuver. The geometrical meaning of eqn 4.6 is illustrated in Figure 4.1.
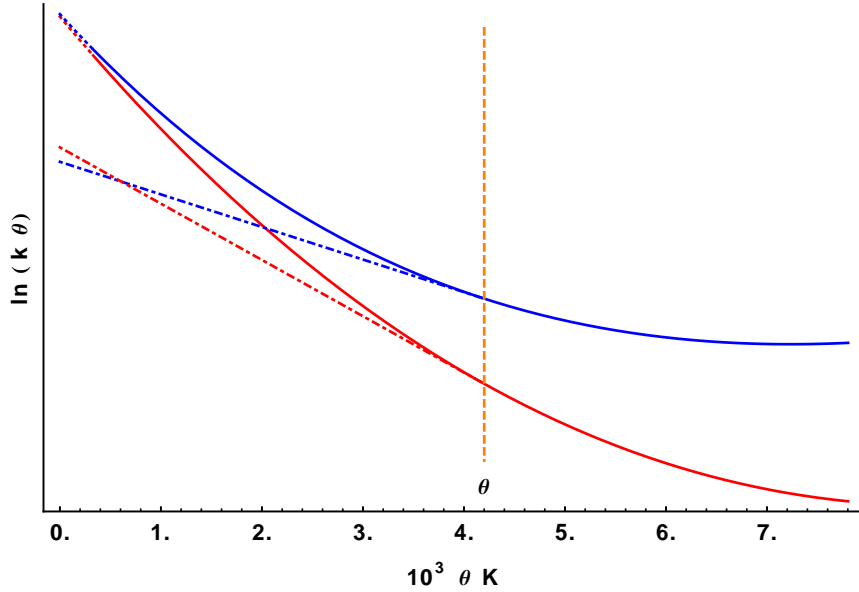
Figure 4.1: Demonstration of the first order approximation for intercepts

Let θ be any point $\in (0,\infty)$. The zero point can be expressed using the Taylor expansion.

$$f(0) = \sum_{n=0}^{\infty} \frac{f^{(n)}(\theta)}{n!}(-\theta)^n \tag{4.7}$$

Truncate to the linear terms of eqn 4.7 and substitute in eqn 4.6, the intercept at $\theta = 0$ of tangent of function $\ln(k\,\theta)$ at θ :

$$\text{Intercept} = \ln(k\,\theta) - \frac{\mathrm{d}\,\ln(k\,\theta)}{\mathrm{d}\,\theta}\,\theta = \ln\left(\frac{k_B}{h}\right) + \frac{\theta^2}{R}\left(\frac{\mathrm{d}\,\Delta G^{\ddagger}}{\mathrm{d}\,\theta}\right) \tag{4.8}$$

Eqn 4.8 clearly shows that the derivative $\left(\dfrac{\mathrm{d}\,\Delta G^{\ddagger}}{\mathrm{d}\,\theta}\right)$ determines the sign for the intercept difference between the two isotopologues. To evaluate it, statistical thermodynamics approach is employed. It can be argued that the major contribution to the free energy that can reflect the difference between H and D is the vibrational term. Based on the quantum mechanic harmonic oscillator model, the vibrational partition function can be expressed in eqn 4.9

$$q = \left(1 - \exp\left(-\frac{\epsilon\,\theta}{k_B}\right)\right)^{-1} \tag{4.9}$$

The activation free energy $\Delta G^{\ddagger}$ is the free energy difference between the transition state and the ground state. The difference between $\Delta G_H^{\ddagger}$ and $\Delta G_D^{\ddagger}$ is thus can be decomposed into four terms (eqn 4.10). It should be noted that the four terms have asymmetrical influence on activation free energy difference between isotopologues ^{1}H and ^{2}H, i.e. $\Delta G_H^{\ddagger} - \Delta G_D^{\ddagger}$. The transition state is the combination of the two molecules on the ground states. As a result, the transition state has greater total number of the vibrational modes than the sum the reactants on ground state. What's more, one of the vibrational mode according to the atom transfer is lost on the transition state. The net effect is then the free energy difference between the two isotopologues on the transition state is miniscule compared to its counterpart on the ground state. Therefore, the second term of eqn 4.10 dominates. Based on the quantum mechanic harmonic oscillator model, the energy gap (ϵ) between modes is larger for H than D.

The derivative $\left(\dfrac{\mathrm{d}\,\Delta G}{\mathrm{d}\,\theta}\right)$ can be shown to be a monotonic decreasing function with respect to θ. Collecting all the relations stated above, one reached the inequality 4.11.

$$\frac{\mathrm{d}\,\Delta G^{\ddagger}}{\mathrm{d}\,\theta} = \frac{\mathrm{d}\,\Delta G^{\mathrm{TS}}}{\mathrm{d}\,\theta} - \frac{\mathrm{d}\,\Delta G^{\mathrm{GS}}}{\mathrm{d}\,\theta} \implies$$

$$\frac{\mathrm{d}\Delta G_{\mathrm{H}}^{\ddagger}}{\mathrm{d}\,\theta} - \frac{\mathrm{d}\,\Delta G_{\mathrm{D}}^{\ddagger}}{\mathrm{d}\,\theta} = \left(\frac{\mathrm{d}\,\Delta G_{\mathrm{H}}^{\mathrm{TS}}}{\mathrm{d}\,\theta} - \frac{\mathrm{d}\,\Delta G_{\mathrm{D}}^{\mathrm{TS}}}{\mathrm{d}\,\theta}\right) + \left(\frac{\mathrm{d}\,\Delta G_{\mathrm{D}}^{\mathrm{GS}}}{\mathrm{d}\,\theta} - \frac{\mathrm{d}\,\Delta G_{\mathrm{H}}^{\mathrm{GS}}}{\mathrm{d}\,\theta}\right) \qquad (4.10)$$

$$\left|\epsilon_{\mathrm{D}}^{\mathrm{TS}} - \epsilon_{\mathrm{H}}^{\mathrm{TS}}\right| < \left|\epsilon_{\mathrm{D}}^{\mathrm{GS}} - \epsilon_{\mathrm{H}}^{\mathrm{GS}}\right| \qquad \implies \qquad \left|\frac{\mathrm{d}\,\Delta G_{\mathrm{D}}^{\mathrm{GS}}}{\mathrm{d}\,\theta} - \frac{\mathrm{d}\,\Delta G_{\mathrm{H}}^{\mathrm{GS}}}{\mathrm{d}\,\theta}\right| > \left|\frac{\mathrm{d}\,\Delta G_{\mathrm{D}}^{\mathrm{TS}}}{\mathrm{d}\,\theta} - \frac{\mathrm{d}\,\Delta G_{\mathrm{H}}^{\mathrm{TS}}}{\mathrm{d}\,\theta}\right|$$

$$\epsilon_{\mathrm{H}} > \epsilon_{\mathrm{D}}$$

$$\frac{\mathrm{d}^2\,\Delta G}{\mathrm{d}\,\theta\,\mathrm{d}\,\epsilon} = \frac{-\exp\left(\frac{\epsilon\,\theta}{k_B}\right)\epsilon}{\left(1 - \exp\left(\frac{\epsilon\,\theta}{k_B}\right)\right)^2 k_B} < 0 \implies \qquad \frac{\mathrm{d}\,\Delta G_{\mathrm{D}}^{\mathrm{GS}}}{\mathrm{d}\,\theta} - \frac{\mathrm{d}\,\Delta G_{\mathrm{H}}^{\mathrm{GS}}}{\mathrm{d}\,\theta} > 0$$

$$\implies \frac{\mathrm{d}\,\Delta G_{\mathrm{H}}^{\ddagger}}{\mathrm{d}\,\theta} - \frac{\mathrm{d}\,\Delta G_{\mathrm{D}}^{\ddagger}}{\mathrm{d}\,\theta} > 0 \qquad (4.11)$$

Therefore, the phenomenological $\Delta S_{\mathrm{H}}^{\ddagger} - \Delta S_{\mathrm{D}}^{\ddagger}$ obtained by extrapolation will always yield a positive sign in the domain of $\theta \in (0, \infty)$. As shown in Table 4.3, $\theta\left(\dfrac{\mathrm{d}\,\Delta G_{\mathrm{H}}^{\ddagger}}{\mathrm{d}\,\theta} - \dfrac{\mathrm{d}\,\Delta G_{\mathrm{D}}^{\ddagger}}{\mathrm{d}\,\theta}\right) \doteq \dfrac{\theta\,\Delta\Delta G}{\Delta\,\theta}$ is indeed a positive number. Additional support can be found on the ZPE graph Figure 4.4, where ZPE drops almost twice for the ground state compared to the transition state.

Thus, a negative intercept difference the extrapolated tangents of the kinetic curves for ^{1}H and ^{2}H transfer $(\mathrm{Int}(^1\mathrm{H}) - \mathrm{Int}(^2\mathrm{H}) < 0)$ can used as a temperature-independent signature to show the kinetic behavior of a reaction system is outside the regime where classical theory can be approximately applicable.

Table 4.3: Activation free energy based on DFT calculations for EtBZ and EtBZ-d1[a]

Terms	ΔG	$\dfrac{\theta\,\Delta\Delta G}{\Delta\theta}$
TS(H)	-7.6314728×10^6	1.879×10^2
GS(H)	-7.6315357×10^6	2.257×10^2
TS(D)	-7.6314774×10^6	1.879×10^2
GS(D)	-7.6315448×10^6	2.259×10^2
TS(H) - TS(D)	4.6	0.0
GS(H) - GS(D)	9.0	-0.2
(TS(H)-TS(D)) - (GS(H)-GS(D))	-4.4	0.2

Note : [a] refers to the transferring atom being ^2H. TS refers to the transition state; GS refers to the ground state. The unit for the physical quantities in table is $kJ \cdot mol^{-1}$

4.4.3 Kinetic Deviation from the Classical Transition State Theory Expectations Under the Influence of Nuclear Tunneling

As seen in the previous section (4.4.2), $(\mathrm{d}\Delta G_H/\mathrm{d}\theta < \mathrm{d}\Delta G_D/\mathrm{d}\theta)$ holds for any positive value θ. Consequently, the tangents of the kinetic curves for EtBZ and EtBZ-d10 at a given value of θ cross at $\theta_{\mathrm{cross}} \leq 0$, leading to intercepts appearing in the order $\mathrm{Int(EtBZ)} > \mathrm{Int(EtBZ\text{-}d10)}$. The linear extrapolations of the simulated kinetic curves from DFT calculations well supported this conclusion, as illustrated in Figure 4.2b. The extrapolations of the tangents of the kinetic curves for EtBZ and EtBZ-d10, shown as cyan and purple dash-dotted lines, cross slightly to the left of the origin $\theta = 0$, leaving a small positive difference of 0.86 J K^{-1} mol^{-1} at $\theta = 0$. This number is in good agreement with the value 0.85 J K^{-1} mol^{-1} obtained from direct prediction of DFT calculations at 243.16 K and 0.90 J K^{-1} mol^{-1} at 233.16 K. However, the extrapolation of the experimental data yields a large, negative intercept difference, $\mathrm{Int(EtBZ)}$ - $\mathrm{Int(EtBZ\text{-}d10)} \approx$ -35 J K^{-1} mol^{-1} (Table 4.2). Given the low mass of the transferring atom (^1H or ^2H), nuclear tunneling is considered to be the most likely

source of this discrepancy.

In order to set up a quantitative description of tunneling effects in the kinetic framework, a semiclassical approach was adopted which incorporates a tunneling factor as a pre-exponential factor in the classical rate expression as seen below.

$$k = \kappa \, Q_T \, \exp\left(\frac{-\Delta G^{\ddagger}}{RT}\right) \qquad (4.12)$$

The expression in eqn 4.12 is the product of a temperature independent pre-exponential factor (κ) with the dimension of rate constant, a dimensionless tunneling factor (Q_T), and an exponential factor depending on the Gibbs free energy of activation ($\Delta G^{\ddagger}$). The tunneling factor Q_T was calculated with Bell's expression for tunneling through a quadratic barrier, using DFT values for the imaginary frequency of the reaction coordinate at the transition state and the width of the tunneling energy range.

In qualitative terms the effect of tunneling on the kinetic curve can be understood as follows. Instead of having a single-valued activation energy as it is assumed in the classical transition state theory, there is a continuum of energies at which the transfers occur in the case of tunneling. As upon lowering the temperature the importance of transfer events occurring at lower tunneling energies gain in importance relative to those proceeding at higher energies, the effective barrier height and associated slope in the kinetic curve tend to become lower. As a result the kinetic curves are convex functions, with the plot for the EtBZ-d10 substrate being less curved and running below the one for EtBZ (shown as the blue and red solid curves in Figure 4.2a). It should be noted that the corresponding classical curves shown in cyan and purple also demonstrate certain curvature but to a much smaller magnitude. This curvature can be accounted by the last two first order terms in eqn 4.6.

By introducing the nuclear tunneling factor (eqn 4.12), $\dfrac{\mathrm{d}\ln(k\,\theta)}{\mathrm{d}\,\theta}$ becomes eqn 4.13
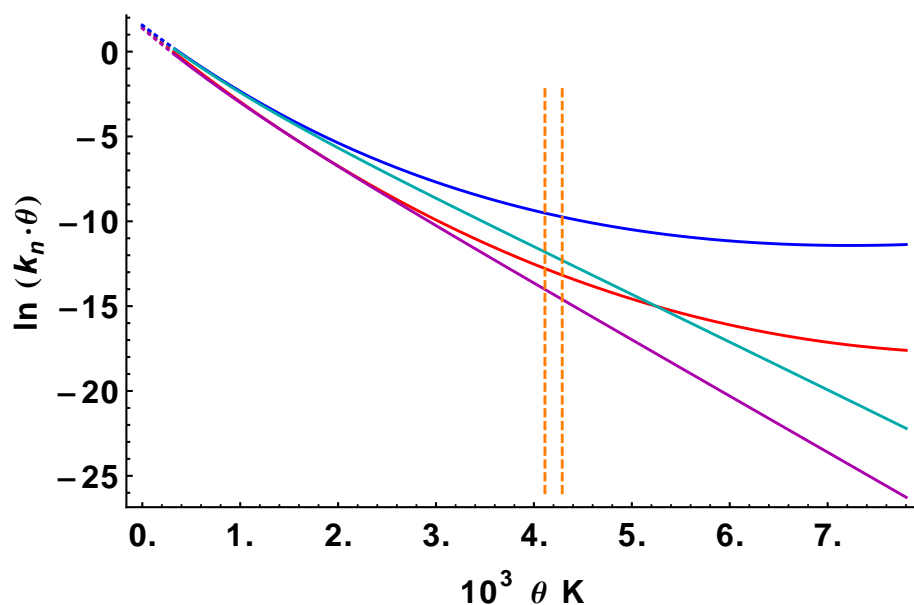
(a) simulated kinetic curves
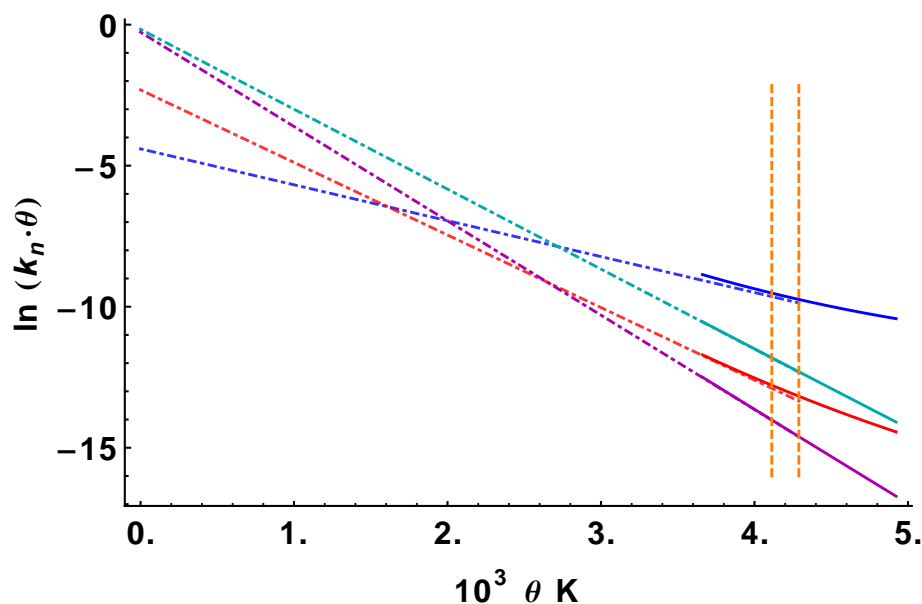
(b) linear extrapolations

Figure 4.2: $\ln(k_n \theta)$ vs. θ plot. (a) simulated kinetic curves in the θ range $(0 - 8 \times 10^{-3}\,\mathrm{K}^{-1})$. (b) kinetic curves and linear extrapolation from the experimental temperature range in the θ range $(0 - 5 \times 10^{-3}\,\mathrm{K}^{-1})$. k_n is the normalized rate constants obtained from DFT calculations. Color coding: blue, kinetic curve for EtBZ ^{1}H transfer including nuclear tunneling; red, kinetic curve for EtBZ-d10 ^{2}H transfer including nuclear tunneling; cyan, classical kinetic curve for ^{1}H transfer excluding tunneling; purple classical kinetic curve for ^{2}H transfer excluding tunneling; orange dotted vertical bars, the experimental temperature range; solid curves, theoretical results from DFT calculations; broken curves, linear extrapolations.

$$\frac{\mathrm{d}\ln(k\,\theta)}{\mathrm{d}\,\theta} = -\frac{1}{R}\left(\Delta H^{\ddagger} + \underbrace{\frac{\mathrm{d}\,\Delta H^{\ddagger}}{\mathrm{d}\,\theta}\theta - \frac{\mathrm{d}\,\Delta S^{\ddagger}}{\mathrm{d}\,\theta} - \frac{R}{Q_T}\frac{\mathrm{d}\,Q_T}{\mathrm{d}\,\theta} - \frac{R}{\theta}}_{\text{Error}}\right) \tag{4.13}$$

So, approximating $\Delta H^{\ddagger}$ obtained from conventional treatment (eqn 4.8) bear a even larger error as indicated in eqn 4.13.

The intercept for eqn 4.12 has changed correspondingly.

$$\text{Int} = (-1 + \ln\kappa + \ln\theta) + \frac{\theta^2}{R}\left(\frac{\mathrm{d}\,\Delta G^{\ddagger}}{\mathrm{d}\,\theta}\right) + \ln(Q_T) - \frac{\theta}{Q_T}\frac{\mathrm{d}\,Q_T}{\mathrm{d}\,\theta} \tag{4.14}$$

The first term is almost identical for EtBZ and EtBZ-d10 and contributes little to Int(EtBZ) - Int(EtBZ-d10). The second, third, and fourth terms are positive, positive, and negative, respectively, and have the increasing order of the relative magnitudes in the experimental temperature range. As the fourth term dominates, the total of the second, third and fourth term give together a negative contribution to the intercepts for both EtBZ and EtBZ-d10. Since this negative contribution is larger for EtBZ, $\left|\frac{\theta}{Q_T}\frac{\mathrm{d}\,Q_T}{\mathrm{d}\,\theta}\right|_{\text{EtBZ-d10}} > \left|\frac{\theta}{Q_T}\frac{\mathrm{d}\,Q_T}{\mathrm{d}\,\theta}\right|_{\text{EtBZ}}$ (see Table 4.4), the tangents of the kinetic curves for EtBZ and EtBZ-d10 cross at $\theta_{\text{cross}} > 0$, leading to a negative intercept difference, $\text{Int}(\text{EtBZ}) - \text{Int}(\text{EtBZ}-\text{d}_{10}) < 0$.

The tangents crossing behavior in fully portrayed in Figure 4.2. While the kinetic curves excluding tunneling effects are nearly linear (Figure 4.2a) with EtBZ only marginally more curved than EtBZ-d10, the introduction of tunneling drastically enhances the curvatures for both curves with the one for EtBZ being the most articulate (Figure 4.2a). The larger curvature in the kinetic plot for EtBZ gives rise to an intercept that is below the one for EtBZ-d10, as shown by the red and blue dash-dotted lines in Figure 4.2b. Consequently, the large negative difference between the inter-

cepts, Int(EtBZ) - Int(EtBZ-d10) < 0, is due to tunneling and not the result of an isotope effect on the entropy as suggested by the conventional analysis of Eyring plots (cf. Table 1) according to which the intercept is interpreted as an activation entropy.

There are two major contributions to the KIE, viz. tunneling and ZPE. Only the former contributes to Int(EtBZ) - Int(EtBZ-d10). As the intercept of a tangent of a kinetic curve depends on $(\mathrm{d}\Delta G^{\ddagger}/\mathrm{d}\theta)$ (see eqn 4.6) none of the θ independent terms in $\Delta G^{\ddagger}$, including the ZPE, can contribute. In contrast, the tunneling contribution, $(\theta/Q_T)(\mathrm{d}Q_T/\mathrm{d}\theta)$, which is a function of θ, has an important effect on the intercept. As the classical description predicts that Int(EtBZ) - Int(EtBZ-d10) > 0 (see above), tunneling is the only viable explanation for the large negative intercept difference.

This intercept can be accessed using the reminder terms of the Taylor expansion, which reveals higher order derivative of the kinetic curves can affect the intercept difference between isotopologues in an anisotropic fashion.

Let $f(x)$ and $g(x)$ represent H and D curve respectively. H and D curve meet at $x = 0 \Leftrightarrow f(0) = g(0)$

$$f(x)-f'(x)x+\frac{f''(x)}{2}x^2-\frac{f^{(3)}(x)}{6}x^3+O(x^4) = g(x)-g'(x)x+\frac{g''(x)}{2}x^2-\frac{g^{(3)}(x)}{6}x^3+O(x^4)$$

$$\mathrm{int_H}-\mathrm{int_D} = (f(x)-f'(x)x)-(g(x)-g'(x)x) = \frac{g''(x) - f''(x)}{2}x^2+\frac{f^{(3)}(x) - g^{(3)}(x)}{6}x^3$$

$$(4.15)$$

As seen in Figure 4.3 (a), the first derivatives of the classical kinetic curves (cyan and purple) in which nuclear tunneling effects are no considered almost invariant to θ. This can be understood from the fact that the two temperature dependent term $\frac{\theta \, \Delta\Delta E^{\ddagger}_{\mathrm{therm}}}{\Delta \theta}$ and $-\frac{\Delta\Delta S^{\ddagger}}{\Delta \theta}$ nearly cancel out each other (see Table 4.4). One the other hand, with nuclear tunneling effects, the first derivatives of the kinetic curves (blue and red) show obvious changes as θ varies. As a consequence, the second derivatives

of the kinetic curves demonstrate even stronger deviation from the classical curves as a result of nuclear tunneling as shown in Figure 4.3 (b). The kinetic curve approach plateaus as θ increase and this process is complete faster for ^{1}H than that of ^{2}H indicated by the blue curve running above the red on in Figure 4.3 (a). However, the pace of changing the first derivatives themselves are not necessarily following the same pattern. As seen in Figure 4.3 (b), the blue and red curves cross right before the experimental temperature zone. This means the curvature alteration caused by nuclear tunneling can produce parallel or antiparallel contribution to the intercept difference as the first order derivative. This result has significant impact on the intercept difference between isotoplogues. Notice from eqn 4.15 that the first derivative and the second derivative always has the same sign when evaluating the difference between intercepts. The difference between the second derivatives for H and D varies as a function of θ and bears a stationary point. This means the intercept difference can bear opposite signs depending on the choice of θ of interest. Now the role of the third derivative become significant. Unlike the second, the difference between the third derivatives for the two isotopologues shows as a monotonic function of θ (see Figure 4.3 (c)) and they always have the opposite sign to the second derivatives (see eqn 4.15). Their magnitude is comparable with the second derivatives. Thus, the final determination of the sign of the intercept difference between H and D is on the sum of the second and third derivatives of their kinetic curves. Even though the second derivative can swing between two sides, the third derivative appear to be consistent based on our analysis and finally governs the sign of the difference between the two intercepts. A sample calculation shows that the intercept difference between ^{1}H and ^{2}H using the first order approximation is -0.56. Using the reminder of Taylor expansion (eqn 4.15), the result is -0.51, in good agreement with linear approximation of the intercepts.
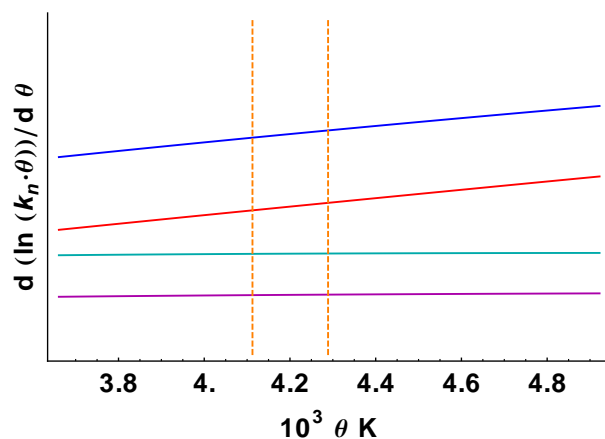
(a) first derivative
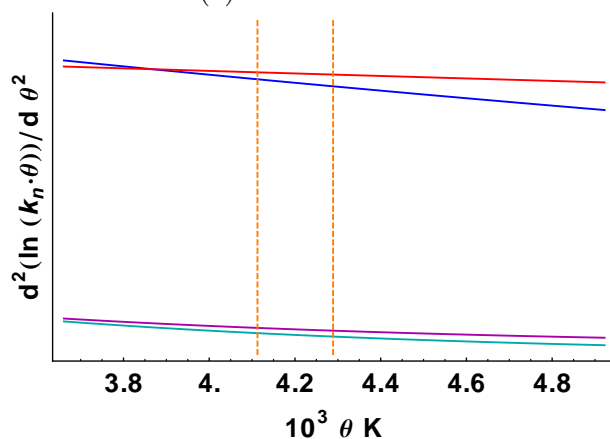
(b) second derivative
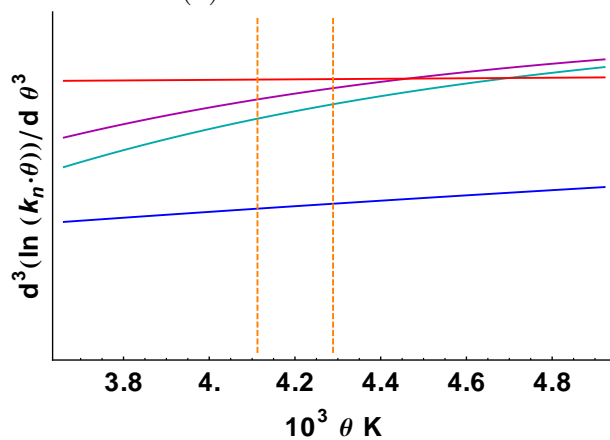
(c) third derivative

Figure 4.3: First(a), second(b) and third(c) derivatives of $\ln(k_n\,\theta)$ vs. θ plots where k_n is the normalized rate constants obtained from DFT calculations. Color coding: blue, EtBZ H transfer including nuclear tunneling; red, D transfer including nuclear tunneling; cyan, H transfer excluding tunneling; purple D transfer excluding tunneling; orange dotted vertical bars, the experimental temperature range.

4.4.4 Analytical Dissection of the Slopes of the Kinetic Curves

Define the apparent energy (E_{app}) :

$$E_{\text{app}} \equiv -R\frac{\mathrm{d}\,\ln(k\,\theta)}{\mathrm{d}\,\theta} \tag{4.16}$$

Substitute the free energy breakdown terms into the nuclear tunneling corrected rate expression and express E_{app} in those terms, eqn 4.18 and eqn 4.19 result. To evaluate the contribution of individual terms in eqn 4.19 to E_{app}, the thermodynamic parameters from DFT calculations and the nuclear tunneling factors based on Bell's model were computed . The numerical results are summarized in Table 4.4.

Table 4.4: DFT-based decomposition of E_{app} in the experimental temperature range

State	EtBZ (kJ/mol)	EtBZ-d10 (kJ/mol)
$\Delta E_{\text{ele}}^{\ddagger}$	40.12	40.12
$\Delta ZPE^{\ddagger}$	-15.67	-11.59
$\Delta E_{\text{therm}}^{\ddagger}$	3.01	3.15
$\dfrac{\theta\,\Delta\Delta E_{\text{therm}}^{\ddagger}}{\Delta\theta}$	-2.89	-3.31
$-\dfrac{\Delta\Delta S^{\ddagger}}{\Delta\theta}$	2.93	3.35
Subtotal	27.51	31.74
$-\dfrac{R}{Q_T}\dfrac{\Delta(Q_T)}{\Delta\theta}$	-13.37	-6.67
Total	14.14	25.07

The definition of E_{app} converts a negative contribution to the slope of the kinetic curve into a positive contribution to the effective activation energy, and vice versa. Eqn 4.18 reveals that the slope of a kinetic curve is composed of a number of contributions. These include not only the common electronic and zero point contributions to the activation energy but also contributions from the thermal energies of vibration, rotation and translation, entropy, and tunneling.

$$k = Q_T \frac{k_B T}{h} \exp\left(-\frac{\Delta G^{\ddagger}}{RT}\right) \implies \ln\left(\frac{k}{T}\right) = \ln\left(\frac{k_B}{h}\right) + \ln\left(Q_T\right) - \frac{\Delta G^{\ddagger}}{RT}$$

$$\Delta G^{\ddagger} = \Delta E_{\text{ele}}^{\ddagger} + \Delta ZPE^{\ddagger} + \Delta E_{\text{therm}}^{\ddagger} + RT - T\Delta S^{\ddagger}$$

$$\Delta E_{\text{therm}}^{\ddagger} = \Delta H^{\ddagger} - RT - \Delta ZPE^{\ddagger}$$

$$\theta \equiv T^{-1}$$

$$E_{\text{app}} \equiv -R\frac{\mathrm{d}\,\ln(k\,\theta)}{\mathrm{d}\,\theta}$$

$$\implies E_{\text{app}} = k_B \frac{\mathrm{d}\,\ln\left(Q_T\right)}{\mathrm{d}\,\theta} + \theta\, \frac{\mathrm{d}\left(\Delta E_{\text{ele}}^{\ddagger} + \Delta ZPE^{\ddagger} + \Delta E_{\text{therm}}^{\ddagger} + R\,\theta^{-1} - \Delta\,S^{\ddagger}\,\theta^{-1}\right)}{\mathrm{d}\,\theta}$$

$$+ \left(\Delta E_{\text{ele}}^{\ddagger} + \Delta\, ZPE^{\ddagger} + \Delta E_{\text{therm}}^{\ddagger} + R\,\theta^{-1} - \Delta S^{\ddagger}\,\theta^{-1}\right) \tag{4.17}$$

$$= -R\frac{\mathrm{d}\,\ln\left(Q_T\right)}{\mathrm{d}\,\theta} + \theta\,\frac{\mathrm{d}\,\Delta E_{\text{therm}}^{\ddagger}}{\mathrm{d}\,\theta} - \frac{\mathrm{d}\Delta\,S^{\ddagger}}{\mathrm{d}\,\theta} + \Delta E_{\text{ele}}^{\ddagger} + \Delta ZPE^{\ddagger} + \Delta E_{\text{therm}}^{\ddagger}$$

$$\tag{4.18}$$

$$\doteq\ -R\frac{\Delta\,\ln\left(Q_T\right)}{\Delta\,\theta} + \frac{\theta\,\Delta\Delta E_{\text{therm}}^{\ddagger}}{\Delta\,\theta} - \frac{\Delta\Delta S^{\ddagger}}{\Delta\,\theta} + \Delta E_{\text{ele}}^{\ddagger} + \Delta ZPE^{\ddagger} + \Delta E_{\text{therm}}^{\ddagger}$$

$$\tag{4.19}$$

A comparison of the data in for EtBZ and EtBZ-d10 in Table 4.4 reveals both similarities and differences. The electronic energies for EtBZ and EtBZ-d10 are equal because they have been calculated using clamped nuclei. As usual $\Delta E_{\text{ele}}^{\ddagger}$ is the largest contribution to E_{app}. The second largest contribution, $\Delta ZPE^{\ddagger}$, is mainly determined by the ZPE of the C-H bond stretch of the abstracted hydrogen, which raises the ground state energy relative to the energy of the transition state in which this mode

is converted to mode with an imaginary frequency, resulting in a large negative value for this quantity.

The third largest contribution is from nuclear tunneling and it has a negative sign because lowering temperature (increase in θ) is associated with lowering the effective activation energy due enhancement of tunneling. The two thermal energy terms nearly cancel, consistent with the result predicted in the classical limit of equipartition where their sum is zero. The entropic term is small but becomes an increasingly important factor at higher temperatures. $(\theta\,\Delta\Delta E^{\ddagger}_{\text{therm}}/\Delta\theta)$ and $(\Delta\Delta S^{\ddagger}/\Delta\theta)$ have similar magnitudes but opposite signs. The difference between these two terms accounts for the curvature of the classical kinetic curves shown in Figure 4.2a. The kinetic curves become more horizontal for EtBZ than EtBZ-d10 in the experimental temperature range primarily because the contribution of $-(R/Q_T)(\Delta(Q_T)/\Delta\theta)$ to E_{app} is almost doubled for the former compared to the latter.

4.4.5 Analysis of ZPE and Imaginary Frequency

4.4.5.1 Monodeuteration Scenario

Table 4.5: ZPE differences obtained from multiple methods

method	$(\Delta ZPE^{\ddagger}_{\text{D}} - \Delta ZPE^{\ddagger}_{\text{H}})/\text{cm}^{-1}$
Simplified	404
Stretching mode	403
Direct ΔZPE	364

Table 4.5 presents estimates of the effect of ^{2}H isotope labeling on the $\Delta ZPE^{\ddagger}$ contribution to the activation energy at various levels of approximation. In the single mode approximation, the isotope effect is assumed to reside entirely in the vibration of the C-H bond that is to be cleaved (1st and 2nd row of Table 4.5). The 1st row lists the

value obtained by estimating the difference $({}^{h\nu_\text{C-H}}/_2 - {}^{h\nu_\text{C-D}}/_2)$ using the approximation $h\nu_\text{C-D} = \sqrt{7/13}\, h\nu_\text{C-H}$, where the numerical factor is the square root of the effective mass ratio of diatomic C-H and C-D oscillators and the value for $h\nu_\text{C-H}$ is the DFT frequency for EtBZ-^{1}H. The second row presents the difference $({}^{h\nu_\text{C-H}}/_2 - {}^{h\nu_\text{C-D}}/_2)$ evaluated by two independent frequency calculations for the EtBZ-^{1}H and EtBZ-^{2}H. The two approaches yield nearly equal values for the isotope effect on the $\Delta ZPE^\ddagger$. In the third approximation the $\Delta ZPE^\ddagger$ contribution to the activation energy has been obtained as the difference of the total ZPE at both the transition state and the ground state. These totals were evaluated by summing over all normal modes, with the exception of the imaginary frequency mode in the summation for the transition state. The difference between the total ZPE for the ^{1}H and ^{2}H labeled substrates is 737 cm^{-1}, while that for the ^{1}H and ^{2}H labeled transition complexes is 373 cm^{-1}. As these numbers represent the effect of ^{2}H isotope labeling on the ZPE of initial state and transition complex state, respectively, the net isotope effect on the activation energy is the difference 364 cm^{-1} (third row of Table 4.5). The resulting isotope effect is about 35 cm^{-1} lower than obtained in the single mode approximations. The multimode description appears to yield much larger values for the isotope shifts in the ZPEs of the individual states than obtained in the single mode approximation, indicating that the isotope substitution must affect several modes. However, these shifts nearly cancel in the difference of ZPE that defines the net isotope effect on the activation barrier.

4.4.5.2 Multideuteration Scenario

To examine the primary kinetic isotope effect originated from ZPE, isotopic substitution should be placed on the atom(s) whose bonding connection is(are) reformed at the transition states. However, it might not be a straightforward, if at all possible,

process to solely label a specific atom in a molecule experimentally. Therefore, primary isotope effects are almost always contaminated with secondary isotopes effects, in which atom(s) that are not involved in bonding reorganization at the transition state contribute to the effects. This is actually the case of our study, where EtBZ-d10 is used as an experimental probe for the kinetic isotope effect. Therefore, it necessitates a theoretical investigation on the distinction between the primary and secondary contributions to the kinetic isotope effects by varying the isotopologues of EtBZ. Computation of six variations of EtBZ isotopologues (d0, d1, d2, d8, d9, and d10, see Figure 4.4 for their definitions) based on DFT is summarized in Figure 4.4.

The first notice on Figure 4.4 is the ZPE drop after introducing the deuterating H38 (Figure 4.6) and the difference of this drop between the ground state (-737 cm^{-1}) and transition state (-373 cm^{-1}). This discrepancy on the order about a factor of two in energy reflects the significant impact of atomic mass on the reaction barrier and thus reaction rates. It also supports the assumptions made in deriving the inequality 4.11. Introducing the secondary ^{2}H into EtBZ sags ZPE further down for both the ground state and transition state. However, the magnitude is very similar for the two states, 739 cm^{-1} (GS) vs. 735 cm^{-1} (TS). The fact these two quantities do not cancel each other completely is the cause of the secondary isotope effect. Clearly, the secondary kinetic isotope effect is far way smaller or even negligible compared to the primary kinetic isotope effect (4 cm^{-1} vs. 364 cm^{-1}). Coming from the other end, undeuterating H38 (Figure 4.6) of the d10 species gives rises similar phenomenon on the ZPE increasing as what the first deuteration does to the ZPE decreasing. Further undeuteration of the other methylene hydrogen (d8 species) diminishes the difference in ZPE upward laddering between the ground state and transition state. So this bottom-up analysis is in good agreement with the top-down analysis. In summary, the secondary kinetic isotope effect is miniscule in comparison to the primary kinetic

isotope effect. EtBZ-d10 is a good approximate surrogate to obtain experimental kinetic data with the aim of examining the primary kinetic effects. The theoretical model of EtBZ-d10 is expected to produce similar influences on chemical kinetics as EtBZ-d1.
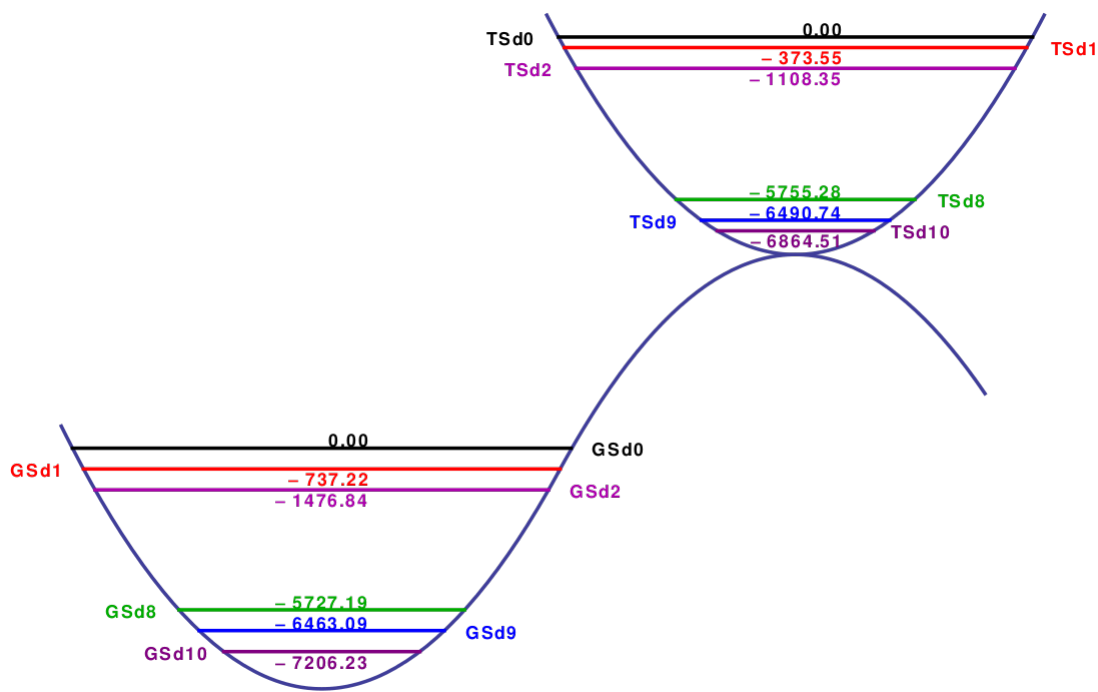
Figure 4.4: Computed ZPEs for $[Fe(O)(B^*)-EtBZ]^{-1}$ and its multiple isotopologues at ground their ground states and transition states. The left upward parabola represents the vibrational energy well at the ground state (GS) and the right upward parabola represents the vibrational energy well at the transition states (TS). The "d[number]+" formula is used to indicate the number of ^2H has been introduced into EtBZ. d0 means, no deuteration. d1 means atom H38 is deuterated. d1 means both H38 and the other methylene hydrogen connected to C36 are deuterated. d10 means all hydrogens on EtBZ are deuterated. d9 means all hydorgens on EtBZ except for H38 are deuterated. d8 means all hydrogens on EtBZ except for H38 and the other methylene hydrogen connected to C36 are deuterated. Please refer to Figure 4.6 to the atom numbers notation. The ZPE of the none deuteriated species (d0) was arbitrarily set to be zero. The energy unit of the numerical quantities in the graph is cm^{-1}.

4.5 Model Fitting and Absolute Rate Constants Prediction

Multiple spectroscopic evidence and DFT calculations support the identification of $[Fe^V(O)(B^*)]^{-1}$.[50] To follow the kinetic decay process of $[Fe^V(O)(B^*)]^{-1}$ when it is subjected to a reducing agent, low temperature UV-Vis spectroscopy was used to register the electronic transition signals. The experimental temperatures were selected in the range of [233.16 K, 243.16K] to accommodate the life time of $[Fe^V(O)(B^*)]^{-1}$. It is strongly desirable to be able predict the absolute rate constants outside the experimental temperature range for multiple purposes, such as comparing the reactivity with other catalysts reported at different temperatures, comparing the reactivity change with temperature, estimate the nuclear tunneling effects contribution to the rate constant as a function of temperature and etc. Linearization of kinetic curves (eqn 4.3) can be a powerful to this end when nuclear tunneling can be excluded. However, this is not the case in EtBZ study.

In order to create a model with the capability of projecting the absolute rate constants of $[Fe^V(O)(B^*)]^{-1}$ mediated EtBZ hydroxylation reaction in a temperate range beyond the experimental probe, DFT calculated thermodynamic parameters combined with nuclear tunneling factor from Bell's model and experimental information were integrated and optimized for the predefined goal. This is the central topic for this section.

4.5.1 Computational Details

The DFT calculations were performed with Gaussian 09 rev.B.01,[49] using Becke's three parameter hybrid functional (B3)[51,52] along with the Lee-Yang-Parr correlation functional (LYP)[53] and basis set 6-311G. The effect of the solvent acetonitrile,

in which the abstraction reaction occurred experimentally, on the electronic states and geometries was simulated using the SMD continuum model.[54] The geometries for $[\mathrm{Fe^V(O)(B^*)}]^{-1}$, EtBZ, the reaction complex $[\mathrm{Fe^V(O)(B^*)-EtBZ}]^{-1}$, the transition state, and the broken-symmetry product state $[\mathrm{Fe^V(O)(B^*)-EtBZ\bullet}]^{-1}$, were obtained by full optimization until the default convergence criteria are met. The spin multiplicity of the $\mathrm{Fe^V(O)}$ species was set to 2 on the basis of previous spectroscopic characterization[50] and the same for the entire reaction system. The transition state structure for the hydrogen atom abstraction reaction was obtained from relaxed potential surface scans and confirmed by frequency analysis.

4.5.2 Predictive Model Construction and Optimization

Comparison of the values for E_app obtained experimentally (27 kJ mol^{-1} and 41 kJ mol^{-1}) and theoretically (14 kJ mol^{-1} and 25 kJ mol^{-1}, cf. Table 4.4) for EtBZ and EtBZ-d10, respectively. This suggests that the DFT calculations have underestimated the isotope independent electronic contribution, E_ele. Discrepancies of this magnitude are not unprecedented in the DFT literature on transition state calculations.[55–57]

The DFT/tunneling calculations predict for the difference Int(EtBZ) - Int(EtBZ-d10) a large negative value of -17.4 kJ mol^{-1}, which is rooted in the tunneling factor of eqn 4.12. The predicted and experimental values for the intercept difference (-35 kJ mol^{-1}) have the same sign and are of comparable magnitude. To predict the rate constant outside the experimental temperature range we have improved the theoretical representation of the experimental data by using eqn 4.12 and treating E_ele, κ and $i\,h\,\nu$ as adjustable parameters. Variation of E_ele leaves the value for Int(EtBZ) - Int(EtBZ-d10) unchanged, whereas the adjustments in κ and $i\,h\,\nu$ affect the intercept difference.

After introduction of corrections, the rate constant equation become

$$k = \kappa \cdot Q_T' \cdot \exp\left(-\frac{\theta\left(\Delta G^{\ddagger} + \lambda\right)}{R}\right) \tag{4.20}$$

$$\implies \ln\left(k\right) = \ln\left(\kappa\right) + \ln\left(Q_T'\right) - \frac{\theta\left(\Delta G^{\ddagger} + \lambda\right)}{R}$$

$$\implies \frac{\mathrm{d}\ln\left(k\right)}{\mathrm{d}\theta} = \frac{\mathrm{d}\ln\left(Q_T'\right)}{\mathrm{d}\theta} - \frac{1}{R}\frac{\mathrm{d}\left(\theta\left(\Delta G^{\ddagger} + \lambda\right)\right)}{\mathrm{d}\theta} = \frac{\mathrm{d}\ln\left(Q_T'\right)}{\mathrm{d}\theta} - \frac{1}{R}\frac{\mathrm{d}\left(\theta\,\Delta G^{\ddagger}\right)}{\mathrm{d}\theta} - \frac{\lambda}{R}$$

$$\implies \frac{\Delta\ln\left(Q_T'\right)}{\Delta\theta} - \frac{\Delta\left(\theta\left(\Delta G^{\ddagger} + \lambda\right)\right)}{R\,\Delta\theta} = \frac{\Delta\ln\left(Q_T'\right)}{\Delta\theta} - \frac{\Delta\left(\theta\,\Delta G^{\ddagger}\right)}{R\,\Delta\theta} - \frac{\lambda}{R}$$

$$\implies \Delta(\ln\left(k\right)) = \Delta(\ln\left(Q_T'\right)) - \frac{\Delta\left(\theta\,\Delta G^{\ddagger}\right)}{R} - \frac{\lambda\,\Delta\theta}{R}$$

$$\implies \frac{\lambda\,\Delta\theta}{R} = \Delta(\ln\left(Q_T'\right)) - \Delta(\ln\left(k\right)) - \frac{\Delta\left(\theta\,\Delta G^{\ddagger}\right)}{R} \tag{4.21}$$

Considering both H and D transfer cases, two equations with three unknowns (λ, $Q_{T,\mathrm{H}}'$, $Q_{T,\mathrm{D}}'$) reveal (eqn 4.22).

$$\begin{cases} \dfrac{\lambda\,\Delta\theta}{R} = \Delta(\ln\left(Q_{T,\mathrm{H}}'\right)) - \Delta(\ln\left(k_{\mathrm{H}}\right)) - \dfrac{\Delta(\theta\,\Delta G_{\mathrm{H}}^{\ddagger})}{R} \\[4mm] \dfrac{\lambda\,\Delta\theta}{R} = \Delta(\ln\left(Q_{T,\mathrm{D}}'\right)) - \Delta(\ln\left(k_{\mathrm{D}}\right)) - \dfrac{\Delta(\theta\,\Delta G_{\mathrm{D}}^{\ddagger})}{R} \end{cases} \tag{4.22}$$

There is no unique solution to this set of equations. A stepwise optimization strategy is used to approximate solutions. First, λ is obtained by minimizing the R.H.S of eqn 4.21 between H and D.

$$\min_{\lambda}\left(\left(\Delta(\ln\left(Q_{T,H}\right)) - \Delta(\ln\left(k_H\right)) - \frac{\Delta(\theta\,\Delta G_H^{\ddagger})}{R} - \lambda\right)^2 \right.$$
$$\left. + \left(\Delta(\ln\left(Q_{T,D}\right)) - \Delta(\ln\left(k_D\right)) - \frac{\Delta(\theta\,\Delta G_D^{\ddagger})}{R} - \lambda\right)^2\right) \tag{4.23}$$

Minimum was attained at $\lambda = 1346\,\text{cm}^{-1}$. Second, substituting λ in eqn 4.21 and Q'_T were obtained by brute-force searching in the imaginary frequency space. The correction factor for the imaginary frequency is 64 cm^{-1} for EtBZ and -70 cm^{-1} for EtBZ-d10.

Finally, the preexponential factor can be obtained by fitting the question below with the experimentally determined rate constants.

$$\ln(k) = \ln(\kappa) + \ln(Q'_T) - \frac{\Delta G^{\ddagger} + \lambda}{RT} \tag{4.24}$$

The fitted $\ln(\kappa)$ for H and D are 33.8 and 34.8 respectively. Theoretically, the difference between these two factors are expected to be very small since H and D should have to quite similar translational motions. The fitted results are larger than expectation can rise from three sources. First,experimentally determined rate constants were used to correct the theoretical model. It is noted that the kinetic isotope effects for the temperature points 236.16 K and 239.16 K (Table 4.6 row 2 and 3) are identical. This exemplifies the uncertainty in the experimental results, which can be propagated through the parameters fitting process. Second, the method to acquire λ is not exact. This can be another step to introduce uncertainty to ν. Third, the imaginary frequency is also a result of fitting, which can contribute errors to certain degree.

4.5.3   Fitted Model Evaluation and Absolute Rate Constants Prediction

The intercept difference between EtBZ and EtBZ-d10 obtained from the theoretical curve becomes -34.31 kJ mol^{-1}. The corresponding quantity determined from experiment is -34.19 kJ mol^{-1}. Apparently, theoretical model has successfully reproduced
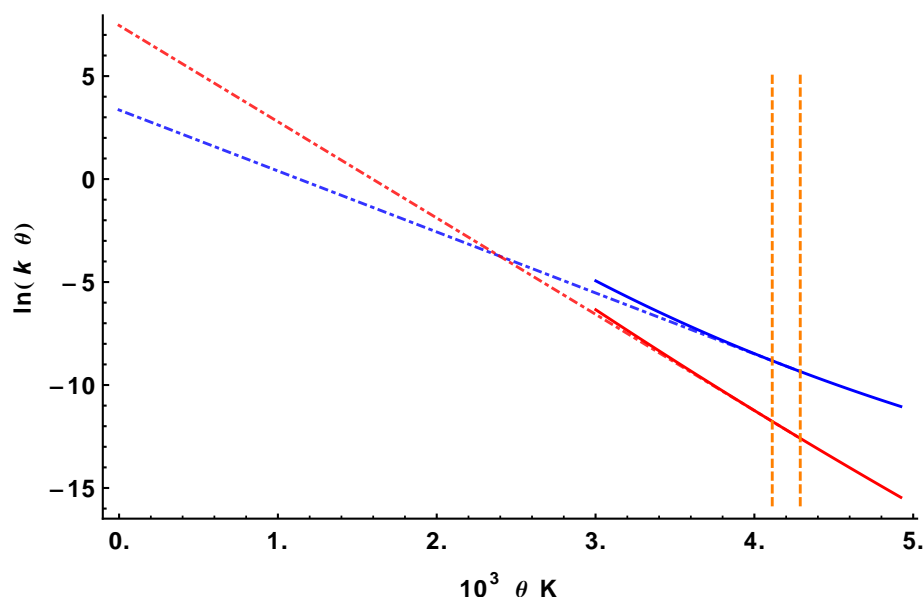
Figure 4.5: $\ln(k\,\theta)$ vs. θ plot using data generated by the fitted model. Color coding : blue for EtBZ, red for EtBZ-d10; dot-dashed lines for extrapolation; dotted vertical lines for experimental temperature range.

the experimental results after parameters optimization. The $\ln(k\,\theta)$ vs. θ plot produced by the optimized theoretical model is shown in Figure 4.5. The comparison between the absolute rate constants obtained from experimental measure and prediction by fitted theoretical model is summarized in Table 4.6. Apparently, the predicted rate constants are very close to the experimental measured results, with the relative errors bounded between 1% to 5%. It should also be noted that the two experimentally reported identical KIEs highlighted in Table 4.6 are split apart in the theoretical model. This suggests efficacy of the theoretical model and also denotes its limitation inherited from the uncertainty of the experimental data.

Table 4.7 listed the rate constant ratios at three temperatures, 233.16 and 273.16, 298.16 K. The rate constants were obtained by three methods, the conventional kinetic model excluding the nuclear tunneling, linear extrapolation of the kinetic data from the experimental temperature range and the general theoretical model including nuclear tunneling.

Table 4.6: Rate constants comparison between the experimental measures and the theoretical model predictions

$T/(K)$	$k_{expr}^H/(M^{-1}s^{-1})$	$k_{theo}^H/(M^{-1}s^{-1})$	$k_{expr}^D/(M^{-1}s^{-1})$	$k_{theo}^D/(M^{-1}s^{-1})$	KIE_{expr}	KIE_{theo}
233.16	2.00×10^{-2}	2.04×10^{-2}	7.08×10^{-4}	7.94×10^{-2}	25.6	25.6
236.16	2.48×10^{-2}	2.42×10^{-2}	1.09×10^{-3}	1.04×10^{-3}	22.7	23.4
239.16	2.89×10^{-2}	2.87×10^{-2}	1.28×10^{-3}	1.34×10^{-3}	22.7	21.3
243.16	3.54×10^{-2}	3.59×10^{-2}	1.92×10^{-3}	1.89×10^{-3}	18.5	19.0

Note : T is the absolute temperature, subscript "expr" stands for experimental measurement and subscript "theo" stands for theoretical prediction.

Table 4.7: Rate constant ratios at various temperatures

$T/(K)$	$\dfrac{k_{gen}^{EtBZ}}{k_{con}^{EtBZ}}$	$\dfrac{k_{gen}^{EtBZ}}{k_{ext}^{EtBZ}}$	$\dfrac{k_{gen}^{EtBZ\text{-}d10}}{k_{con}^{EtBZ\text{-}d10}}$	$\dfrac{k_{gen}^{EtBZ\text{-}d10}}{k_{ext}^{EtBZ\text{-}d10}}$	$\dfrac{k_{con}^{EtBZ}}{k_{con}^{EtBZ\text{-}d10}}$	$\dfrac{k_{ext}^{EtBZ}}{k_{ext}^{EtBZ\text{-}d10}}$	$\dfrac{k_{gen}^{EtBZ}}{k_{gen}^{EtBZ\text{-}d10}}$
233.16	17.2	1.0	2.7	1.0	4.0	25.7	25.7
273.16	6.3	1.1	1.9	1.0	2.9	8.7	9.4
298.16	4.3	1.3	1.7	1.1	2.5	5.2	6.2

T is the absolute temperature. The subscript "con" stands for the conventional kinetic model excluding tunneling effects, "ext" for the linear extrapolation from the experimental temperature range, and "gen" for the general theoretical model including tunneling effects.

It is noticed from Table 4.7 that the rate constants and KIEs predicted by the general model are larger than those predicted by the other two models for all three temperatures and the magnitude of the difference is temperature dependent. $k_{\mathrm{gen}}^{\mathrm{EtBZ}}/k_{\mathrm{con}}^{\mathrm{EtBZ}}$ stands out with a remarkable increment on the rate constant, a factor of 17.2 at 133.16 K. This observation signifies the contribution of nuclear tunneling to the chemical reaction mechanism of H atom abstractions. In the conventional picture, the portion of the reactants who possess energies higher than the reaction barrier can proceed to arrive at the product state and the rest with energies are below this threshold can not. Tunneling changed this paradigm by rendering probabilities to the populations with insufficient energies overcoming the barrier to penetrate it through and appear on the other side. This unconventional mechanism concerns the overall shape of the reaction barrier, unlike the conventional treatment, which cares only the barrier height. Thus nuclear tunneling as an alternate means to impel a chemical reaction deserves attention. $k_{\mathrm{gen}}^{\mathrm{EtBZ}}/k_{\mathrm{ext}}^{\mathrm{EtBZ}}$ represents a less pronounced deviation. It originates the non-linearity of the kinetic curves. More significantly, it is important to realized the primary source for the non-linearity of the kinetic curves is the nuclear tunneling. Thus, the uncertainty adhered to the linear extrapolation method is largely rooted in the nulcear tunneling phenomenon. As temperature goes higher, the discrepancy between the predicted rate constants based on the linear extrapolation method and the general theoretical model considering tunneling effects enlarges. This is understandable from the non-linearity nature of the kinetic curves as well. As the inference points move farther away from the experimental points, the true rate constants on the curve deviate more from the tangent drawn from the experimental range. Therefore, it is expected that the accuracy and reliability in predicting rate constants using the linear extrapolation model lessens as the temperature rises. The trend with temperature for the rate constant ratio between the general model and the conventional model

goes in the opposite direction, i.e. the rate constant ratio drops as the temperature ascents. This phenomenon is interpretable from the fact that tunneling effects minify as temperature increases. It is also important to notice that above analysis apply for both EtBZ and EtBZ-d10; however, the rate constants ratios are much larger for EtBZ than EtBZ-d10 across all temperatures. The rationale for it is the mass effect on nuclear tunneling, viz. the nuclear tunneling probability wanes as the tunneling nucleus becomes heavier. D, weighing twice as much as its isotope H, represents one of the most dramatic case for observing the tunneling probability decline among all the elements across the periodic table. Owing to the subaltern tunneling probability of D, its curvature of the kinetic curve is less protrudent compared to H and that leads to that the errors in the rate constants prediction using the conventional model and the linear extrapolation abate measurably. Consequently, the rate constant ratios for D are more narrowly distributed among the three models. It is important to point out that the reduced rate constant ratio between the general model and the conventional model did not settle at one indicates that tunneling phenomenon did not vanish on D.

The KIEs shows a negative correlation with temperature for all three models due to two reasons, zero point energy and nuclear tunneling. The KIE based on the conventional model reflects the pure zero point contribution to the rate constant difference and its temperature dependent feature. As seen in the column 6 of Table 4.7, the quotient of KIE at 233.16 K and 298.16 K yields a factor of 1.6. On the other hand, the quotient of KIE for the same two temperatures based on the general model (column 8) gives a factor of 4.1, which is a combinatorial result of both zero point energy and nuclear tunneling. From the fact that 4.1 is much larger than 1.6, one can tell the temperature dependence of the nuclear tunneling effect works in the same direction as the zero point energy, i.e. they both shrink with the temperature

ascent. Therefore, the nuclear tunneling effect dominates the contribution to KIE and rate constant propulsion and this stresses its position in gaining more accurate description of the kinetic process of a chemical reaction and better understanding of reaction mechanisms.

4.6   Conclusions

In the study of $[Fe^{V}(O)(B^{*})]^{-1}$ mediated C-H bond activation of EtBZ reaction, I analyzed the kinetic isotope effects of this process based on a nuclear tunneling corrected transition state theory.

Nuclear tunneling effects arc the kinetic curves to such a pronounced level that failed the conventional linear extrapolation approach in obtaining thermodynamic quantities (activation enthalpy and entropy). Insistence on applying the linear extrapolation approach in the presence of nuclear tunneling gave rise to a puzzling observation of the negative intercept difference between the tangents of the kinetic curves for EtBZ and EtBZ-d10. It was proved in the text that the intercept difference between naturally predominant isotope and its heavier counterparts as hydrogen and deuterium, the intercept difference (Int(H)-Int(D)) should always bear a positive sign for any temperature. Thus, a negative sign of (Int(H)-Int(D)) is a temperature independent indicator for quantum mechanical effects such as nuclear tunneling.

By introducing a nuclear tunneling factor into the classical rate constant equation and combing thermodynamic properties derived from DFT calculation with experimental kinetic information, a theoretical model was constructed with the capability of predicting rate constants outside the experimental temperature range. Based on this model, nuclear tunneling effect exhibited a boost of the reaction rate by 17.2 times at 233.16 K and about 4.3 time at room temperature. This signifies the mechanistic

role of nuclear tunneling in $Fe^V(O)$ mediated C-H bond activations and suggests more detailed investigations.

4.7 References

[1] V. I. Goldanskii. Chemical Reactions at Very Low Temperatures. *Annu. Rev. Phys. Chem.* **1976**, *27*, 85–126.

[2] R. Langen, I. J. Chang, J. P. Germanas, J. H. Richards, J. R. Winkler, H. B. Gray. Electron tunneling in proteins: coupling through a beta strand. *Science* **1995**, *268*, 1733–5.

[3] H. B. Gray, J. R. Winkler. Electron tunneling through proteins. *Q. Rev. Biophys.* **2003**, *36*, 341–372.

[4] C. C. Moser, J. M. Keske, K. Warncke, R. S. Farid, P. L. Dutton. Nature of biological electron transfer. *Nature* **1992**, *355*, 796–802.

[5] C. C. Page, C. C. Moser, X. Chen, P. L. Dutton. Natural engineering principles of electron tunnelling in biological oxidation-reduction. *Nature* **1999**, *402*, 47–52.

[6] E. F. Caldin. Tunneling in proton-transfer reactions in solution. *Chem. Rev.* **1969**.

[7] E. F. Caldin, S. Mateo. Kinetic isotope effects and tunnelling corrections in the proton-transfer reactions between 4-nitrophenylnitromethane and some tertiary amines in aprotic solvents. *J. Chem. Soc., Faraday Trans. 1* **1976**, *72*, 112.

[8] G. Brunton, D. Griller, L. R. C. Barclay, K. U. Ingold. Kinetic applications of electron paramagnetic resonance spectroscopy. 26. Quantum-mechanical tunneling in the isomerization of sterically hindered aryl radicals. *J. Am. Chem. Soc.* **1976**, *98*, 6803–6811.

[9] R. J. Le Roy, E. D. Sprague, F. Williams. Quantum mechanical tunneling in hydrogen atom abstraction for solid acetonitrile at 77-87.deg.K. *J. Phys. Chem.* **1972**, *76*, 546–551.

[10] C. Alhambra, J. C. Corchado, M. L. Sánchez, J. Gao, D. G. Truhlar. Quantum Dynamics of Hydride Transfer in Enzyme Catalysis. *J. Am. Chem. Soc.* **2000**, *122*, 8197–8203.

[11] Z. D. Nagel, J. P. Klinman. Update 1 of: Tunneling and dynamics in enzymatic hydride transfer. *Chem. Rev.* **2010**, *110*, PR41—-67.

[12] B. K. Carpenter. Heavy-atom tunneling as the dominant pathway in a solution-phase reaction? Bond shift in antiaromatic annulenes. *J. Am. Chem. Soc.* **1983**, *105*, 1700–1701.

[13] P. S. Zuev, R. S. Sheridan, T. V. Albu, D. G. Truhlar, D. a. Hrovat, W. T. Borden. Carbon tunneling from a single quantum state. *Science* **2003**, *299*, 867–870.

[14] P. Ball. Enzymes: by chance, or by design? *Nature* **2004**, *431*, 396–397.

[15] P. Ball. Physics of life: The dawn of quantum biology. *Nature* **2011**, *474*, 272–274.

[16] J. D. Bernal, R. H. Fowler. A Theory of Water and Ionic Solution, with Particular Reference to Hydrogen and Hydroxyl Ions. *J. Chem. Phys.* **1933**, *1*, 515.

[17] P. M. Kiefer, J. T. Hynes. Theoretical aspects of tunneling proton transfer reactions in a polar environment. *J. Phys. Org. Chem.* **2010**, *23*, 632–646.

[18] X.-Z. Li, B. Walker, A. Michaelides. Quantum nature of the hydrogen bond. *PNAS* **2011**, *108*, 6369–6373.

[19] M. Garcia-Viloca, C. Alhambra, D. G. Truhlar, J. Gao. Hydride transfer catalyzed by xylose isomerase: Mechanism and quantum effects. *J. Comput. Chem.* **2003**, *24*, 177–190.

[20] Y. Cha, C. J. Murray, J. P. Klinman. Hydrogen tunneling in enzyme reactions. *Science* **1989**, *243*, 1325–1330.

[21] a. Kohen, R. Cannio, S. Bartolucci, J. P. Klinman. Enzyme dynamics and hydrogen tunnelling in a thermophilic alcohol dehydrogenase. *Nature* **1999**, *399*, 496–499.

[22] S. R. Billeter, S. P. Webb, P. K. Agarwal, T. Iordanov, S. Hammes-Schiffer. Hydride transfer in liver alcohol dehydrogenase: quantum dynamics, kinetic isotope effects, and role of enzyme motion. *J. Am. Chem. Soc.* **2001**, *123*, 11262–11272.

[23] S. J. Benkovic, S. Hammes-Schiffer. A perspective on enzyme catalysis. *Science* **2003**, *301*, 1196–1202.

[24] L. Masgrau, A. Roujeinikova, L. O. Johannissen, P. Hothi, J. Basran, K. E. Ranaghan, A. J. Mulholland, M. J. Sutcliffe, N. S. Scrutton, D. Leys. Atomic description of an enzyme reaction dominated by proton tunneling. *Science* **2006**, *312*, 237–241.

[25] A. Dybala-Defratyka, P. Paneth, R. Banerjee, D. G. Truhlar. Coupling of hydrogenic tunneling to active-site motion in the hydrogen radical transfer catalyzed by a coenzyme B12-dependent mutase. *PNAS* **2007**, *104*, 10774–10779.

[26] S. Hay, M. J. Sutcliffe, N. S. Scrutton. Promoting motions in enzyme catalysis probed by pressure studies of kinetic isotope effects. *PNAS* **2007**, *104*, 507–512.

[27] H. Eyring. The theory of absolute reaction rates. *Trans. Farady Soc.* **1938**, *34*, 41.

[28] K. J. Laidler, M. C. King. Development of transition-state theory. *J. Phys. Chem.* **1983**, *87*, 2657–2664.

[29] R. P. Bell, *The Proton in Chemistry*, Cornell University Press, Ithaca, N.Y., USA, **1959**.

[30] V. S. Jr, M. Smith. The Arrhenius Parameters of the Deuterium Isotope Rate Effect in a Base-promoted Elimination Reaction1: Evidence for Proton Tunnelling. *J. Am. Chem. Soc.* **1961**, *211*, 593–598.

[31] J. C. Nesheim, J. D. Lipscomb. Large kinetic isotope effects in methane oxidation catalyzed by methane monooxygenase: evidence for C-H bond cleavage in a reaction cycle intermediate. *Biochemistry* **1996**, *35*, 10240–10247.

[32] M. J. Knapp, K. Rickert, J. P. Klinman. Temperature-dependent isotope effects in soybean lipoxygenase-1: correlating hydrogen tunneling with protein dynamics. *J. Am. Chem. Soc.* **2002**, *124*, 3865–3874.

[33] J. Kraut. How do enzymes work? *Science* **1988**, *242*, 533–540.

[34] D. G. Truhlar, J. Gao, C. Alhambra, M. Garcia-Viloca, J. Corchado, M. L. Sánchez, J. Villà. The incorporation of quantum effects in enzyme kinetics modeling. *Acc. Chem. Res.* **2002**, *35*, 341–349.

[35] E. Wigner. Calculation of the Rate of Elementary Association Reactions. *J. Chem. Phys.* **1937**, *5*, 720.

[36] J. Horiuti. On the Statistical Mechanical Treatment of the Absolute Rate of Chemical Reaction. *Bull. Chem. Soc. Jpn.* **1938**, *13*, 210–216.

[37] J. C. Keck. Variational Theory of Chemical Reaction Rates Applied to Three-Body Recombinations. *J. Chem. Phys.* **1960**, *32*, 1035.

[38] C. Alhambra, J. Corchado, M. L. Sánchez, M. Garcia-Viloca, J. Gao, D. G. Truhlar. Canonical Variational Theory for Enzyme Kinetics with the Protein Mean Force and Multidimensional Quantum Mechanical Tunneling Dynamics. Theory and Application to Liver Alcohol Dehydrogenase. *J. Phys. Chem. B* **2001**, *105*, 11326–11340.

[39] M. Garcia-Viloca, J. Gao, M. Karplus, D. Truhlar. How enzymes work: analysis by modern rate theory and computer simulations. *Science* **2004**, *303*, 186–195.

[40] B. J. Berne, D. Thirumalai. On the Simulation of Quantum Systems: Path Integral Methods. *Annu. Rev. Phys. Chem.* **1986**, *37*, 401–424.

[41] G. a. Voth. Feynman path integral formulation of quantum mechanical transition-state theory. *J. Phys. Chem.* **1993**, *97*, 8365–8377.

[42] G. a. Voth, D. Chandler, W. H. Miller. Rigorous formulation of quantum transition state theory and its dynamical corrections. *J. Chem. Phys.* **1989**, *91*, 7749.

[43] E. Geva, Q. Shi, G. a. Voth. Quantum-mechanical reaction rate constants from centroid molecular dynamics simulations. *J. Chem. Phys.* **2001**, *115*, 9209.

[44] J. K. Hwang, A. Warshel. A quantized classical path approach for calculations of quantum mechanical rate constants. *J. Phys. Chem.* **1993**, *97*, 10053–10058.

[45] J. Hwang, A. Warshel. How important are quantum mechanical nuclear motions in enzyme catalysis? *J. Am. Chem. Soc.* **1996**, *7863*, 11745–11751.

[46] S. R. Billeter, S. P. Webb, T. Iordanov, P. K. Agarwal, S. Hammes-Schiffer. Hybrid approach for including electronic and nuclear quantum effects in molecular dynamics simulations of hydrogen transfer reactions in enzymes. *J. Chem. Phys.* **2001**, *114*, 6925.

[47] Q. Wang, S. Hammes-Schiffer. Hybrid quantum/classical path integral approach for simulation of hydrogen transfer reactions in enzymes. *J. Chem. Phys.* **2006**, *125*, 184102.

[48] R. P. Bell. Quantum Mechanical Effects in Reactions Involving Hydrogen. *Proc. R. Soc. A* **1935**, *148*, 241–250.

[49] M. J. Frisch, G. W. Trucks, H. B. Schlegel, G. E. Scuseria, M. A. Robb, J. R. Cheeseman, G. Scalmani, V. Barone, B. Mennucci, G. A. Petersson, H. Nakatsuji, M. Caricato, X. Li, H. P. Hratchian, A. F. Izmaylov, J. Bloino, G. Zheng, J. L. Sonnenberg, M. Hada, M. Ehara, K. Toyota, R. Fukuda, J. Hasegawa, M. Ishida, T. Nakajima, Y. Honda, O. Kitao, H. Nakai, T. Vreven, J. A. Montgomery, J. E. Peralta, F. Ogliaro, M. Bearpark, J. J. Heyd, E. Brothers, K. N. Kudin, V. N. Staroverov, R. Kobayashi, J. Normand, K. Raghavachari, A. Rendell, J. C. Burant, S. S. Iyengar, J. Tomasi, M. Cossi, N. Rega, J. M. Millam, M. Klene, J. E. Knox, J. B. Cross, V. Bakken, C. Adamo, J. Jaramillo, R. Gomperts, R. E. Stratmann, O. Yazyev, A. J. Austin, R. Cammi, C. Pomelli, J. W. Ochterski, R. L. Martin, K. Morokuma, V. G. Zakrzewski, G. A. Voth, P. Salvador, J. J. Dannenberg, S. Dapprich, A. D. Daniels, Farkas, J. B. Foresman, J. V. Ortiz, J. Cioslowski, D. J. Fox, *Gaussian 09, Revision B.01*, **2009**.

[50] F. Tiago de Oliveira, A. Chanda, D. Banerjee, X. Shan, S. Mondal, L. Que, E. L. Bominaar, E. Münck, T. J. Collins. Chemical and spectroscopic evidence for an FeV-oxo complex. *Science* **2007**, *315*, 835–8.

[51] A. D. Becke. Density-functional thermochemistry. III. The role of exact exchange. *J. Chem. Phys.* **1993**, *98*, 3–7.

[52] A. D. Becke. Density-functional exchange-energy approximation with correct asymptotic behavior. *Phys. Rev. A* **1988**, *38*, 3098–3100.

[53] C. Lee, W. Yang, R. G. Parr. Development of the Colle-Salvetti correlation-energy formula into a functional of the electron density. *Phys. Rev. B* **1988**, *37*, 785–789.

[54] A. V. Marenich, C. J. Cramer, D. G. Truhlar. Universal Solvation Model Based on Solute Electron Density and on a Continuum Model of the Solvent Defined by the Bulk Dielectric Constant and Atomic Surface Tensions. *J. Phys. Chem. B* **2009**, *113*, 6378–6396.

[55] F. Claeyssens, J. N. Harvey, F. R. Manby, R. a. Mata, A. J. Mulholland, K. E. Ranaghan, M. Schütz, S. Thiel, W. Thiel, H.-J. Werner. High-accuracy computation of reaction barriers in enzymes. *Angew. Chem. Int. Ed.* **2006**, *45*, 6856–6859.

[56] G. Gopakumar, P. Belanzoni, E. J. Baerends. Hydroxylation catalysis by mononuclear and dinuclear iron oxo catalysts: a methane monooxygenase model system versus the Fenton reagent Fe(IV)O(H2O)5(2+). *Inorg. Chem.* **2012**, *51*, 63–75.

[57] Y. Zhao, D. G. Truhlar. The M06 suite of density functionals for main group thermochemistry, thermochemical kinetics, noncovalent interactions, excited states, and transition elements: two new functionals and systematic testing of four M06-class functionals and 12 other function. *Theor. Chem. Acc.* **2007**, *120*, 215–241.

4.8 Appendices

4.8.1 DFT Optimized Geometry of the Transition State Structure of Hydrogen Atom Abstraction from EtBZ by $[Fe^V(O)(B^*)]^{-1}$
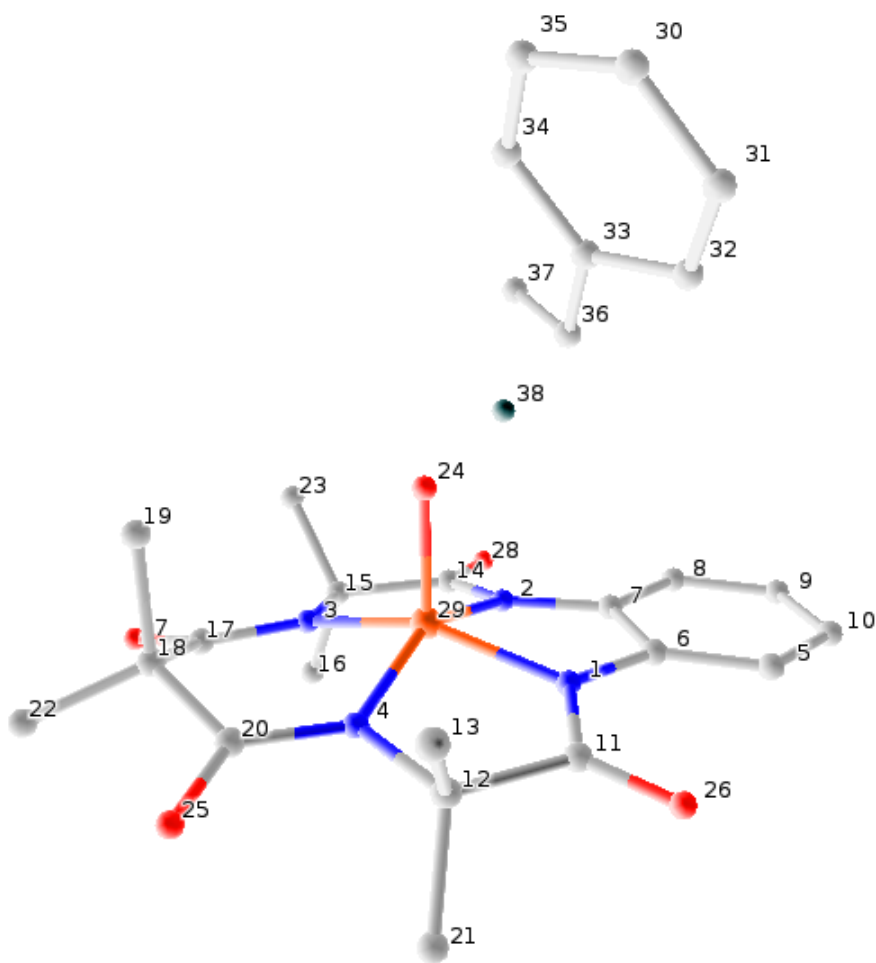
Figure 4.6: DFT calculation optimized transition state structure of H abstraction from EtBZ by $[Fe^V(O)(B^*)]^{-1}$. Hydrogen atoms excepted the one being transferred are omitted for clarity. Color coding : brown — Fe, red — O, blue — N, gray — C, cyan — H. Key interatomic distances : Fe29-O24 = 1.71 Å, O24-H38 = 1.34 Å, H38-C36 = 1.24 Å, Fe29-N1 = 1.89 Å, Fe29-N2 = 1.88 Å, Fe29-N3 = 1.90 Å, Fe29-N4 = 1.89 Å.

4.8.2 Thermodynamic Data from DFT Calulation Used in the Kinetic Analysis

Name SCF(Ha) ZPE(Ha) NegFreq(cm-1) H(Ha) G(Ha)

Temperature / / / (173K) (173K) (203K) (203K) (233K) (233K) (236K) (236K) (239K) (239K) (243K) (243K) (273K) (273K) (303K) (303K) (333K) (333K) (363K) (363K) (393K) (393K) (423K) (423K) (453K) (453K) (573K) (573K) (693K) (693K) (813K) (813K) (933K) (933K) (1233K) (1233K) (1533K) (1533K) (1833K) (1833K) (2133K) (2133K) (2433K) (2433K) (2733K) (2733K) (3030K) (3030K) (3033K) (3033K)

GS

EtBZ -310.885582442 0.157155 NA 0.159099 0.147323 0.159445 0.145740 0.159815 0.1565 0.162711 0.133190 0.162824 0.132815 0.162976 0.132311 0.164198 0.128457 0.165560 0.124461 0.167067 0.120323 0.168717 0.116042 0.170510 0.111620 0.172440 0.107055 0.174503 0.102349 0.183953 0.082129 0.195030 0.059749 0.207409 0.035332 0.220843 0.009004 0.257916 -0.064391 0.298491 -0.147323 0.341357 -0.238471 0.385769 -0.336795 0.431258 -0.441461 0.477519 -0.551799 0.523880 -0.666078 0.524350 -0.667257

EtBZd1 -310.885582442 0.153796 NA 0.155750 0.143937 0.156099 0.142349 0.156472 0.0126 0.159411 0.129750 0.159526 0.129372 0.159682 0.128867 0.160927 0.124992 0.162317 0.120973 0.163854 0.116810 0.165538 0.112501 0.167366 0.108047 0.169334 0.103449 0.171435 0.098706 0.181047 0.078313 0.192292 0.055727 0.204836 0.031073 0.218431 0.004485 0.255860 -0.069641 0.296724 -0.153384 0.339818 -0.245394 0.384412 -0.344613 0.430047 -0.450199 0.476427 -0.561472 0.522886 -0.676689 0.523358 -0.677877

EtBZd2 -310.885582442 0.150426 NA 0.152388 0.140543 0.152739 0.138951 0.153116 0.1685 0.156095 0.126307 0.156212 0.125928 0.156370 0.125420 0.157639 0.121528 0.159056 0.117488 0.160625 0.113301 0.162343 0.108966 0.164208 0.104482 0.166215 0.099851 0.168356 0.095073 0.178136 0.074513 0.189552 0.051724 0.202265 0.026838 0.216021 -0.000007 0.253809 -0.074857 0.294962 -0.159403 0.338285 -0.252269 0.383060 -0.352377 0.428840 -0.458874 0.475340 -0.571075 0.521896 -0.687223 0.522369 -0.688420

EtBZd8 -310.885582442 0.131060 NA 0.133100 0.121022 0.133475 0.119398 0.133879 0.1809 0.137172 0.106419 0.137303 0.106028 0.137481 0.105503 0.138911 0.101475 0.140510 0.097280 0.142274 0.092919 0.144198 0.088392 0.146275 0.083700 0.148498 0.078843 0.150859 0.073824 0.161525 0.052163 0.173829 0.028085 0.187422 0.001756 0.202034 -0.026661 0.241778 -0.105877 0.284552 -0.195232 0.329182 -0.293196 0.375008 -0.398597 0.421642 -0.510521 0.468842 -0.628246 0.515976 -0.749931 0.516454 -0.751185

EtBZd9 -310.885582442 0.127707 NA 0.129756 0.117647 0.130135 0.116019 0.130543 0.1386 0.133881 0.102994 0.134015 0.102601 0.134196 0.102074 0.135650 0.098026 0.137276 0.093810 0.139071 0.089424 0.141029 0.084869 0.143142 0.080146 0.145403 0.075256 0.147802 0.070200 0.158630 0.048370 0.171101 0.024087 0.184859 -0.002475 0.199631 -0.031149 0.239730 -0.111089 0.282792 -0.201248 0.327649 -0.300067 0.373656 -0.406356 0.420435 -0.519192 0.467755 -0.637844 0.514986 -0.760459 0.515465

-0.761722

EtBZd10 -310.885582442 0.124321 NA 0.126378 0.114238 0.126760 0.112604 0.127171 0.1929 0.130550 0.099536 0.130686 0.099141 0.130869 0.098612 0.132347 0.094546 0.134001 0.090308 0.135827 0.085899 0.137820 0.081317 0.139970 0.076564 0.142270 0.071641 0.144709 0.066550 0.155707 0.044551 0.168350 0.020065 0.182277 -0.006732 0.197212 -0.035665 0.237671 -0.116333 0.281022 -0.207301 0.326109 -0.306980 0.372299 -0.414163 0.419224 -0.527916 0.466663 -0.647501 0.513993 -0.771053 0.514472 -0.772325

B*-Fe(V)(ms=1/2)-O -2596.30534746 0.397241 NA 0.401705 0.383387 410838 0.366181 0.414847 0.359310 0.415273 0.358593 0.415704 0.357870 0.416285 0.356898 0.420895 0.349302 0.425945 0.341176 0.431427 0.332528 0.437327 0.323368 0.443630 0.313703 0.450318 0.303542 0.457373 0.292895 0.488859 0.245605 0.524697 0.191228 0.563947 0.130324 0.605912 0.063409 0.719603 -0.127293 0.841936 -0.346988 0.969830 -0.591326 1.101441 -0.856995 1.235625 -1.141420 1.371651 -1.442546 1.507652 -1.755476 1.509031 -1.758708

EtBZ-B*-Fe(V)(ms=1/2)-O -2907.19195868 0.554914 NA 0.561747 0.536636 0.5683 0.513123 0.579122 0.503788 0.579678 0.502816 0.580239 0.501836 0.580997 0.500518 0.587013 0.490238 0.593610 0.479265 0.600781 0.467611 0.608516 0.455286 0.616796 0.442298 0.625599 0.428659 0.634901 0.414378 0.676579 0.351042 0.724241 0.278305 0.776616 0.196872 0.832766 0.107406 0.985412 -0.147649 1.150207 -0.441695 1.322857 -0.768973 1.500772 -1.125069 1.682340 -1.506530 1.866522 -1.910598 2.050761 -2.330691 2.052630 -2.335030

EtBZd1-B*-Fe(V)(ms=1/2)-O -2907.19195868 0.551531 NA 0.558375 0.533234 0.5542 0.509690 0.575798 0.500342 0.576356 0.499367 0.576920 0.498386 0.577680 0.497066 0.583720 0.486768 0.590344 0.475774 0.597546 0.464096 0.605314 0.451744 0.613630 0.438727 0.622471 0.425056 0.631812 0.410739 0.673653 0.347239 0.721483 0.274301 0.774026 0.192638 0.830337 0.102919 0.983342 -0.152852 1.148427 -0.447695 1.321308 -0.775820 1.499406 -1.132798 1.681120 -1.515164 1.865423 -1.920154 2.049761 -2.341172 2.051631 -2.345520

EtBZd2-B*-Fe(V)(ms=1/2)-O -2907.19195868 0.548155 NA 0.555009 0.529840 0.5502 0.506267 0.572475 0.496905 0.573035 0.495929 0.573601 0.494946 0.574365 0.493624 0.580427 0.483309 0.587079 0.472296 0.594313 0.460595 0.602116 0.448217 0.610469 0.435172 0.619349 0.421468 0.628730 0.407117 0.670740 0.343454 0.718742 0.270316 0.771454 0.188425 0.827927 0.098452 0.981291 -0.158034 1.146665 -0.453673 1.319774 -0.782645 1.498054 -1.140504 1.679914 -1.523773 1.864335 -1.929683 2.048771 -2.351624 2.050642 -2.355981

EtBZd8-B*-Fe(V)(ms=1/2)-O -2907.19195868 0.528782 NA 0.535725 0.510338 0.5340 0.486533 0.553541 0.477063 0.554115 0.476075 0.554695 0.475080 0.555479 0.473742 0.561702 0.463295 0.568534 0.452131 0.575964 0.440261 0.583972 0.427696 0.592537 0.414445 0.601633 0.400521 0.611234 0.385933 0.654130 0.321185 0.703020 0.246776 0.756611 0.163458 0.813941 0.071930 0.969260 -0.188879 1.136256 -0.489285 1.310672 -0.823313 1.490003 -1.186422 1.672716 -1.575077 1.857838 -1.986468 2.042851 -2.413904 2.044727 -2.418317

EtBZd9-B*-Fe(V)(ms=1/2)-O -2907.19195868 0.525395 NA 0.532348 0.506934 0.5395 0.483099 0.550214 0.473615 0.550790 0.472626 0.551373 0.471629 0.552159 0.470289 0.558406 0.459824 0.565266 0.448639 0.572727 0.436745 0.580769 0.424153 0.589370 0.410873 0.598504 0.396917 0.608143 0.382294 0.651203 0.317381 0.700262 0.242771

0.754020 0.159225 0.811511 0.067442 0.967190 -0.194083 1.134477 -0.495285 1.309123 -0.830161 1.488636 -1.194152 1.671497 -1.583712 1.856739 -1.996025 2.041851 -2.424385 2.043728 -2.428808

EtBZd10-B*-Fe(V)(ms=1/2)-O -2907.19195868 0.522014 NA 0.528977 0.503537 0.5353 0.479674 0.546889 0.470176 0.547467 0.469185 0.548052 0.468187 0.548841 0.466845 0.555111 0.456363 0.562000 0.445159 0.569492 0.433242 0.577569 0.420625 0.586207 0.407316 0.595380 0.393328 0.605060 0.378671 0.648288 0.313594 0.697519 0.238785 0.751447 0.155010 0.809100 0.062974 0.965139 -0.199268 1.132714 -0.501266 1.307589 -0.836990 1.487284 -1.201862 1.670290 -1.592326 1.855651 -2.005559 2.040861 -2.434843 2.042739 -2.439275

TS

EtBZ-B*-Fe(V)(ms=1/2)-O -2907.17564783 0.548426 -1005.2162 0.554759 0.8228 0.566692 0.510259 0.571885 0.501568 0.572437 0.500659 0.572995 0.499744 0.573747 0.498513 0.579729 0.488882 0.586300 0.478562 0.593452 0.467562 0.601172 0.455893 0.609442 0.443563 0.618240 0.430581 0.627540 0.416958 0.669224 0.356255 0.716896 0.286147 0.769265 0.207344 0.825382 0.120510 0.977809 -0.127931 1.142213 -0.415290 1.314341 -0.735790 1.491639 -1.085015 1.672521 -1.459513 1.855966 -1.856530 2.039439 -2.269562 2.041300 -2.273829

EtBZd1-B*-Fe(V)(ms=1/2)-O -2907.17564783 0.546724 -795.4556 0.553064 0.6509 0.565030 0.508533 0.570246 0.499830 0.570801 0.498921 0.571361 0.498004 0.572118 0.496771 0.578132 0.487124 0.584740 0.476784 0.591933 0.465761 0.599697 0.454065 0.608012 0.441704 0.616855 0.428688 0.626200 0.415027 0.668052 0.354146 0.715867 0.283828 0.768354 0.204791 0.824568 0.117708 0.977170 -0.131399 1.141690 -0.419461 1.313900 -0.740683 1.491258 -1.090642 1.672185 -1.465880 1.855666 -1.863644 2.039168 -2.277417 2.041029 -2.281692

EtBZd2-B*-Fe(V)(ms=1/2)-O -2907.17564783 0.543376 -780.1757 0.549724 0.3139 0.561720 0.505153 0.566956 0.496439 0.567513 0.495528 0.568076 0.494610 0.568836 0.493375 0.574876 0.483713 0.581514 0.473355 0.588741 0.462310 0.596542 0.450588 0.604896 0.438199 0.613779 0.425152 0.623164 0.411457 0.665184 0.350415 0.713165 0.279899 0.765815 0.200637 0.822185 0.113304 0.975136 -0.136506 1.139939 -0.425348 1.312373 -0.747400 1.489910 -1.098223 1.670982 -1.474348 1.854581 -1.873015 2.038180 -2.287694 2.040042 -2.291977

EtBZd8-B*-Fe(V)(ms=1/2)-O -2907.17564783 0.522203 -1004.3398 0.528661 0.1671 0.540888 0.483585 0.546245 0.474753 0.546815 0.473830 0.547391 0.472899 0.548170 0.471647 0.554360 0.461845 0.561167 0.451329 0.568577 0.440110 0.576572 0.428196 0.585127 0.415599 0.594218 0.402328 0.603816 0.388394 0.646716 0.326262 0.695613 0.254467 0.749196 0.173764 0.806491 0.084854 0.961592 -0.169379 1.128200 -0.463134 1.302098 -0.790424 1.480817 -1.146701 1.662848 -1.528432 1.847237 -1.932812 2.031487 -2.353226 2.033356 -2.357568

EtBZd9-B*-Fe(V)(ms=1/2)-O -2907.17564783 0.518852 -980.0863 0.525319 0.8300 0.537577 0.480204 0.542953 0.471361 0.543526 0.470436 0.544105 0.469504 0.544886 0.468250 0.551103 0.458432 0.557940 0.447898 0.565383 0.436657 0.573413 0.424719 0.582007 0.412094 0.591136 0.398792 0.600774 0.384825 0.643838 0.322533 0.692902 0.250543 0.746647 0.169617 0.804098 0.080459 0.959549 -0.174470 1.126441 -0.469001 1.300565 -0.797116 1.479463 -1.154252 1.661640 -1.536865 1.846148 -1.942142 2.030496 -2.363457 2.032365 -2.367809

EtBZd10-B*-Fe(V)(ms=1/2)-O -2907.17564783 0.517149 -779.5687 0.523622 0.6580 0.535912 0.478477 0.541312 0.469623 0.541888 0.468697 0.542469 0.467764 0.543255 0.466508 0.549504 0.456675 0.556379 0.446121 0.563865 0.434856 0.571940 0.422891 0.580579 0.410235 0.589755 0.396898 0.599439 0.382893 0.642674 0.320422 0.691882 0.248219 0.745746 0.167057 0.803294 0.077647 0.958919 -0.177955 1.125926 -0.473193 1.300130 -0.802036 1.479088 -1.159910 1.661309 -1.543269 1.845853 -1.949298 2.030229 -2.371360 2.032098 -2.375719

Int

EtBZ(ms=-1/2)-B*-Fe(IV)(ms=1)-O -2907.19599090 0.550804 NA 0.557520.519060 0.569903 0.510694 0.575260 0.501581 0.575829 0.500629 0.576403 0.499670 0.577178 0.498381 0.583328 0.488300 0.590066 0.477512 0.597383 0.466028 0.605264 0.453860 0.613689 0.441017 0.622635 0.427512 0.632076 0.413354 0.674256 0.350433 0.722328 0.278012 0.775029 0.196832 0.831434 0.107576 0.984504 -0.147064 1.149542 -0.440777 1.322341 -0.767760 1.500354 -1.123581 1.681989 -1.504779 1.866220 -1.908591 2.050496 -2.328436 2.052365 -2.332772

EtBZd1(ms=-1/2)-B*-Fe(IV)(ms=1)-O -2907.19599090 0.547862 NA 0.554620.516043 0.567087 0.507645 0.572472 0.498495 0.573043 0.497539 0.573621 0.496577 0.574400 0.495282 0.580578 0.485160 0.587344 0.474327 0.594688 0.462796 0.602594 0.450578 0.611044 0.437685 0.620014 0.424126 0.629477 0.409913 0.671741 0.346759 0.719896 0.274087 0.772685 0.192642 0.829185 0.103106 0.982502 -0.152284 1.147770 -0.446807 1.320769 -0.774641 1.498949 -1.131345 1.680724 -1.513447 1.865073 -1.918179 2.049447 -2.338946 2.051317 -2.343292

EtBZd2(ms=-1/2)-B*-Fe(IV)(ms=1)-O -2907.19599090 0.544715 NA 0.551490.512856 0.564011 0.504440 0.569423 0.495270 0.569997 0.494312 0.570577 0.493347 0.571360 0.492049 0.577568 0.481902 0.584366 0.471040 0.591743 0.459477 0.599684 0.447223 0.608168 0.434291 0.617172 0.420692 0.626671 0.406436 0.669073 0.343087 0.717367 0.270192 0.770296 0.188498 0.826931 0.098694 0.980560 -0.157436 1.146089 -0.452771 1.319298 -0.781464 1.497648 -1.139056 1.679561 -1.522069 1.864022 -1.927728 2.048490 -2.349424 2.050361 -2.353779

EtBZd8(ms=-1/2)-B*-Fe(IV)(ms=1)-O -2907.19599090 0.524791 NA 0.531630.492651 0.544277 0.484161 0.549792 0.474902 0.550378 0.473935 0.550971 0.472960 0.551771 0.471648 0.558125 0.461392 0.565096 0.450404 0.572667 0.438697 0.580819 0.426280 0.589526 0.413167 0.598762 0.399370 0.608499 0.384899 0.651886 0.320538 0.701178 0.246420 0.755087 0.163332 0.812666 0.071991 0.968397 -0.188459 1.135628 -0.488583 1.310187 -0.822368 1.489610 -1.185253 1.672387 -1.573694 1.857555 -1.984878 2.042602 -2.412115 2.044479 -2.416526
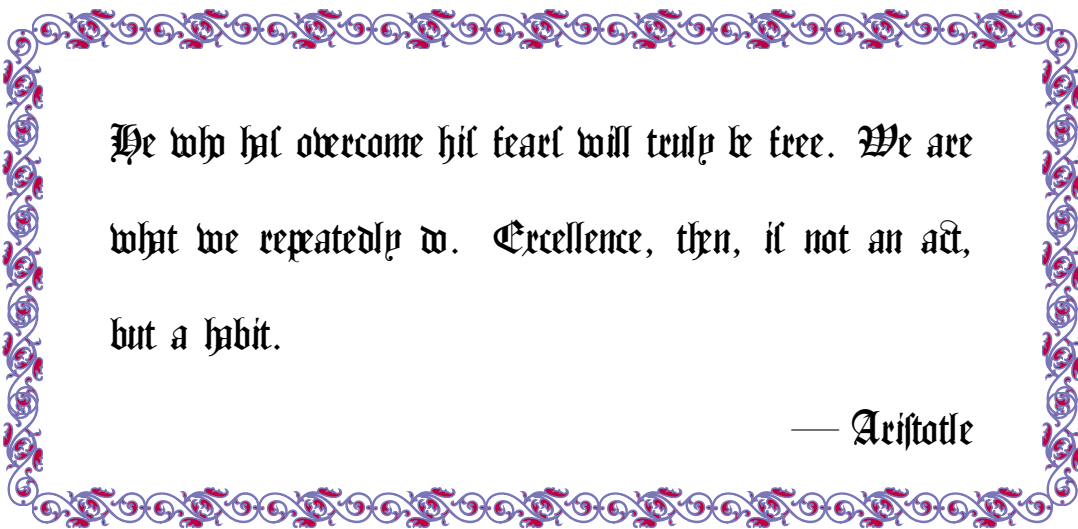
EtBZd9(ms=-1/2)-B*-Fe(IV)(ms=1)-O -2907.19599090 0.521849 NA 0.528730.489634 0.541460 0.481111 0.547004 0.471816 0.547593 0.470845 0.548189 0.469866 0.548992 0.468549 0.555375 0.458252 0.562373 0.447220 0.569972 0.435465 0.578149 0.422999 0.586881 0.409835 0.596141 0.395984 0.605900 0.381458 0.649371 0.316863 0.698746 0.242495 0.752744 0.159141 0.810417 0.067521 0.966395 -0.193678 1.133856 -0.494613 1.308614 -0.829250 1.488205 -1.193016 1.671122 -1.582362 1.856408 -1.994466 2.041553 -2.422625 2.043430 -2.427045

EtBZd10(ms=-1/2)-B*-Fe(IV)(ms=1)-O -2907.19599090 0.518699 NA 0.525600.486445 0.538382 0.477905 0.543952 0.468590 0.544544 0.467616 0.545142 0.466635 0.545950 0.465315 0.552363 0.454993 0.559393 0.443932 0.567025 0.432145 0.575237 0.419644 0.584004 0.406441 0.593298 0.392549 0.603092 0.377981 0.646703 0.313192

0.696217 0.238600 0.750354 0.154998 0.808163 0.063109 0.964453 -0.198831 1.132175 -0.500576 1.307144 -0.836071 1.486904 -1.200727 1.669959 -1.590984 1.855357 -2.004014 2.040596 -2.433102 2.042474 -2.437532

Chapter 5

Fe-TAML Mirroring Cytochrome P450 in Degrading Sertraline — the Active Ingredient in Zoloft®

> He who has overcome his fears will truly be free. We are what we repeatedly do. Excellence, then, is not an act, but a habit.
>
> — Aristotle

5.1 Abstract

Iron TAML activators (oxidation catalysts based upon tetraamido macrocyclic ligands) at nanomolar concentrations in water activate hydrogen peroxide to rapidly degrade sertraline, the persistent, active pharmaceutical ingredient (API) in the widely used drug, Zoloft. While all the API is readily consumed, degradation slows significantly at one intermediate, sertraline ketone. The process occurs from neutral to basic pH. The pathway has been characterized through four early intermediates which reflect the metabolism of sertraline, providing further evidence that TAML activator/peroxide reactive intermediates mimic those of cytochrome P450 enzymes. TAML catalysts have been designed to exhibit considerable variability in reactivity and this provides an excellent tool for observing degradation intermediates of widely differing stabilities. Two elusive, hydrolytically sensitive intermediates and likely human metabolites, sertraline imine and N-desmethylsertraline imine, could be identified only by using a fast-acting catalyst. The more stable intermediates and known human metabolites, desmethylsertraline and sertraline ketone, were most easily detected and studied using a slow-acting catalyst. The resistance of sertraline ketone to aggressive TAML activator/peroxide treatment marks it as likely to be environmentally persistent and signals that its environmental effects are important components of the full implications of sertraline use.

5.2 Introduction

In many countries, antidepressants are the most frequently prescribed drugs and selective serotonin reuptake inhibitors (SSRIs) lead the category.[1] Sertraline (SER, Scheme 5.2) is the API in Zoloft, an important SSRI. As with many APIs, SER is highly bioactive and resistant to degradation. However, these advantageous properties for

treating human maladies can lead to adverse effects on aquatic organisms when even trace quantities are released to water.[2–6] This presents intriguing research challenges for green chemists who aim to reduce or eliminate hazardous substances.[7] Treatment with TAML activators (Scheme 5.1) and peroxide has been shown to deeply oxidize and significantly mineralize recalcitrant water contaminants such as pentachlorophenol and trichlorophenol[8] and toxic thiophosphate pesticide hydrolysates[9] among other things.[10] The approach is also known to effectively eliminate estrogenicity from water contaminated with natural and synthetic estrogens.[11] However, TAML activator/peroxide treatment does not decompose all oxidizable substrates rapidly and we are working to understand what controls the reactivity with the goal of extending the already wide generality through iterative catalyst design.[12,13]

In this work, we present an example of a degradation process that commences rapidly only to slow dramatically long before mineralization is reached. We show that SER degradation chemistry starts off with the API being degraded rapidly and completely. The process moves from SER quickly through several species, but then slows significantly at one intermediate, sertraline ketone (SEK, Scheme 5.2). The process does not stop completely at SEK, but progress from that stage toward the theoretical end-point of mineralization is very slow and remains to be further defined. Additional recalcitrant intermediates may arise as SEK is slowly oxidized.

This near stalling of the process at SEK highlights a significant environmental issue with drugs while pointing to a new potential use for TAML activators. Persistent API degradation intermediates raise in theory all the same questions about adverse impacts on biota that the parent APIs do, but usually little is known about the environmental occurence, fate and impacts of such species. Here for SER, we demonstrate that TAML activators with peroxide can be used to (i) degrade the parent API rapidly and completely in water, (ii) identify oxidative degradation intermediates, (iii) create
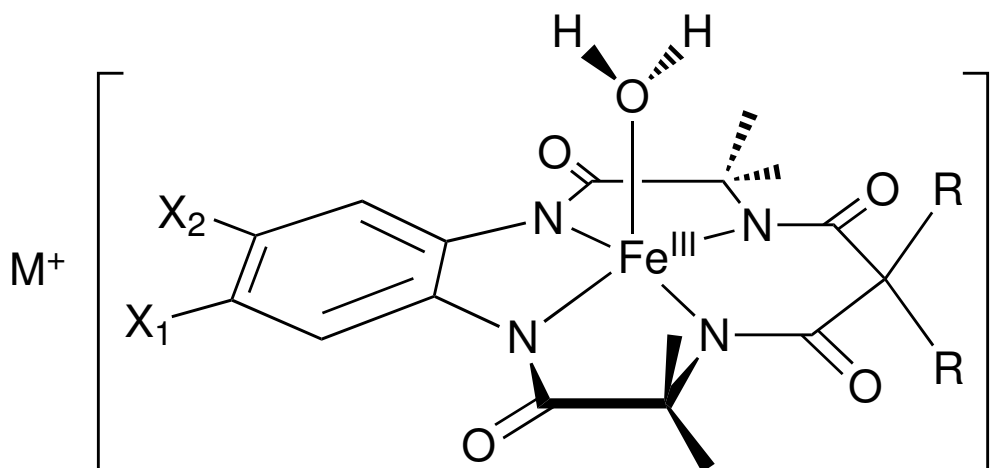
Scheme 5.1: Structures of TAML catalysts used: **1a**, $X_1 = X_2 = H$, R = Me, $M^+ =$ Na$^+$; **1b**, $X_1 = X_2 = $ Cl, R = F, $M^+ = $ Li$^+$; **1c**, $X_1 = $ NO$_2$, $X_2 = $ H, R = F, $M^+ = $ Li$^+$.

degradation conditions of differing aggressiveness to give, on the one hand, beneficial systems for detecting and studying fast-hydrolyzing intermediates and, on the other, propitious systems for following the chemistry of slow-degrading intermediates and, (iv) test easily for a degradation intermediate that is likely to be environmentally persistent and therefore worthy of detailed ecotoxicological studies. There is a positive implication for drug development. The TAML activator/peroxide degradation approach could be used to show whether or not an API or API candidate is likely to produce persistent degradation products. Additional APIs beyond SER are the subject of ongoing studies to explore the generality of the approach.

5.3 Experimental

5.3.1 Materials

Sertraline Hydrochloride ((1S,4S)-4-(3,4-dichloro-phenyl)-N-methyl-1,2,3,4-tetrahydronaphthalen-1-amine), SER, was purchased from Toronto Research Chemicals Inc. Sertraline imine

(N-((1E)-4-(3,4-dichlorophenyl)-3,4-dihydro-1(2H)naphthalenylidene)methanamine), SIM, was purchased from a rare chemical library at Sigma Aldrich. N-desmethylsertraline ((1S,4S)-4-(3,4-dichlorophenyl)-1,2,3,4-tetrahydronaphthalen-1-amine), DMS, and sertraline ketone (4-(3,4-dichloropenyl)-3,4-dihydronaphthalen-1(2H)-one), SEK, were synthesized according to published procedures.[14] Hydrogen peroxide 30% w/w) was purchased from Fisher Scientific. Formic acid, potassium hydroxide, sodium carbonate, sodium bicarbonate, monopotassium phosphate, dipotassium phosphate, HPLC grade water, methanol, and acetonitrile were obtained from commercial sources (Aldrich, Fisher, Acros and Fluka). The TAML activators were synthesized according to the published method.[15] The concentration of hydrogen peroxide stock solution was calibrated by UV-Vis spectroscopy using the molar absorption coefficient ($72.4~M^{-1}cm^{-1}$) at 230 nm.[16] The pH of the reactions was controlled with sodium carbonate/sodium bicarbonate (10^{-2} M) for pH 9.5 and pH 10.25 and monopotassium phosphate/dipotassium phosphate (10^{-2} M) for pH 8.25.

5.3.2 Instrumentation

A Waters 600E HPLC system equipped with a 2996 photodiode array detector and 717 autosampler was employed for quantitative analysis in the SER degradation process and to monitor the SIM hydrolysis process. Atmospheric pressure MS analysis was performed on a ThermoFisher LCQ 3D quadrupole ion trap equipped with electric spray ionization and atmospheric pressure chemical ionization (APCI) sources. The analyses were performed either through flow injection or hyphenated LC-MS methodologies, in which the above-mentioned HPLC was used. GC-MS analyses were performed on a Thermo DSQ MS coupled to a TRACE GC equipped with a programmed temperature vaporizing injector (PTV) and LEAP Combi PAL autosampler. Solid phase extraction (SPE) was performed using Waters Oasis HLB cartridges. Total

organic carbon (TOC) analyses were obtained from Analytical Laboratory Services, Inc. on solution samples prepared at Carnegie Mellon University.

5.3.3 Reactions

SER and DMS stock solutions were prepared in methanol. In a typical degradation reaction, the reagents were added in the following order into either HPLC or GC sample vials: buffer, SER or DMS, TAML catalyst **1**, and H_2O_2. The reaction mixture was homogenized using Pasteur pipettes and the medium was analyzed at various times by HPLC, LC–MS and GC–MS.

5.3.4 Total Organic Carbon (TOC) Analyses

TOC determinations were made on samples using catalyst **1c** with three different catalyst and peroxide concentrations. All stock solutions were prepared in 0.01 M phosphate buffer (pH 9.5). The phosphate buffer was prepared by dissolving KH_2PO_4 in HPLC grade water and adjusting the pH to 9.5 with concentrated KOH solution. Organic solvents were not used at any stage in the sample preparations for TOC analyses. SER stock solution (6.29×10^{-5} M) was prepared by dissolving setraline hydrochloride in the buffer solution and sonicating for 4 h. Three **1c** stock solutions (6×10^{-5} M, 1.2×10^{-4} M, 3×10^{-4} M) and three H_2O_2 stock solutions (0.4, 0.8, 2.0 M) were prepared and used as appropriate for the reactions; TOC-1, TOC-2 and TOC-3 respectively. Aliquots (0.1 mL) of stock solutions of **1c** and H_2O_2 were added according to the details explained in the footnote of Table 5.1 to each reaction vessel. The total reaction volume in all cases was 20 mL. The reactions were quenched after 24 h by adding HCl to reduce the pH to < 2. The samples were sent to ALS Environmental (over ice) for the TOC analyses.

Table 5.1: TOC Data for Setraline Degradation Reactions

Sample I.D.	TOC (ppm)	Description of Additives
SER Control	23.7	[SER] (5×10^{-5} M)
TOC-1 Control [a]	23.8	[SER] (5×10^{-5} M), [1c] (3.0×10^{-7} M)
TOC-1 [a]	21.1	[SER] (5×10^{-5} M), [1c] (3.0×10^{-7} M), [H$_2$O$_2$] (2.0×10^{-3} M)
TOC-2 Control [b]	25.5	[SER] (5×10^{-5} M), [1c] (6.0×10^{-7} M)
TOC-2 [b]	25.5	[SER] (5×10^{-5} M), [1c] (6.0×10^{-7} M), [H$_2$O$_2$] (4.0×10^{-3} M)
TOC-3 Control [c]	22.0	[SER] (5×10^{-5} M), [1c] (1.5×10^{-6} M)
TOC-3 [c]	23.9	[SER] (5×10^{-5} M), [1c] (1.5×10^{-6} M), [H$_2$O$_2$] (1.0×10^{-2} M)

[a] added at once
[b] added in 2 aliquots (each 50 μL) at 0 and 15 min
[c] added in 5 aliquots (each 20 μL) at 15 min intervals.

5.4 Results and Discussion

It is an important green chemistry challenge to be able to purify water of traces of bioactive organic contaminants, especially when low doses are known to alter the normal development of living things.[7] An ideal degradation system is almost certain to be based upon oxidation catalysis, since this is the approach of the natural world. Such a system would function efficiently under environmentally relevant conditions, i.e., at ambient temperature and pressure, in water, employing an oxidant that is used widely in biochemistry so that the products are more likely to be environmentally acceptable, and in a pH regime that is commonly found in natural waters.

Through the design of TAML activators, many of these criteria have been adequately achieved and research is being pursued to optimize the entire set. A critical criterion for green catalysts for water purification is the avoidance of endocrine disruptors, which can impair aquatic life. To begin to examine the many questions surrounding this, we have demonstrated that three TAML activators do not alter transcription mediated by mammalian thyroid, androgen, or estrogen hormone receptors, suggesting that these do not bind to the receptors and reducing concerns that the catalysts might have endocrine disrupting activity.[13] Further toxicity studies are ongoing with an emphasis on endocrine disruption assays. And TAML catalysts are not persistent in water, at least under operating conditions—the degradation rate behavior of a series of TAML catalysts has been determined.[17]

The catalytic cycles of TAML activators are well characterized,[12] although the level of discovered complexity suggests that many additional nuances remain to be revealed. In broad strokes, TAML activators are quite faithful peroxidase mimics, producing with peroxide high valent iron-oxo species[18,19] related to the reactive intermediates of CYP450[20–22] and peroxidase enzymes.[23–25] The TAML oxidants are by one and two electrons oxidized above the ferric state and include the first well-characterized iron(V)-oxo complex where both oxidation equivalents are localized on the iron, in contrast to the corresponding peroxidase and cytochrome P450 reactive intermediates where one equivalent is located on iron and the other is delocalized over the ligand system.[19] Thus, projecting from the enzymes, TAML activator driven oxidation catalysis, which is typically not wasteful of peroxide,[8,25] likely involves a combination of catalyst and substrate dependent atom transfer and electron transfer processes and is unlikely to be dominated by hydroxyl radical pathways. The intimate mechanistic details of how the reactive species in TAML activator catalytic cycles oxidise substrates are currently the subject of focused studies in our laboratory.

Because TAML reactive intermediates reflect those of cytochrome P450 enzymes, we considered it likely that TAML activator/H_2O_2 oxidations of SER would proceed through SER metabolites. The major human metabolites for SER are desmethylsertraline (Scheme 1, DMS) and SEK.[26–29] Additionally, sertraline imine (SIM, Scheme 1) has been identified as an animal metabolite.[26] As shown below, these three compounds are precisely the early intermediates that we have identified. Furthermore, evidence is presented that an hydrolytically sensitive intermediate forms fleetingly, namely desmethylsertraline imine (Scheme 5.2, DMSI), and this compound is also a likely metabolite indicating that TAML activator/H_2O_2 processes might provide a good approach for observing likely metabolites that are too reactive to accumulate in biological media.

5.4.1   pH and Catalyst Dependencies of Degradation Processes

For water treatment processes, the pH is a critical parameter. Process waters being released to the environment should have a pH near that of the receiving water. The rates of TAML activator/H_2O_2 oxidations are strongly pH dependent in a manner that has been rationalized mechanistically.[12] The rate determining step is often the formation of the catalytically reactive intermediate(s). The ferric state produces an axial bisaqua complex in water[30] and this complex is a polyprotic acid. The mono-deprotonated form is the fastest reacting with peroxide.[25] Thus, the pKa of iron TAML aqua complexes is a critical parameter for environmental applications. The pKa values of the catalysts used here are **1a** 10.1,[30] **1b** 9.4[25] and **1c** 9.3.[31] The maximum reactivity with peroxide arises for each TAML activator at about one half a pKa unit above the pKa of the bis(aqua) ferric complex, because this is where the

aqua ligand acid equilibrium has reached the stage of nearly complete deprotonation and the concentration of the most reactive ferric species is at a maximum. Thinking broadly, the most generally useful TAML catalyst for water purification would have a pKa of 6–7, so that its most reactive form would be in highest concentration around neutral pH and approximately in the most common pH regime for environmental waters. Using the Collins iterative catalyst design protocol, we have been able to deliberately lower the iron TAML activator pKa value to 8.4[13,31] and ongoing design work is aimed at lowering this key reactivity parameter even further. However, for the present study, the more reactive catalysts, **1b** and especially **1c**, have provided ample catalytic activity for degrading SER rapidly in the mildly basic pH regime and **1c** has exhibited reasonable reactivity near neutral pH.

In this work, we have examined the degradation of SER at solution pH values corresponding to the pHs of optimal performance for the different catalysts studied and at other values that are important for water treatment. Five specific pHs were explored using buffered reaction media: pH 6.25 and 7.25 (values common to environmental waters, but lower than the pH of maximum activity for all of the catalysts), pH 8.25 (near Pittsburgh's drinking water pH and also within the environmental range), 9.5 (near the maximum rates for **1b** and **1c**, but above common environmental values) and 10.25 (near the maximum rate for **1a**).[12] Beyond the impact of pH on the rate of formation of the reactive intermediates, the key oxidizing species once formed vary significantly in agressiveness depending on the substituents on the TAML ligand system with **1a** < **1b** < **1c**.[12]

In Figure 5.1 SER half-life data are presented that summarize the dependency of the TAML/H_2O_2 degradation of SER on both the nature of the TAML activator and on the pH of the solution. As the data show, even with the least reactive **1a**, at pH 9.5 and 10.25 SER degradation is rapid with $t_{1/2}$ values of less than 15 min. Catalysts

1a and **1b** do not give $t_{1/2}$ values below 60 min at this pH. At pH 8.25, the more reactive **1b** and **1c** catalysts degrade sertraline to 50% in less than 15 min. At the higher pHs, the $t_{1/2}$ values are less than 1 min for these catalysts. In the case of the least acidic and least aggressive **1a**, the $t_{1/2}$ values are less than 30 min at pH values of 9.5 and 10.25, but the oxidation process is very slow at pH 8.25 (see caption to Figure 5.1). At pH 7.25, **1c**, delivers a halflife of 52 min at 3×10^{-7} M. This drops to below 30 min at 9×10^{-7} M. At pH 6.25, all the oxidations are too slow to be useful for the most reactive **1c**. Thus, SER can be degraded reasonably rapidly to very rapidly by TAML activator/H_2O_2 at each pH explored except 6.25.
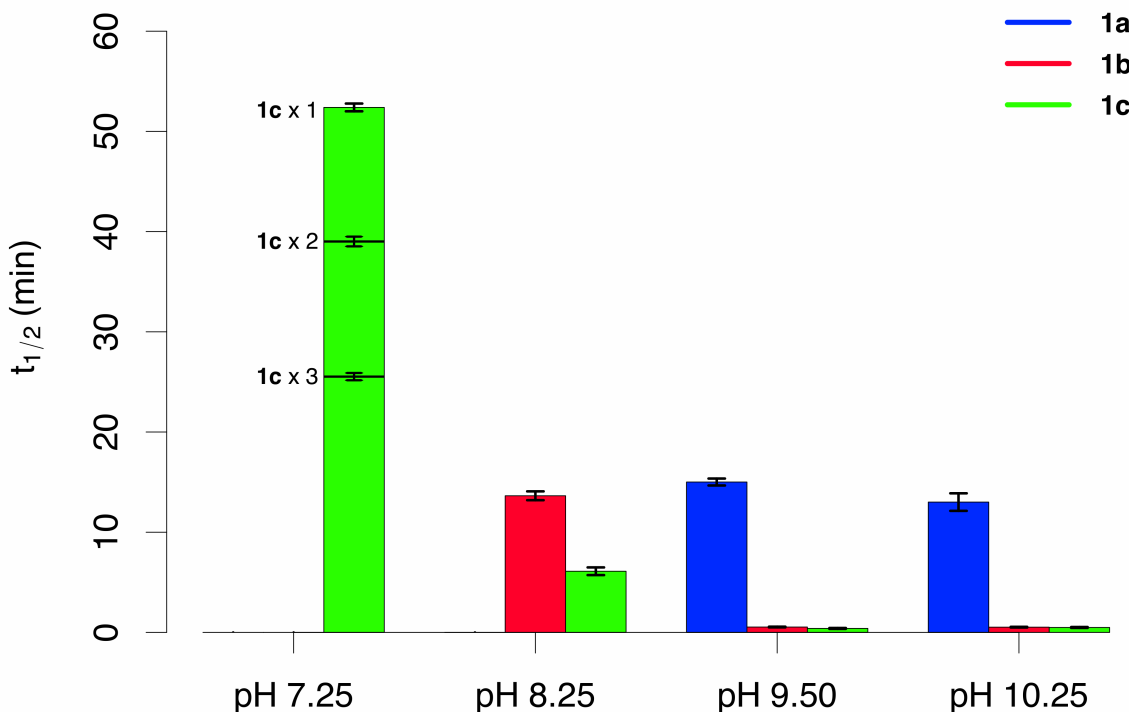
Figure 5.1: HPLC measured half-lives of SER under **1a**, **1b**, and **1c** catalyzed H_2O_2 treatment at four different pHs and room temperature with $[\mathbf{1}] = 3 \times 10^{-7}$ M, [SER] $= 5 \times 10^{-5}$ M and $[H_2O_2] = 2 \times 10^{-3}$ M. The pH was controlled with 0.01 M K_2HPO_4/KH_2PO_4 (pH 7.25 and 8.25) or 0.01 M $Na_2CO_3/NaHCO_3$ (pH 9.50 and 10.25). All experiments were performed in triplicate. At pH 8.25, SER halflife under **1a**/H_2O_2 (not shown) treatment was slow (17% after 2 h).

5.4.2 Degradation Pathway and the Observation of Elusive Intermediates
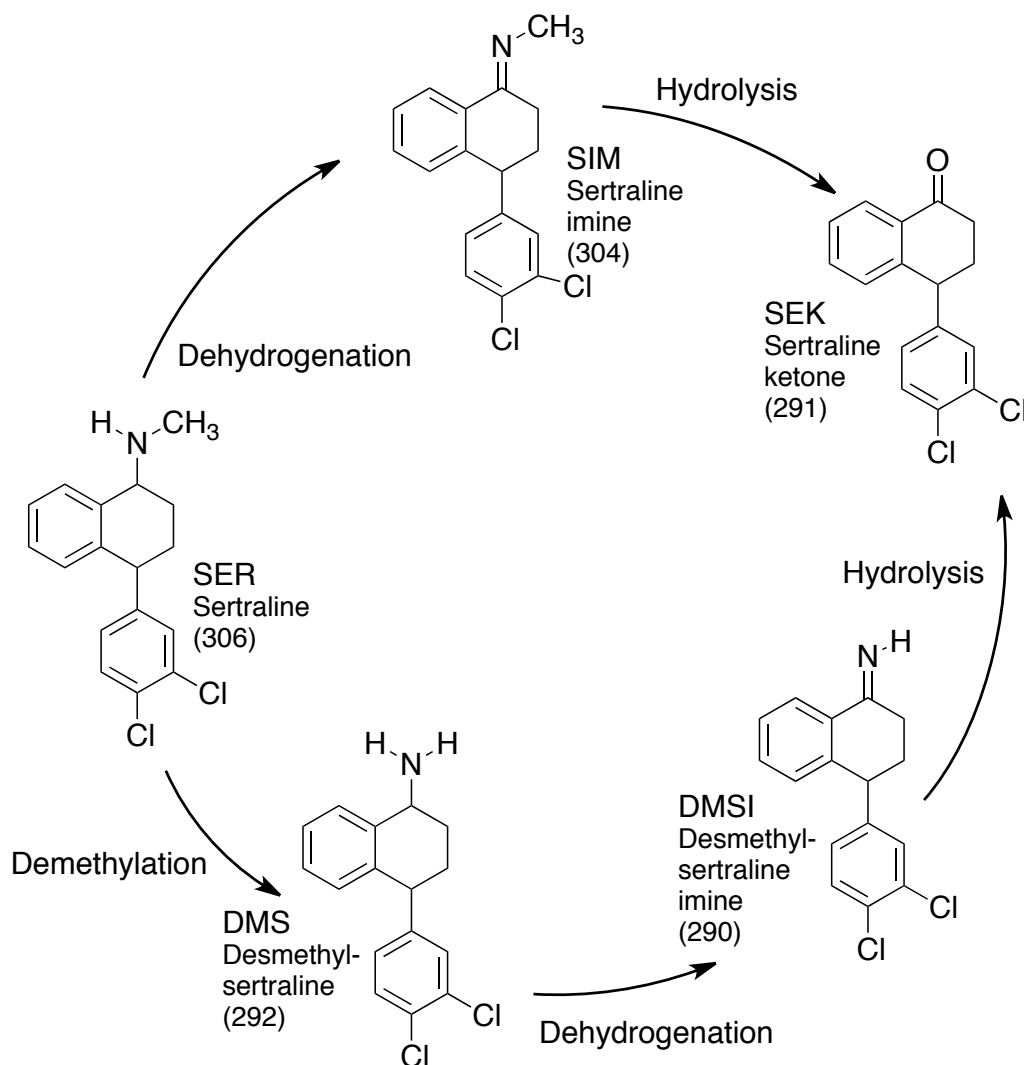
Scheme 5.2: TAML activator/H_2O_2 SER degradation pathway showing early identifiable intermediates. Nominal ion masses, for each $[M+H]^+$ ion are indicated in parentheses. The demethylation step, SER to DMS, likely proceeds in two steps—dehydrogenation across the RNH–CH_3 bond followed by hydrolysis of the resulting methylene imine. The process proceeded rapidly to SEK which was then more slowly degraded as described in the text.

HPLC, atmospheric pressure ionization mass spectrometry and GC–MS data obtained

from the reaction media and from independently prepared or purchased compounds

(see below) reveal the degradation steps shown in Scheme 5.2. Two separate pathways lead from SER to SEK.

Compared with the metabolism pathway of SER (Scheme 5.3), great similarity unfolds. Except for the most right branch in (Scheme 5.3), conjugation product of glucuronoside which does not present in TAML treatment system, Scheme 5.2 seizes all other SER metabolites. In addition, two transient intermediate SIM and DMSI were uncovered with the aid of multiple advanced analytical technology. Their reveal augments the knowledge of SER degradation chemistry under the oxidative stress.
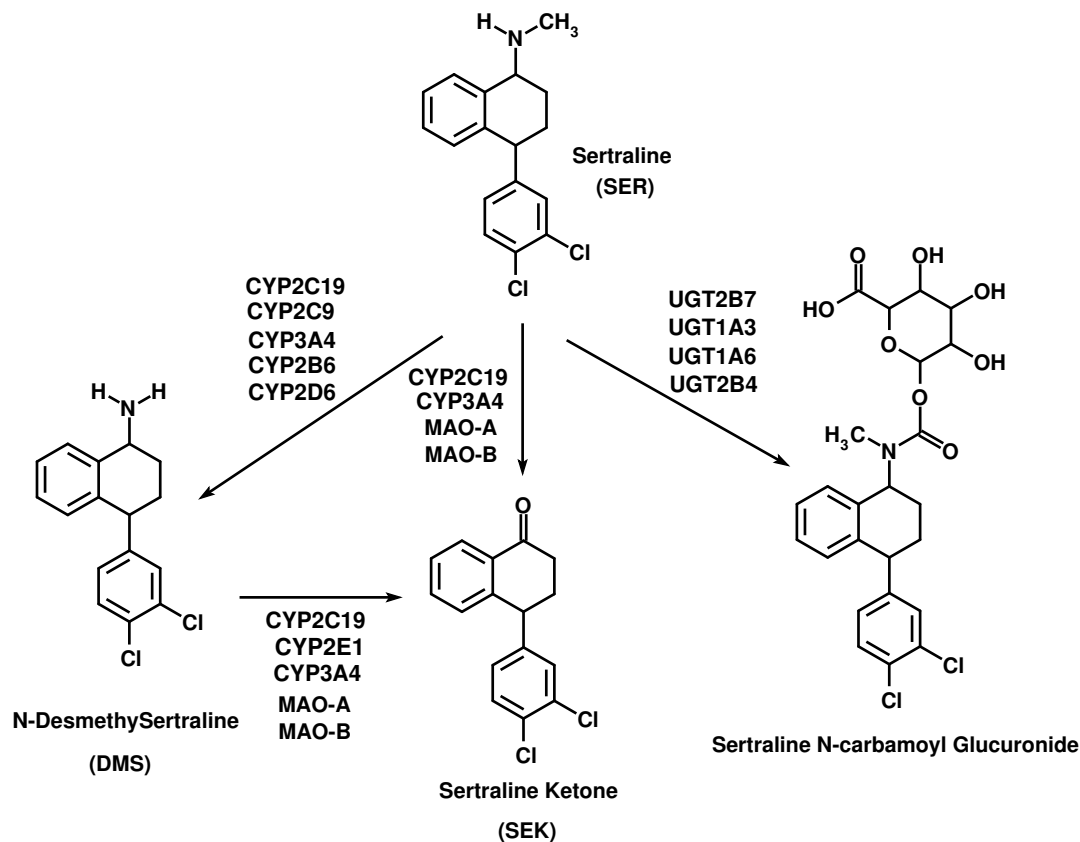
Scheme 5.3: SER metabolism pathway by CYP450 and monoamine oxidase(MAO).[29]

When SER was degraded using the least aggressive **1a** catalyst at pH 9.5 in the presence of 40 eq of H_2O_2, early SER degradation was accompanied by both DMS and

SEK formation (Figure 5.2). At later reaction times ($\geq$50 min), DMS was observed to also convert to SEK. The value of using the quite slow reacting **1a** can be seen from Figure 5.2 —the different species are oxidized on timescales that are convenient for accurate experimental observation. After 120 min, the three species in Figure 5.2 accounted for 85.6% of the starting SER. SEK was slowly decomposed by **1c**/H_2O_2 (30% decomposed after 350 min by [**1c**]:[SEK]:[H_2O_2] = 1:100:6400, [**1c**] = 5×10^{-7} M at pH 9.5).

These results clearly show that SER can be rapidly transformed to SEK within the qualifications introduced above concerning the pH and the nature of the catalyst. In all experiments (except for the TOC studies), for each equivalent of SER present, 40 equivalents of H_2O_2 were used, or slightly less than the mineralization requirement of 44 equivalents. TOC analyses of solutions produced by SER degradation using **1c** under a variety of conditions (Table 5.1) show that mineralization does not follow quickly once the SEK has been oxidized and hint that while SEK can be further decomposed slowly, additional recalcitrant intermediates may well be formed. SER was treated with 1 to 5 aliquots of **1c** (3×10^{-7} M)] and H_2O_2 (2×10^{-3} M) (multiple aliquots were added at 15 min intervals) to produce solutions that were subsequently shipped for TOC analyses (see Table 5.1). While it took just one aliquot to rapidly produce SEK as explained above, there is no evidence in the TOC results for any significant amount of mineralization. Progression toward mineralization with TAML activator/peroxide systems are known to slow down at small molecule diacids before complete mineralization in effect leading to nearly complete degradation, but not to a high degree of mineralization.[8] TOC analyses reveal only how much organic carbon has been totally mineralized. However in this case, because of the significant degradation resistance observed for SEK, we favor the conservative position that the bulk of the unoxidized material is likely to consist of quite large molecules. If

this is correct, additional species could also be significant in determining the full environmental implications of the use of SER.
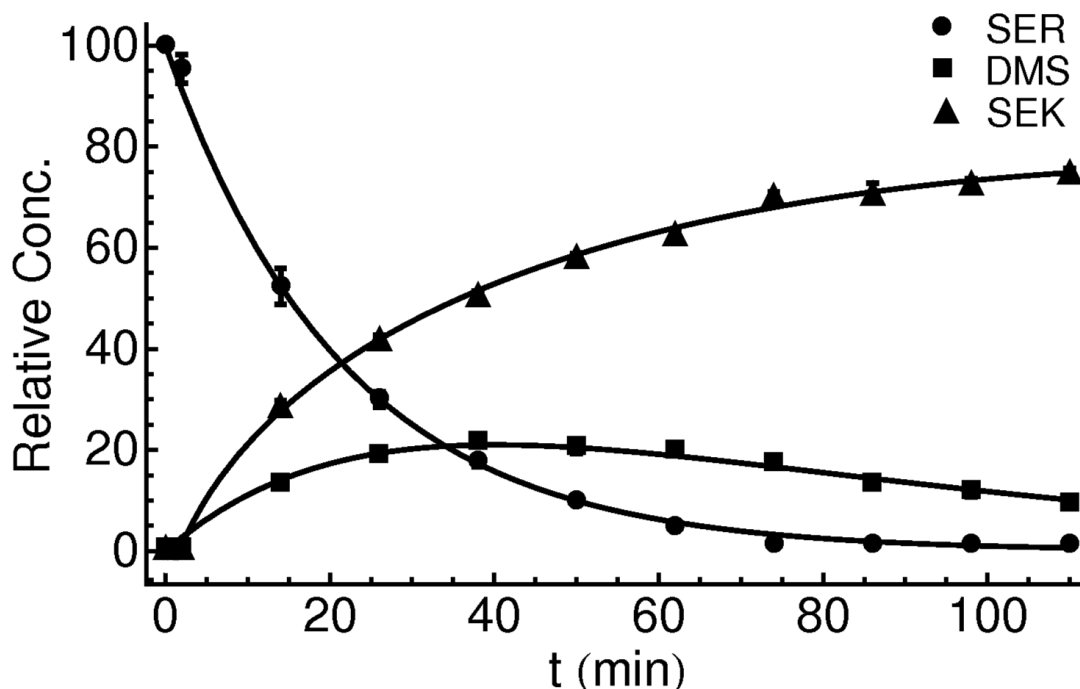
Figure 5.2: Time evolution of [SER], [DMS] and [SEK] during a SER degradation reaction monitored by HPLC. Conditions: $[\mathbf{1a}] = 3 \times 10^{-7}$ M, $[\text{SER}] = 5 \times 10^{-5}$ M and $[\text{H}_2\text{O}_2] = 2 \times 10^{-3}$ M at pH 9.50. $[\mathbf{1a}]:[\text{SER}]:[\text{H}_2\text{O}_2] = 1:167:6667$. The process was run in triplicate employing a Varian Microsorb C18 column (250×4.6 mm I.D., 5 mm) with a mobile phase of 70:30, v/v acetonitrile and phosphate buffer ($\sim 10^{-2}$M, pH 3.0) containing 0.1% triethylamine. The sample injection volume was 10 μL. Calibration curves were generated for SER, DMS and SEK using purchased or synthesized samples and were used to determine quantities in the reaction media.

5.4.2.1 Characterization of Sertralineimine (SIM)

In Scheme 5.2, SIM is presented as a clearly detected intermediate arising directly from SER. But SIM could not be observed using the slow oxidizing conditions described in Figure 5.2. This process is based upon the least aggressive catalyst **1a** and it delivers a convenient reaction timescale for temporal analyses by the rather slow HPLC technique. The transformation of SER to its more stable degradation

intermediates, DMS and SEK, is easily followed and the pathway linking them is conveniently revealed. However, when either of the more aggressively oxidizing catalysts **1b** or **1c** was used under otherwise identical conditions, SIM was the major early product as determined by HPLC (Figure 5.3) and FIA atmospheric mass spectrometry. The success in observing SIM under faster oxidizing conditions likely results from the SIM production rate by oxidation being fast compared to its subsequent hydrolysis to SEK.
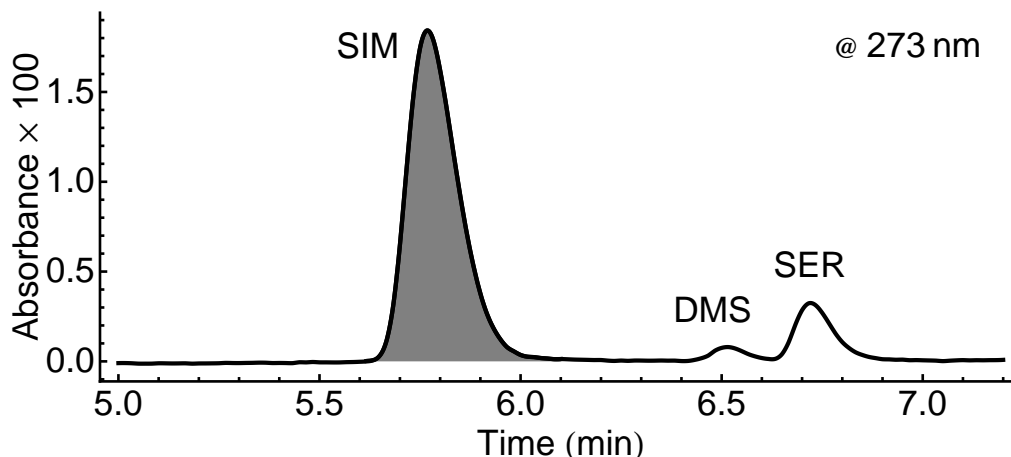
Figure 5.3: HPLC chromatogram of SER degradation showing SIM as an intermediate after 2 min of reaction. Conditions: [**1c**]:[SER]:[H_2O_2] = 1:100:6000 with [SER] = 3×10^{-5} M at pH 9.50. Separation was performed on a Waters XTerra RP18 column (150 × 4.6 mm I.D., 5 mm) with 0.1% formic acid acidified acetonitrile and water as mobile phases under gradient elution conditions (see Table 5.2 for details). The sample injection volume was 20 μL.

Table 5.2: HPLC gradient elution table used to monitor SER degradation reactions SIM hydrolysis. A : Acetonitrile with 0.1% formic acid. B: Water with 0.1% formic acid. Injection volume: 20 μL. The same elution method is used in Figure 5.7.

Time (min)	Flow Rate (mL/min)	% Solvent A	% Solvent B
00.00	1.00	30	70
10.00	1.00	90	10
13.00	1.00	90	10
13.01	1.00	30	70
20.00	1.00	30	70

The confirmation of SER dehydrogenation and inference for the double bond position invoked Flow Injection Analysis (FIA) atmospheric mass spectroscopic study of time-elapsed decay process of SER and its isotopologue SER-d3 Figure 5.4. The reaction condition is : [**1b**]:[Sub]:[H_2O_2]=1:100:6500, [Sub]= 1×10^{-5}M, [Sub] = [SER] or [SER-d3]. pH = 9.25, buffered by 10^{-2} M [$NaHCO_3$]/[Na_2CO_3].

SER
(306/308/310)
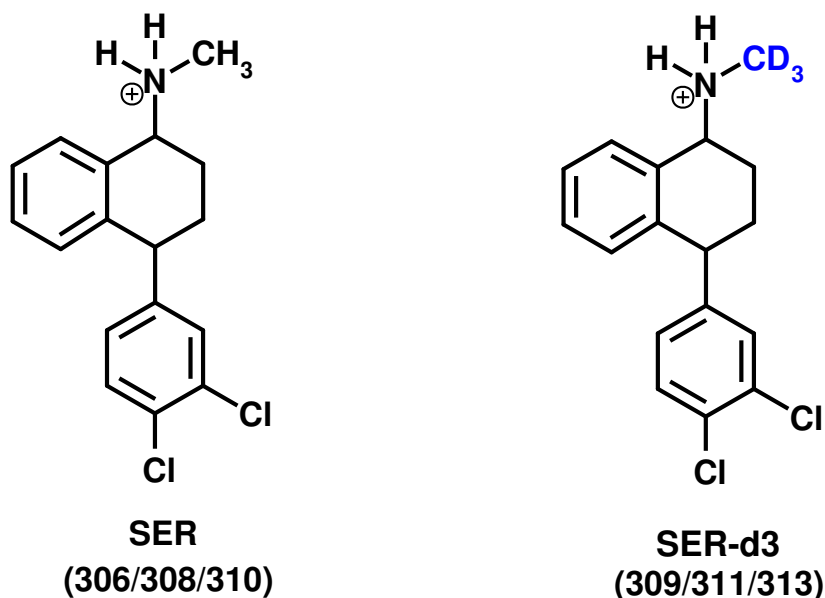
SER-d3
(309/311/313)

Figure 5.4: Molecular structures of SER and SER-d3. The nominal mass for each [M+H]$^{+}$ species and the mass numbers of their mono- and di- ^{37}Cl isotopologues are indicated in the parenthesis.

As shown in Figure 5.5, the nominal mass of SER-d3 is shifted from 306 to 309 as three ^{2}H are introduced to the molecule. If the double bond were formed on the methyl group SER-d3 after the dehydrogenation step, it is expected to observe a 3 Da loss product on the mass spectrum. Otherwise, a 2 Da loss product should show up similar to the case of SER decay (Figure 5.5 (b)). The FIA atmospheric mass spectroscopic resolves the latter case (Figure 5.5 (d)). This evidence supports that the dehydrogenation products bears a double bond on the ring or between N and C1.
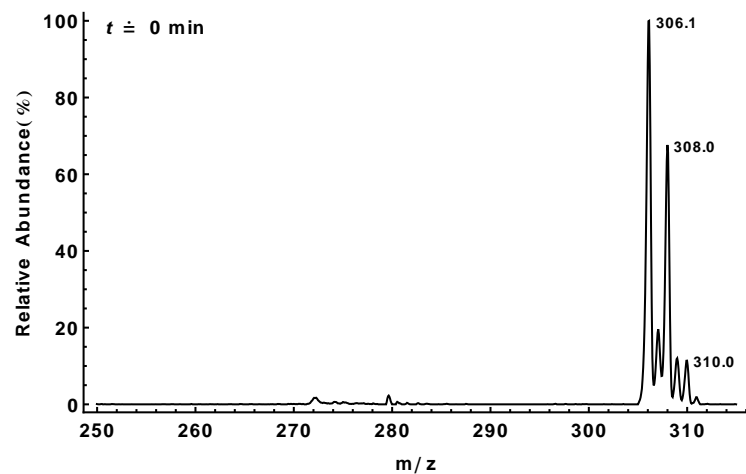
(a) Full scan mass spectrum of SER decay at t≈0 min
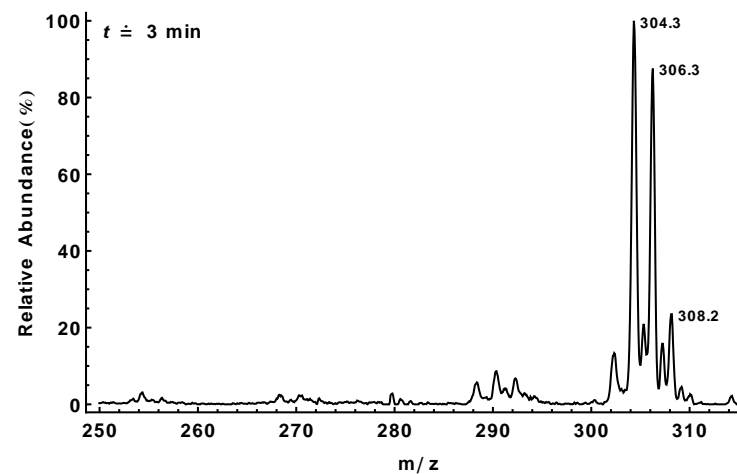
(b) Full scan mass spectrum of SER decay at t≈3 min
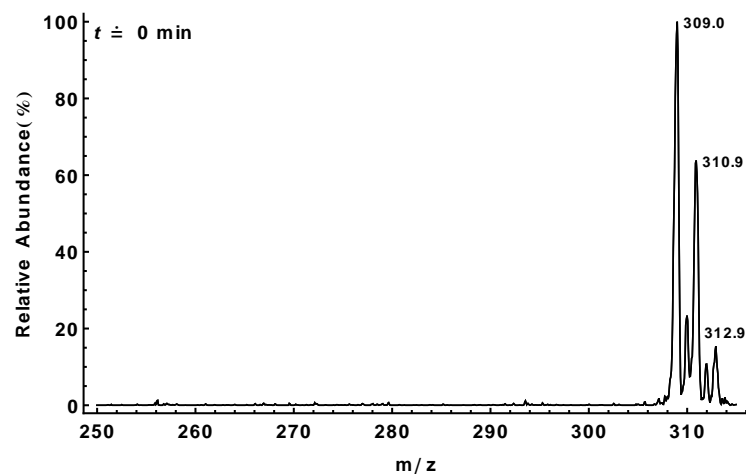
(c) Full scan mass spectrum of SER-d3 decay at t≈0 min
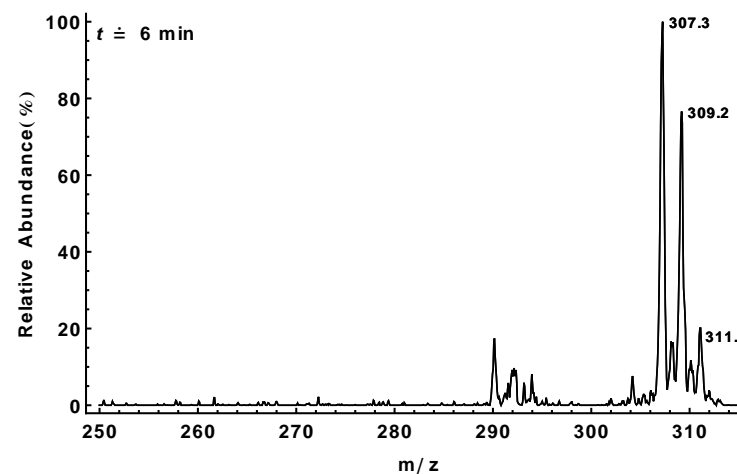
(d) Full scan mass spectrum of SER-d3 decay at t≈6 min

Figure 5.5: FIA mass spectra for time-elapsed SER and SER-d3 decay processes.
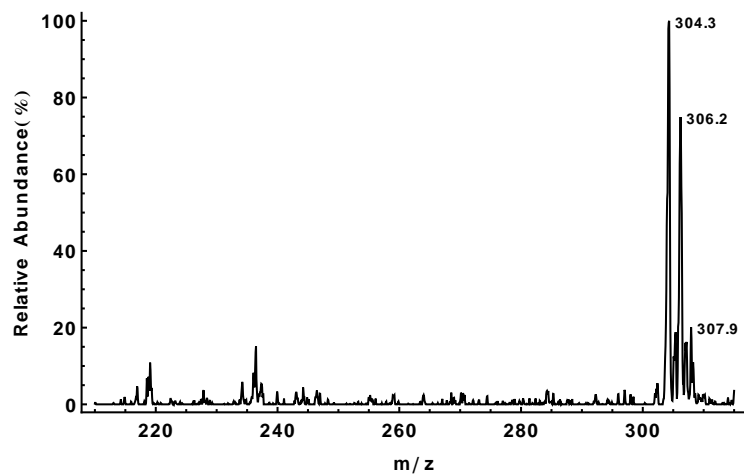
(a) Full scan mass spectrum of SIM standard
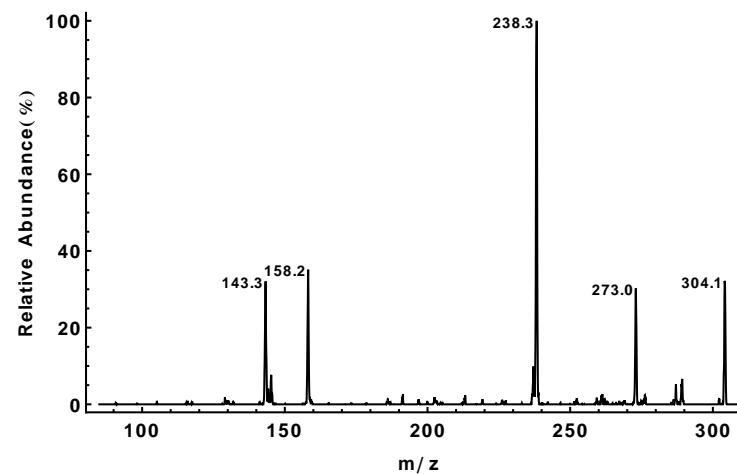
(b) Product scan mass spectrum of SIM standard
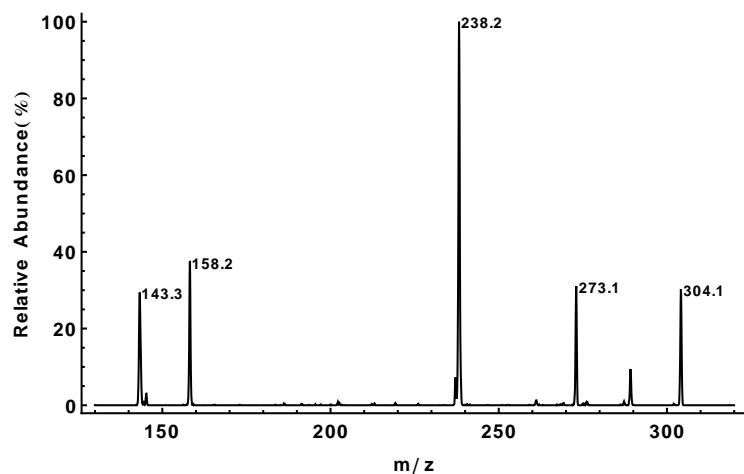
(c) Product scan mass spectrum of 304 in the SER oxidation reaction
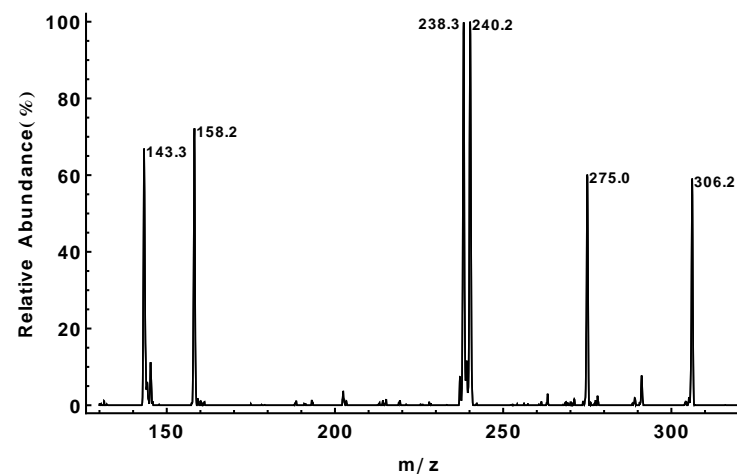
(d) Product scan mass spectrum of 306 in the SER oxidation reaction

Figure 5.6: FIA mass spectra comparison between SIM standard and SIM as the intermediate in SER oxidation

Comparison of the mass spectra between SIM standard and peaks with m/z = 304 and 306 in the SER degradation reaction mixture enhanced the confidence of this diagnosis. As seen in Figure 5.6(a), the fulls scan mass spectrum of SIM standard shows its isotopic distribution mass pattern. To analyze this pattern, we should consider the element composition of the parent compound (SIM) and the natural abundance of each constitutional element. In the case of SIM, both Cl and C have detectable isotopes based on the mass spectrometers at our molecular analysis center. Apparently, with such a small molecular mass, Cl dominates the distribution as shown in Figure 5.6(a). This will simplify the problem to a binomial probability distribution. The probability mass function is given below.

$$P(X = k) = \binom{n}{k} p^k \left(1 - p\right)^{n-k} \tag{5.1}$$

where X is the random variable, k is the event of interest, n is the sample space, p is the probability for each Bernoulli trial.

Substitute the dichloro composition into eqn 5.1, we get the mass spectrum signal intensity ratio : $^{35}Cl^{35}Cl/^{35}Cl^{37}Cl/^{37}Cl^{37}Cl$=1/6/9. This ratio is approximated by mass abundance ratio of 304/306/308 in Figure 5.6(a). Selecting the ion 304 with a mass window 1 Da to perform product scan, we get a fragmentation pattern shown in Figure 5.6(b). Mass 304 is also shown as a product in SER decay reaction (Figure 5.5(b)). Targeting this ion and performing the product scan, Figure 5.6(c) results, which has very strong similarity with the product scan spectrum of SIM standard (Figure 5.6(b)). Another peak with high abundance in shows on Figure 5.5(b) is 306. The fragments of this peaks reveal a spectrum (Figure 5.6(d)) with 2 Da upward shift compared to Figure 5.6(c) except for the peak 238, which also exists on the product scan spectrum of 304. More importantly, the ratio between 238 and 240 is almost

identical and their mass difference is 2 Da. This observation complies with the isotopic mass redistribution phenomenon in tandem mass spectrometry, which points 306 to be SIM with the combination of $^{35}Cl^{37}Cl$. Therefore, the 304 and 306 appearing on Figure 5.5(b) are highly likely to be associated with each other. The product scan of 304 has almost identical mass peak distribution as the 304 peak in SIM standard. (The 306 peak of SIM standard does not have enough intensity to produce clear and reliable mass spectrum.) Based on second order tandem mass in time analysis, SIM stands a great chance to one of the products in SER decay. Further study on the hydrolysis (see below) and quantification of SEK as the major end-point (Figure 5.2) of SER degradation process suggest that SIM is the mostly likely product of the dehydrogenation step of SER.
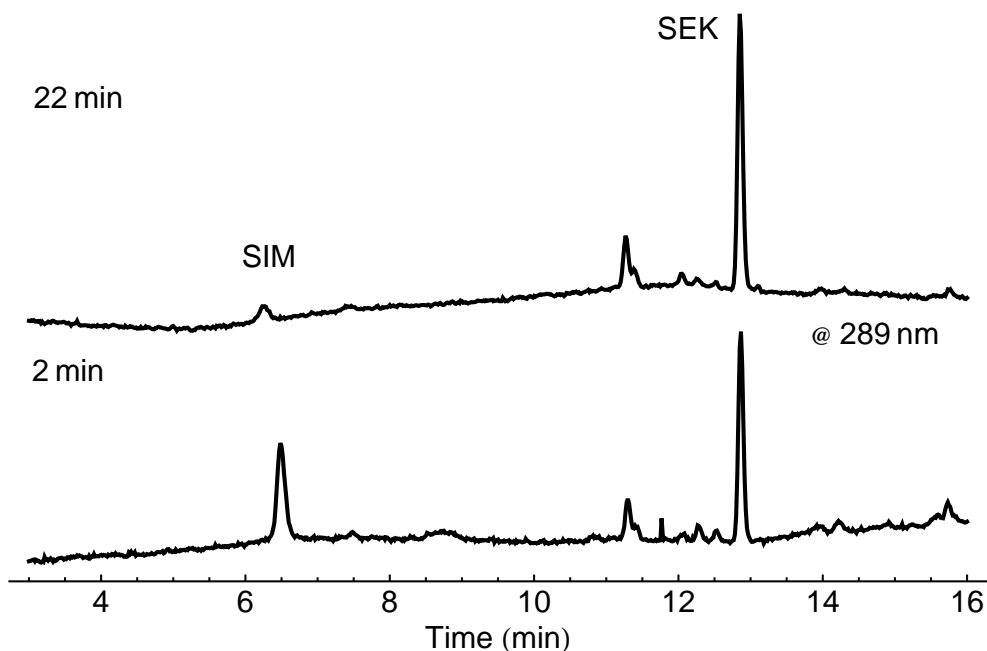
Figure 5.7: HPLC chromatograms for SIM hydrolysis at pH 9.5 showing its conversion to SEK. Peaks for unidentified impurities in the purchased SIM standard are visible on the chromatogram. The analysis was performed using a Waters XTerra® RP8 column (150 × 4.6 mm I.D., 5 m) where the eluting solvent was not buffered with gradient elution as described in Table 5.2

The hydrolysis of a commercially obtained sample of SIM was studied in buffered solution (pH 9.5, 0.01 M $Na_2CO_3/NaHCO_3$) in the absence of peroxide resulting in fast SEK formation. SIM of unguaranteed purity was purchased from a rare chemical library of Sigma-Aldrich which, because of the sensitivity of the compound to hydrolysis, was used as received with focus on the reaction of the SIM component. This SIM standard (ca. 5×10^{-5} M) was added to pH 9.5 buffer and immediately subjected to HPLC analysis (Figure 5.7) revealing that it is quickly converted into SEK in the aqueous medium consistent with it being an intermediate in the SER degradation pathway.

This ability both to produce a slower oxidative degradation rate to facilitate HPLC detection and monitoring of hydrolytically stable intermediates and a faster oxidation rate to detect fast hydrolyzing species is a benefit of the diverse reactivity profile of the TAML activator family.

5.4.2.2   Inference for Desmethlysertralineimine(DMSI)
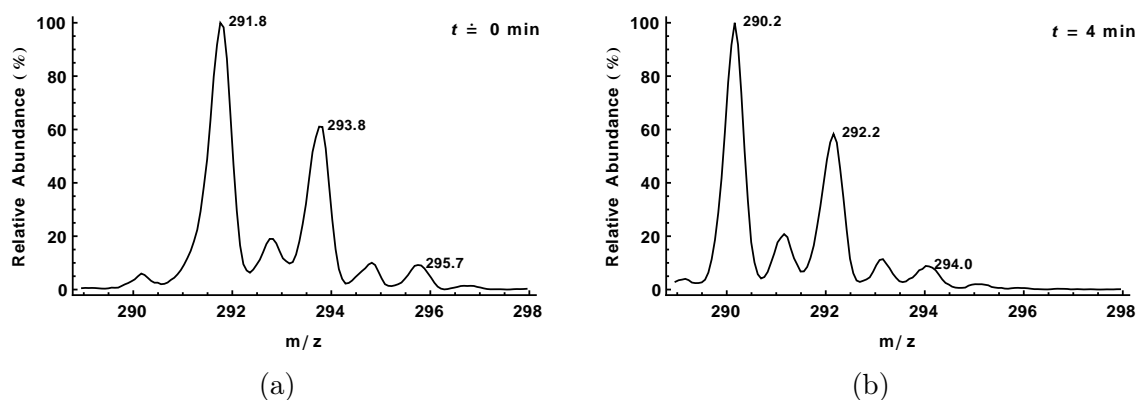
Figure 5.8: Selected ion monitoring over $\Delta m/z$ 10 by FIA-APCI-MS of the DMS oxidation medium immediately following mixing (a) and after 4 min (b). Reaction conditions: [DMS] = 1×10^{-5} M with [**1c**]:[DMS]:[H_2O_2] = 1:100:7500 in pH 9.5 buffer. The mass distributions on both spectra accord with isotopic mass pattern of a pure dicholor hydrocarbon with the molecular with the same nominal mass.
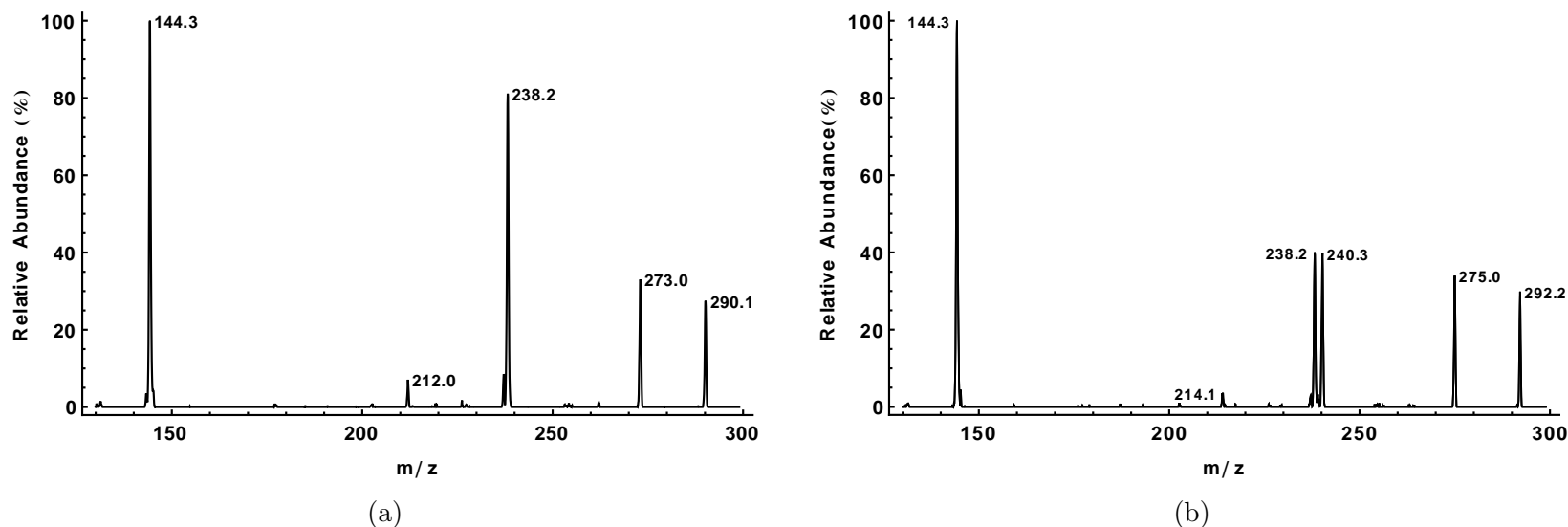
Figure 5.9: Product scan mass spectra for the peak with mass number of 290 (a) and 292 (b) appearing in the DMS degradation reaction. See Figure 5.8 for the reaction conditions.

For the intermediate DMS, it was anticipated that further decomposition would be related to that of SER by dehydrogenation of the DMS amine to desmethylsertraline imine (DMSI) followed by hydrolysis of DMSI to SEK. DMSI was not detected over a range of LC–MS conditions, presumably because it is likely to be very hydrolytically sensitive. However, when the more rapid FIA technique was employed, peaks with appropriate mass distribution for DMSI (two Da lower than those for DMS) were observed upon analysis of a degrading DMS reaction medium (Figure 5.8).

The relative abundance ratio between the peak with the mass number 290 and 292 on Figure 5.8(b) suggests they are isotopically related. Second order tandem mass spectra (Figure 5.9) provide further evidence on their isotopic nature.

Peaks 238 and 240 having equal intensities is an indication of the isotopic mass redistribution observed in tandem mass spectra (cf. 5.4.2.1). Therefore, peak with the mass number 290 and its associates are highly likely to be one chemical entity, suggesting substantial conversion of DMS to a product with the correct mass for DMSI. Collectively, the mass spectra information suggests the intermediacy of DMSI as another chemically reasonable species on the multipathway route to SEK (Scheme 5.2).

5.5   Conclusions

This study shows that SER is rapidly and efficiently decomposed under ambient conditions of temperature and pressure from pH 7.25 to 10.25 by various TAML activator/H_2O_2 processes. The rates of TAML activator/H_2O_2 oxidations are pH dependent and the three catalysts used here have maximum rates from pH 9.3 to 10.1. The reactivity falls off for each catalyst as the pH is moved toward neutral, but the most aggressive **1c** still delivers a reasonable rate at pH 7.25. However at pH 6.25 even, **1c** has a slow rate of SER oxidation under the concentration conditions used. The oxidative metabolism of SER is significantly mimicked in the product distribution providing further evidence that the reactive intermediates in TAML activator catalysis mimic those in cytochrome P450 and peroxidase processes. Overall, SER degradation proceeds rapidly to SEK, which is then much more slowly degraded. The variable reactivity of the TAML catalysts provided a novel tool for following the evolution and fate both of the more stable early sertraline degradation intermediates and for several reactive intermediates that are susceptible to hydrolysis. The TAML activator/H_2O_2 degradation process for SER is rapid and complete, but the process nearly stalls at SEK for all three catalysts. In this regard, the behavior of SEK con-

trasts with other exceptionally recalcitrant water pollutants such as pentachlorophenol and trichlorophenol that are rapidly oxidized nearly to complete mineralization[8] and points to a need to better understand the mechanisms by which TAML activator reactive intermediates oxidize the various substrates they attack—appropriate studies are being carried out in our lab. The study also highlights that there is a need for even more reactive TAML activators for advancing water treatment goals which is another major research focus. Finally, in an emerging and related research frontier,[32–34] various lab-scale oxidation systems are being studied to simulate, better understand and advance the prediction of drug metabolism.[35,36] The work presented here in pursuit of API degradation systems represents a complementary endeavor to drug metabolism research. If what has been found for SER can be extended to other APIs, TAML activator/H_2O_2 systems would provide more detailed snapshots of the intermediates in oxidative drug metabolism than are currently available through a form of artificial metabolism that can be carried out easily in water. At the same time, this would represent a new and simple tool for predicting the environmental fate of drugs and drug candidates that would quickly highlight persistent degradation products that need to be studied for potential adverse environmental effects.

5.6 References

[1] C. Y. Stanga, R. Ross, S. H. Preskorn, *Antidepressants: Past, Present and Future*, Vol. 157 of *Handbook of Experimental Pharmacology*, Springer, Berlin, **2004**.

[2] S. M. Richards, S. E. Cole. A toxicity and hazard assessment of fourteen pharmaceuticals to Xenopus laevis larvae. *Ecotoxicology* **2006**, *15*, 647–656.

[3] T. B. Henry, J. W. Kwon, K. L. Armbrust, M. C. Black. Acute and chronic toxicity of five selective serotonin reuptake inhibitors in Ceriodaphnia dubia. *Environ. Toxicol. Chem.* **2004**, *23*, 2229–2233.

[4] T. B. Henry, M. C. Black. Mixture and single-substance acute toxicity of selective serotonin reuptake inhibitors in Ceriodaphnia dubia. *Environ. Toxicol. Chem.* **2007**, *26*, 1751–1755.

[5] A. M. Christensen, S. Faaborg-Andersen, F. Ingerslev, A. Baun. Mixture and single-substance toxicity of selective serotonin reuptake inhibitors toward algae and crustaceans. *Environ. Toxicol. Chem.* **2007**, *26*, 85–91.

[6] C. G. Daughton, T. A. Ternes. Pharmaceuticals and personal care products in the environment: Agents of subtle change? *Environ. Health Perspect.* **1999**, *107*, 907–938.

[7] S. K. Khetan, T. J. Collins. Human pharmaceuticals in the aquatic environment: A challenge to green chemistry. *Chem. Rev.* **2007**, *107*, 2319–2364.

[8] S. S. Gupta, M. Stadler, C. A. Noser, A. Ghosh, B. Steinhoff, D. Lenoir, C. P. Horwitz, K.-W. Schramm, T. J. Collins. Rapid total destruction of chlorophenols by activated hydrogen peroxide. *Science* **2002**, *296*, 326–8.

[9] A. Chanda, S. K. Khetan, D. Banerjee, A. Ghosh, T. J. Collins. Total degradation of fenitrothion and other organophosphorus pesticides by catalytic oxidation employing Fe-TAML peroxide activators. *J. Am. Chem. Soc.* **2006**, *128*, 12058–12059.

[10] P. T. Anastas, *Chemistry and applications of Iron-TAML catalysts in green oxidation processes based on hydrogen peroxide 1st ed.*, Vol. 1, Wiley-VCH Verlag GmbH & Co. KGaA, Weiheim, Germany, **2009**.

[11] N. W. Shappell, M. A. Vrabel, P. J. Madsen, G. Harrington, L. O. Billey, H. Hakk, G. L. Larsen, E. S. Beach, C. P. Horwitz, K. Ro, P. G. Hunt, T. J. Collins. Destruction of estrogens using Fe-TAML/peroxide catalysis. *Environ. Sci. Technol.* **2008**, *42*, 1296–1300.

[12] A. D. Ryabov, T. J. Collins. Mechanistic considerations on the reactivity of green Fe-III-TAML activators of peroxides. *Adv. Inorg. Chem.* **2009**, *61*, 471–521.

[13] W. C. Ellis, C. T. Tran, R. Roy, M. Rusten, A. Fischer, A. D. Ryabov, B. Blumberg, T. J. Collins. Designing Green Oxidation Catalysts for Purifying Environmental Waters. *J. Am. Chem. Soc.* **2010**, *132*, 9774–9781.

[14] K. Vukics, T. Fodor, J. Fischer, I. Fellegvári, S. Lévai. Improved industrial synthesis of antidepressant sertraline. *Org. Process Res. Dev.* **2002**, *6*, 82–85.

[15] C. P. Horwitz, A. Ghosh, *Synthesis of macrocyclic tetraamido compounds and new metal insertion process (http://freepatentsonline.com/7060818.html)*, **2006**. http://freepatentsonline.com/7060818.html.

[16] P. George. The chemical nature of the 2nd-hydrogen peroxide compound formed by cytochrome-c-peroxidase and horseradish peroxidase .2. formation and decomposition. *Biochem. J.* **1953**, *55*, 220–230.

[17] A. Chanda, A. D. Ryabov, S. Modanl, L. Alexandrova, A. Ghosh, Y. Hangun-Balkir, C. P. Horwitz, T. J. Collins. Activity-stability parameterization of homogeneous of green oxidation catalysts. *Chem. Eur. J.* **2006**, *12*, 9336–9345.

[18] A. Chanda, F. T. de Oliveira, T. J. Collins, E. Münck, E. L. Bominaar. Density Functional Theory Study of the Structural, Electronic, and Magnetic Properties of a μ-oxo Bridged Dinuclear Fe-IV Complex Based on a Tetra-Amido Macrocyclic Ligand. *Inorg. Chem.* **2008**, *47*, 9372–9379.

[19] F. T. de Oliveira, A. Chanda, D. Banerjee, X. P. Shan, S. Mondal, L. Que, E. L. Bominaar, E. Münck, T. J. Collins. Chemical and spectroscopic evidence for an Fe-V-Oxo complex. *Science* **2007**, *315*, 835–838.

[20] P. F. Hollenberg. Mechanisms of cytochrome-P450 and peroxidase-catalyzed xenobitoic metabolism. *Faseb. J.* **1992**, *6*, 686–694.

[21] F. P. Guengerich. Common and uncommon cytochrome P450 reactions related to metabolism and chemical toxicity. *Chem. Res. Toxicol.* **2001**, *14*, 611–650.

[22] B. Meunier, S. P. de Visser, S. Shaik. Mechanism of oxidation reactions catalyzed by cytochrome P450 enzymes. *Chem. Rev.* **2004**, *104*, 3947–3980.

[23] H. B. Dunford, *Heme Peroxidases*, John Wiely & Sons, New York, **1999**.

[24] A. D. Ryabov. Transition metal chemistry of glucose oxidase, horseradish peroxidase, and related enzymes. *Adv. Inorg. Chem.* **2004**, *55*, 201–269.

[25] A. Ghosh, D. A. Mitchell, A. Chanda, A. D. Ryabov, D. L. Popescu, E. C. Upham, G. J. Collins, T. J. Collins. Catalase-Peroxidase Activity of Iron(III)-TAML Activators of Hydrogen Peroxide. *J. Am. Chem. Soc.* **2008**, *130*, 15116–15126.

[26] L. M. Tremaine, W. M. Welch, R. A. Ronfeld. Matabolism and disposition of the 5-hydroxytryptamine uptake blocker sertraline in the rat and dog. *Drug Meta. Dispos.* **1989**, *17*, 542–550.

[27] C. Hiemke, S. Härtter. Pharmacokinetics of selective serotonin reuptake inhibitors. *Pharmacol. Ther.* **2000**, *85*, 11–28.

[28] C. L. DeVane, H. L. Liston, J. S. Markowitz. Clinical pharmacokinetics of sertraline. *Clin. Pharmacokinet.* **2002**, *41*, 1247–1266.

[29] R. S. Obach, L. M. Cox, L. M. Tremaine. Sertraline is metabolized by multiple cytochrome P450 enzymes, monoamine oxidases, and glucuronyl transferases in human: An in vitro study. *Drug Metab. Dispos.* **2005**, *33*, 262–270.

[30] A. Ghosh, A. D. Ryabov, S. M. Mayer, D. C. Horner, D. E. Prasuhn, S. S. Gupta, L. Vuocolo, C. Culver, M. P. Hendrich, C. E. F. Rickard, R. E. Norman, C. P. Horwitz, T. J. Collins. Understanding the mechanism of H^+-induced demetalation as a design strategy for robust iron(III) peroxide-activating catalysts. *J. Am. Chem. Soc.* **2003**, *125*, 12378–12379.

[31] D. L. Popescu, A. Chanda, M. J. Stadler, S. Mondal, J. Tehranchi, A. D. Ryabov, T. J. Collins. Mechanistically inspired design of Fe-III-TAML peroxide-activating catalysts. *J. Am. Chem. Soc.* **2008**, *130*, 12260–122261.

[32] S. Zuehlke, U. Duennbier, T. Heberer. Investigation of the behavior and metabolism of pharmaceutical residues during purification of contaminated ground water used for drinking water supply. *Chemosphere* **2007**, *69*, 1673–1680.

[33] R. Rosal, A. Rodriguez, J. A. Perdigon-Melon, M. Mezcua, M. D. Hernando, P. Leton, E. Garcia-Calvo, A. Aguera, A. R. Fernandez-Alba. Removal of pharmaceuticals and kinetics of mineralization by O_3/H_2O_2 in a biotreated municipal wastewater. *Water Res.* **2008**, *42*, 3719–3728.

[34] J. Radjenović, M. Petrović, F. Ventura, D. Barcelo. Rejection of pharmaceuticals in nanofiltration and reverse osmosis membrane drinking water treatment. *Water Res.* **2008**, *42*, 3601–3610.

[35] U. Jurva, H. V. Wikström, L. Weidolf, A. P. Bruins. Comparison between electrochemistry/mass spectrometry and cytochrome P450 catalyzed oxidation reactions. *Rapid Commun. Mass Spectrom.* **2003**, *17*, 800–810.

[36] W. Lohmann, U. Karst. Biomimetic modeling of oxidative drug metabolism. *Anal. Bioanal. Chem.* **2008**, *391*, 79–96.

[37] B. A. Shainyan, A. N. Mirskova. The Carbon-Nitrogen Triad Prototropic Tautomerism. *Russ. Chem. Rev.* **1979**, *48*, 107–117.

[38] K. Lammertsma, B. V. Prasad. Imine .dblharw. enamine tautomerism. *J. Am. Chem. Soc.* **1994**, *116*, 642–650.

[39] S. Hammerum. Distonic radical cations in gaseous and condensed phase. *Mass Spectrom. Rev.* **1988**, *7*, 123–202.

[40] D. M. Tomazela, A. a. a. Sabino, R. Sparrapan, F. C. Gozzo, M. N. Eberlin. Distonoid ions. *J. Am. Soc. Mass Spectrom.* **2006**, *17*, 1014–22.

[41] M. Alcamí, O. Mó, M. Yáñez. Computational chemistry: a useful (sometimes mandatory) tool in mass spectrometry studies. *Mass Spectrom. Rev.* **2002**, *20*, 195–245.

[42] J. Mercero, J. Matxain, X. Lopez, D. York, a. Largo, L. Eriksson, J. Ugalde. Theoretical methods that help understanding the structure and reactivity of gas phase ions. *Int. J. Mass Spectrom.* **2005**, *240*, 37–99.

[43] M. J. Frisch, G. W. Trucks, H. B. Schlegel, G. E. Scuseria, M. A. Robb, J. R. Cheeseman, G. Scalmani, V. Barone, B. Mennucci, G. A. Petersson, H. Nakatsuji, M. Caricato, X. Li, H. P. Hratchian, A. F. Izmaylov, J. Bloino, G. Zheng, J. L. Sonnenberg, M. Hada, M. Ehara, K. Toyota, R. Fukuda, J. Hasegawa, M. Ishida, T. Nakajima, Y. Honda, O. Kitao, H. Nakai, T. Vreven, J. A. Montgomery, J. E. Peralta, F. Ogliaro, M. Bearpark, J. J. Heyd, E. Brothers, K. N. Kudin, V. N. Staroverov, R. Kobayashi, J. Normand, K. Raghavachari, A. Rendell, J. C. Burant, S. S. Iyengar, J. Tomasi, M. Cossi, N. Rega, J. M. Millam, M. Klene,

J. E. Knox, J. B. Cross, V. Bakken, C. Adamo, J. Jaramillo, R. Gomperts, R. E. Stratmann, O. Yazyev, A. J. Austin, R. Cammi, C. Pomelli, J. W. Ochterski, R. L. Martin, K. Morokuma, V. G. Zakrzewski, G. A. Voth, P. Salvador, J. J. Dannenberg, S. Dapprich, A. D. Daniels, Farkas, J. B. Foresman, J. V. Ortiz, J. Cioslowski, D. J. Fox, *Gaussian 09, Revision B.01*, **2009**.

[44] A. D. Becke. Density-functional thermochemistry. III. The role of exact exchange. *J. Chem. Phys.* **1993**, *98*, 3–7.

[45] A. D. Becke. Density-functional exchange-energy approximation with correct asymptotic behavior. *Phys. Rev. A* **1988**, *38*, 3098–3100.

[46] C. Lee, W. Yang, R. G. Parr. Development of the Colle-Salvetti correlation-energy formula into a functional of the electron density. *Phys. Rev. B* **1988**, *37*, 785–789.

[47] O. Almarsson, M. B. Hickey, M. L. Peterson, S. L. Morissette, S. Soukasene, C. McNulty, M. Tawa, J. M. MacPhee, J. F. Remenar. High-Throughput Surveys of Crystal Form Diversity of Highly Polymorphic Pharmaceutical Compounds. *Cryst. Growth Des.* **2003**, *3*, 927–933.

[48] R. Banerjee, P. M. Bhatt, N. V. Ravindra, G. R. Desiraju. Saccharin Salts of Active Pharmaceutical Ingredients, Their Crystal Structures, and Increased Water Solubilities. *Cryst. Growth Des.* **2005**, *5*, 2299–2309.

[49] F. Caruso, a. Besmer, M. Rossi. The absolute configuration of sertraline (Zoloft) hydrochloride. *Acta Crystallogr., Sect. C: Cryst. Struct. Commun.* **1999**, *55*, 1712–1714.

[50] Q. He, S. Rohani, J. Zhu, H. Gomaa. Sertraline Racemate and Enantiomer: Solid-State Characterization, Binary Phase Diagram, and Crystal Structures. *Cryst. Growth Des.* **2010**, *10*, 1633–1645.

[51] K. Ravikumar, B. Sridhar, M. N. Bhanu. Sertraline hydrochloride form II. *Acta Crystallogr., Sect. E: Struct. Rep. Online* **2006**, *62*, o565–o567.

[52] J. F. Remenar, J. M. MacPhee, B. K. Larson, V. A. Tyagi, J. H. Ho, D. A. McIlroy, M. B. Hickey, P. B. Shaw, O. Almarsson. Salt Selection and Simultaneous Polymorphism Assessment via High-Throughput Crystallization: The Case of Sertraline. *Org. Process Res. Dev.* **2003**, *7*, 990–996.

5.7 Appendices

5.7.1 SER Degradation Products Characterization

5.7.1.1 SER Degradation : LC–MS
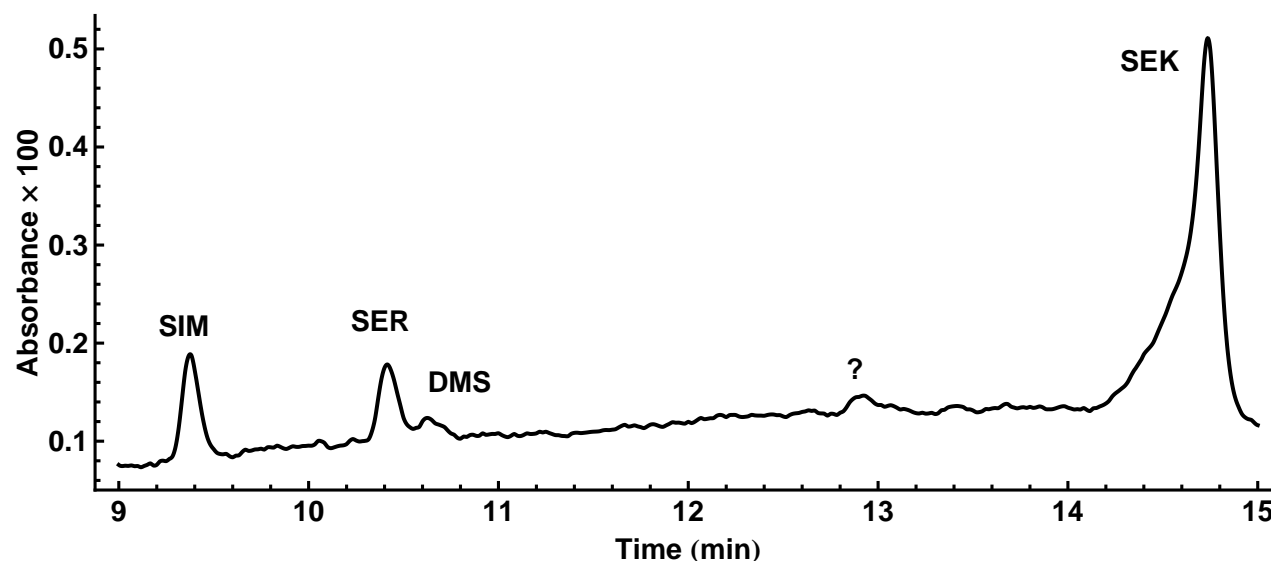
(a) HPLC chromatogram of SER degradation. Question mark (?) indicates an unidentified species

Figure 5.10: LC-MS analysis of SER degradation reaction mixture: $[\mathbf{1c}]:[\text{SER}]:[\text{H}_2\text{O}_2] = 1{:}167{:}1200$ with $[\text{SER}] = 5 \times 10^{-5}$ M in pH 9.50 buffer. HPLC chromatogram after background subtraction (top) and mass spectra for all characterized chemical species injected after 6 min reaction time. The broadening of the SEK peak is thought to arise from the continuous production of SEK from SIM hydrolysis on the column. The mass spectra were compared with those of standards to confirm their identities. Separations were effected on a Waters XTerra RP18 column (100×4.6 mm I.D., 3.5 μm). The gradient elution employed in the LC-MS analysis is listed in Table 5.3. Figure is continued on the next page.
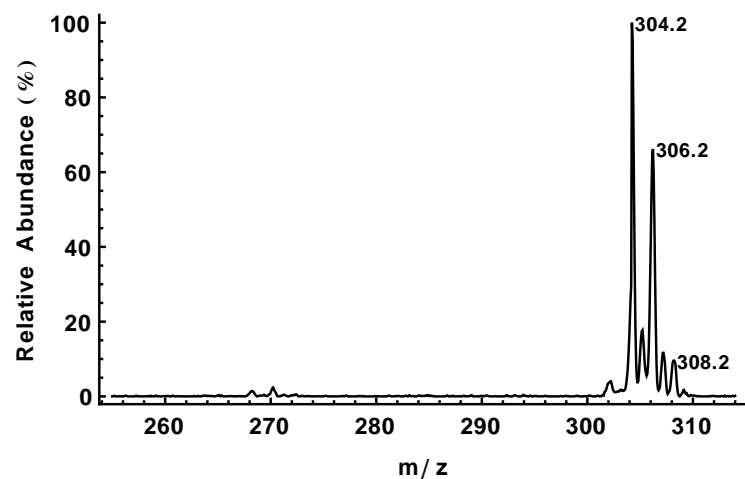
(a) Full Scan MS Spectrum for SIM
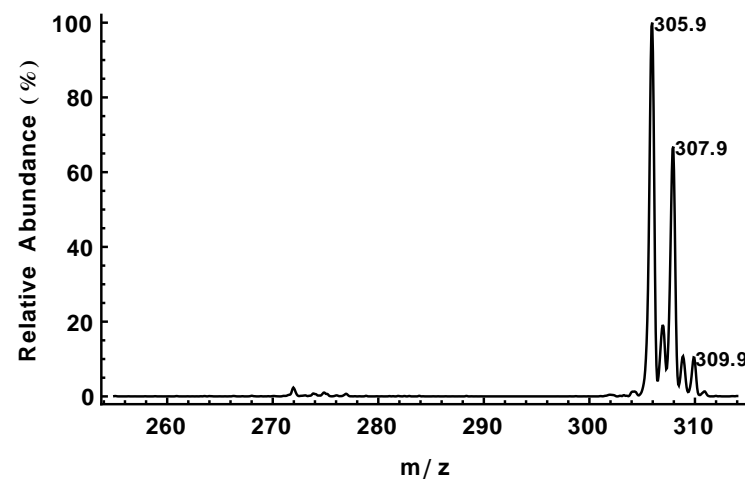
(b) Full Scan MS Spectrum for SER
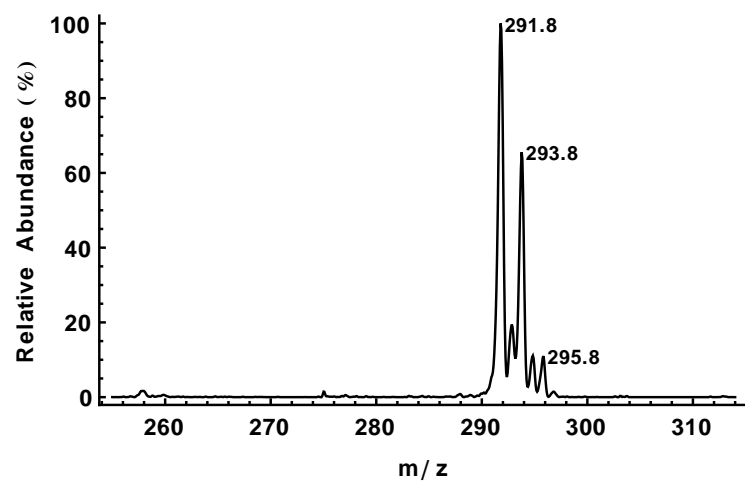
(c) Full Scan MS Spectrum for DMS
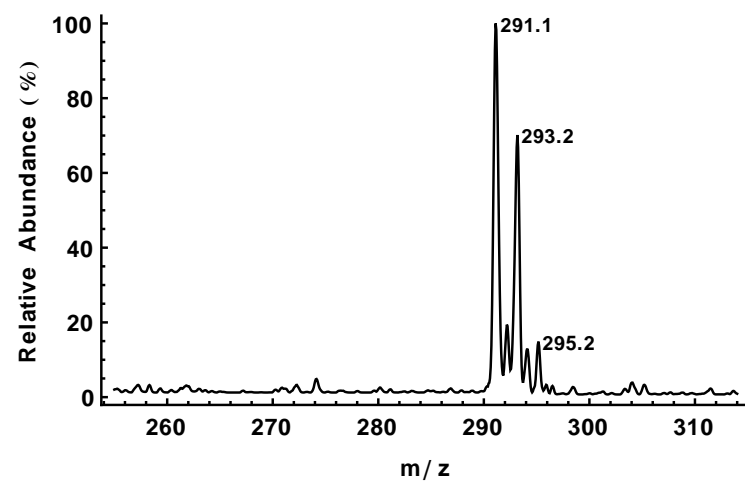
(d) Full Scan MS Spectrum for SEK

Figure 5.10 continued
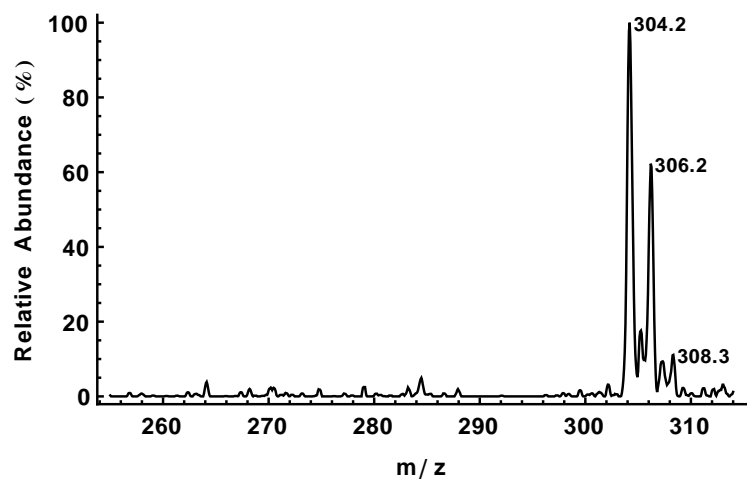
(a) Full Scan MS Spectrum for SIM STD
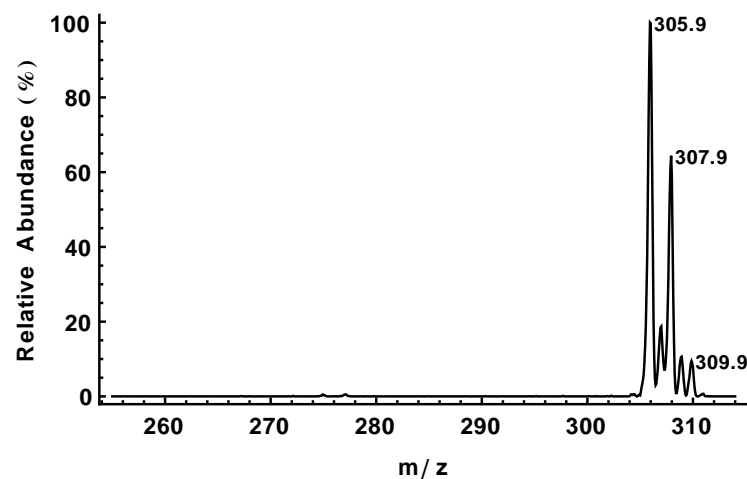
(b) Full Scan MS Spectrum for SER
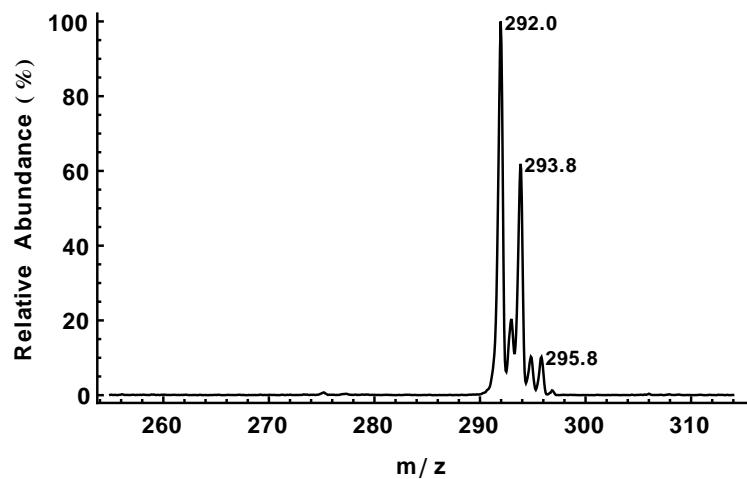
(c) Full Scan MS Spectrum for DMS
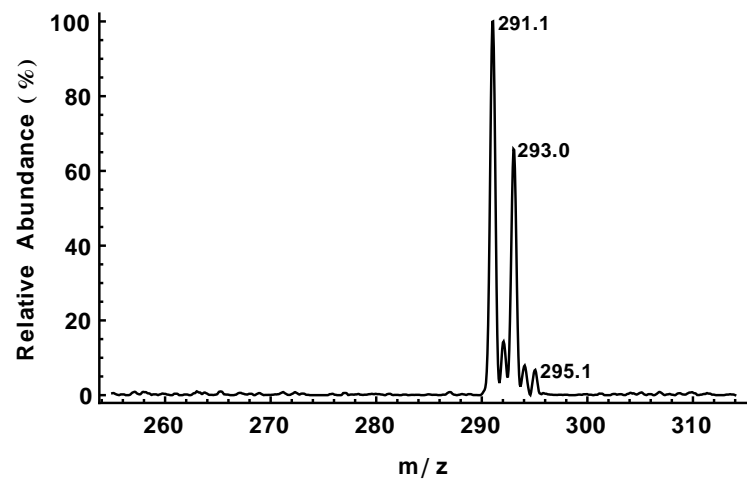
(d) Full Scan MS Spectrum for SEK

Figure 5.12: FIA-APCI full scan mass spectra for SIM, SER, DMS, SEK

Table 5.3: HPLC gradient elution table for SER degradation products characterization. A : MeOH with 0.1% formic acid. B: Water with 0.1% formic acid. Injection volume: 20 μL.

Time (min)	Flow Rate (mL/min)	% Solvent A	% Solvent B
00.00	1.00	30	70
10.00	1.00	90	10
13.00	1.00	90	10
13.01	1.00	30	70
20.00	1.00	30	70

5.7.1.2   SER Degradation : SPE-GC–MS

• **SPE Conditions for Reaction Medium :**

Cartridges: Oasis HLB, 3cc (part# WAT094226)

Conditioning step: 1 mL CH_3OH followed by 1 mL CH_3CN

Rinse step: 1 mL H_2O

Sample Loading: 1 mL reaction mixture

Rinse step: 1 mL H_2O

Elution step: 1 mL CH_3CN

The final CH_3CN elution mixture (1 μL injection volume) was injected into the GC-MS.

• **GC-MS Conditions :**

Column: Restek Rxi5Sil MS (30 m, 0.25 mm id, 0.25 m film thickness)(Cat# 13623). The transfer line temperature was 300 °C. The mass spectrometer was operated in the positive electron ionization mode at 70 eV. An m/z range of $40 - 350$ was scanned and the detector was turned off for the first 4 min of the run.

Table 5.4: GC oven temperature ramp table for SER degradation prodcut characterization

Temperature (°C)	Hold Time (min)	Rate (°C/min)
100	2	20
230	0	3
265	0	20
310	3	
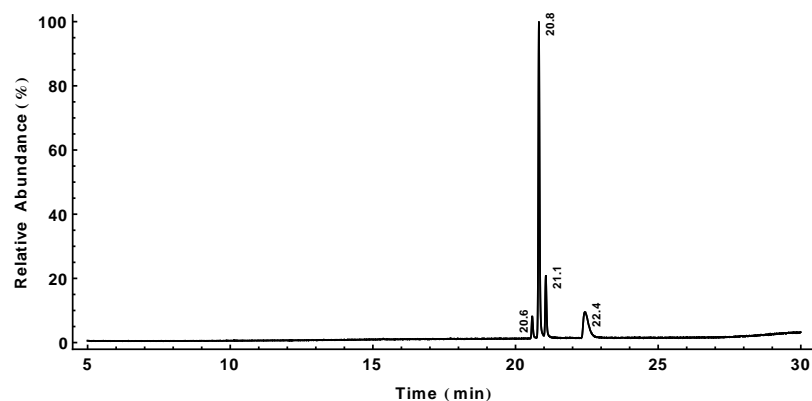
(a) Total ion count chromatogram — Full View
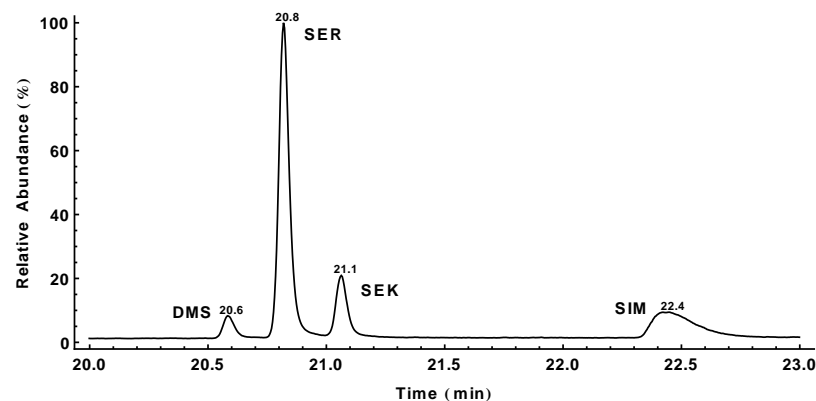
(b) Total ion count chromatogram — Zoom View

Figure 5.13: GC–MS analysis of SER degradation reaction mixture following SPE treatment as described below. A standard library (NIST MS library or user customized library) was used to identify all four eluents appearing on the TIC with minimum matching probability 94.9%.The reaction conditions were $[\mathbf{1c}]{:}[\text{SER}]{:}[\text{H}_2\text{O}_2] = 1{:}300{:}18000$, $[\text{SER}] = 3 \times 10^{-5}$ M in pH 9.5 buffer and the sample was loaded on to the SPE cartridge after 1.5 min reaction time. Figure is continued on the next page.
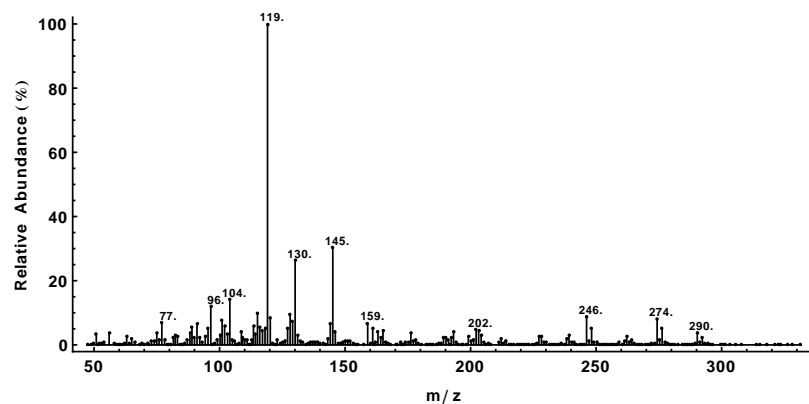
(a) EI MS spectrum for DMS
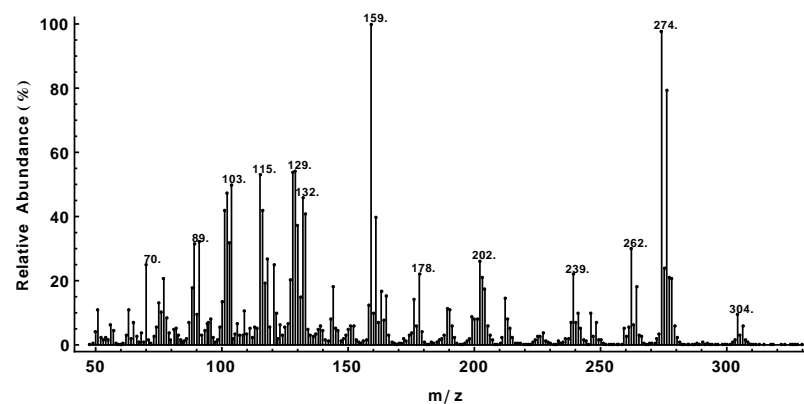
(b) EI MS spectrum for SER
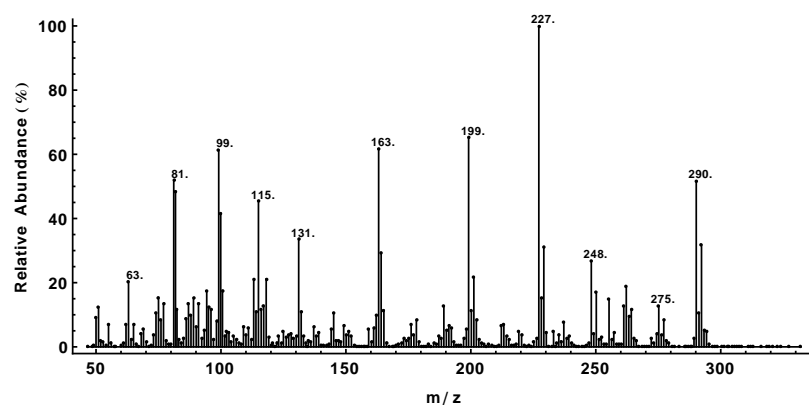
(c) EI MS spectrum for SEK
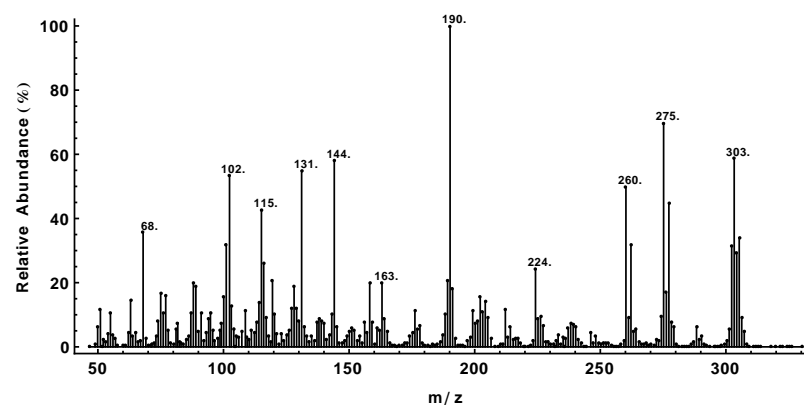
(d) EI MS spectrum for SIM

Figure 5.13 continued
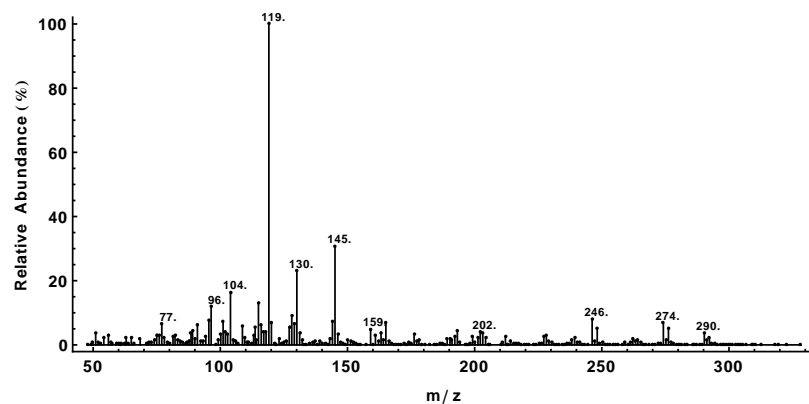
(a) EI MS spectrum for DMS STD
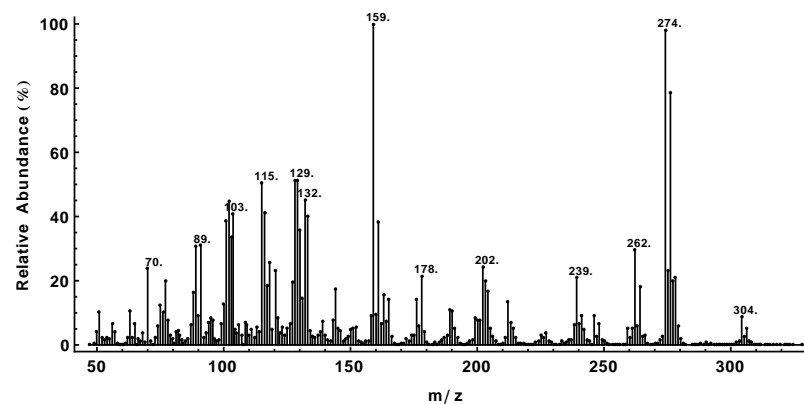
(b) EI MS spectrum for SER STD
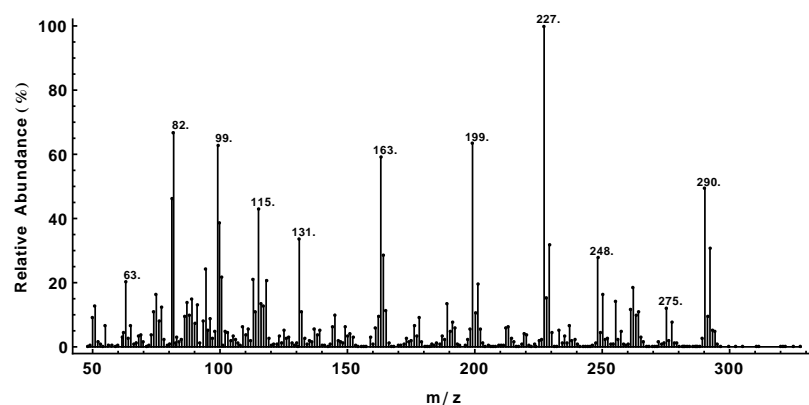
(c) EI MS spectrum for SEK STD
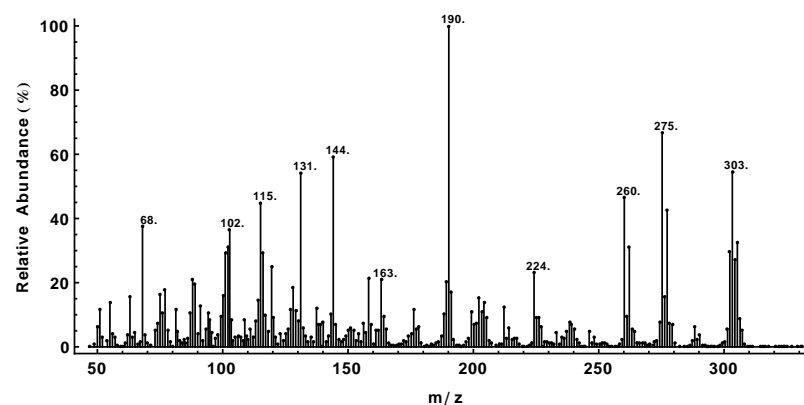
(d) EI MS spectrum for SIM STD

Figure 5.14: GC-MS spectra of DMS, SER, SEK and SIM standards

5.7.1.3   DMS Conversion to SEK : FIA-APCI-MS

Under the treatment of Fe-TAML/H_2O_2, DMS was quickly converted to DMSI as evidenced in Figure 5.8 and Figure 5.9. Further evolution of the reaction leads to one dominant species on the FIA-APCI mass spectrum with nominal mass distribution of 291/293/295 and their signal intensity ratio complies with a dichlorinated compound as seen in Figure 5.15.
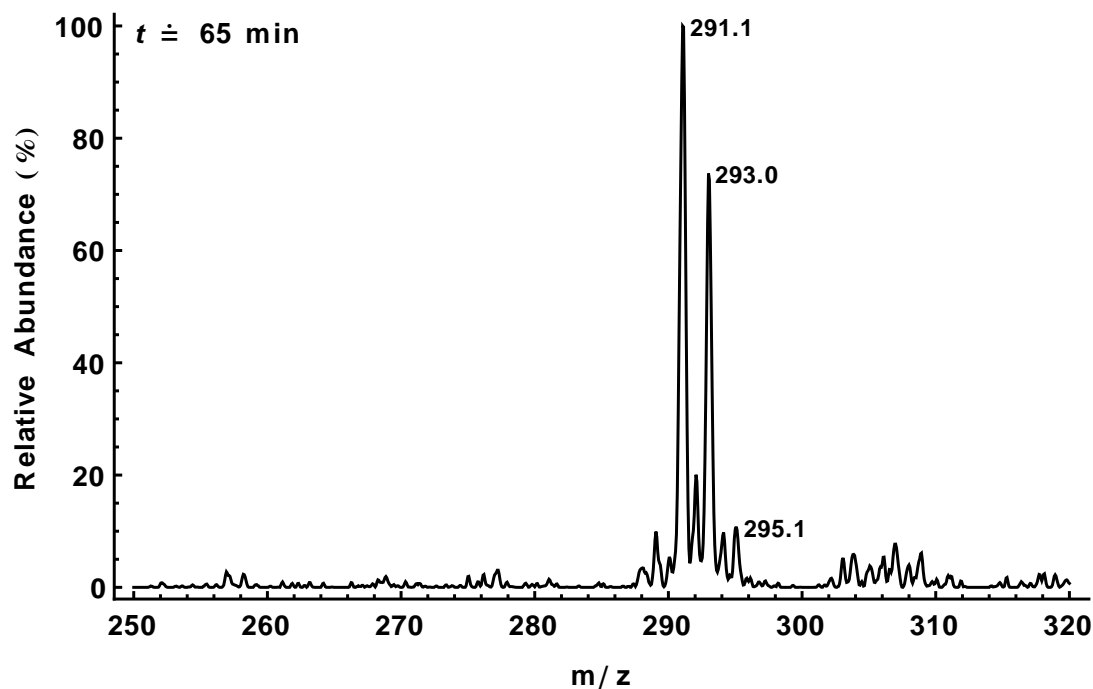
Figure 5.15: Time elapsed FIA-APCI-MS spectra for DMS degradation. Reaction condition : [**1c**]:[DMS]:[H_2O_2] = 1:800:8600, [DMS]=5× 10^{-5}M. pH at 9.25.

Product scan on this mass cluster revealed a fragmentation pattern almost identical to the second order mass spectrum of SEK standard. For a comparison, the product scan mass spectra for this species and SEK standard is displayed in Figure 5.16.

This information suggests that the fate of DMS under the treatment of FE-TAML/H2O2 is SEK, the same as that of SER.
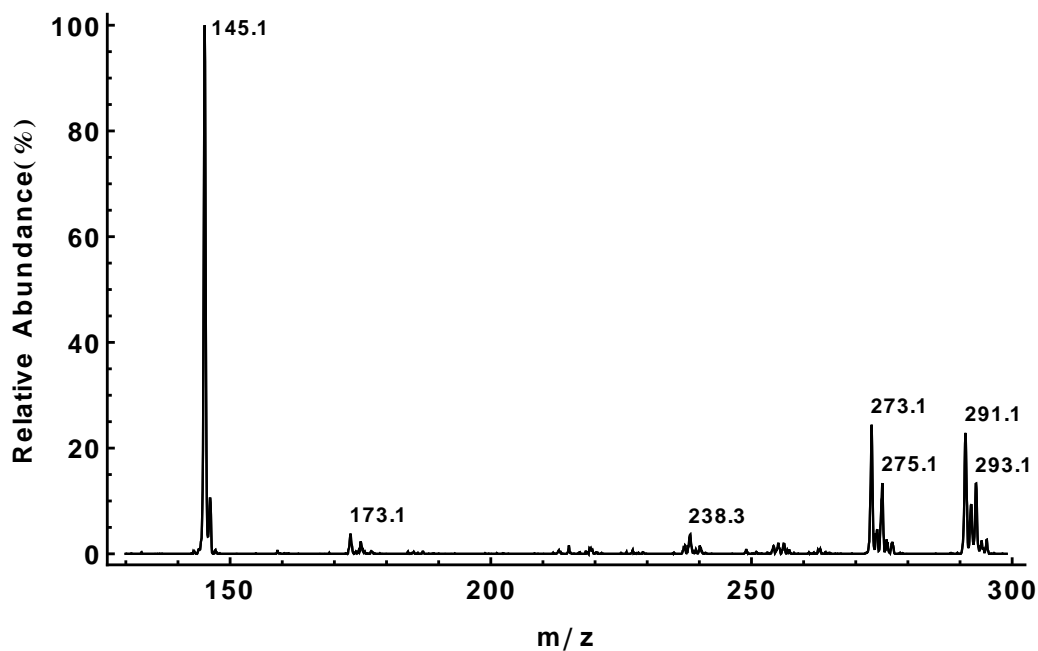
(a) DMS reaction mixture at t ≈ 65 min
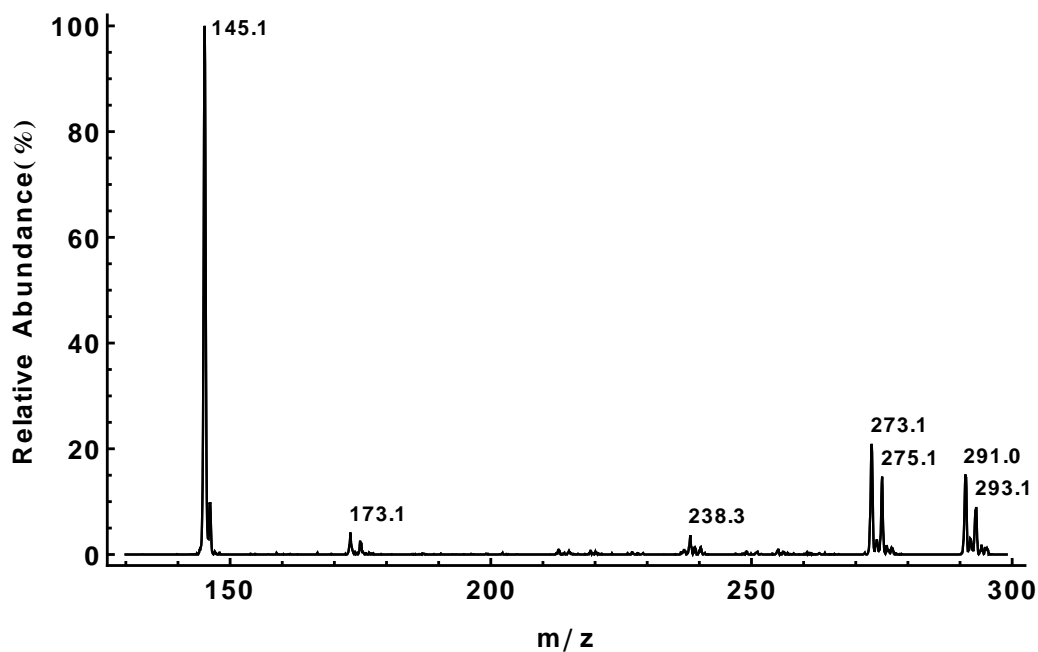
(b) SEK standard

Figure 5.16: Second order tandem mass spectra of SEK standard and the final dominant species in the degradation process of DMS. cf. Figure 5.15 for the reaction condition

5.7.2 Mass Spectra of Analytical Standards and Structure Interpretation

5.7.2.1 SER and DMS
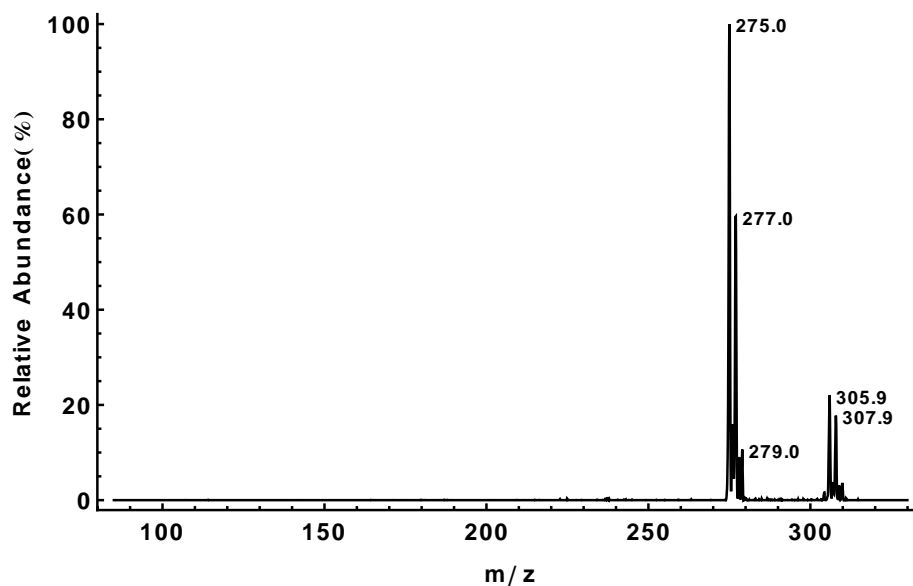
(a) Second order tandem mass spectrum
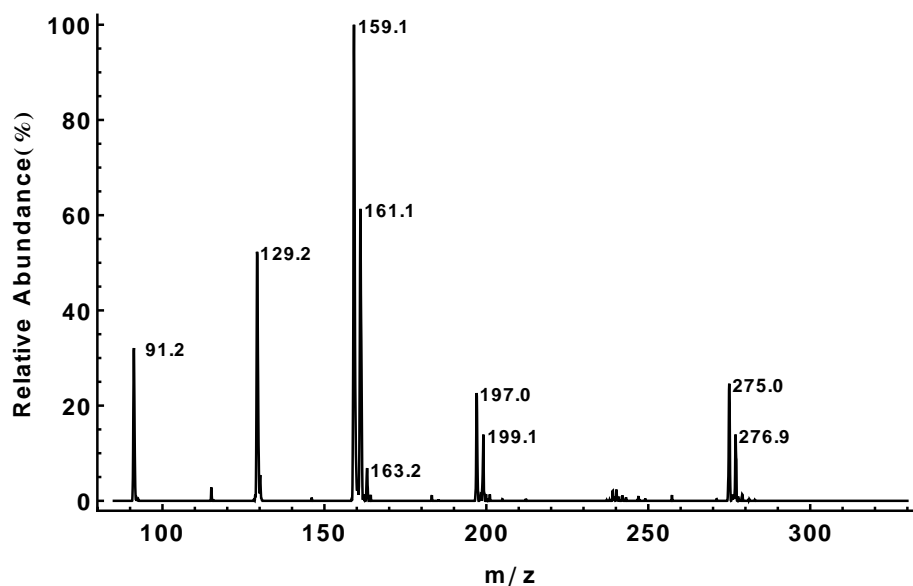
(b) Third order tandem mass spectrum

Figure 5.17: FIA-API mass spectra for SER standard
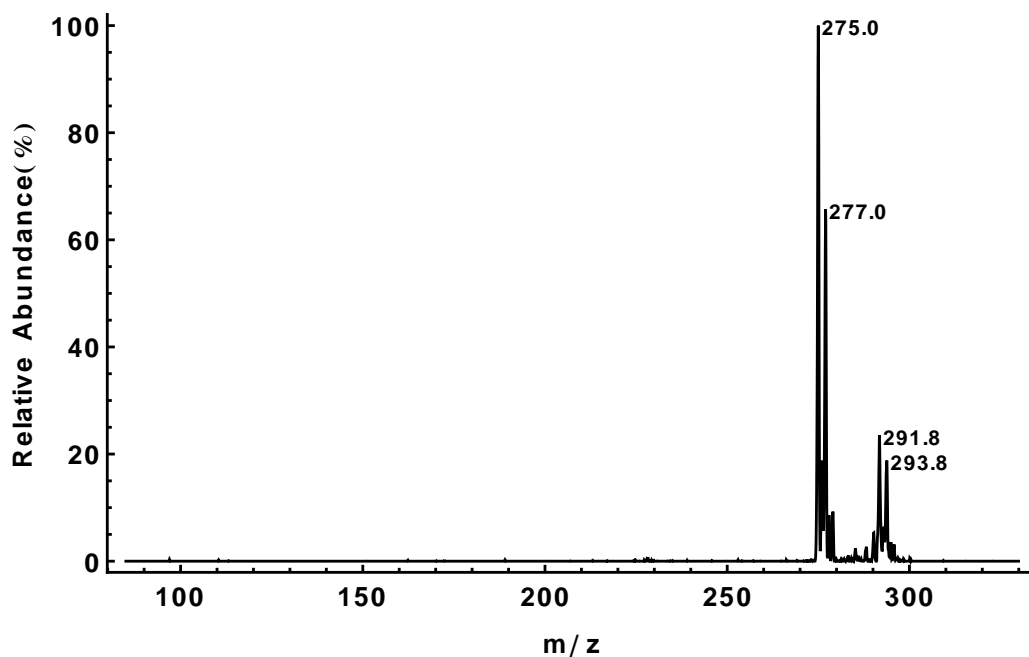
(a) Second order tandem mass spectrum
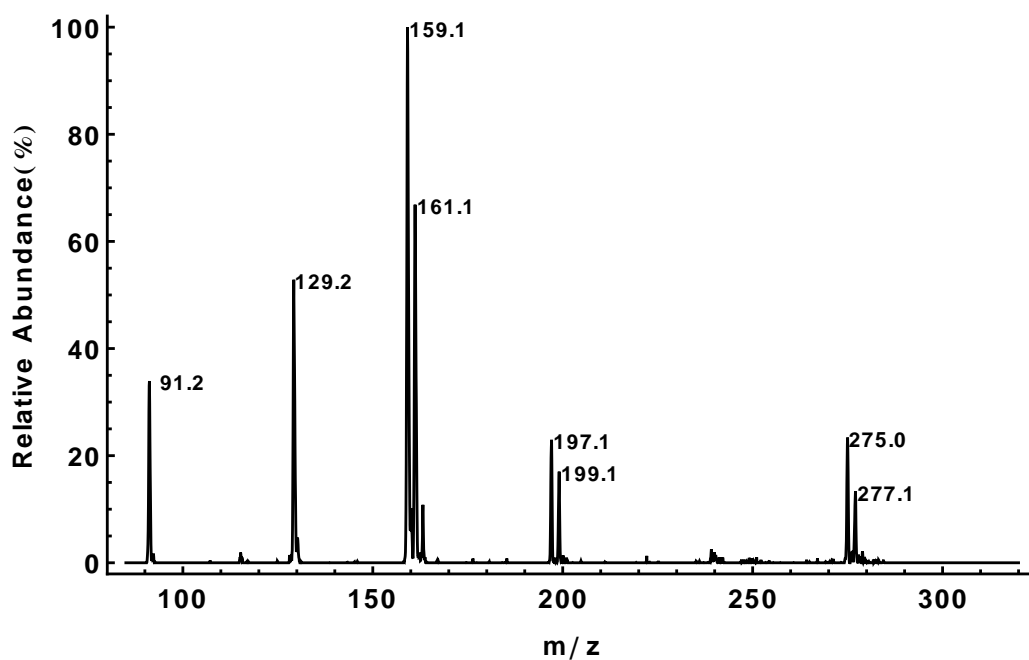
(b) Third order tandem mass spectrum

Figure 5.18: FIA-API mass spectra for DMS standard
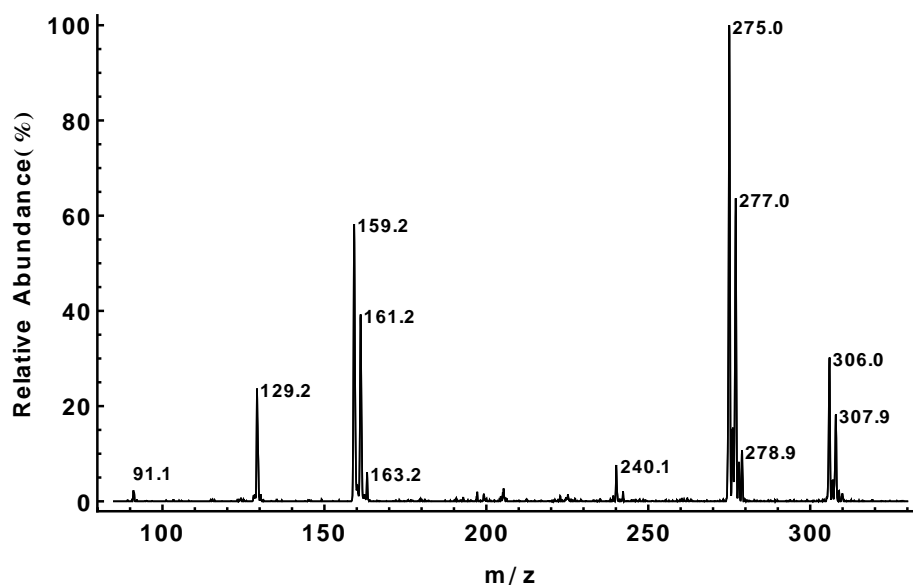
(a) mass spectrum for SER
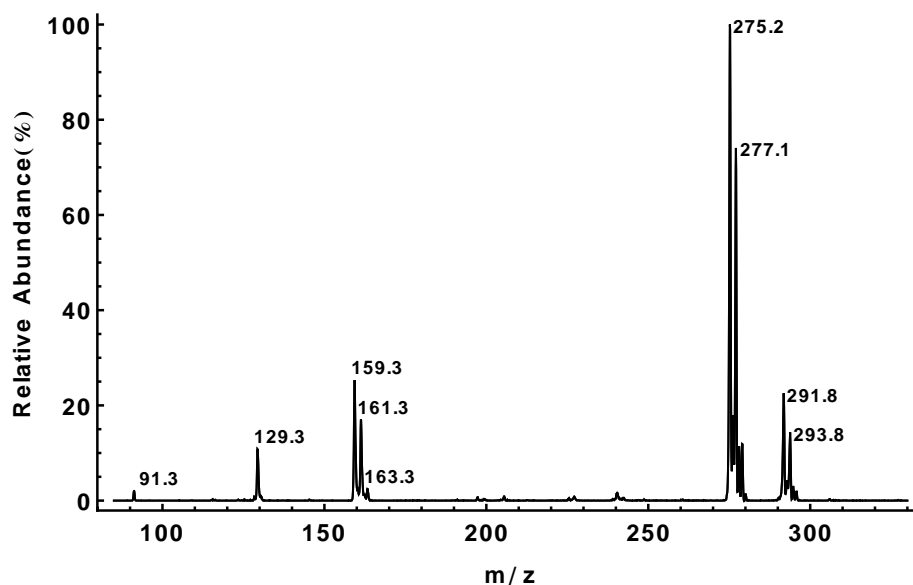
(b) mass spectrum for DMS

Figure 5.19: Comparison of FIA-API in-source fragmentation mass spectra for for SER and DMS standards

Comparison between the in-source fragmentation mass spectra (Figure 5.19) of SER and DMS standards reveals great similarity in the fragmentation patterns since 275/277/279

and downward. This suggests 275/277/279 as common product ion between SER and DMS, and higher order fragmentation are all originated from this species. Compare the in-source fragmentation mass spectra (Figure 5.19) for SER and DMS with their post-source fragmentation spectra (Figure 5.17 and Figure 5.18), substantial similarity unfolds. The almost only difference resides on peak 159/161/163, which does not present appreciably on the in-source fragmentation mass spectra (Figure 5.19). It emphasizes that the in-source fragmentation is not an exact replicate of post-source fragmentation. The former can be a powerful and complimentary tool to the latter in molecular structure elucidation using mass spectrometry.

Based on the tandem mass spectra, the molecular structures for the peaks shown on Figure 5.17 and Figure 5.18 are summarized in Figure 5.20. Structures derivation is shown in Figure 5.23.
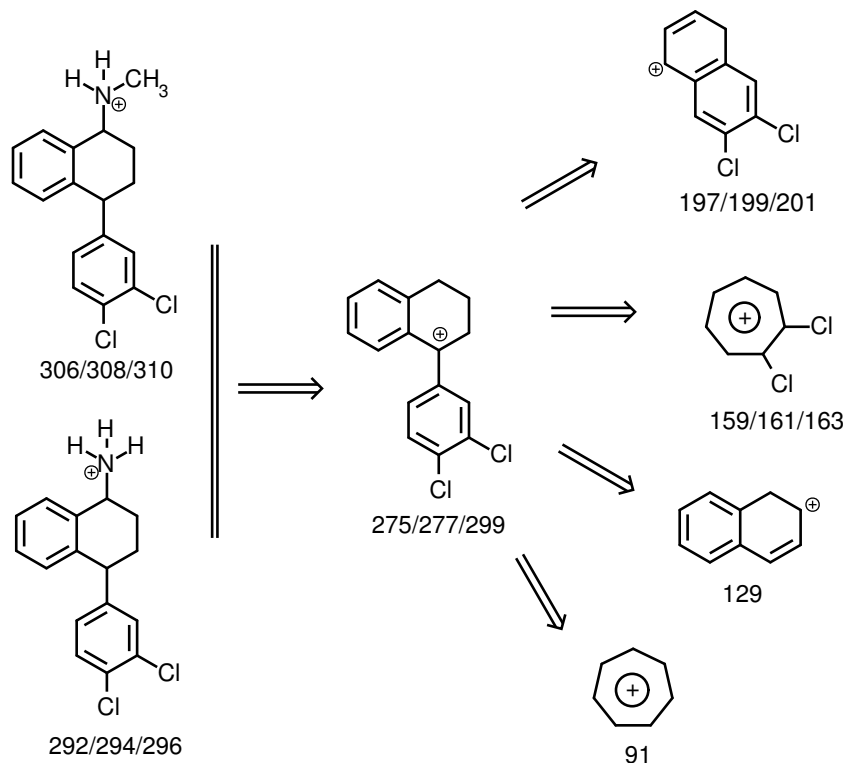
Figure 5.20: Interpretation of tandem mass spectra for SER and DMS standards
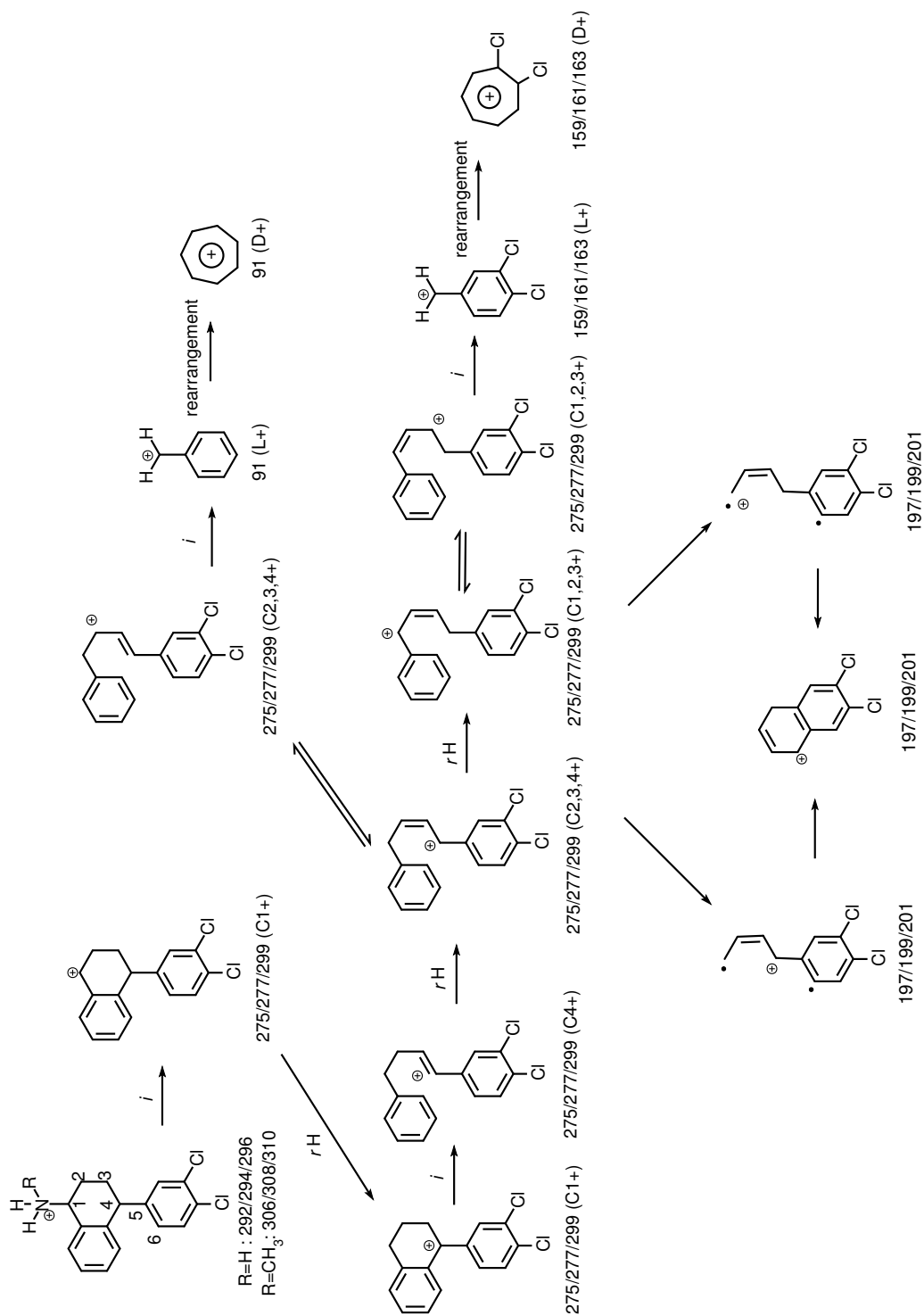
Figure 5.21: Structure derivation for the product ions of SER and DMS for the FIA-API mass spectra

In many cases, there are multiple structural possibilities for one product ion with a specific observed mass number(s) on the spectra Figure 5.17 and Figure 5.18. In those scenarios, the energies of the highly likely structural candidates were computed and compared to decide on the most stable geometries for the assignment on Figure 5.23. More will be discussed in 5.7.3

5.7.2.2 SIM

The proposed structures for SIM product ions (see mass spectra Figure 5.6(a) and (b)) are shown in Figure 5.22. The derivation is demonstrated in Figure 5.23.
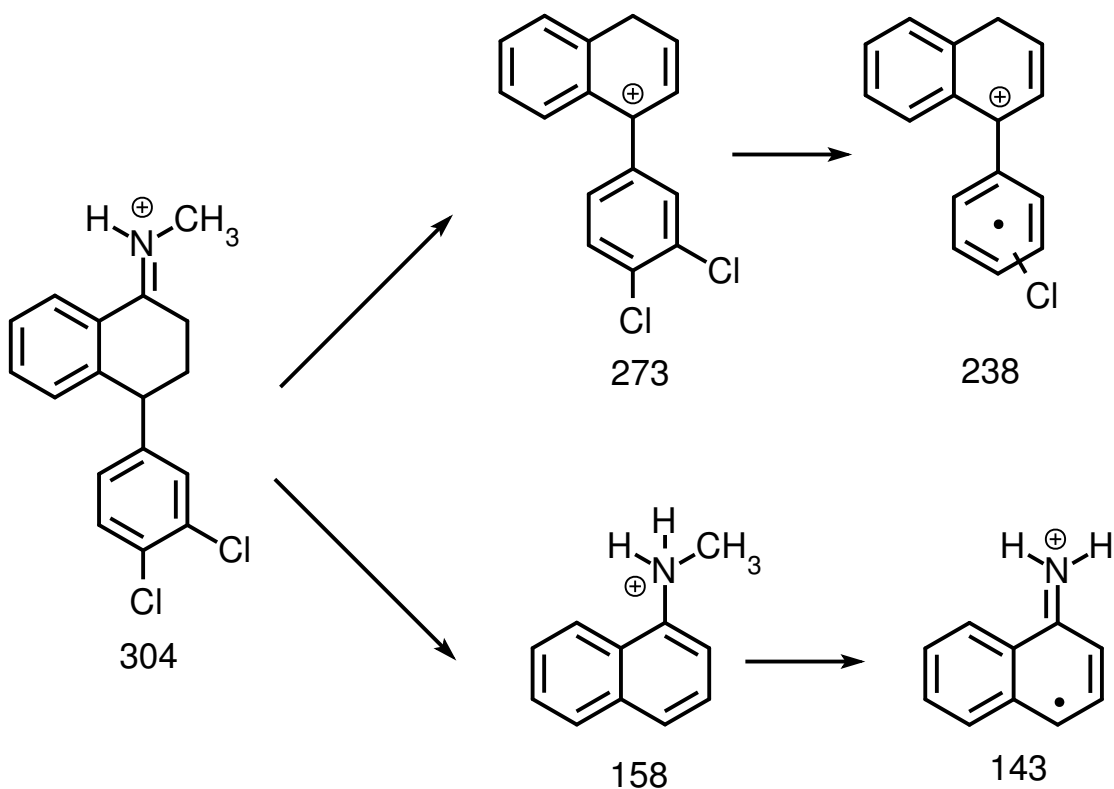
Figure 5.22: Structure derivation for the product ions of SIM for the FIA-API mass spectra
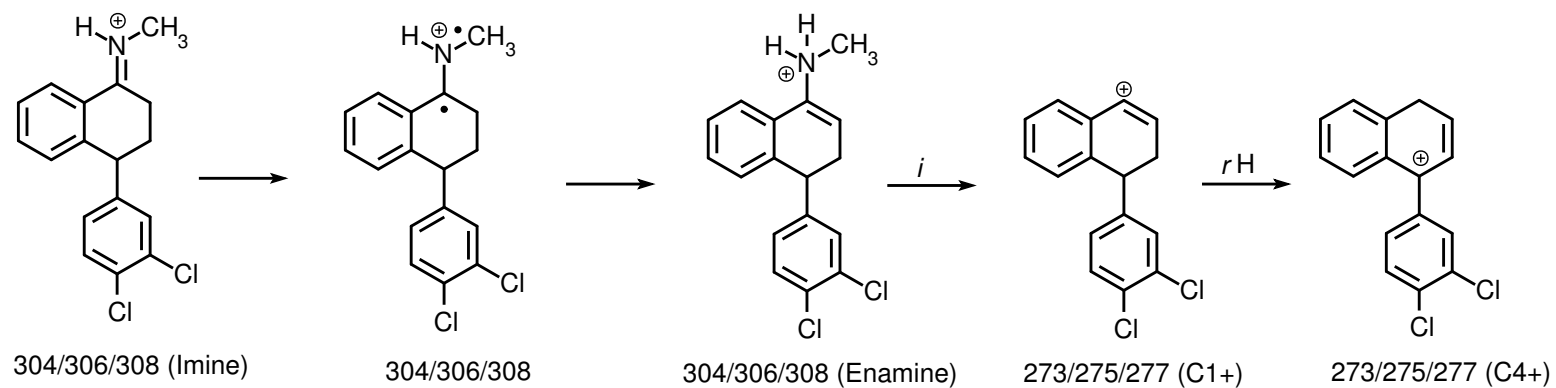
(a) Structure derivation for product ion 273
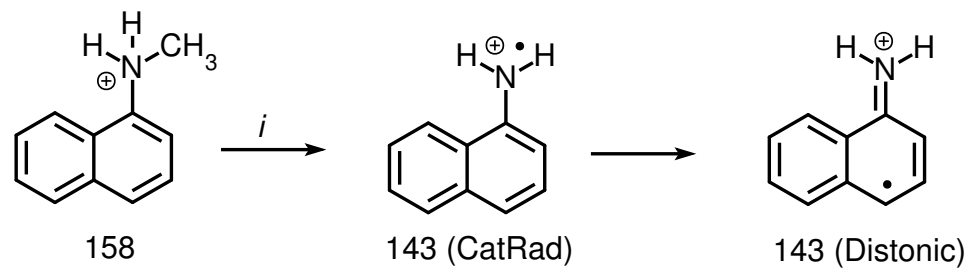
(b) Structure derivation for product ion 143

Figure 5.23: FIA-MS-SIM-STD-Structs

The conversion from 304/306/308 (Imine) to 304/306/308 (Enamine) was conjured via a cation radical intermediate as illustrated in Figure 5.23 (a). Although imine and enamine tautomerization is known in literature,[37,38] DFT calculation disfavors the ground state transition from the imine form of SIM to its enamine form (Figure 5.6(a)).

Another interesting proposal on the SIM standard fragmentation pathway is the product ion structure for 143 (Distonic) (Figure 5.23 (b)). Loss of a methyl group from 158 appears to be very plausible for its given structure to yield a cation radical 143 (CatRad) (Figure 5.23 (b)). However, the electronic structure is likely to be isomerized into its distonic form as reported on many molecules in mass spectrometry.[39,40] Spin density plot (Figure 5.24) based on DFT calculation on this ion also supports this electronic configuration. The spin density share on the α C is about 40% and while N only takes up less than 30% of the total spin density. This indicates that the unpaired electron is highly delocalized and more prone to reside on the α C instead of N. Therefore, the distonic representation is a more accurate description of the electronic configuration of this species.

5.7.3   SER Conformational Analysis and Computation for the Stability of Product Ions in Mass Spectrometry

Isobaric ions present a challenge in assigning the molecular structures to a mass spectrometric peak with a specific mass over charge value. Under such circumstance, computational chemistry can be very helpful and informative in elucidating the more likely answer among all the candidates.[41,42] In our analysis, theoretically projected electronic energies and zero point energies were pursued to provide insightful guidance in determining the most stable configuration among all possible isobaric ions.
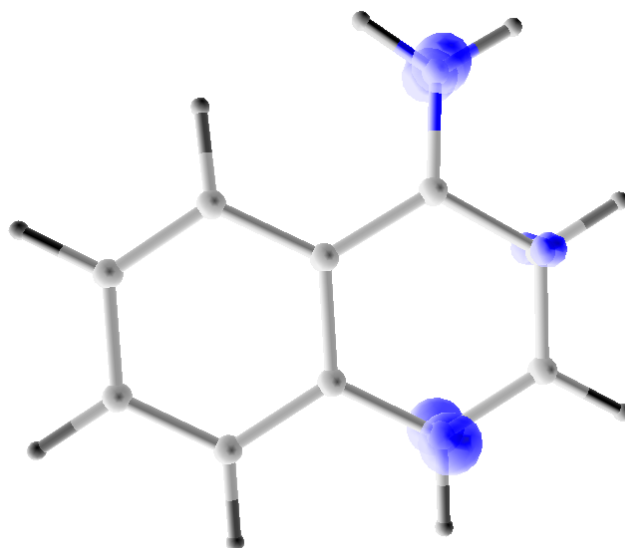
Figure 5.24: Spin density plot of the product ion with nominal mass 143 of SIM standard

Computational suite Gaussian 09[43] was employed to carry out Becke's three parameter hybrid functional (B3)[44,45] along with the Lee-Yang-Parr correlation functional (LYP).[46] The basis set 6-31G(d) was applied to all elements in the molecule and 6-31+G(d) was applied to Cl atom solely. All geometry optimizations converged to the default criteria set by Gaussian.

5.7.3.1   SER Conformational Analysis

The reported crystals of SER show polymorphism.[47–52] This entails a conformal analysis on SER prior to investigating energetic information. Observing the molecular structure of SER, it has two major rotatable bonds, one connecting the methylamine moiety to the three ring part of the molecule and the other one connecting the dichlorobenzene moiety to the 1-methylamine naphthalene moiety. Sampling the dihedral angle space of R-N-C1-C2 and C3-C4-C5-C6 (Figure 5.23) using the relaxed potential surface scan method, a 2D energy profile for SER is generated (Figure 5.25).
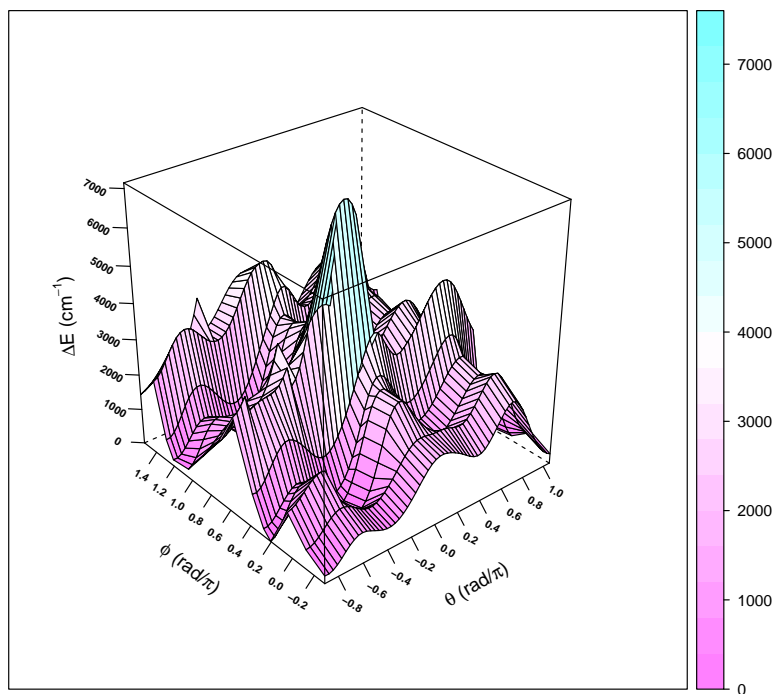
(a) 3D profile
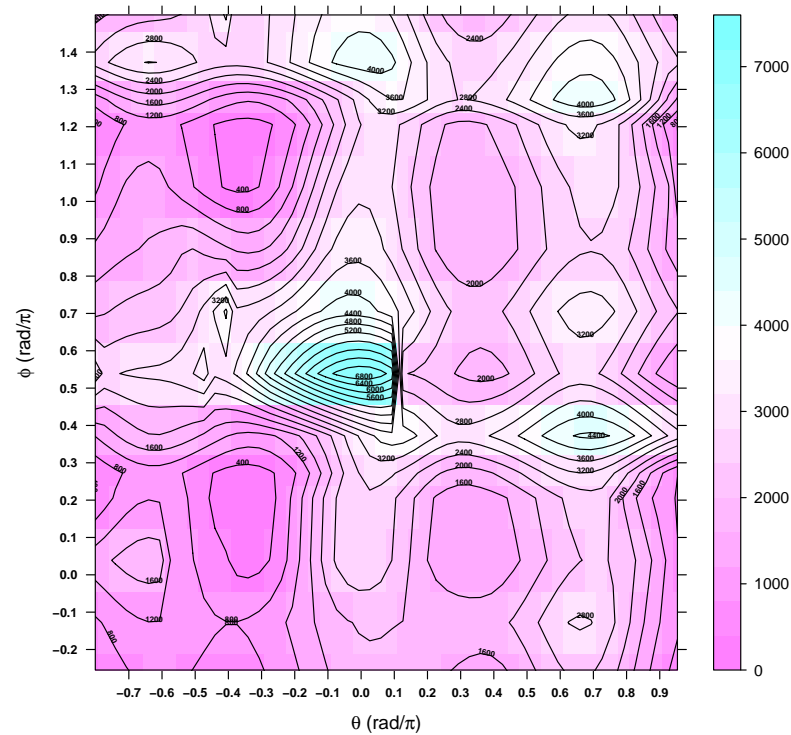
(b) 2D contour

Figure 5.25: Potential surface of protonated SER generated by DFT calculation. (a) z-axis energy is the electronic energy. (b) the energy of the contours has the unit cm^{-1}. In both (a) and (b), ϕ is defined as the dihedral angle C3-C4-C5-C6 and θ represents the dihedral angle R-N-C1-C2 (Figure 5.23).

As seen in the Figure 5.25 (a), two global energy minima reveal at the approximate (θ, ϕ) coordinates (-0.35 , 0.05) and (-0.35 , 1.15). They can probably be more obviously spotted on the contour plot (Figure 5.25 (b)) with contour labeled with 400. These two minima correspond to two configurations of the dichlorobenzene moiety. One has one chloro group pointing upward (Figure 5.26, red and blue) with respect to the cyclohexane semiplane and the other one has one chloro group pointing downward (Figure 5.26, yellow and green). In addition, two small local minima are seen on the 3D profile or the 2D contour plot (Figure 5.25 (a) and (b)). These two local minima are located in the vicinity of (0.4 , 0.1) and (0.4 , 1.0). They correspond to two configurations of the methylamine moiety. As shown on Figure 5.26, the methylamine moiety can orient toward (red and blue) the benzene ring or away from the benzene ring (green and yellow).

Figure 5.26 is an overlay plot of four optimized SER crystal structures that available in the Cambridge Structural Database (http://www.ccdc.cam.ac.uk/Solutions/CSDSystem/Pages/CSD.aspx). The four conformers mostly overlap with each other in the three-ring region of the molecule. The difference primarily originates from the orientation of the dichlorobenzene moiety and the methylamine moiety. This structural variation divides the four conformers into to two large groups, red and blue, and yellow and green. Clearly, the polymorphism of SER crystals can be well approximated by variation of the two dihedral angles R-N-C1-C2 and C2-C3-C4-C5 (Figure 5.23). Sampling these two variables results four major minima on the potential surface (Figure 5.25) and they have good correspondence from the crystal structures. Therefore, relaxed potential surface scan presents a powerful tool to explore the energy profile of small organic molecules. The geometry corresponds to the global minimum in energy is obtained and used as the initial conformation for the energy computation for product ions resolved on mass spectra.
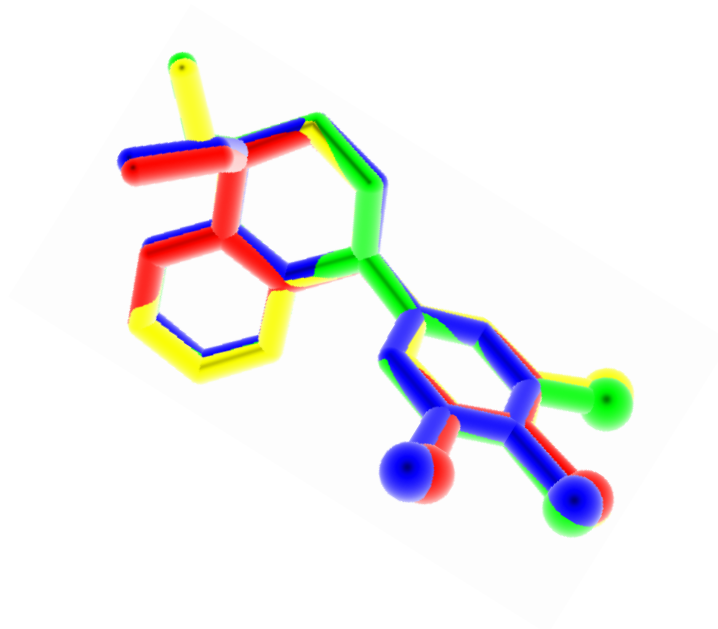
Figure 5.26: Optimized SER crystal structures overlay. Hydrogen atoms are removed for clarity. Colors (red, yellow, green and blue) are used to differentiate four crystal structures of SER. C and N are shown in as sticks and Cl atoms are shown as van der Waals sphere.

5.7.3.2 Computed Enegies for Product Ions of Interest

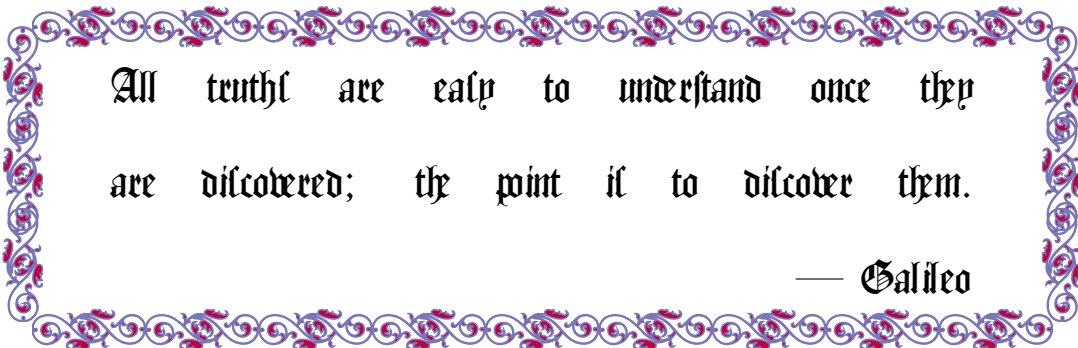The computed electronic energy plus zero point energy for the isobaric product ions on the mass spectra (Figure 5.6, Figure 5.17, and Figure 5.18) is summarized in the Table 5.5.

Table 5.5: Energy table for the isobaric product ions of interest.

precursor ion	isobaric ion 1	isobaric ion 2	Δ E (cm^{-1})
SER/DMS	275/277/279 (C1+)	275/277/279 (C4+)	-4305
SER/DMS	275/277/279 (C1,C2,C3+)	275/277/279 (C2,C3,C4+)	-2485
SER/DMS	91 (L+)	91 (D+)	-3165
SER/DMS	159/161/163 (L+)	159/161/163 (D+)	-496
SIM	273/275/277 (C1+)	273/275/277 (C4+)	-22400

Δ E refers to E(isobaric ion 2) - E(isobaric ion 1)

Chapter 6

Degradation of Fluoxetine — the active ingredient in Prozac® — by Fe-TAML/Hydrogen Peroxide Inspiring Green Pharmaceutical Design

> All truths are easy to understand once they are discovered; the point is to discover them.
>
> — Galileo

6.1 Abstract

Fluoxetine, the active ingredient in antidepressant Prozac, represents the first member of the serotonin receptor reuptake inhibitors (SSRIs) family and is one of the most successful among all members. Its top prescription record among SSRIs and extra stability leads to prevalent occurrence in the environment. Environmental studies showed that FLX can be toxic to aquatic species at trace level of exposure and disruptive to their neurosystems. Therefore, it is urgent to seek an environmentally friendly solution to diminish the harm FLX can potentially bring to the environment. TAML$^{\circledR}$ plus hydrogen peroxide system is thus employed in this study to treat FLX in the laboratory settings. As a result, FLX was degraded to harmless endpoints. An elusive intermediate along the degradation pathway was proposed and its fleet fate was studied using DFT calculations. The cascade breakdown feature of FLX under TAML$^{\circledR}$/H$_2$O$_2$ treatment inspires green pharmaceutical design.

6.2 Introduction

Pharmaceuticals are increasingly detected in the environment.[1–5] Among all prescribed drugs, antidepressant is ranked on the top in US.[6] The most prescribed antidepressants are serotonin receptor reuptake inhibitors (SSRIs).[7] As the first molecule of a new generation of SSRI, fluoxetine (FLX) soon became the mostly prescribed SSRI after its introduction in 1988.[8] Correspondingly, FLX occurrence in the environment is frequently encountered.[9–12]

FLX is a very stable synthetic compound. It resists hydrolytical and photolytical degradation over 30 days in aqueous solutions.[13] Apart from its defiant to natural attenuation, FLX shows high potency of soliciting biological responses at minute levels. Ecotoxic studies have shown FLX bears aquatic and sediment toxicity to

certain organisms.[14,15] It was also reported that FLX was able to inhibit cytochrome P450 3A4 by metabolic intermediate complex formation.[16] More recently, research has discovered that FLX can delay the development of Rana pipiens larvae[17] and disrupt the neurosystem of fish.[18]

With the mounting evidence listed above, the risk FLX poses to the environment tolerates no ignorance. It motivates researchers to seek a solution to reduce or eliminate the harm from FLX. In this chapter, TAML®/H_2O_2 system is employed for such a purpose. Molecular structure of TAML® is provided in Scheme 5.1. Only catalysts **1a** and **1c** were used in the FLX degradation study.

6.3 Experimental

6.3.1 Materials

Fluoxetine hydrochloride (($\pm$)$-$N$-$Methyl$-\gamma$-[4-(trifluoromethyl)phenoxy]benzenepropanamine hydrochloride), norfluoxetine (NFLX) hydrochloride (($\pm$)$-\gamma$-(4-Trifluoromethylphenoxy) benzenepropanamine hydrochloride), benzaldehyde, 4-trifluoromethylphenol, and 4-hydroxybenzoic acid were purchase from Sigma Aldrich. Cinnamaldehyde-E, hydrogen peroxide 30% w/w) was purchased from Fisher Scientific. Formic acid, potassium hydroxide, sodium carbonate, sodium bicarbonate, monopotassium phosphate, dipotassium phosphate, HPLC grade water, methanol, and acetonitrile were obtained from commercial sources (Aldrich, Fisher, Acros and Fluka). The TAML activators were synthesized according to the published method.[19] The concentration of hydrogen peroxide stock solution was calibrated by UV-Vis spectroscopy using the molar absorption coefficient (72.4 $M^{-1}cm^{-1}$) at 230 nm.[20]

6.3.2 Sample Preparation

Fluoxetine(FLX) and norfluoxetine(NFLX) stock solutions were prepared in methanol. In a typical degradation reaction, the reagents were added in the following order into either HPLC or GC sample vials: buffer, FLX or NFLX, TAML catalyst **1/c**, and H_2O_2. The pH of the reactions was controlled with sodium carbonate/sodium bicarbonate (10^{-2} M) for pH 9.25 and pH 10.25 and monopotassium phosphate/dipotassium phosphate (10^{-2} M) for pH 8.25. The reaction mixture was homogenized using Pasteur pipettes for the reaction development and the medium was analyzed at various times by HPLC and GC–MS.

6.4 Analysis and Discussions

6.4.1 HPLC Analysis

6.4.1.1 Instrumentation Parameters

HPLC analysis was performed on a Shimadzu Prominence HPLC equipped with a SPD-M20A photodiode array detector and a SIL-20AC UFLC autosampler. A gradient elution method was used and is provided in Table 6.1.

Table 6.1: LC Gradient elution method in FLX degradation analysis

Time (min)	Flow Rate (mL/min)	% Solvent A	% Solvent B
00.00	1.00	30	70
10.00	1.00	90	10
13.00	1.00	10	90
15.00	1.00	30	70
20.00	1.00	30	70

Mobile phase : A = ACN with 0.1% formic acid; B = H_2O with 0.1% formic acid. Injection volume: 20 μL. Stationary phase : Phenomenex Lura Phenyl-Hexyl 150 mm × 4.6 mm column with the particle size of 3.0 μm. Flow rate is at 1 ml/min.

6.4.1.2   FLX Decay Monitoring

FLX degradation were treated by two catalysts, $[\mathbf{1a}]{:}[\text{FLX}]{:}[\text{H}_2\text{O}_2] = 7 : 150 : 8400$ and $[\mathbf{1c}]{:}[\text{FLX}]{:}[\text{H}_2\text{O}_2] = 1 : 100 :$ 5600 with $[\text{FLX}] = 3{\times}10^{-5}$ M. The two sets of reactions were run in parallel under three pH regimes, 8.25, 9.25 and 10.25 (cf. 6.3.2). Time-elapsed FLX decay curves were generated based HPLC analysis (Figure 6.1).
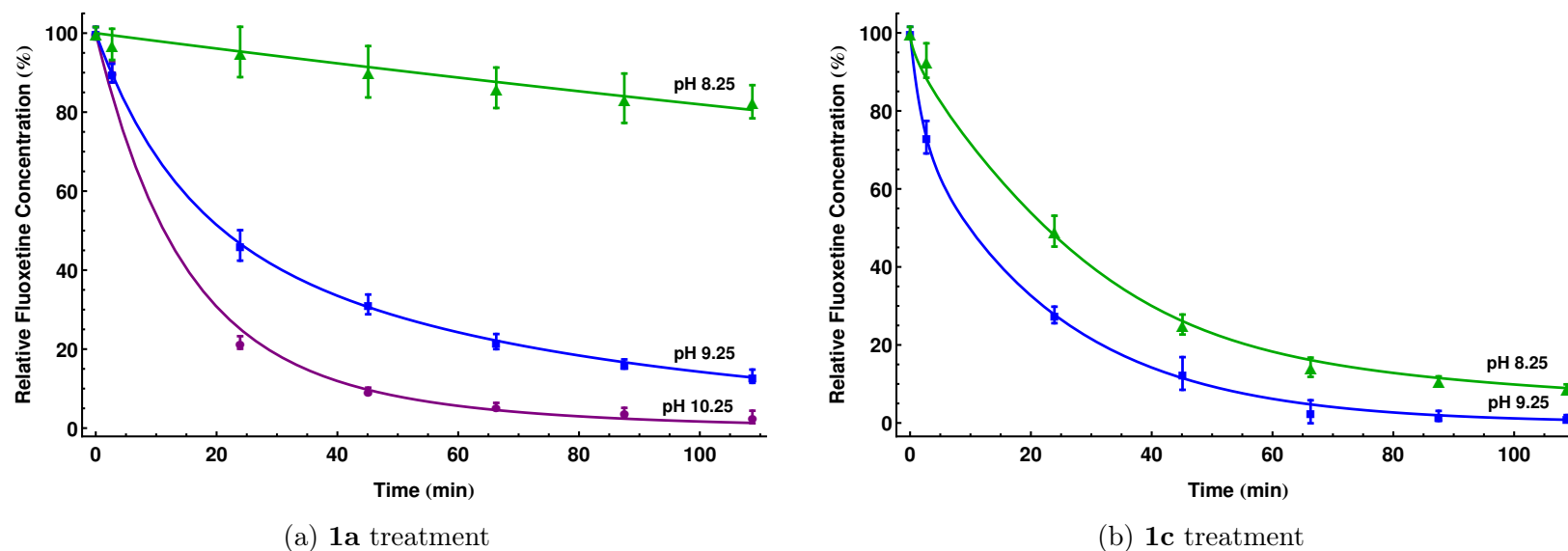

(a) **1a** treatment (b) **1c** treatment

Figure 6.1: FLX decay curve monitored by HPLC observation. Reaction at pH 10.25 for **1c** treatment is too fleeting to record sufficient data points for plotting.

As noticed from Figure 6.1, 50% of FLX degradation can be achieved less than 25 min under pH 9.25 and pH 10.25 for **1a** and all pH conditions for **1c**.

6.4.1.3   FLX Degradation Products Characterization

HPLC analysis of FLX reaction mixtures revealed several peaks on the chromatogram.
By comparing the retention times of the peaks for standards (Figure 6.2) and the reac-
tion mixture (Figure 6.3), reaction product peaks A, C, D, F, and G were identified as
4-hydroxybenzoic acid, norfluoxetine, fluoxetine, cinnamic acid and cinnamaldehyde
respectively . This characterization was further confirmed by spiking those peaks
with standards, which shows an increase in intensity for all in Figure 6.4.
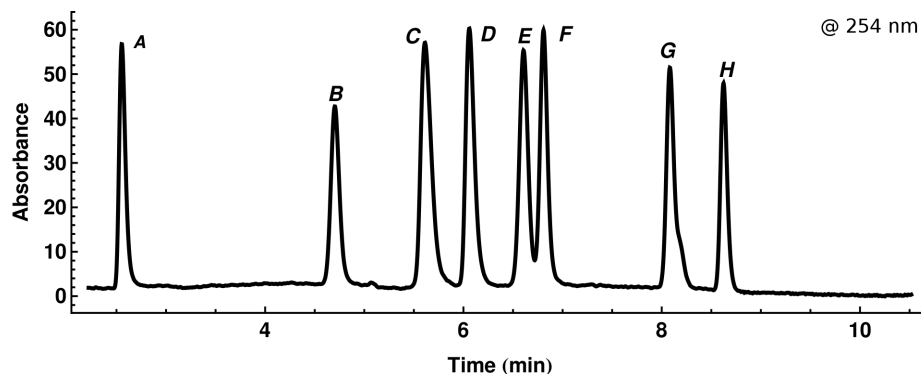
Figure 6.2: HPLC chromatogram of analytical standards : A — 4-hydroxybenzoic
acid ; B — Benzoic acid; C — Norfluoxetine; D — Fluoxetine; E — Bezaldehyde; F
— Cinnamic acid; G — Cinnamaldehyde; H — 4-trifluoromethyl phenol
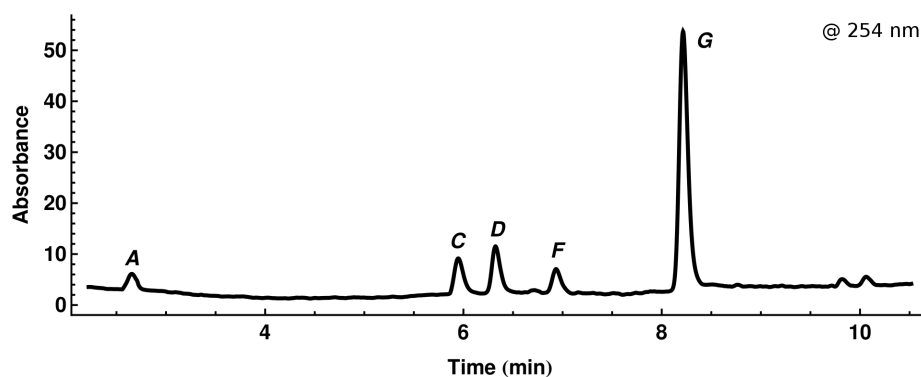
Figure 6.3: HPLC chromatogram of reaction mixture in FLX degradation study. Rxn
condition : [**1c**]:[FLX]:[H_2O_2] = 1:100:5600, [FLX]=5E-5M, pH 8.25 buffer. A — 4-
hydroxybenzoic acid ; B — Benzoic acid; C — Norfluoxetine; D — Fluoxetine; E
— Bezaldehyde; F — Cinnamic acid; G — Cinnamaldehyde; H — 4-trifluoromethyl
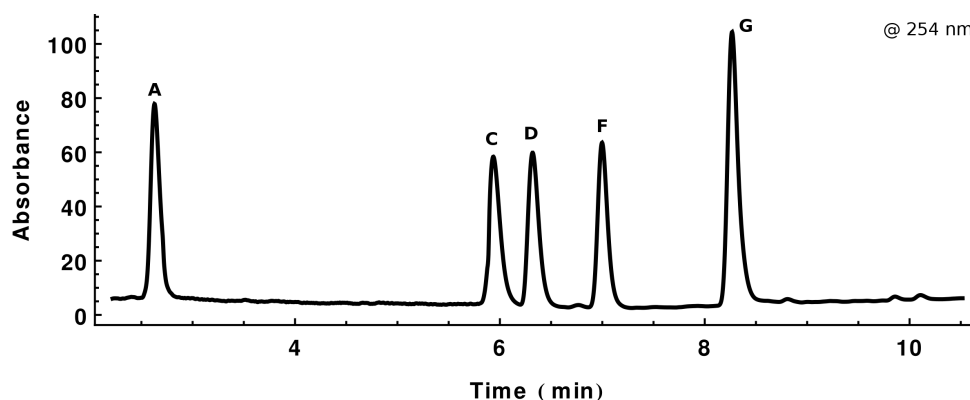phenol

Figure 6.4: HPLC chromatogram of reaction mixture in FLX degradation study. A — 4-hydroxybenzoic acid ; B — Benzoic acid; C — Norfluoxetine; D — Fluoxetine; E — Bezaldehyde; F — Cinnamic acid; G — Cinnamaldehyde; H — 4-trifluoromethyl phenol

6.4.2   SPME-GC-MS Analysis

6.4.2.1   Instrumentation Parameters

GC-MS analysis of FLX degradation products were performed on a Thermo scientific DSQ MS with TRACE GC equipped with a LEAP Combi PAL® autosampler. Direction immersion(DI) solid phase microextraction(SPME) method was employed as the sampling method. Optimized parameters for SPME operation are listed in Table 6.2.

Table 6.2: Parameters for SPME-GC-MS analysis of FLX degradation products

preincubation time	10.0 sec
incubation temperature	100 °C
extraction time	3.0 min
desorption time	3.0 min

SPME fiber : Supelco®, PA 85 μm, 57294-U. SPME liner : 75×1 PTV, Thermo, P/N 45322054.

Analysts were introduced into the GC column (Restek, Rxi®-XLB MS) via the splitless injection mode. The oven temperature ramping program is given in Table 6.3.

Table 6.3: Oven temperature ramping program for GC-MS analysis of FLX degradation products

	Rate (°C/min)	Temp (°C)	Hold Time (min)
Initial		45	1.00
Ramp 1	25.0	260	0.00
Ramp 2	2.0	270	0.00
Ramp 3	20.0	300	1.00

6.4.2.2 FLX Degradation Products Characterization

SPME-GC-MS analysis of FLX degradation reaction mixture reveals the total ion chromatogram in Figure 6.5. Cinnamaldehyde, Bezaldehyde and 4-hydroxybenzoic acid were identified as the degradation products of FLX under TAML treatment.
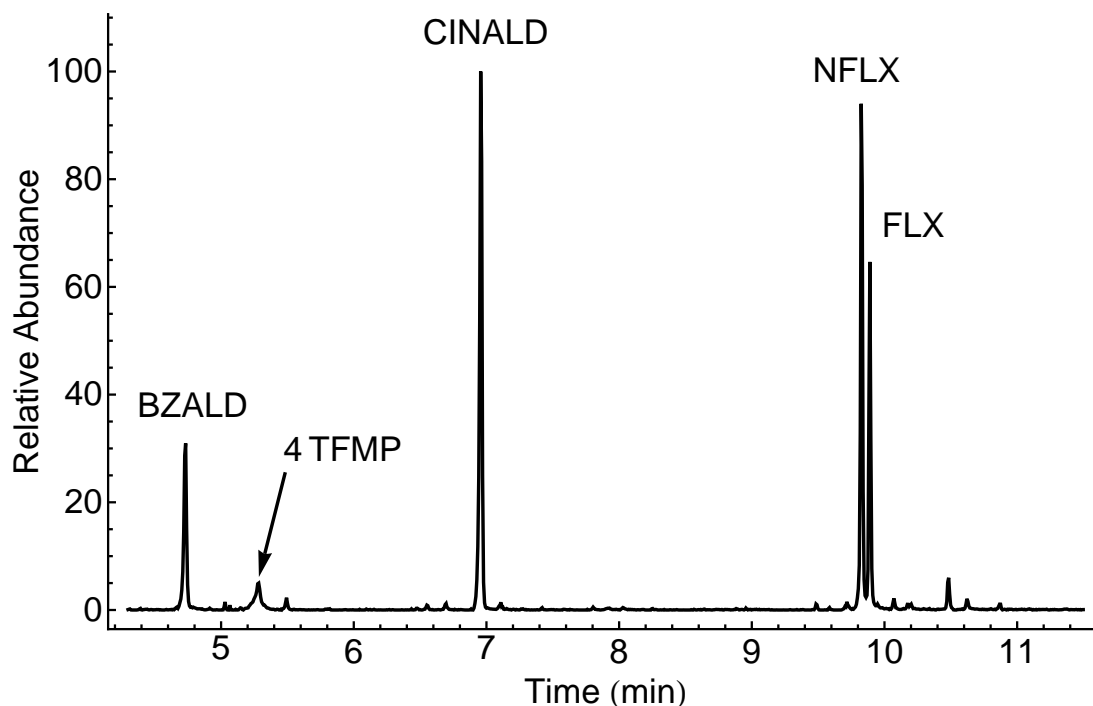
Figure 6.5: GC-MS total ion chromatogram for FLX degradation reaction mixture. Reaction condition : [**1c**]:[FLX]:[H_2O_2] = 5:100:5600, [FLX]=5E-5M, pH 10.25 buffer
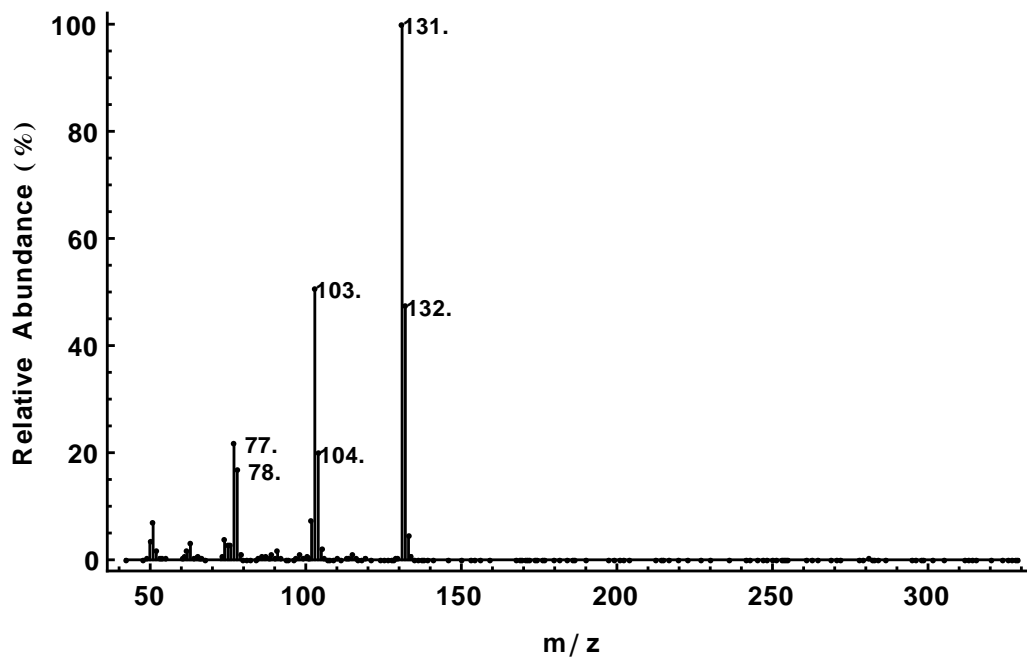
Figure 6.6: EI full scan mass spectrum for BZALD in the FLX degradation mixture. Reaction conditions refers to Figure 6.5.
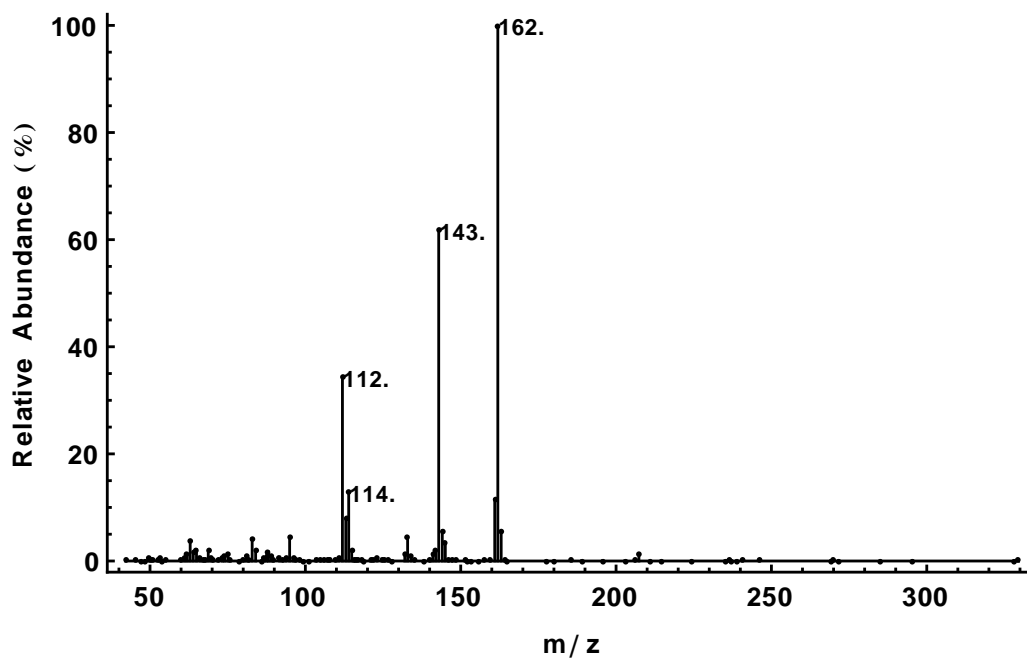

Figure 6.7: EI full scan mass spectrum for 4-TFMP in the FLX degradation mixture. Reaction conditions refers to Figure 6.5.

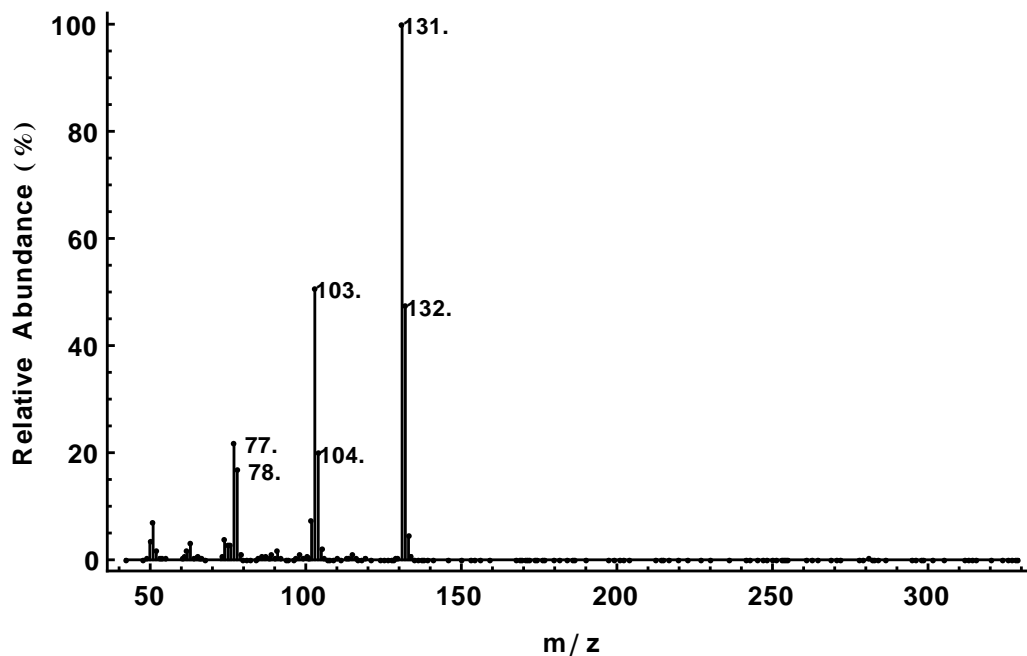Figure 6.8: EI full scan mass spectrum for CINALD in the FLX degradation mixture. Reaction conditions refers to Figure 6.5.

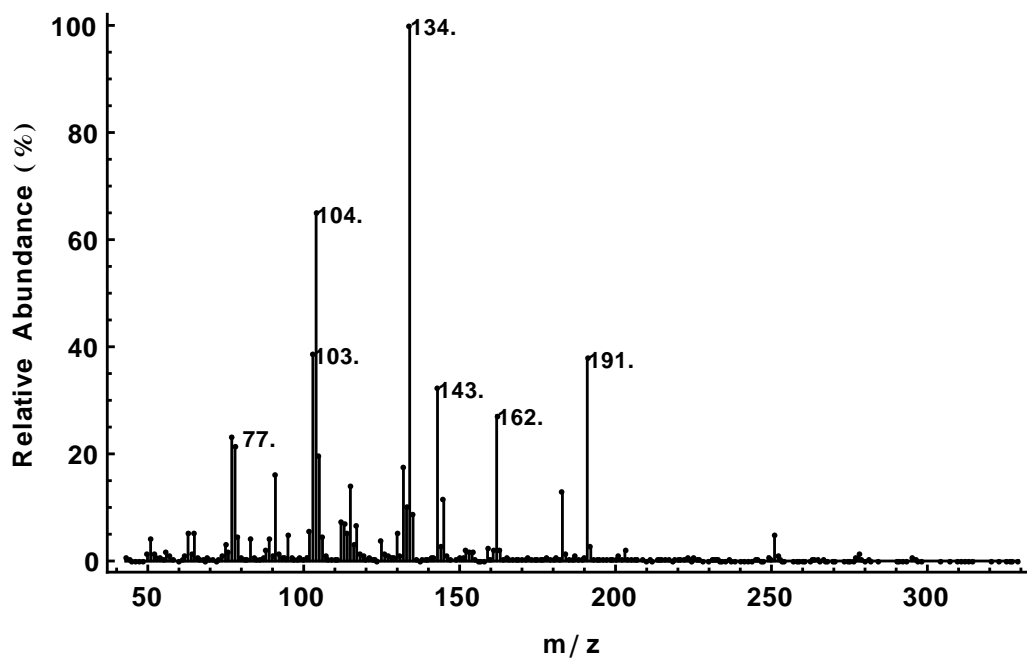Figure 6.9: EI full scan mass spectrum for FLX in the FLX degradation mixture. Reaction conditions refers to Figure 6.5.

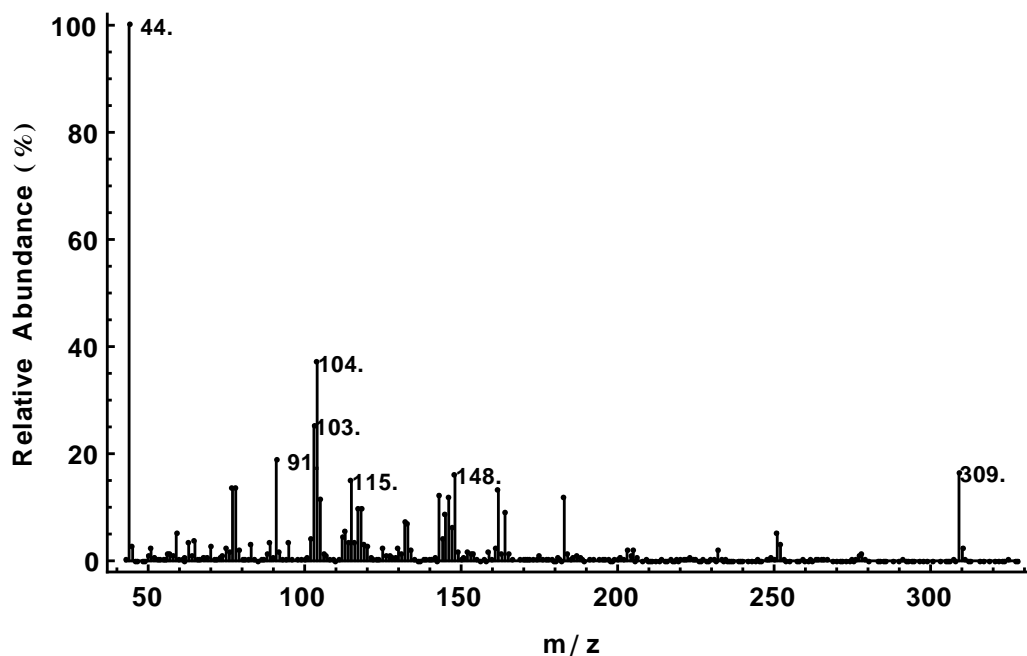Figure 6.10: EI full scan mass spectrum for FLX in the FLX degradation mixture. Reaction conditions refers to Figure 6.5.

6.4.3 NMR Analysis

Nuclear magnetic resonance analysis was performed on a Bruker Avance™ 500 MHz NMR facility. Samples subject to NMR analysis were prepared in a solvent system with 90% H_2O and 10% D_2O. Watergate technique was employed to suppress the water signal on the spectra.

Comparing the spectrum (1), (2) and (3) (Figure 6.11), one can see that the -CH_3 and -CH_2 signals on the FLX degradation mixture, indicating NFLX is a degradation product of FLX. Additionally, the peak near 8.5 ppm corresponding to $HCOO^-$ on the spectrum (3) appears as a distinctive signal not observed on FLX or NFLX standards. This observation suggests $HCOO^-$ is one of the oxidation products of FLX under TAML treatment. Such a hypothesis is supported by the spiking experiment (spectrum (4)), in which the $HCOO^-$ signal intensity increased after addition of $HCOO^-$ into the FLX degradation mixture.
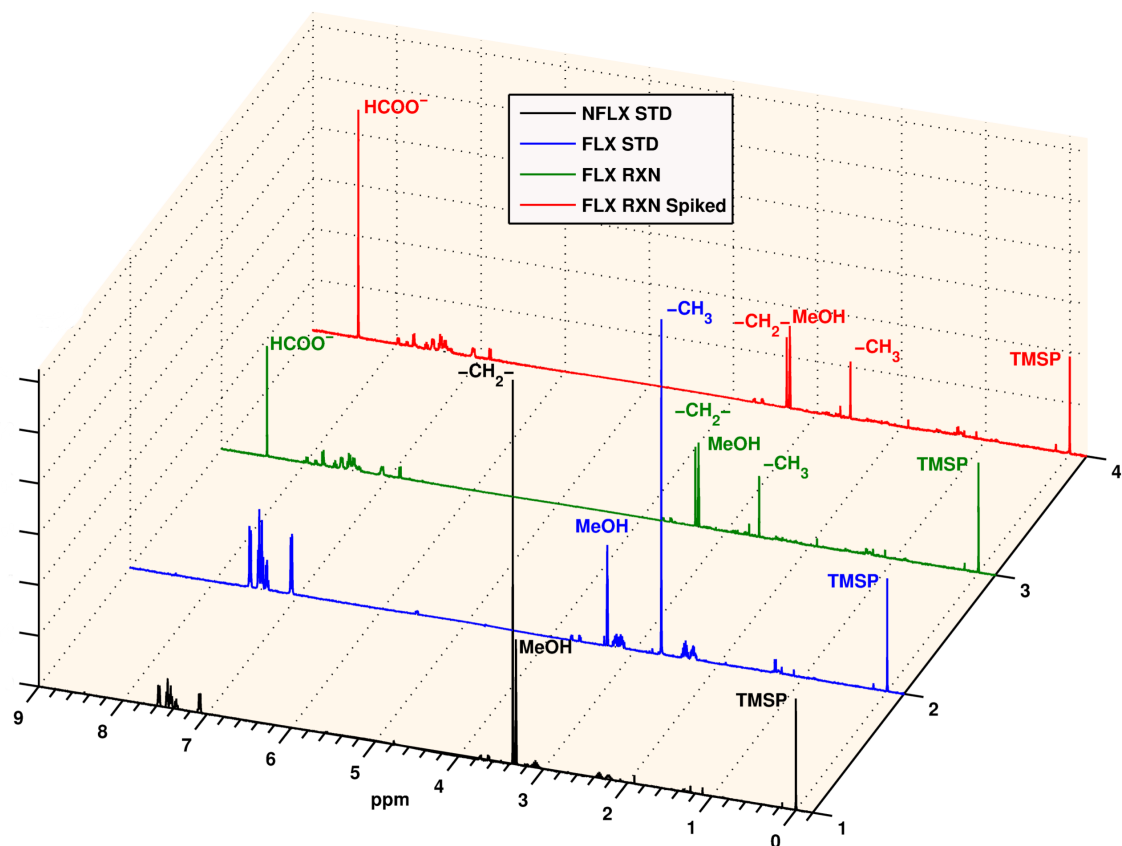
Figure 6.11: NMR stack plot to compare FLX, NFLX standards with FLX degradation reaction mixture. NMR Spectra of NFLX standard (1), FLX standard (2), FLX reaction mixture (3) and FLX reaction mixture spiked with formic acid (4). MeOH signal originated from the FLX or NFLX stock solution. Rxn condition : [**1a**]:[FLX]:[H$_2$O$_2$] = 1:1000:8000, [FLX]=2E-4M, pH 9.25 buffer.

## 6.4.4 Hydrolysis of 4-trifluormethylphenol

GC-MS analysis of FLX degradation mixture shows that 4-trifluormethylphenol (4TFMP) as a degradation production of FLX with small signal intensity on the total ion chromatogram (Figure 6.5). However, this signal did not show up on the HPLC chromatogram (Figure 6.3). This triggers the curiosity of studying the hydrolytic sensitivity of this compound. As shown in Figure 6.12, 4TFMP rapidly turns into 4HYBA in a basic medium in the absence of oxidizing agents. Figure 6.12(a) is the time-elapsed UV-Vis spectra stack plot, indicating 4TFMP conversion to 4HYBA.
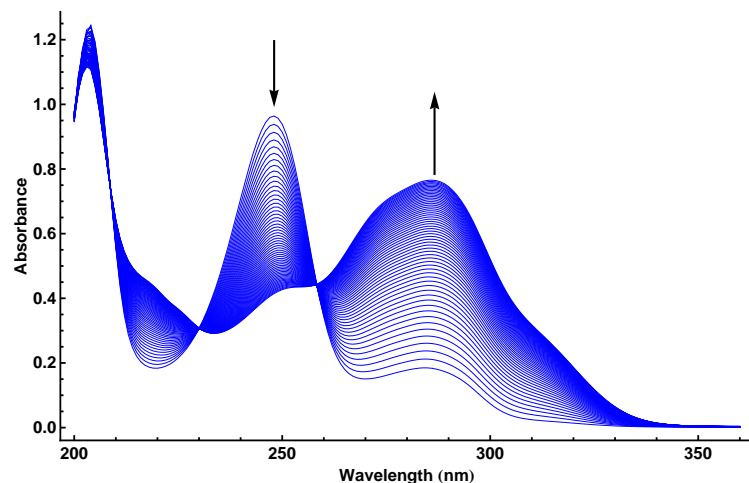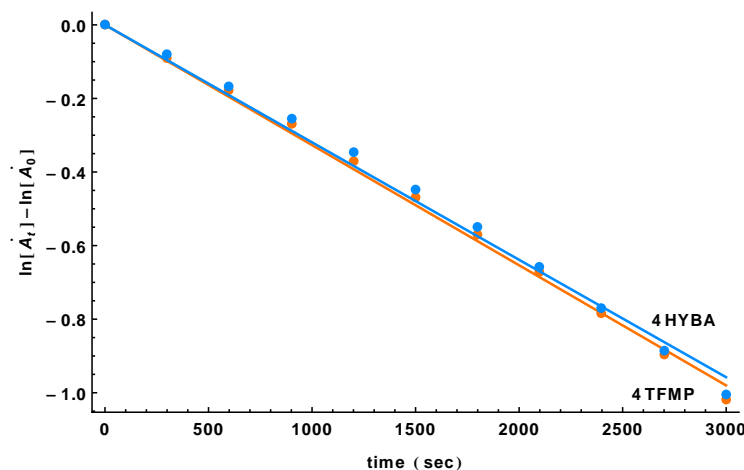
(a) 4TFMP Overlay Plot
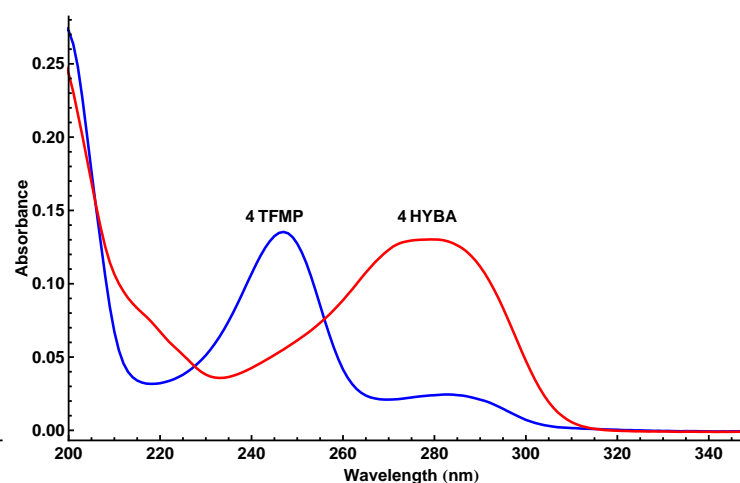
(b) 4TFMP and 4HYBA Overlay
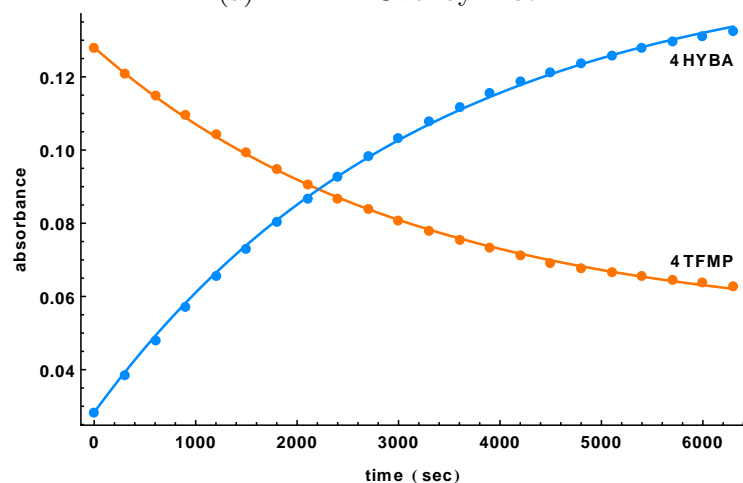
(c) Kinetic Curves

(d) Linearization

Figure 6.12: 4TFMP Hydrolysis at pH 10.25 monitored by UV-Vis spectroscopy. See 6.7.1 for the mathematical treatment in linearizing the kinetic data.
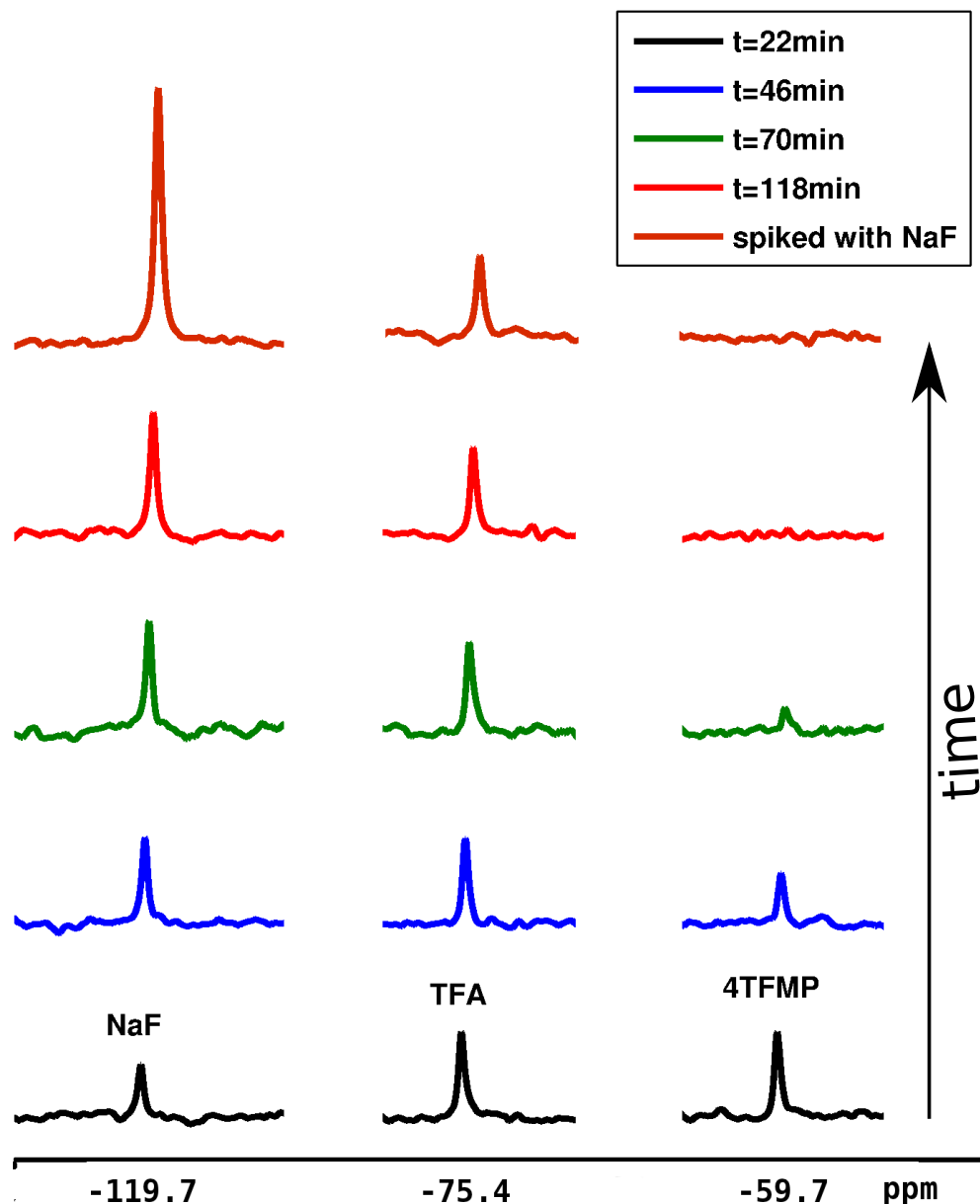
Figure 6.13: 4TFMP Hydrolysis at pH 10.25 monitored by ^{19}F NMR

The initial and the final spectrum of Figure 6.12(a) take a great resemblance of standard 4TFMP and 4HYBA UV-Vis spectrum shown in Figure 6.12(b). Selecting the maxium absorbance for 4TFMP and 4HYBA respectively and plot their intensities evolution vs. time resulted in Figure 6.12(c). It can been seen that the trend of 4TFMP decay and 4HYBA growth show great correlations. After linearization (6.7.1),

the decay rate of 4TFMP and the growth rate of 4HYBA almost overlap each other (Figure 6.12(d)). This strongly suggest that 4TFMP hydrolysis to produce 4HYBA. Another test of this hypothesis comes from ^{19}F NMR experiment. 3×10^{-5} M 4TFMP was dissolved in pH10.25 buffer according to the procedure described in 6.3.2. Time elapsed ^{19}F signals, 4TFMP, F$^-$ and TFA(trifluoroaceticacid) were recorded and presented in Figure 6.13. Due to the low sample quantity, 1024 scans were used to produce one spectrum with acceptable signal to noise level. It is noticed from the Figure 6.13 that the 4TFMP signal decreases in company with the F$^-$ signal increase as experiment progresses. The internal reference TFA does not show noticeable change in signal intensity among all the spectra in Figure 6.13. In the end of experiment, F$^-$ was spiked into the reaction mixture and this caused the enhancement of the F$^-$ signal on NMR. This evidence supports the 4TFMP produces F$^-$ after hydrolysis. Literature survey also support 4TFMP conversion to 4HYBA in a basic environment.[21–25]

6.4.5   Fluxoetine aldehyde — the missing piece of the puzzle

6.4.5.1   FLXALD — A Fleeting Species

Collecting all the evidence from HPLC, GC-MS, NMR, UV-Vis and IC(ion chromatography) studies, the degradation pathway of FLX under TAML treatment can be constructed (Figure 6.15). Clearly, something is missing along the path in Figure 6.15 — the amine group. The hint to this riddle can be found in the sertraline case study. As shown in Scheme 5.2 and Scheme 5.3, TAML can simulate CYP450 to convert amine to a ketone. If one pieces CINALD and 4TFMP together, it comes out as an aldehyde, inked blue in Figure 6.15. If this compound were on the FLX's degradation pathway, then the follow-up question would be why it was not detected by the analytical screening.
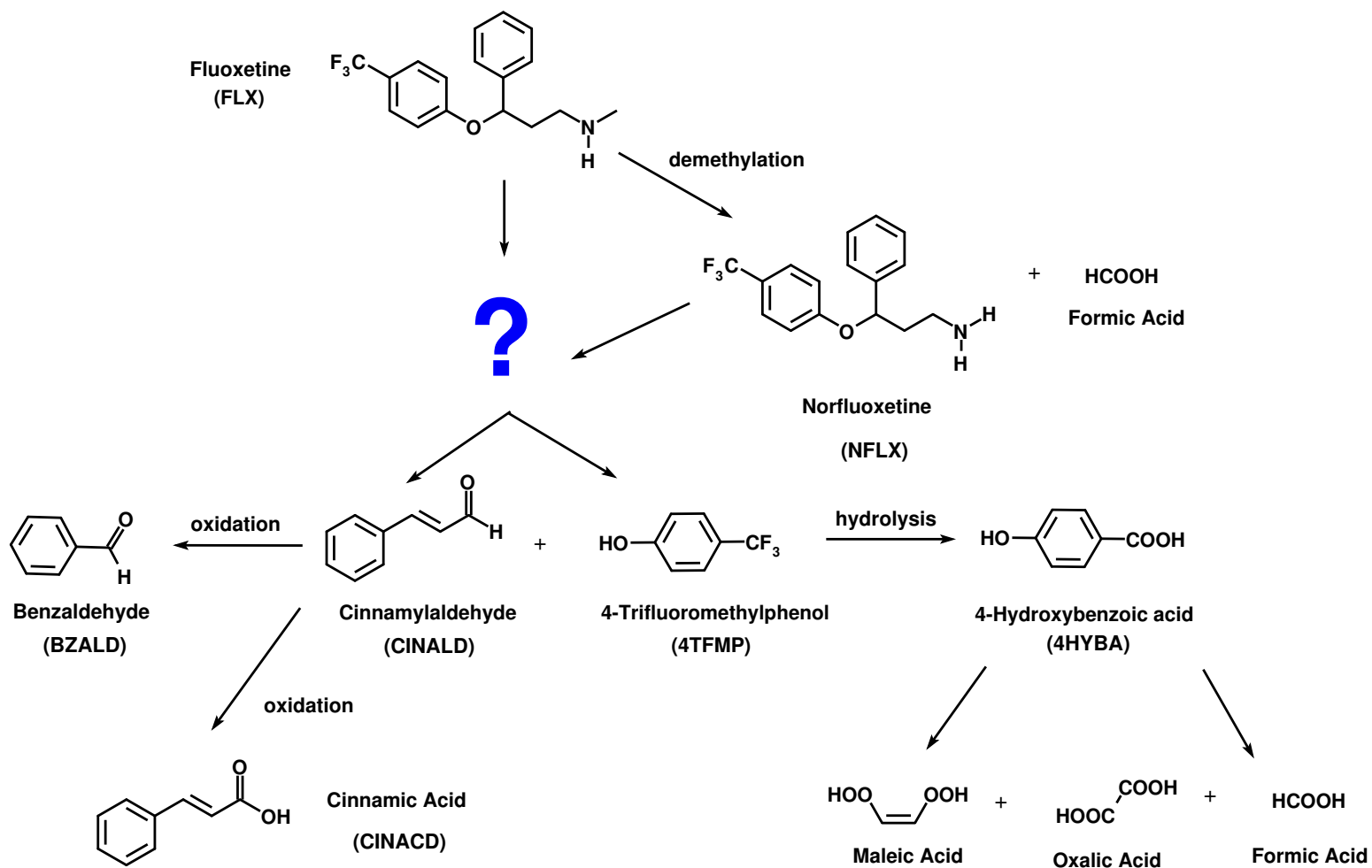
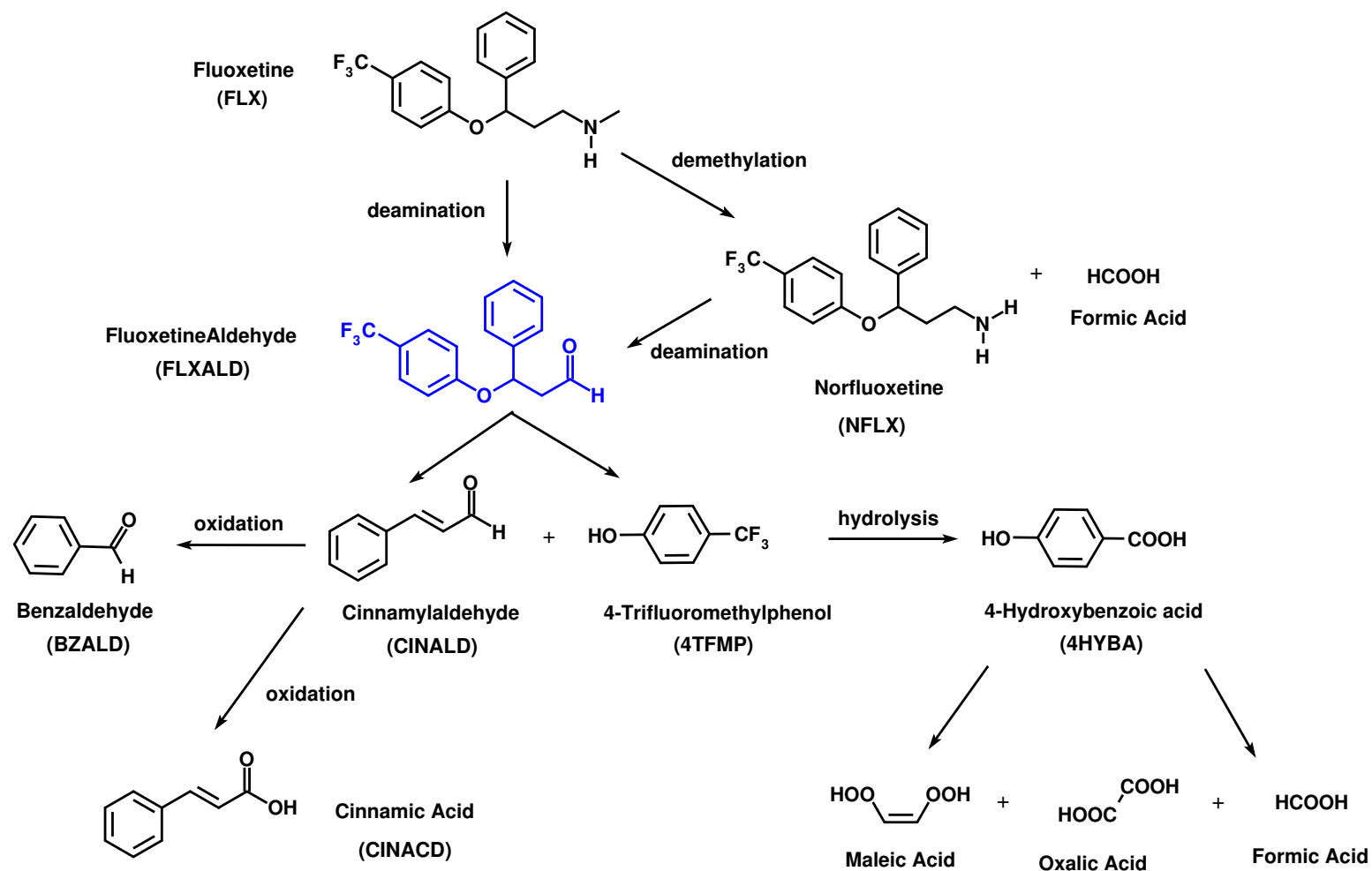Figure 6.14: Proposed incomplete FLX degradation pathway under TAML treatment

Figure 6.15: Proposed complete FLX degradation pathway under TAML treatment

The hypothesized pathway for FLXALD decomposition is via β-elimination as illustrated in Figure 6.16.
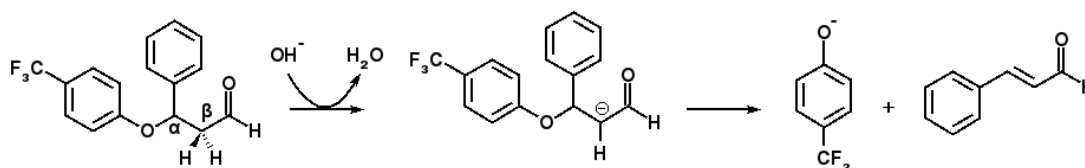
Figure 6.16: FLXALD β-elimination mechanism

To test this hypothesis and probe the possible elimination mechanism, an in silico investigation was performed. DFT-based theoretical calculations were performed with Gaussian 09 rev.B.01,[26] using Becke's three parameter hybrid functional (B3)[27,28] along with the Lee-Yang-Parr correlation functional (LYP)[29] and basis set 6-31G(d). The solvent effect was considered using the SMD continuum model.[30] A 3D reaction potential profile(Figure 6.17) was constructed to gain insight into the reaction mechanism.

Figure 6.17: FLXALD β-elimination 3D potential profile

Two transition states and one intermediate state revealed in Figure 6.17. This sug-

gests the reaction mechanism is more likely to be E1 or E1cb. Given the huge re-
action barrier for the $O-C_{alpha}$ bond dissociation without the induction from the
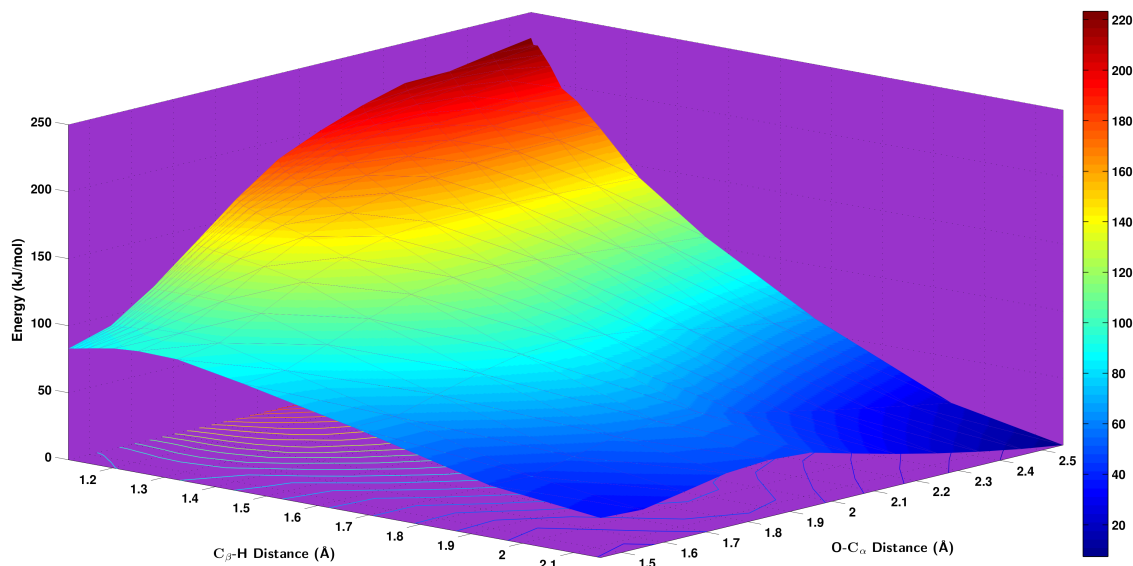nucleophile, the E1 mechanism is out of the question. So, E1cb is likely to be best
mechanistic description to account for the β-elimination for FLXALD. The energy
barriers are 7.3 kJ/mol and 10.5 kJ/mol for the two consecutive steps respectively.
These reaction barriers are even lower than the free rotation barrier ($\sim$ 12 kJ/mol) at
room temperature. Therefore, it is no wonder that FLXALD escaped the analytical
scrutinization.

6.4.5.2   Solvent Effects on the Elimination Mechanism
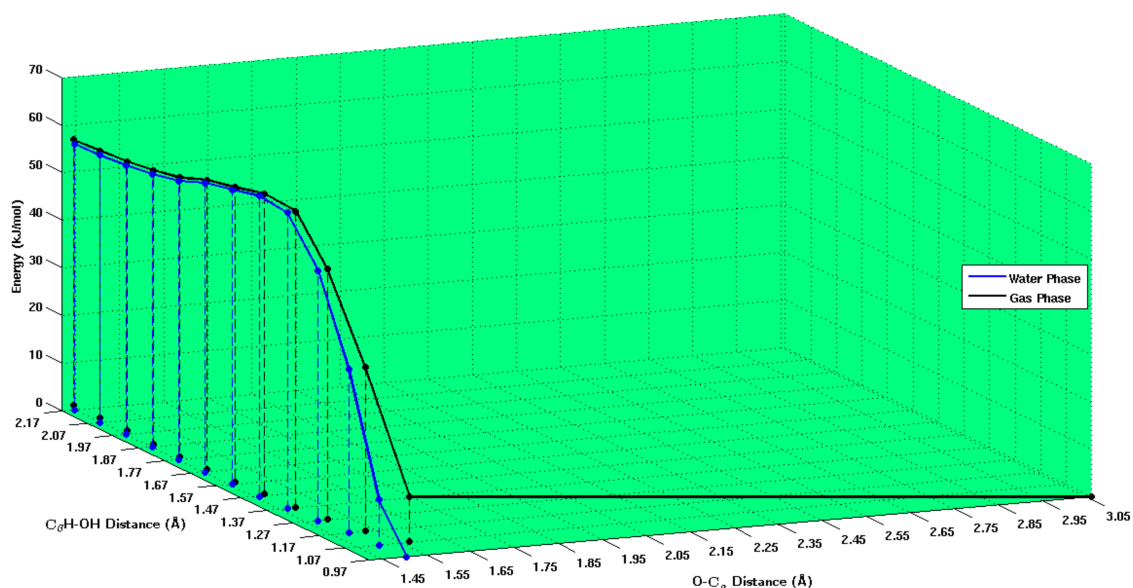
Figure 6.18: Comparison of OH^- attacking FLXALD in water and gas phase

A closer study on the simulation results discloses the solvent impact on FLXALD's
elimination mechanism. Figure 6.18 plots the $O-C_\alpha$ distance as a function of OH^-
approaching in the water phase (blue curve) and gas phase (black curve). The com-
mon feature of the two curves is that they both deviate from their original distance
as OH^- gets closer. This result reflects the inductive effect of the OH^- group, i.e.

it weakens the $O-C_{\alpha}$ bonds as it moves in. In this sense, the E1cb mechanism of FLXALD is contaminated with the E2 feature and this contamination is more severe for the gas phase than the water phase. Up to certain point in the gas phase, the $O-C_{\alpha}$ bond disengaged automatically. So, FLXALD elimination should be better described as a borderline case between E2 and E1cb, and it shifts more toward E2 as the reaction moves into the gas phase.

Table 6.4: $O-C_{\alpha}$ bond length variation as OH^- approaches in multiple reaction media

$HO\cdots H$ (Å)	$O-C_{\alpha}$ (Å)	Medium	ϵ_r
1.070	1.500	Water	78.3553
0.970	1.504	Water	78.3553
1.070	1.500	1,2-EthaneDiol	40.245
0.970	1.506	1,2-EthaneDiol	40.245
1.070	1.513	Acetone	20.493
0.970	1.523	Acetone	20.493
1.070	1.518	Pentanal	10.0
0.970	1.530	Pentanal	10.0
1.070	1.526	Diethylether	4.24
0.970	1.541	Diethylether	4.24
1.070	1.542	CycloPentane	1.9608
0.970	1.567	CycloPentane	1.9608
1.070	1.571	Vacuum	1.00
0.970	3.060	Vacuum	1.00

To further explore the effects of solvent on the reaction mechanism of FLXALD, a series of simulations of OH^- attack were performed in multiple media. The result is summarized in Table 6.4. Clearly, as the dielectric constant of the medium becomes smaller, the $O-C_{\alpha}$ bond extenuation aggravates. This suggests the stability of the intermediate carbonanion depends on the medium. Born model can give a qualitative

explanation for this phenomenon.

$$\Delta G_{\text{sol}} = -\frac{z_i^2 \, e^2 \, N_A}{8 \, \pi \, \epsilon_0 \, r_i} \left(1 - \frac{1}{\epsilon_r} \right) \tag{6.1}$$

where z_i is the charge and r_i is the radius of ion.

Eqn 6.1 shows that solvation energy favors small and highly charged species in a medium with high relative permittivity. There it is plausible for the charged species, the FLXALD carbonanion intermediate, to gain stability as the relative permittivity of the medium increases. When the system is deprived of solvent, the situation changed dramatically. Eqn 6.1 is essentially a energy difference for a charged species between in the solvent phase and the gas phase. When the solvent phase is not involved, the relative permittivity term $^1/_{\epsilon_r}$ disappeared and eqn 6.1 flips the sign. Consequently, a charged species with a smaller volume in the gas phase is favored because of less energy penalty. On the case of FLXALD attacked by OH^- in the gas phase, the large energy penalty on the FLXALD carbonanion intermediates drives it shred off a fragment to reduce its energy debt and thus makes the FLXALD elimination mechanism more E2 like.

The process of the FLXALD carbonanion intermediate scission in the gas is also quite intriguing. If the invading OH^- and FLXALD is carved into two moieties according to Figure 6.19 and plot their Mulliken charge evolution vs. the distance between OH^- and the β H, Figure 6.20 results. FLXALD alone is a neutral species. Induced by the distant OH^-, nearly half minus charge has already shifted onto moiety 2 to make moiety half positive. As OH^- draws in, the positive charge on moiety 1 sinks to about 0.8 and so does the negative charge on moiety 2. When the critical point arrives, suddenly the charge on moiety 1 and 2 swapped and simultaneously the FLXALD carbonanion intermediates collapses into $4TFMP^-$ and CINALD.
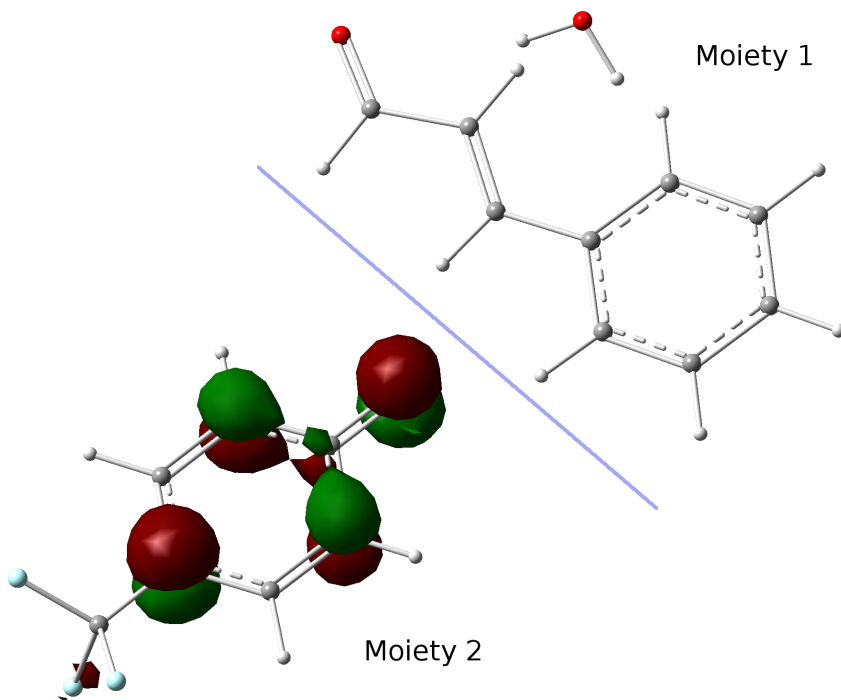
Figure 6.19: HOMO molecular orbital of FLXALD carbonanion after charge separation in the gas phase

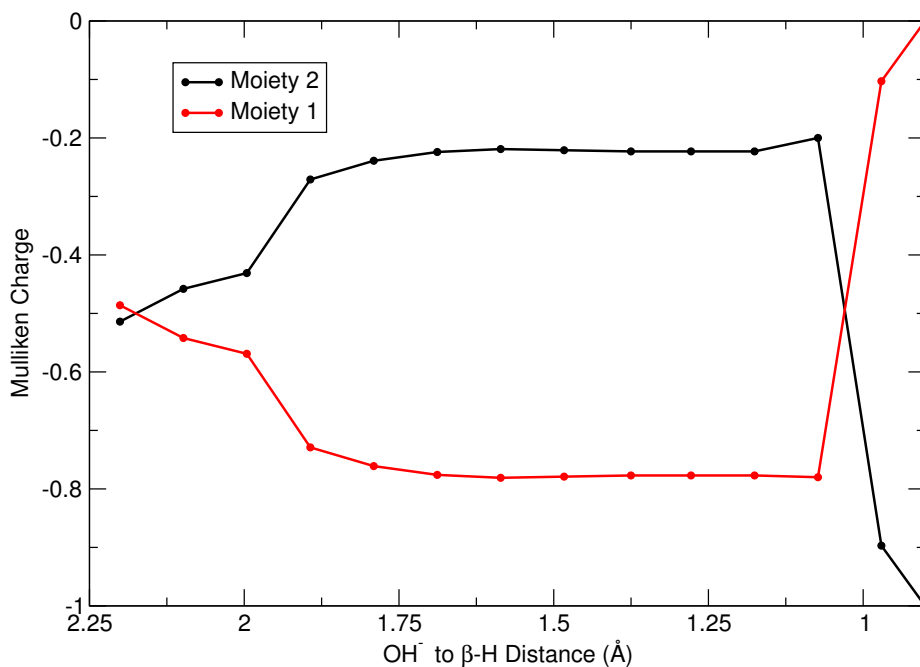

Figure 6.20: Mulliken charge evolution during the process of OH⁻ attack FLXALD in the gas phase

The computational elucidation of the fate of FLXALD closed the chemistry circle of FLX degradation. However, the interesting finding on the elusive intermediate FLX-ALD provokes thoughts far and beyond. FLX and NFLX exhibit herculean resilience to natural attenuation. However, when the external stress exceeds the threshold, a exquisitely fragile intermediate produces, FLXALD. It is this labile identity that hubs to the cascade breakdown pathway of FLX until harmless endpoints. This observation sparkle an idea in green pharmaceutical design — enfolding vulnerability into the stability of molecule. That is designing a stable pharmaceutical molecule with certain debile building blocks. Once the environmental tension surpasses the limit of safety fuse, a central feeble intermediate will be created and conduces further downstream debacle. With the realization of such a vision, the seemingly paradoxical dual need for a pharmaceutical to be stable as well as degradable can be harmonized on the contemplative choice of stress conditions and sagacious molecular engineering.

6.5 Conclusions

This chapter studied the oxidative degradation of fluoxetine by Fe-TAML activators. The experimental results demonstrate that the Fe-TAML/H_2O_2 system can rapidly degrade this environmentally stubborn molecule. A combination of analytical techniques and computer simulation unveil the scenic degradation pathway of FLX. The in scilico exploration of the fugitive intermediate FLXALD reveals its evanescent thermodynamic kernel. Computational results also suggests the elimination mechanism of FLXALD is a borderline case between E1cb and E2 and solvent has great influence on the mechanism. The discovery of this hub species inspires the design idea for green pharmaceuticals — a vision to integrate degradability under specific stress in parallel with the necessarily therapeutic stability. If the vulnerability of the interme-

diate can be carefully calibrated, it can be used as an internal witch to trigger the decomposition of the entire module in response of a proper external stress.

6.6 References

[1] I. S. Ruhoy, C. G. Daughton. Types and quantities of leftover drugs entering the environment via disposal to sewage–revealed by coroner records. *Sci. Total Environ.* **2007**, *388*, 137–48.

[2] S. C. Monteiro, A. B. A. Boxall. Occurrence and fate of human pharmaceuticals in the environment. *Rev. Environ. Contam. Toxicol.* **2010**, *202*, 53–154.

[3] K. Kümmerer. Pharmaceuticals in the Environment. *Annu. Rev. Environ. Resour.* **2010**, *35*, 57–75.

[4] S. Webb, T. Ternes, M. Gibert, K. Olejniczak. Indirect human exposure to pharmaceuticals via drinking water. *Toxicol. Lett.* **2003**, *142*, 157–167.

[5] E. Vulliet, C. Cren-Olivé, M.-F. Grenier-Loustalot. Occurrence of pharmaceuticals and hormones in drinking water treated from surface waters. *Environ. Chem. Lett.* **2009**, *9*, 103–114.

[6] http://www.sfgate.com/health/article/Antidepressants\-nation-s-top-prescription-4034392.php.

[7] D. T. Wong, K. W. Perry, F. P. Bymaster. Case history: the discovery of fluoxetine hydrochloride (Prozac). *Nat. Rev. Drug Discov.* **2005**, *4*, 764–74.

[8] A. Rossi, A. Barraco, P. Donda. Fluoxetine: a review on evidence based medicine. *Annals of general hospital psychiatry* **2004**, *3*, 2.

[9] T. Vasskog, U. Berger, P. J. Samuelsen, R. Kallenborn, E. Jensen. Selective serotonin reuptake inhibitors in sewage influents and effluents from Tromso, Norway. *J. Chromatogr. A* **2006**, *1115*, 187–195.

[10] A. J. Ramirez, M. A. Mottaleb, B. W. Brooks, C. K. Chambliss. Analysis of pharmaceuticals in fish using liquid chromatography-tandem mass spectrometry. *Anal. Chem.* **2007**, *79*, 3155–3163.

[11] M. M. Schultz, E. T. Furlong. Trace analysis of antidepressant pharmaceuticals and their select degradates in aquatic matrixes by LC/ESI/MS/MS. *Anal. Chem.* **2008**, *80*, 1756–62.

[12] M. M. Schultz, E. T. Furlong, D. W. Kolpin, S. L. Werner, H. L. Schoenfuss, L. B. Barber, V. S. Blazer, D. O. Norris, A. M. Vajda. Antidepressant pharmaceuticals in two U.S. effluent-impacted streams: occurrence and fate in water and sediment, and selective uptake in fish neural tissue. *Environ. Sci. Technol.* **2010**, *44*, 1918–25.

[13] J.-W. Kwon, K. L. Armbrust. Laboratory persistence and fate of fluoxetine in aquatic environments. *Environ. Toxicol. Chem.* **2006**, *25*, 2561–8.

[14] B. W. Brooks, P. K. Turner, J. K. Stanley, J. J. Weston, E. a. Glidewell, C. M. Foran, M. Slattery, T. W. La Point, D. B. Huggett. Waterborne and sediment toxicity of fluoxetine to select organisms. *Chemosphere* **2003**, *52*, 135–42.

[15] B. W. Brooks, C. M. Foran, S. M. Richards, J. Weston, P. K. Turner, J. K. Stanley, K. R. Solomon, M. Slattery, T. W. La Point. Aquatic ecotoxicology of fluoxetine. *Toxicol. Lett.* **2003**, *142*, 169–183.

[16] B. Mayhew, D. Jones, S. Hall. An in vitro model for predicting in vivo inhibition of cytochrome P450 3A4 by metabolic intermediate complex formation. *Drug Metab. Dispos.* **2000**, *28*, 1031–1037.

[17] H. R. Foster, G. A. Burton, N. Basu, E. E. Werner. Chronic exposure to fluoxetine (Prozac) causes developmental delays in Rana pipiens larvae. *Environ. Toxicol. Chem.* **2010**, *29*, 2845–50.

[18] J. a. Mennigen, P. Stroud, J. M. Zamora, T. W. Moon, V. L. Trudeau. Pharmaceuticals as neuroendocrine disruptors: lessons learned from fish on Prozac. *J. Toxicol. Environ. Health B Crit. Rev.* **2011**, *14*, 387–412.

[19] C. P. Horwitz, A. Ghosh, *Synthesis of macrocyclic tetraamido compounds and new metal insertion process (http://freepatentsonline.com/7060818.html)*, **2006**. http://freepatentsonline.com/7060818.html.

[20] P. George. The chemical nature of the 2nd-hydrogen peroxide compound formed by cytochrome-c-peroxidase and horseradish peroxidase .2. formation and decomposition. *Biochem. J.* **1953**, *55*, 220–230.

[21] R. Jones. Ortho and para substituted derivatives of benzotrifluoride. *J. Am. Chem. Soc.* **1947**, *69*, 2346–2350.

[22] D. N. Kozachuk, Y. A. Serguchev, Y. A. Fiakov, L. M. Yagupol'skii. Hydrolysis of trifluomethyl group attached to aromatic system IV. Kinetics of alkali hydrolysis of p-hydroxybenzotrifluoride and 4-trifluoromethyl-4'-hydroxyazobenzene. *Journal of Organic chemistry of the USSR* **1973**, *9*, 1936–1938.

[23] T. T. Sakai, D. V. Santi. Hydrolysis of hydroxybenzotrifluorides and fluorinated uracil derivatives. A general mechanism for carbon-fluorine bond labilization. *J. Med. Chem.* **1973**, *16*, 1079–84.

[24] D. C. Thompson, K. Perera, R. London. Spontaneous hydrolysis of 4-trifluoromethylphenol to a quinone methide and subsequent protein alkylation. *Chem.-Biol. Interact.* **2000**, *126*, 1–14.

[25] U. M. Reinscheid, J. Vervoort, H. Zuilhof. Mild hydrolysis of 2-trifluoromethylphenol: kinetics, mechanism and environmental relevance. *Chemosphere* **2006**, *65*, 318–23.

[26] M. J. Frisch, G. W. Trucks, H. B. Schlegel, G. E. Scuseria, M. A. Robb, J. R. Cheeseman, G. Scalmani, V. Barone, B. Mennucci, G. A. Petersson, H. Nakatsuji, M. Caricato, X. Li, H. P. Hratchian, A. F. Izmaylov, J. Bloino, G. Zheng, J. L. Sonnenberg, M. Hada, M. Ehara, K. Toyota, R. Fukuda, J. Hasegawa, M. Ishida, T. Nakajima, Y. Honda, O. Kitao, H. Nakai, T. Vreven, J. A. Montgomery, J. E. Peralta, F. Ogliaro, M. Bearpark, J. J. Heyd, E. Brothers, K. N. Kudin, V. N. Staroverov, R. Kobayashi, J. Normand, K. Raghavachari, A. Rendell, J. C. Burant, S. S. Iyengar, J. Tomasi, M. Cossi, N. Rega, J. M. Millam, M. Klene, J. E. Knox, J. B. Cross, V. Bakken, C. Adamo, J. Jaramillo, R. Gomperts, R. E. Stratmann, O. Yazyev, A. J. Austin, R. Cammi, C. Pomelli, J. W. Ochterski, R. L. Martin, K. Morokuma, V. G. Zakrzewski, G. A. Voth, P. Salvador, J. J. Dannenberg, S. Dapprich, A. D. Daniels, Farkas, J. B. Foresman, J. V. Ortiz, J. Cioslowski, D. J. Fox, *Gaussian 09, Revision B.01*, **2009**.

[27] A. D. Becke. Density-functional thermochemistry. III. The role of exact exchange. *J. Chem. Phys.* **1993**, *98*, 3–7.

[28] A. D. Becke. Density-functional exchange-energy approximation with correct asymptotic behavior. *Phys. Rev. A* **1988**, *38*, 3098–3100.

[29] C. Lee, W. Yang, R. G. Parr. Development of the Colle-Salvetti correlation-energy formula into a functional of the electron density. *Phys. Rev. B* **1988**, *37*, 785–789.

[30] A. V. Marenich, C. J. Cramer, D. G. Truhlar. Universal Solvation Model Based on Solute Electron Density and on a Continuum Model of the Solvent Defined by the Bulk Dielectric Constant and Atomic Surface Tensions. *J. Phys. Chem. B* **2009**, *113*, 6378–6396.

6.7 Appendices

6.7.1 Mathematical Treatment for Analyzing the case of A→B Conversion based on UV-Vis Observations

System : A$\longrightarrow$ B

Let D be the UV-Vis signal intensity, ϵ be the absorbance coefficient, subscript i represent the initial state and subscript f represent the final state and 0 for state when the system contains A only.

$$\left\{ \begin{array}{c} A_i = (1 - \lambda)A_0 \\ B_i = \lambda A_0 \end{array} \right\}$$

$$\Longrightarrow D_t = D_{A,t} + D_{B,t} + D_{B,i}$$

$$= \epsilon_A A_i e^{-kt} + \epsilon_B A_i \left(1 - e^{-kt}\right) + \epsilon_B B_i$$

$$= \epsilon_B A_0 + (1 - \lambda)A_0 \left(\epsilon_A - \epsilon_B\right) \exp(-kt)$$

$$\Longrightarrow \left\{ \begin{array}{c} \dot{D}_t = (1 - \lambda)A_0 \left(\epsilon_A - \epsilon_B\right) (-k) \exp(-kt) \\ \dot{D}_{t_i} = (1 - \lambda)A_0 \left(\epsilon_A - \epsilon_B\right) (-k) \exp\left(-kt_i\right) \end{array} \right\}$$

$$\Longrightarrow \frac{\dot{D}_t}{\dot{D}_{t_i}} = \exp\left(-kt\right)$$

$$\Longrightarrow \ln\left(\frac{\dot{D}_t}{\dot{D}_{t_i}}\right) = -kt$$

6.7.2 Mathematica Code for HPLC Data Processing

used with data exported from Shimazu labSolution® software

TimePositionSearch[timeseries_, targetstart_, targetend_,

timestartrownum_] := **Module**[{pstart, pend, i},

  For[i = 1, i <= **Length**[timeseries], i++,

   If[**Abs**[timeseries[[i]] − targetstart] <= 0.01, pstart = i];

   If[**Abs**[timeseries[[i]] − targetend] <= 0.01, pend = i]

   ];

  pstart += timestartrownum;

  pend += timestartrownum;

  {pstart, pend}

  ]

WavelengthPositionSearch[wavelengthseries_, target_] :=

 Module[{p, i},

  For[i = 1, i <= **Length**[wavelengthseries], i++,

   If[**Abs**[wavelengthseries[[i]] − target] <= 0.5, p = i, **Break**];

   ];

  p++;

  p

  ]

SingleTrace[HPLCrawdata_, targetwavelength_, smoothfactor_] :=

 Module[{timeseries, wavepos, waveseries, i, targettrace,

  wavelengthrownum, timestartrownum},

  wavelengthrownum = 26;*(∗the row # of the wavelength∗)*

  timestartrownum = 27;*(∗the row # where time series starts∗)*

   timeseries =

  HPLCrawdata[[timestartrownum ;; **Length**[HPLCrawdata] − 1, 1]];

  waveseries = HPLCrawdata[[wavelengthrownum, **All**]]/100;

  wavepos = WavelengthPositionSearch[waveseries, targetwavelength];

  targettrace =

  ExponentialMovingAverage[

   HPLCrawdata[[timestartrownum ;; **All**, wavepos]], smoothfactor]

  ]

TRACEEXTRACT[HPLCrawdata_, timestart_, timeend_, targetwavelength_,

  smoothfactor_] :=

```
Module[{i, timeseries, waveseries, timestartp, timeendp, wavelengthp,
    singletrace, corrtrace, smoothtrace, wavelengthrownum,
  timestartrownum},
 wavelengthrownum = 26;
 timestartrownum = 27;
 timeseries =
  HPLCrawdata[[timestartrownum ;; Length[HPLCrawdata] − 1, 1]];
 waveseries = HPLCrawdata[[wavelengthrownum, All]]/100;
 {timestartp, timeendp} =
  TimePositionSearch[timeseries, timestart, timeend, timestartrownum];
 wavelengthp = WavelengthPositionSearch[waveseries, targetwavelength];
 timeseries = HPLCrawdata[[timestartp ;; timeendp, 1]];
 singletrace = HPLCrawdata[[timestartp ;; timeendp, wavelengthp]];
 smoothtrace = ExponentialMovingAverage[singletrace, smoothfactor];
 {timeseries, smoothtrace}
 ]


TRACEBGSUBSTRACT[HPLCrawdata_, BGrawdata_, timestart_, timeend_,
  targetwavelength_, smoothfactor_] :=
 Module[{i, timeseries, waveseries, timestartp, timeendp, wavelengthp,
    corrstartp, correndp, singletrace, bgtrace, substractedtrace,
   corrtrace, smoothtrace, wavelengthrownum, timestartrownum},
 wavelengthrownum = 26;
 timestartrownum = 27;
 timeseries =
  HPLCrawdata[[timestartrownum ;; Length[HPLCrawdata] − 1, 1]];
 waveseries = HPLCrawdata[[wavelengthrownum, All]]/100;
 {timestartp, timeendp} =
  TimePositionSearch[timeseries, timestart, timeend, timestartrownum];
 wavelengthp = WavelengthPositionSearch[waveseries, targetwavelength];
 timeseries = HPLCrawdata[[timestartp ;; timeendp, 1]];
 singletrace = HPLCrawdata[[timestartp ;; timeendp, wavelengthp]];
 bgtrace = BGrawdata[[timestartp ;; timeendp, wavelengthp]];
 substractedtrace = singletrace − bgtrace;
```

```
  smoothtrace =
   ExponentialMovingAverage[substractedtrace, smoothfactor];
  {timeseries , smoothtrace}
  ]

TRACESUMSLOPE[extractedtrace_, pointslist_] :=
 Module[{interpolatefunc, i, j, x1, x2, y1, y2, sumstartp, sumendp,
    peakarealist , area, intensity , timeseries , baseline },
  timeseries  = extractedtrace [[1]];
  intensity  = extractedtrace [[2]];
  peakarealist  = {};
  For[i = 1, i  <= Length[pointslist], i += 2,
   x1 = pointslist [[ i ,  1]];
   y1 = pointslist [[ i ,  2]];
   x2 = pointslist [[ i  + 1,  1]];
   y2 = pointslist [[ i  + 1,  2]];
   baseline [x_] := (y2 − y1)/(x2 − x1) (x − x1) +
     y1;(∗baseline  linear  equation∗)

   For[j = 1, j  <= Length[extractedtrace[[1]]], j++,
    If[extractedtrace [[1,  j ]]  <= x1 &&
       extractedtrace [[1,  j  + 1]]  > x1, sumstartp = j];
    If[( extractedtrace [[1,  j ]]  <= x2 &&
        extractedtrace [[1,  j  + 1]]  >
        x2 )  ||  (extractedtrace [[1,  j ]]  <= x2 &&
        j  == Length[extractedtrace]), sumendp = j];
    area = 0;
    ];
   For[j = sumstartp, j < sumendp, j++,
    area += (timeseries[[j  + 1]]  − timeseries [[ j ]]) ∗( intensity [[ j ]]  −
        baseline [ timeseries [[ j ]]])
    ];
   peakarealist  = Append[peakarealist, area];
   ];
  peakarealist
```

]

6.7.3 Mathematica Code for UV-Vis Data Processing

used with data exported from Aglient 845 UV-Visible System

```
KineticSpectraStack[rawdata_, startp_, endp_, step_, startw_, endw_,
  curvecolor_, framethickness_, fontsize_, fontweight_] :=
 Module[{i, f, nframes, wavestart, waveend, wavelengthList,
   selwavelengthList, absorbanceList, UVSpectraListPlot},
  wavelengthList =
   rawdata[[6,
    2  ;;]]; (*Wavelength list ofthe  full  spectra*){wavestart,
    waveend} = PosSearch[wavelengthList, startw, endw];
  selwavelengthList = wavelengthList[[wavestart ;; waveend]];
  nframes = Floor[(endp − startp)/step] + 1;(*number of frames*)
  absorbanceList =
   Array[f, nframes];(*Absorbance list  for  each time point*)
  For[i = startp, i <= endp, i += step,
   absorbanceList[[(i − startp)/step + 1]] =
    rawdata[[i, wavestart ;; waveend]]];
  UVSpectraListPlot =
   Array[f, nframes];(*UV spectrum listplot  for  each time point*)
  For[i = 1, i <= nframes, i++,
   UVSpectraListPlot[[i]] =
    ListPlot[{selwavelengthList, absorbanceList[[i]]}\[ Transpose],
     PlotStyle −> curvecolor, Joined −> True, PlotRange −> All]];
  Show[UVSpectraListPlot, Frame −> {{True, False}, {True, False}},
   FrameLabel −> {"Wavelength␣(nm)", "Absorbance"},
   FrameStyle −> AbsoluteThickness[framethickness],
   ImageSize −> Large,
   BaseStyle −> {FontFamily −> "Helvetica", FontSize −> fontsize,
     FontWeight −> fontweight}, AxesOrigin −> {Automatic, 0}]]
```

Needs["PlotLegends`"]

SpectraOverlay[rawspectralist_, startw_, endw_, curvecolorlist_,
  framethickness_, fontsize_, fontweight_] :=
 Module[{i, f, wavestart, waveend, spectranum, spectralist,
    spectralistplot , plotstyle }, spectranum = **Length**[rawspectralist];
 (∗legendmarkerseq=Array[f,spectranum];∗)(∗For[i=1,i<=spectranum,i++,
 legendmarkerseq[[i]]=Style["−",Hue[i/
 spectranum]]];∗){wavestart, waveend} =
  PosSearch[rawspectralist [[1]][[2 ;;, 1]], startw, endw];
  spectralist = **Array**[f, spectranum];
 For[i = 1, i <= spectranum, i++,
   spectralist [[i]] =
    rawspectralist [[i]][[wavestart ;; waveend, 1 ;; 2]]];
  spectralistplot = **Array**[f, **Length**[rawspectralist]];
 For[i = 1, i <= spectranum, i++,
   spectralistplot [[i]] =
   ListPlot[spectralist [[i]], Joined −> **True**,
    PlotRange −> {{startw, endw}, **All**},
    Frame −> {{**True**, **False**}, {**True**, **False**}},
    FrameLabel −> {"Wavelength␣(nm)", "Absorbance"},
    FrameStyle −> **AbsoluteThickness**[framethickness],
    PlotStyle −> {curvecolorlist[[i]], Thick},
    BaseStyle −> {**FontFamily** −> "Helvetica", **FontSize** −> fontsize,
      FontWeight −> fontweight}, **ImageSize** −> Large]];
  Show[spectralistplot]

EvolutionPeek[rawspectrum_, startw_, endw_, startt_, endt_, step_,
  color_] :=
 Module[{i, f, wavesel, tstart , tend, npoints, timeseries ,
    absorbancelist },
  wavesel = PosSearch[rawspectrum[[6, 2 ;;]], startw, endw][[1]];
  {tstart , tend} = PosSearch[rawspectrum[[7 ;;, 1]], startt , endt];
  npoints = **Floor**[(tend − tstart)/step] + 1;*(∗number of points∗)*
  timeseries = **Array**[f, npoints];
  absorbancelist =
   Array[f, npoints];*(∗Absorbance list for each time point∗)*

```
  For[i = tstart, i <= tend, i += step,
    timeseries [[( i − tstart)/step + 1]] = rawspectrum[[i + 6, 1]];
    absorbancelist [[( i − tstart)/step + 1]] =
     rawspectrum[[i + 6, wavesel ]];];
  ListPlot[{timeseries, absorbancelist}\[Transpose], Joined −> False,
   PlotRange −> All, Axes −> False,
   Frame −> {{True, False}, {True, False}},
   FrameLabel −> {"time (sec)", "Absorbance"}, PlotStyle −> {color},
   ImageSize −> Large]]

TimeEvolution[rawspectrum_, targetw_, startt_, endt_, step_,
  kguess_] :=
 Module[{i, f, k, Ab, timeweight, wavesel, tstartpos, tendpos,
    timeseries, absorbancelist, Dabsorbancelist, Dabsortancelistlength,
    npoints, evolutionlist, tangent, spanlist, Devolutionlist,
    nonlinfitfunc, Ai, Af, Afguess, logDabsorbancelist,
    logDevolutionlist, linfitfunc, t, x},
  wavesel = PosSearch[rawspectrum[[6, 2 ;;]], targetw, targetw ]][[1]];
  {tstartpos, tendpos} =
   PosSearch[rawspectrum[[7 ;;, 1]], startt, endt];
  npoints = tendpos − tstartpos + 1;(*number of points*)

  timeseries = Array[f, npoints];
  absorbancelist =
   Array[f, npoints];(*Absorbance list for each time point*)

  Dabsorbancelist = Array[f, npoints − step];
  For[i = tstartpos, i <= tendpos, i += 1,
    timeseries [[ i − tstartpos + 1]] =
     rawspectrum[[i + 6, 1]] − rawspectrum[[tstartpos + 6, 1]];
    absorbancelist [[ i − tstartpos + 1]] =
     rawspectrum[[i + 6, wavesel ]];];
   evolutionlist = {timeseries, absorbancelist}\[Transpose];
  Ai = absorbancelist [[1]];
  Afguess = absorbancelist [[−1]];
```

```
nonlinfitfunc =
 NonlinearModelFit[evolutionlist,
   Af + (Ai − Af) Exp[−k t], {{k, kguess}, {Af, Afguess}}, t];
 Dabsortancelistlength = npoints − step;
 For[i = 1, i <= Dabsortancelistlength, i += 1,
  spanlist =
   Transpose[{timeseries[[i ;; i + step − 1]],
     absorbancelist [[ i ;; i + step − 1]]}];
  tangent =
   LinearModelFit[spanlist, x, x][ "BestFitParameters" ][[2]];
  Dabsorbancelist[[i ]] = tangent;
  ];
 Devolutionlist = {timeseries [[1 ;; −step − 1]],
    Dabsorbancelist}\[Transpose];
 logDabsorbancelist = Log[Dabsorbancelist/Dabsorbancelist[[1]]];
 logDevolutionlist = {timeseries [[1 ;; −step − 1]],
    logDabsorbancelist}\[Transpose];
 linfitfunc = NonlinearModelFit[logDevolutionlist, k x, k, x];
 { evolutionlist , nonlinfitfunc , logDevolutionlist , linfitfunc }]

ShowPlot[rawpairlist_, timelabel_, step_, xlabel_, ylabel_,
 framethickness_, fontsize_, fontweight_] :=
 Module[{i, j, f, plotnum, plotarray, timeweight, absorbancelistsel ,
   transpair, newpair, newtimeseq, newtimeseqsel, newtimeseqLen,
   newtimeseqselLen}, plotnum = Length[rawpairlist];(*number of pairs*)
  plotarray = Array[f, plotnum];
  Which[timelabel == "sec", timeweight = 1, timelabel == "min",
   timeweight = 60];
  For[i = 1, i <= plotnum, i++,
   If[Mod[i, 2] > 0, {transpair = Transpose[rawpairlist[[i ]]];
     newtimeseq = transpair[[1]]/timeweight;
     newtimeseqLen = Length[newtimeseq];
     newtimeseqselLen = Floor[newtimeseqLen/step];
     newtimeseqsel = Array[f, newtimeseqselLen];
     absorbancelistsel = Array[f, newtimeseqselLen];
```

```
  For[j = 1, j <= newtimeseqLen, j += step,
    newtimeseqsel[[Ceiling[j/step ]]]  = newtimeseq[[j]];
    absorbancelistsel [[ Ceiling[j/step ]]]  = transpair [[2]][[ j ]];];
  newpair = {newtimeseqsel, absorbancelistsel}\[Transpose];
  plotarray [[ i ]]  =
    ListPlot[newpair, Joined -> False, PlotRange -> All,
      Axes -> False, Frame -> {{True, False}, {True, False}},
      FrameLabel -> {xlabel, ylabel},
      FrameStyle -> AbsoluteThickness[framethickness],
      PlotStyle -> {Hue[i/plotnum], Thick, PointSize -> 0.015},
      BaseStyle -> {FontFamily -> "Helvetica", FontSize -> fontsize,
        FontWeight -> fontweight}, ImageSize -> Large];},
  plotarray [[ i ]]  =
    Plot[rawpairlist [[ i ]][[ x], {x,  rawpairlist [[ i -   1]][[1]][[1]],
      timeweight rawpairlist [[ i -   1]][[-1]][[1]]},
      PlotRange -> All, Axes -> False,
      Frame -> {{True, False}, {True, False}},
      FrameLabel -> {xlabel, ylabel},
      FrameStyle -> AbsoluteThickness[framethickness],
      PlotStyle -> {Hue[(i - 1)/plotnum], Thick},
      BaseStyle -> {FontFamily -> "Helvetica", FontSize -> fontsize,
        FontWeight -> fontweight}, ImageSize -> Large];];];
Show[plotarray]]
```

6.7.4   Mathematica Code for Mass Spectra Data Processing

used with data exported from Thermo-Fisher XCaliber® software

```
MSProcss[rawdata_, startt_, endt_, smoothfactor_, normcoef_] :=
 Module[{startp, endp, i, xaxis,  intensitylist ,  intensitylistsmooth ,
    normfactor, intensitylistsmoothnorm},
  For[i = 1, i <= Length[rawdata], i++,
   If[NumberQ[rawdata[[i, 1]]] && rawdata[[i, 1]] <= startt &&
      rawdata[[i + 1, 1]]  > startt,  startp = i];
```

```
  If[NumberQ[rawdata[[i, 1]]] && rawdata[[i, 1]] <= endt &&
    rawdata[[i + 1, 1]] >= endt, {endp = i, Break}]];
 xaxis = rawdata[[startp ;; endp, 1]];
 intensitylist  = rawdata[[startp ;; endp, 2]];
 intensitylistsmooth =
 ExponentialMovingAverage[intensitylist, smoothfactor];
 normfactor = Max[intensitylistsmooth];
 intensitylistsmoothnorm = normcoef*intensitylistsmooth/normfactor;
 {xaxis, intensitylistsmoothnorm}
 ]


MSSubstractProcss[bgdata_, rawdata_, startt_, endt_, smoothfactor_] :=
 Module[{startp, endp, i, xaxis,  intensitylist ,  intensitylistsmooth ,
  normfactor, intensitylistsmoothnorm},
  For[i = 1, i <= Length[rawdata], i++,
   If[NumberQ[rawdata[[i, 1]]] && rawdata[[i, 1]] <= startt &&
     rawdata[[i + 1, 1]] > startt, startp = i];
   If[NumberQ[rawdata[[i, 1]]] && rawdata[[i, 1]] <= endt &&
     rawdata[[i + 1, 1]] >= endt, endp = i, Break]
       ];
 xaxis = rawdata[[startp ;; endp, 1]];
  intensitylist  =
  rawdata[[startp ;; endp, 2]] − bgdata[[startp ;; endp, 2]];
 For[i = 1, i <= Length[intensitylist], i++,
  If[ intensitylist [[ i ]] < 0,  intensitylist [[ i ]] = RandomReal[10]]
  ];
 intensitylistsmooth =
  ExponentialMovingAverage[intensitylist, smoothfactor];
 normfactor = Max[intensitylistsmooth];
 intensitylistsmoothnorm = 100*intensitylistsmooth/normfactor;
 {xaxis, intensitylistsmoothnorm}
 ]


funMSPlot[flag_, data_, xaxislabel_, curvecolor_, fontsize_,
```

```
curvethickness_, framethickness_, aspectratio_, imagesize_] :=
Module[{interpolatefunc, dataDimension, MSplot},
  Which[flag == "list",
  MSplot =
   ListPlot[Transpose[{data[[1]], data [[2]]}],  Joined −> True,
    PlotRange −> Full, PlotStyle −> curvecolor,
    ImageSize −> imagesize,
    BaseStyle −> {FontFamily −> "Helvetica", FontWeight −> Bold,
      FontSize −> fontsize, AbsoluteThickness[curvethickness]},
    Axes −> {False, False}, Frame −> {{True, False}, {True, False}},
    FrameLabel −> {xaxislabel, "Relative_Abundance_(%)"},
    FrameStyle −> AbsoluteThickness[framethickness],
    AspectRatio −> aspectratio],
  flag  == "centroid",
  MSplot =
   ListPlot[Transpose[{data[[1]], data [[2]]}],  Joined −> False,
    PlotRange −> Full, PlotStyle −> curvecolor,
    ImageSize −> imagesize,
    BaseStyle −> {FontFamily −> "Helvetica", FontWeight −> Bold,
      FontSize −> fontsize, AbsoluteThickness[curvethickness]},
    Axes −> {False, False}, Frame −> {{True, False}, {True, False}},
    FrameLabel −> {xaxislabel, "Relative_Abundance_(%)"},
    FrameStyle −> AbsoluteThickness[framethickness], Filling −> Axis,
     FillingStyle  −> curvecolor, AspectRatio −> aspectratio],
  flag  == "inter",
  {interpolatefunc = Interpolation[Transpose[{data[[1]], data[[2]]}]],
   MSplot =
    Plot[interpolatefunc[x],  {x, Min[data [[1]]],  Max[data[[1]]]},
     PlotRange −> Full, PlotStyle −> curvecolor,
     ImageSize −> imagesize,
     BaseStyle −> {FontFamily −> "Helvetica", FontWeight −> Bold,
       FontSize −> fontsize, AbsoluteThickness[curvethickness]},
     Axes −> {False, False}, Frame −> {{True, False}, {True, False}},
     FrameLabel −> {xaxislabel, "Relative_Abundance_(%)"},
```

```
      FrameStyle -> AbsoluteThickness[framethickness],
      AspectRatio -> aspectratio
      ]
    }
  ];
 If[ flag == "centroid",
  Show[MSplot,
   Graphics[Line[{{data[[1, 1]], 0}, {data[[1, -1]], 0}}]],
   PlotRangeClipping -> False],
  Show[MSplot, PlotRangeClipping -> False]
  ]
 ]


funManualLabel[data_, masslist_, massspace_, format_, textcolor_,
  fontsize_, orientation_, offset_] :=
 Module[{datalen, masslistlen, massposlist, Abundancelist, i, j, f},
  datalen = Length[data[[1]]];
  masslistlen = Length[masslist];
  massposlist = Array[f, masslistlen];
  Abundancelist = Array[f, masslistlen];
  For[i = 1, i <= masslistlen, i++,
   For[j = 1, j <= datalen, j++,
    If[ Abs[masslist[[i]] - data[[1, j]]] < massspace,
      {massposlist[[i]] = j, Abundancelist[[i]] = data[[2, j]],
       Continue}];
    ];
   ];
  Graphics[
   Table[Rotate[
    Text[Style[PaddedForm[masslist[[i]], format], "Helvetica", Bold,
      fontsize, textcolor], {masslist[[i]] + offset[[1]],
      Abundancelist[[i]] + offset[[2]]}], orientation Degree], {i, 1,
     masslistlen}]
   ]
```

```
]

funMSPlotLabel[flag_, data_, xaxislabel_, curvecolor_, fontsize_,
  curvethickness_, framethickness_, aspectratio_, imagesize_,
  massspace_, threshold_, labelformat_, labelfontsize_, labelcolor_,
  orientation_, offset_] :=
 Module[{interpolatefunc, dataDimension, MSplot, i, j, datalen,
   dataRanked, peakList, massLabel, labelNum},
  datalen = Length[data[[1]]];
  Which[flag == "list",
   MSplot =
    ListPlot[Transpose[{data[[1]], data [[2]]}],  Joined −> True,
     PlotRange −> Full, PlotStyle −> curvecolor,
     ImageSize −> imagesize,
     BaseStyle −> {FontFamily −> "Helvetica", FontWeight −> Bold,
       FontSize −> fontsize, AbsoluteThickness[curvethickness]},
     Axes −> {False, False}, Frame −> {{True, False}, {True, False}},
     FrameLabel −> {xaxislabel, "Relative_Abundance_(%)"},
     FrameStyle −> AbsoluteThickness[framethickness],
     AspectRatio −> aspectratio],
   flag  == "centroid",
   MSplot =
    ListPlot[Transpose[{data[[1]], data [[2]]}],  Joined −> False,
     PlotRange −> Full, PlotStyle −> curvecolor,
     ImageSize −> imagesize,
     BaseStyle −> {FontFamily −> "Helvetica", FontWeight −> Bold,
       FontSize −> fontsize, AbsoluteThickness[curvethickness]},
     Axes −> {False, False}, Frame −> {{True, False}, {True, False}},
     FrameLabel −> {xaxislabel, "Relative_Abundance_(%)"},
     FrameStyle −> AbsoluteThickness[framethickness], Filling −> Axis,
       FillingStyle  −> curvecolor, AspectRatio −> aspectratio],
   flag  == "inter",
   {interpolatefunc = Interpolation[Transpose[{data[[1]], data[[2]]}]],
    MSplot =
```

```
  Plot[interpolatefunc[x], {x, Min[data[[1]]], Max[data[[1]]]},
    PlotRange -> Full, PlotStyle -> curvecolor,
    ImageSize -> imagesize,
    BaseStyle -> {FontFamily -> "Helvetica", FontWeight -> Bold,
      FontSize -> fontsize, AbsoluteThickness[curvethickness]},
    Axes -> {False, False}, Frame -> {{True, False}, {True, False}},
     FrameLabel -> {xaxislabel, "Relative_Abundance_(%)"},
    FrameStyle -> AbsoluteThickness[framethickness],
    AspectRatio -> aspectratio
    ]
  }
 ];
dataRanked = data[[All, Ordering@-data[[2]]]];
peakList = {};
For[i = 1, i <= datalen, i++,
 {If[dataRanked[[1, i]] >= threshold[[1, 1]] &&
    dataRanked[[1, i]] <= threshold[[1, 2]] &&
    dataRanked[[2, i]] >= threshold[[2, 1]] &&
    dataRanked[[2, i]] <= threshold[[2, 2]],
   If[peakList == {},
   peakList =
    Append[peakList, {dataRanked[[1, i]], dataRanked[[2, i]]}],
   If[RankedMin[Abs[peakList[[;; , 1]] - dataRanked[[1, i]]]], 1] >=
      massspace,
    peakList =
     Append[peakList, {dataRanked[[1, i]], dataRanked[[2, i]]}]
     ]
    ]
   ],
  If[dataRanked[[2, i]] < threshold [[1]], Break[]
   ]
  }
 ];
(*massspace is a measure of distance between peaks. For most cases,
```

```
 it  is  1  amu.*)
labelNum = Length[peakList[[;; , 1]]];
massLabel =
 Graphics[
  Table[Rotate[
    Text[Style[
      PaddedForm[
        peakList[[j, 1]], {labelformat [[1]], labelformat [[2]]}],
       "Helvetica", Bold, labelfontsize ,
       labelcolor ], {peakList[[j, 1]] + offset [[1]],
       peakList[[j, 2]] + offset [[2]]}], orientation Degree], {j, 1,
    labelNum}]];
If[ flag == "centroid",
 Show[MSplot, massLabel,
  Graphics[Line[{{data[[1, 1]], 0}, {data[[1, −1]], 0}}]],
  PlotRangeClipping −> False],
 Show[MSplot, massLabel, PlotRangeClipping −> False]
 ]
]
```